Universitat Autònoma de Barcelona

Design, characterization and fabrication of electrochromic flexible materials for the development of smart devices

Sara Santiago Malagón

Universitat Autònoma de Barcelona

Doctoral Thesis

Design, characterization and fabrication of electrochromic flexible materials for the development of smart devices

Sara Santiago Malagón

Directors:

Dr. Gonzalo Guirado López

Dr. Xavier Muñoz Berbel

Department of Chemistry

Faculty of Science

PhD in Electrochemistry. Science and Technology

July, 2022

The present doctoral thesis entitled '**Design, characterization and fabrication of electrochomic flexible materials for the development of smart devices**' is presented by Sara Santiago Malagón as a partial fulfilment of the requirements to obtain the degree of Doctor of Philosophy in Electrochemistry.

The present thesis was carried out at the Electrochemistry and Green Chemistry Group at the University Autonomous of Barcelona (UAB) and the Chemical Transducers Group at the Institute of Microelectronics of Barcelona (IMB-CNM, CSIC).

With the approval of:

Dr. Gonzalo Guirado López

(Director and Tutor)

Dr. F. Xavier Muñoz Berbel

(Director)

Sara Santiago Malagón

(Author)

Bellaterra, 2022

Acknlowledgements

I would like to thank the financial support of this thesis through the following projects and contracts:

- SEAMLESS (PROD 0000114) project; Enterprise and Knowledge, Industry Department, Generalitat de Catalunya.
- Associate Professor at Chemistry Department at UAB.
- SINCRO RTC2019-007060-2/AEI/MICIU project.

Hace ya seis años que pisé por primera vez el laboratorio de Electroquímica y Química Verde de la UAB cuando empecé mi TFG. ¡¡Seis!! Quién lo iba a decir, yo que no sabía ni siquiera si hacer un máster... Supongo que al final el mundo de la investigación me despertó curiosidad y me enganchó, y tiempo después aquí sigo, con ganas de continuar. Tengo claro que esto no hubiera ocurrido si parte de mi tesis doctoral no hubiera tenido lugar también en el Centro de Microelectrónica de Barcelona (IMB-CNM), que me ha permitido ver la investigación desde un punto de vista distinto, pero sobre todo práctico y muy enriquecedor.

En primer lloc, m'agradaria agrair als meus directors de tesi totes les oportunitats que m'han brindat: congressos, una estada doctoral i més publicacions de les que hagués imaginat mai... Gràcies! Em considero una afortunada d'haver pogut realitzar aquesta tesi doctoral amb tots dos.

M'agradaria agrair-li al Gonzalo Guirado, a qui dec gran part de la meva formació com a investigadora per haver treballat amb ell ja fa sis anys. T'agreixo molt el teu tracte tan personal que sempre has tingut amb tots nosaltres que ens ha permès treballar amb total llibertat i autonomia. La teva confiança en mi, la teva paciència, i sobretot la capacitat, per fer de les coses complicades una cosa fàcil. Gràcies!!!

Moltíssimes gràcies també al Xavi Muñoz. Tot i que vaig començar a treballar amb tu temps més tard, conèixer-te ha estat un cop d'aire fresc. La teva capacitat per divulgar ciència i idees boges han estat inspiradores per mi i son un exemple a seguir. Gràcies per aquestes xerrades motivacionals i a vegades random, que son dignes d'una TED talk. A tu també, gràcies per la confiança dipositada en mi i també per saber entendre'm i animar-me.

Muchas gracias también a todo el grupo de GTQ por permitirme realizar parte de mi tesis doctoral en vuestro grupo y por prestaros a ayudarme sin pensarlo, no solo a mí, sino a cualquier persona que lo ha necesitado.

I would like to thank Prof. Luisa de Cola for her warm welcome in Milan from the first day to the last. There is a lot of knowledge that I take from the months I was there and great colleagues that I have met. Thanks to the whole group for making me feel one more. I'm grateful for the opportunity to have spent a few months with you guys. Grazie mille per tutto!

Muchas gracias también a Javier del Campo y Miguel Aller, que marcaron mi primera etapa como doctorando y de los cuales he aprendido muchísimo.

Gràcies també al Jordi Hernando per la seva predisposició a ajudar sempre que ha sigut necessari, per la seva dedicació admirable i per les seves correccions mil·limètriques que agreixo de tot cor.

Muchas gracias a ti también Ayllón, por los consejos y por las risas (sobretodo a mi costa). Me has hecho pasar muy buenos momentos y sin duda no podría pensar en mi etapa como doctorando sin recordarte. Me voy a llevar muy buenos recuerdos y anécdotas tuyas.

A mis compañeros doctorandos, estudiantes de máster y grado que han pasado por el laboratorio de UAB y CNM. Por suerte, son muchas las personas que he conocido a lo largo de este trayecto y me siento muy orgullosa de haber podido aprender de cada uno de vosotros. Una de las cosas más gratificantes de haberme decidido a hacer la tesis es la suerte que he tenido de conocer a tantas personas y con ellos distintas maneras de trabajar, por los consejos y ratos fuera del laboratorio compartidos. Gracias.

En especial, a mis amigos de Girona y Barcelona, por saber darme aire cuando más lo necesitaba y escuchar mis laaargas quejas contra el mundo. Os agradezco de manera infinita vuestra paciencia, las risas y momentos que nos hemos llevado. Sabéis que, aunque quejarme es mi pasión en el fondo no soy tan gruñona y que sin decir nombres sabéis lo importantes que sois en mi vida.

A mi familia, que, aunque tenga que explicar mil veces qué hago en mi tesis doctoral lo explicaría otras mil más. Gracias por el apoyo que de manera incondicional me dais siempre.

Y finalmente a ti Eric, porque formamos el mejor equipo del mundo y siempre estaré eternamente agradecida que nos hayamos cruzado en el camino. T’estimo.

Table of Content

List of Abbreviations, Units and Symbols

Abbreviations

ABTS	2,2'-azino-bic(3-ethylbenzothiazoline-6-sulfonic acid)
ACN	Acetonitrile
BG	Berlin Green
Br-BIPS	1,3,3-trimethylindolino-6'-bromobenzopyrylospiran
C	Chemical Reaction
CE	Counter Electrode
CT	Charge Transfer
CV	Cyclic Voltammetry
DMF	*N,N'*- dimethylformamide
DMPU	Dimethylpropylurea
DTE	Dithienylethene
EC	Electrochromic
ECD	Electrochromic Display
ECP	Electrochromic Polymer
EDG	Electrondonor Group
EIS	Electrochemical Impedance Spectroscopy
ET	Electron Transfer
EWG	Electrowithdrawing Group
Fc	Ferrocene
GOx	Glucose Oxidase
HOMO	Highest Energy Occupied Molecular Orbital
HRP	Horseradish Peroxidase
IL	Ionic Liquid
IG	Ionogel
ITO-PET	Indium Tin Oxide on Polyethylene Terephtalate
IVCT	Intervalence Charge Transfer
LMWG	Low Molecular Weight Gelator
LOx	Lactate Oxidase
LUMO	Lowest Energy Unoccupied Molecular Orbital
MOs	Molecular Orbitals
MR	Magnetorheological
MS	Molecular Switch
MLCT	Metal to Ligand Charge Transfer
NO_2BIPS	1',3'-dihydro-1'3',3'-trimethyl-6-nitrospiro[2H-1-benzospyran-2-2'-(2H)-indole]
NPs	Nanoparticles

PANI	Polyaniline
PB	Prussian Blue
PBS	Phosphate-buffered Solution
PC	Photonic Crystal
PEDOT	Poly(3,4-ethylenedioxythiophene)
PEDOT:PSS	Poly(3,4-ethylenedioxythiophene) polystirene sulfonate
PEO	Poly(ethylene oxide)
PPy	Polypyrrole
PSS	Photostationary State
ProDOT	Poly(3,4-propylenedioxythiophene)
PVI	Poly(1-vinylimidazole)
PVI-dmeOs	$Os(4,4'\text{-dimethylbpy})_2Cl$
PW	Prussian White
Ref	Reference Electrode
SF	Silk Fibroin
SMs	Smart Materials
SPR	Surface Plasmon Resonance
TBAOH	Tetrabutylammonium hydroxide
TEMPO	2,2,6,6-Tetramethylpiperidin-1-yl)oxyl
TMB	3,3',5,5'-tetramethylbenzidine
TMO	Transition Metal Oxide
WE	Working Electrode

Symbols

C	Chemical Reaction
E	Electron
$\mathbf{E_{app}}$	Potential applied
$\mathbf{E_{p,a}}$	Anodic Peak Potential
$\mathbf{E_{p,c}}$	Cathodic Peak Potential
$\mathbf{E^o}$	Standard Potential
ΔE	Half Peak Width
F	Faraday constant (96500 $C \cdot mol^{-1}$)
hv	Photon Energy
t_a	Anodic Response Time
t_c	Cathodic Response Time
$\mathbf{T_g}$	Glass Transition Temperature
η	Coloration Efficiency

ΔT	Change in Transmittance
σ	Ionic Conductivity
R	Resistance
v	Scan rate ($V \cdot s^{-1}$)
λ	Wavelength

Units

Å	Angstrom
A	Ampere
C	Coulombs
ºC	Celsius Degree
g	Gram
m	Meter
s	Seconds
T	Temperature
V	Volt
Ω	Ohm

Summary

The advancement in the technological world has boosted the innovation of applications with smart functionalities. The inception of materials whose characteristics may be reversibly changed by an external input has therefore become a research hotspot in recent years. Particularly, electrochromic materials have the ability of changing their color in response to an electric voltage. The control of light transmittance or absorption of materials can contribute significantly to applications like electrochromic displays, smart windows, antiglare rear-view mirrors, and more recently, in colorimetric biosensors. The current PhD thesis describes the electrochomic response of molecules that show “true electrochromism”, such as poly(3,4-(propylenedioxy)thiophene and Prussian Blue, as well as “electrochromism with memory”, such as spiropyran and diarylethene molecular switches. Finally, this thesis shows, as a proof of concept, the design and fabrication of more ecofriendly electrochromic displays and sensors.

Resumen

El avance en el mundo tecnológico ha impulsado la innovación de aplicaciones con funcionalidades inteligentes. Por lo tanto, la creación de materiales cuyas características pueden cambiar de manera reversible por una estímulo externo se ha convertido en un tema de investigación en aumento en los últimos años. En particular, los materiales electrocrómicos tienen la capacidad de cambiar de color en respuesta a un voltaje eléctrico. El control de la transmisión de luz o la absorción de materiales puede contribuir significativamente a aplicaciones como pantallas electrocrómicas, ventanas inteligentes, espejos retrovisores antideslumbrantes y, más recientemente, en biosensores colorimétricos. La tesis doctoral actual describe la respuesta electrocrómica de moléculas que muestran “electrocromismo verdadero”, como el poli(3,4-(propilendioxi)tiofeno y el Azul de Prusia, así como “electrocromismo con memoria”, como los interruptores moleculares de tipo espiropirano y diarileteno. Finalmente, esta tesis muestra, como prueba de concepto, el diseño y fabricación de pantallas y sensores electrocrómicos más respetuosos con el medioambiente.

CHAPTER 1. INTRODUCTION

1. Introduction

1.1. Dynamic-Smart systems. From color changing properties to smart applications

Dynamic systems found in nature that reversibly change their properties in response to environmental stimuli have captivated the interest of the scientific community. Some examples are chameleons change color [1], bacterial heat-shock and flagellar motion [2], the opening/closing of pine-cones in response to relative humidity [3], self-healing properties of tissues in living organisms [4], and the contraction/dilatation of eye pupils for light modulation [5]. Such systems have been the driving force behind the development of novel bioinspired materials and applications that aim to mimic nature's behavior. Figure 1.1.

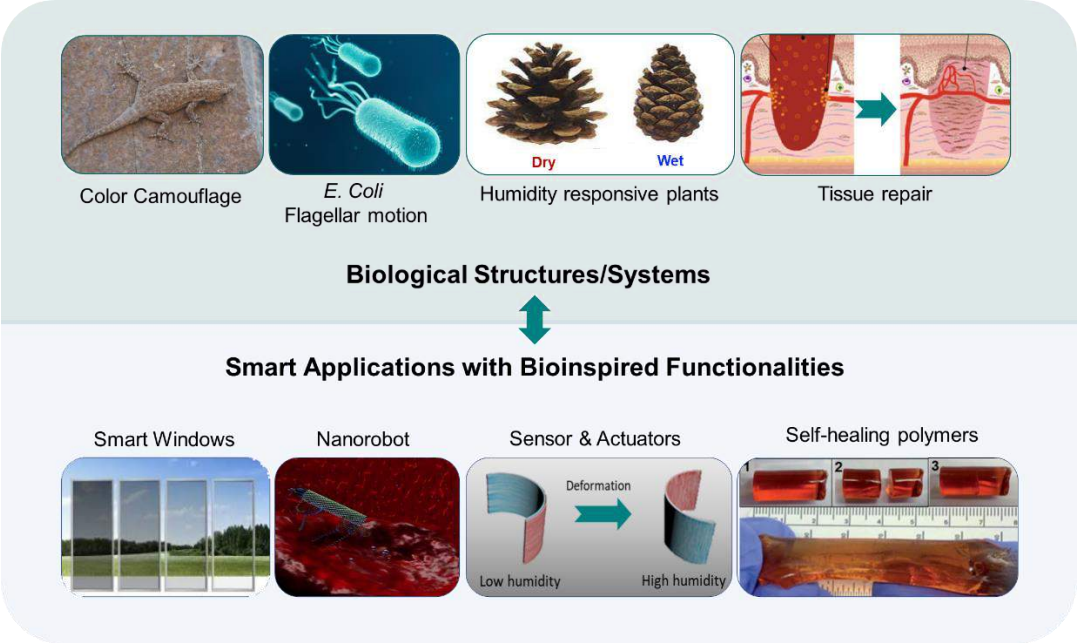

Figure 1.1. Examples of current materials and applications with dynamic or smart functionalities bioinspired by systems found in nature.

The main advantage of using dynamic systems over static-type materials is the possibility of a very precise external modulation of their properties by turning them '*ON'* or *'OFF'* like a switch. For this reason, an increasing amount of research is being done to develop compounds with improved and optimized dynamic properties [6–9]. Figure 1.2.

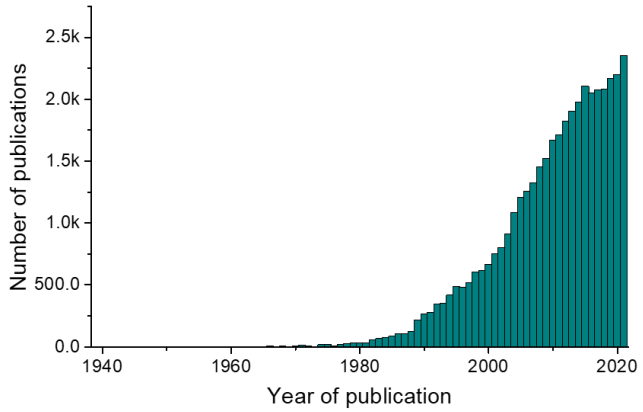

Figure 1.2. Total number of articles over time on molecules and materials with switching properties in response to external changes. (Source: Scopus.com).

In this regard, Smart Materials (SMs) emerged as a class of dynamic systems because they selectively vary some of their properties in response to a stimulus or change in the environment in a controllable and reversible way. Some of the features that distinguish them from classic and static materials are i) stimulus specificity, (i.e., a change to some of the material's properties in response to a single type of stimulus); ii) response consistency, showing the same switching behavior after successive exposures to changes in the environment; iii) multi-stimuli response capacity, being able to respond to different stimuli causing the material to vary its states; iv) Immediacy, the response must be fast [10].

The fancy qualities of SMs have led to a rise in the development of devices and systems with smart functionalities that are able to change their properties when subjected to external stimuli. As a result, new technologies and applications based on this principle are gaining popularity in fields such as material engineering (e.g. shape-memory alloys or magneto-rheological fluids) [11], wearable sensors (e.g. for in situ glucose detection) [12], actuators (e.g. artificial muscles) [13], nanorobotics and medicine (e.g. targeted drug delivery systems) [14–16].

Stimuli to which they might respond include temperature, mechanical stress, strain, hydrostatic pressure, magnetic fields, electric currents, pH, and chemicals [17,18]. Similarly, responses vary greatly depending on the characteristics of the materials. These include changes in size, shape, wettability, viscosity, electric or magnetic field formation and color.

Hence, there is a plethora of ways to categorize SMs, and the main ones are illustrated in the following section to provide a clear overview.

1.1.1. Types of Smart Materials (SMs)

Existing SMs not only respond to a broad variety of stimuli but also have very different responses depending on their properties. For this reason, they cannot be classified under a single definition. Some of the most relevant categories of SMs are highlighted below because their properties are of special interest for the development of promising applications [19].

a) *Shape memory materials:* This category includes those materials that are able to change their shape and return to the original one under an external stimulus (e.g. heating or mechanical stress). Common examples are some polymers (e.g., polytheretherketone, polyurethane) and alloys (e.g., NiTi, CuZnAl). There are different ways in which a material can present the shape memory effect. Polymers typically operate by heating, taking advantage of their glass transition temperature (T_g), above which they change from their crystalline (rigid) phase to the amorphous (flexible) one. Before heating, the structure is frozen, and the material remains static. However, when heated, the rotation around the segment bonds becomes less obstructed, and the material becomes amorphous and viscoelastic. In this situation, the shape can be deformed and frozen again into the desired shape by decreasing the temperature below Tg [20]. Similarly, shape-memory alloys that respond to temperature have two different crystal structures or phases, the martensite phase (that exists at low temperatures) and the austenite phase (which appears at higher temperatures), which can be reversibly accessed when heated/cooled. While the martensite phase allows shape deformation, when the alloy is heated and the austenite phase is reached, the materials recover the same shape as before the deformation [21].

b) *Piezoelectric materials.* These materials convert a mechanical energy into an electrical signal and *vice versa* because of a crystal lattice asymmetry. The effect is reversible and only occurs in non-conductive materials such as quartz, SiO_2. In this case, the charge is balanced in the crystal lattice but when a mechanical stress is applied, the asymmetric lattice is deformed, forming positive and negative located dipole moments, so that the charges no longer cancel one another out and net positive and negative charges appear on opposing crystal faces. In that condition, a voltage has been produced or a current flows through the crystal [22].

c) *Magnetorheological materials (MR):* The exposure of this class of material to a magnetic field produces a change to some of its rheological properties (e.g. stress

and viscosity) or shape. The process is bidirectional, so the case can also arise whereby the external application of a magnetic field causes the shape of the material to be altered, as well as some of its rheological properties. Materials included in this category generally consist of composites based on nano or micro sized magnetic fillers contained in a carrier matrix. Carbonyl iron particles are ideal candidates to prepare MR materials. Depending on the physical state and the type of carrier matrix that contains the ferromagnetic particles, these are classified as MR fluids, elastomers or gels. In MR fluids, the presence of an external magnetic field provokes a change in the material from a Newtonian-like fluid to a semi-solid non-Newtonian [23]. In MR elastomers, magneto-responsive fillers are embedded in the polymer matrix, enabling control of the shear modulus. Exposure of the material to an external magnetic field when curing the polymer allows for preorganization and alignment of the structure, promoting anisotropy [24]. Eventually, the preorganization of the structure determines the field-dependence of the mechanical properties. MR gels have a viscoelastic phase from solid-like to liquid-like under the influence of a magnetic field. The particles tend to align in the direction of the magnetic field with a consequent increase in internal stress and hence, the rheological properties change [23,25].

d) *Chromic materials*. The color of chromic materials is sensitive to environmental variations such as temperature, pH variation, chemical components, pressure, electric potential, etc. The presence of one stimulus leads to a structural or electronic change that in turn provokes an electronic transition with an energy gap that fits in the visible electromagnetic spectrum. As result, a color change is observed. This category of SM is discussed in depth in the following section.

Figure 1.3. Outlines the most common uses of the different classes of SMs.

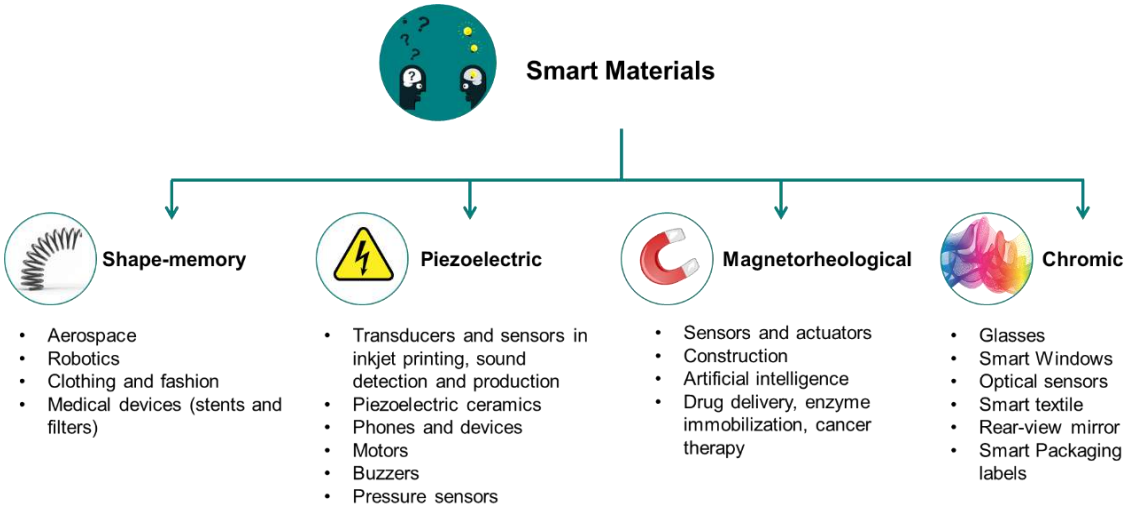

Figure 1.3. General classification of the most relevant smart materials and their fields of application.

Among all the categories summarized above, materials that change color are of special relevance since their response is simple to read and detect with the naked eye Chromic phenomena endow materials with unique qualities for use in a wide variety of applications to solve many human needs, all of which can contribute to overall well-being. This doctoral thesis therefore focuses on the study of different materials and compounds with chromic properties.

1.1.2. Chromic Materials. The origin of color and classification

This section provides an explanation of the color changing phenomena, as well as an overview of the currently available compounds with chromic characteristics that are currently available, as well as an explanation of the color changing phenomena and their most common uses.

The origin of color in materials is the result of specific electronic transitions that occur at the molecular level. In general terms, when the energy gap between the highest occupied molecular orbital (HOMO) and the lowest unoccupied molecular orbital (LUMO) is in the visible range (from 3.26 eV (380 nm) to 1.55 eV (800 nm)), molecules present color.

The phenomenon is observable in those molecules that show any of the electronic transitions listed below, depending on the chemical nature.

a) d-d transitions occur between molecular orbitals (MOs) that are mostly metallic, such as certain inorganic complexes. Figure 1.4.a)

b) Charge transfer (CT) transitions are observable in organometallic complexes where an electron is transferred between metal and ligands (the ligands must be π-donors or π-acceptors). It can also occur in metal oxides where the color changes through intervalence charge transfer induced by an applied potential. Figure 1.4 a)

c) Some organic molecules typically have double bonds or unsaturated systems with pi-electron and heteroatoms with non-bonding valence-shell electron pairs. This generates π - π* electronic transitions (*e.g*. C=C and C≡C groups), π - π* 555 and n- π * (e.g. C=O and N=O), and n- σ* electronic transitions (e.g. I-C and Br-C) (Fig. 1.4b). However, isolated functional groups result in high-energy electronic transitions, in the B-UV spectroscopic range, which is invisible to the naked eye. Only molecules with conjugated bonds significantly decrease the energy gap between HOMO-LUMO levels in such a way that the gap energy couples to the visible wavelength region. The energy levels cease to be discrete in highly conjugated systems (e.g., polymers) due to the overlapping of the MOs (Fig. 1.4c). Thus, electronic bands (conduction band (CB) and valence band (VB)) are formed and therefore the color change is given by the electron excitation between the HOMO and LUMO bands. Figure 1.4. b) and c).

d) Plasmonic effect: The color of some nanoparticles (NPs) is due to the coupling between the incident electromagnetic field and the oscillation energy of free electrons on the surface of the material (Figure 1.4. d)).

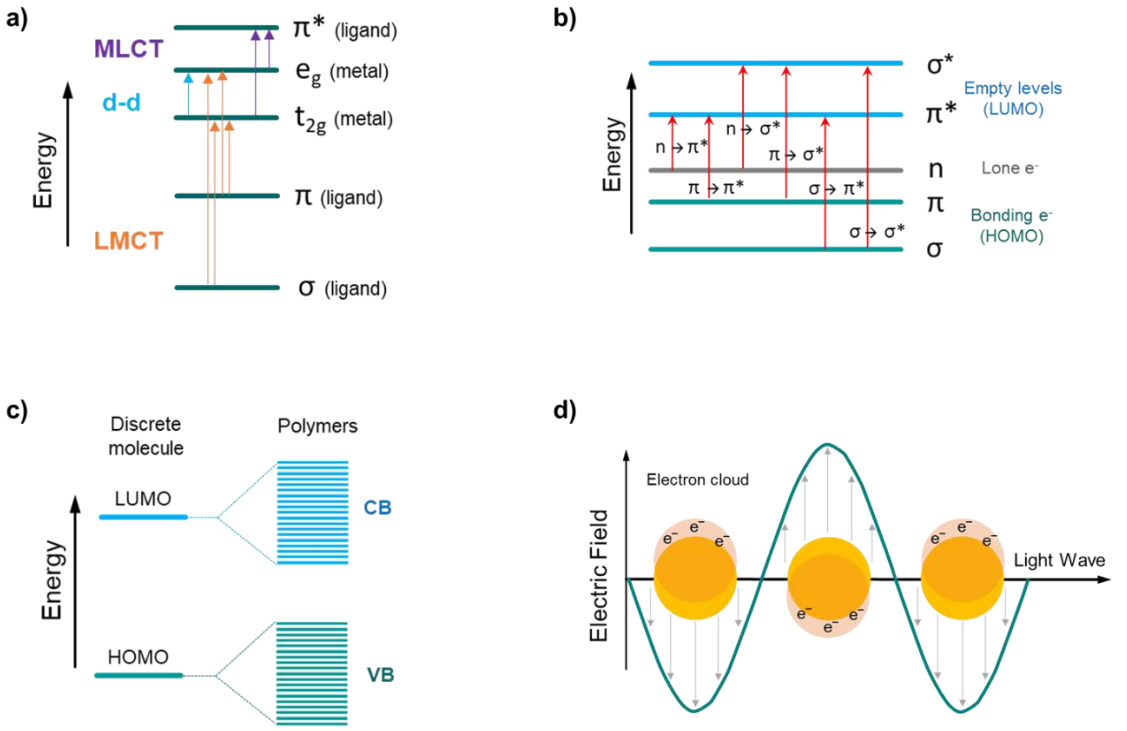

Figure 1.4. Electronic transitions that can cause the origin of color in different molecules **a)** inorganic or organometallic complexes b) organic molecules c) organic polymers and d) interaction of NPs with light.

In the case of color-changing molecules, the external stimulius causes a modification in the energy gap because of the previously described stabilization/destabilization of HOMO-LUIMO electronic states. Accordingly, a different color will be observed. Examples of color changing molecules include those that undergo an isomerization process, a change in oxidation state, the formation of complexes, or photocyclation, among others [26–29] .

Conventionally, compounds with chromic properties present a controlled color change when exposed to an external stimulus such as an electrical potential (electrochromic), light (photochromic), temperature (thermochromic), pH change (halochromic), ions (chemochromic), application of magnetic field (magnetochromic), mechanical stress (piezochromic), radiation (radiochromic) or change in medium polarity (solvatochromism). In addition, the process is reversed to its initial coloration under exposure to a source or stimulus other than the initial one. Hence, depending on the external condition to which it is exposed, the material will shows one coloration or another as many times as the stimuli change [30].

Quantification of the coloring process is of special relevance when assessing the efficiency of chromic molecules. First, *color* is determined by the wavelength at the

maximum absorption value (λ_{max}) of the electromagnetic spectrum in the range from 380-870 nm. *Contrast ratio* is measured at a fixed wavelength and is defined as the percentage of light reflected by the material when it is in the colored form compared to the bleached state. *Coloration efficiency* (η) is the change in absorbance as a function of the total charge used for the color change process. *Response time* is the time needed to generate 90-100% of the colored (or bleached) form. Finally, *fatigue resistance* indicates the percentage of material that can be converted to its colored form again (and *vice versa*) after a high number of conversions. Thus, depending on the application for which the compound is intended, the requirements in terms of chromic features are defined differently. As proof, whereas electrochromic displays require short response times (in the range of ms), smart windows accept response times of several seconds [31,32].

1.1.3. Applications of chromic materials

The ability to induce color change in such a wide variety of ways by means of different stimuli makes these compounds highly versatile and interesting from a technological point of view. Hence, a large body of scientific research is focusing today on both, the synthesis of new and improved compounds, and the design of molecules with multifunctionalities [33–35]. Equally important is the development of technologies to produce factual applications (e.g. physical or chemical vapor deposition, electrodeposition, screen-printing, inkjet, 3D printing, etc.) [36]. Meanwhile, other strategies entail the development of hybrid materials or composites that are decorated with chromic molecules (e.g. chemical modification of particles such as silica NPs or incorporation of chromic molecules in solid-gel like matrices). This approach helps with the subsequent production stage [37–39].

Depending on the type of responsiveness, as well as the nature of the stimulus, applications are developed for very different applications with different functionalities. Representative examples of current applications include data storage devices and memory systems arising from the reversible coloring of electrochromes activated via electricity, which permit access to an '*ON*' and '*OFF*' state [40]. There are also commercially available electrochromic smart devices such as anti-glare rear-view mirrors (Gentex ®) [41,42], electrochromic glasses and price tags [43]. Special mention should be given to the development and improvement of 'smart windows', which are still under

development but have a direct impact on environmental and energy efficiency (SageGlass View, Inc. ®) [44,45].

In turn, photo-controllable molecules have had a greater impact on medical research since they can use light, for example, to trigger drug release at the desired target. This ability to control the properties of materials with minimally invasive tools such as light is a very promising strategy in studied with biological systems. Hence, different photochromic compounds (e.g., azobenzenes, diarylethenes, spiropyrans, among others) are used to functionalize nanoparticles, liposomes, polymers or micelles so that the drug release at target sites is improved in a controlled manner, enhancing their therapeutic efficiency while minimizing side effects [46–48].

Although the most implemented applications to date are those induced by electricity and light due to their simplicity of access and control, thermochromic properties are also being exploited in applications such as smart windows and colorimetric thermometers [49]. Thermochromic materials can also be used as smart labels to detect possible alterations that have occurred during food preservation, i.e., the break-up of the cold chain, for food preservation as well as to control and monitor temperature in routine industrial processes [49]. Aside from these examples, applications based on halochromic and chemochromic features have also been used in the development of colorimetric sensors. For example, these compounds have been used for naked-eye detection of heavy metals such as Co^{2+} and In^{3+}, or even to modify surfaces for detection and identification of a series of metal cations (Cu^{2+}, Ni^{2+}, Fe^{3+}, Hg^{2+}, Zn^{2+}, Mg^{2+}) [50–52].

Finally, upcoming fancy applications such as reusable and wearable sensors are of special interest since they would revolutionize technology in several fields, and especially in the medical healthcare, due to their easy handling, low production cost and small and more transportable size. This would imply greater access to this technology worldwide.

Part of this thesis particularly focuses on the study of compounds with electrochromic properties because they offer the possibility of controlling and implementing electrical circuits in devices and enable high precision and control by means of an electrical potential or current intensity. It should be noted that some of the molecules studied herein not only have electrochromic features, but they are also sensitive to different stimuli (such as light and pH), which are also known as multistimuli responsive molecules. However, they all share the common factor of responding to electric potential. This doctoral thesis specifically aims to develop and study multistimuli

chromic compounds for the manufacture of colorimetric sensors and electrochromic displays. The following section, therefore, presents a classification of the most relevant electrochromic materials.

1.2. Electrochromic Molecules (EC)

The first electrochromic phenomena were observed one century ago in materials such as wolframium tungsten oxide, WO_x. However, it was not until 1961 that the term 'electrochromism' was first defined [53,54]. Since then, our understanding of this phenomenon has expanded and an increasingly significant number of new electrochromes have appeared.

A first categorization is provided in this thesis, which includes substances with so-called ‘true' electrochromism and electrochromism with ‘memory’. Figure 1.5. This first category refers to substances that modify their color because of a change in oxidation state caused by the application of an electrical potential. In this thesis, the particular case of Prussian Blue (PB) and a ProDOT electrochromic polymer (ECP) will be discussed and detailed since they have been used and studied for the design of different applications and belong to the family of compounds with ‘true’ electrochromism.

Less conventionally, this thesis includes a second group of compounds known as molecular switches (MS) that are presented as a new generation of electrochromic compounds and are examples of electrochromism with ‘memory’, whereby the change in color is given by the modification of the conformation or chemical structure of the molecule. The use of MS would confer multifunctionality to materials since, in some cases, they are reversibly returned to its initial structure by a second stimulus that is different from electric potential, for example light. Examples that belong to this family and are studied in this doctoral thesis are spiropyrans and diarylethenes MS.

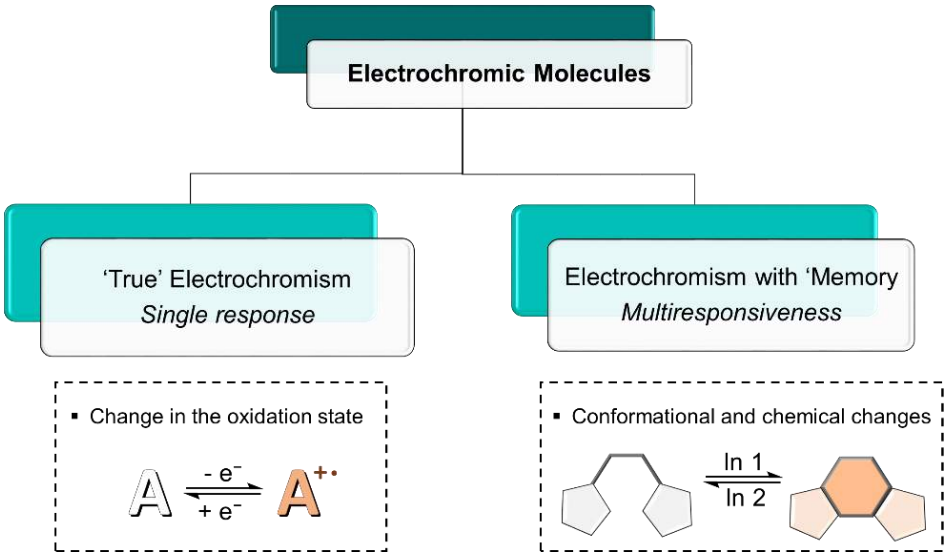

Figure 1.5. Classification of electrochromic families depending on the type of electrochromism they present. In = input. In 1 and 2 do not necessarily have to be of the same nature. For example, In1= electricity and In 2= light.

1.2.1. Molecules with 'True' Electrochromism

The main categories of compounds exhibiting "True" electrochromic characteristics and the main uses for which they are employed are briefly described below. However, for Prussian Blue and ProDOT types, a more detailed description is provided since they are the ones studied in this thesis.

Table 1.1. summarizes the main features of different EC with 'true' electrochromisms as well as the main applications they can be used for.

Table 1.1. Types of Classic Electrochromes. Advantages and main drawbacks of each type of compound as well as their principal uses in applications.

Compound	Examples	Advantages	Disadvantages	Main applications
Transition metal oxides (TMO)	WO_3, NiO, MoO_3, V_2O_5	Robustness Low potential High contrast Modification of large surface areas	Little variety of color change: from bleached to blue-grey range. Costly deposition processes (CVD, PVD, thermal deposition...) Limited solubility	Smart windows for efficient buildings and displays [55]
Metal complexes	$[M^{II}(bpy)_3]^{2+}$ (M = Fe, Ru, Os; bpy = bipyridine derivatives)	Intense coloration Capability of one single molecule switching between three primary colors. Broader variety of colors Hybrid polymer-metal complexes to facilitate electrochemical film formation	Mechanical problems associated to film formation. Electrodeposition limited by small surfaces of electrodes	Colored flexible displays [56,57]
Organic molecules	Viologens, carbazole, triphenylamine...	Color tuning depending on the substituents Fast response time and high contrast ratio High coloration efficiency and fast switching	Electrochromic performance in solution or entrapping of molecules in membranes or nanostructured platforms Synthesis and purification steps. Use of toxic solvents	Redox flow systems [58]
Plasmonic EC	Ag, Bi, Cu, Ni, Mg NPs	Low electrical voltage Color tuning	The color depends on fine control of NPs (size, shape…) Poor long-term stabilization (aggregation)	Electronic paper and smart windows [59,60]
Prussian Blue (PB)	$Fe_4^{III}[Fe^{II}(CN)_6]_3$	Low reduction potentials Robustness Mediator	No option of color tuning	Optical and Electrochemical Biosensors [61–63]
Electrochromic Polymers (ECPs)	polyaniline (PANI), poly-pyrrole (PPy) polythiophenes (PThs), poly(3,4-ethylenedioxythiophene) (PEDOT) and derivatives (PXDOT)	Cost-effective Different coloration depending on the redox state (multicolor) High contrast ratio High coloration efficiency and fast switching Fabrication of flexible devices.	Synthesis and purification stages. Use of toxic solvents Poor conductivity of polymer films and stability	Multicolored Flexible displays [64]

Transition Metal Oxides (TMO): TMO films can be electrochemically switched to a non-stoichiometric redox state, which has an intense electronic absorption band due to intervalence charge transfer. Typically, transition metals such as cerium, chromium, cobalt, copper, iridium, iron, manganese, molybdenum, nickel, niobium, palladium, rhodium, ruthenium, tantalum, titanium, tungsten, and vanadium are combined in the form of oxides and present a coloration switching behavior from bleached to blue-grey. This class of oxides has been widely used since they were the first compounds with electrochromic properties to be discovered. Their main advantages include the low reduction potential to access the bleached state from their colored form and *vice versa*, as well as their major stability after consecutive color switching cycles. TMOs have gone on to be implemented in different applications, the most relevant being smart windows, through film deposition techniques, e.g., such as Physical Vapor Deposition (PVD), among others, which enable the homogeneous modification of large surface areas [65,66]. The chemical reactions implied in the electrochromic process of the most common TMOs are depicted in Scheme 1.1.

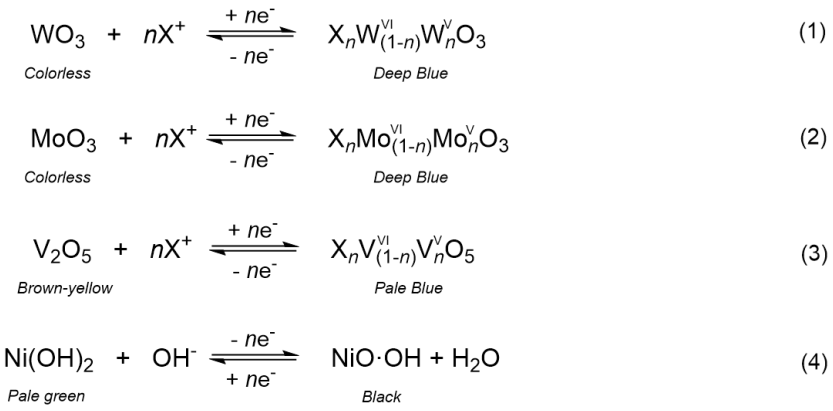

Scheme 1.1. Electrochemical reactions implied in the color change of some TMOs. *X* represents H^+ or Li^+.

Metal complexes: The vivid coloration of this class of molecule arises from metal to ligand (MLCT) charge transfer, of ligand-centered transitions (LC) or metal-centered transitions (MC). As a result, they present different strong electronic absorptions in the visible and NIR spectra that are directly dependent on the redox states of both metal centers and ligands. Thus, palette color varies greatly depending on the specific electronic contribution of both ligand and metallic centers. In this case, colors very often go from red, to orange or green. Because these electronic transitions involve valence

electrons, spectroscopic features are changed or lost when a complex is oxidized or reduced so color can be electrochemically controlled.

Popular examples included in this category are based on transition-metal complexes where a metal center (M^{II}, such as Fe, Ru, Os) is coordinated with bipyridyl or bipyridyl derivative ligands. A notable example is $[Ru(4\text{-}bpy)_3]^{2+}$, which is known to present an intense reddish-orange coloration that becomes green when it is oxidized to $[Ru(4\text{-}bpy)_3]^{3+}$. Scheme 1.2.

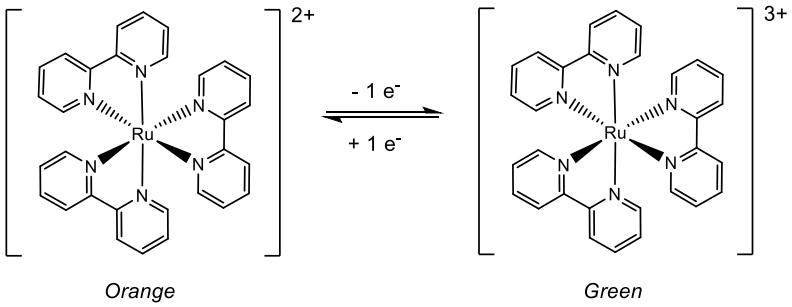

Scheme 1.2. Electrochromic conversion between $[Ru(4\text{-}bpy)_3]^{2+}$ and $[Ru(4\text{-}bpy)_3]^{3+}$ metallocomplex.

Despite the promising spectroscopic and redox properties of metal complexes for ECD, their use in liquid phase limits their expansion. Hence, alternatives such as the polymerization of metal complexes through their organic ligands are being widely explored for their potential utilities in ECD applications. For instance, $[Ru(4\text{-vinyl-4'-methyl-bpy})_3]^{2+}$ can polymerize through vinyl groups upon electrochemical reduction to form films. The injection of electrons generates radicals that initiate the carbon-carbon bond formation and polymerization. When the polymer is oxidized, the color of the film eventually changes. This strategy is highly promising from the point of view of ECD manufacture because it can be used to produce multicolored flexible devices. However, it is limited to polymerization on small areas and requires conductive substrates [57,67].

Organic molecules: The key class of compounds to emphasize in this category are viologens, 4,4'-bipyridinium dications in the form of salts that undergo a reversible reduction accompanied by a color change from transparent to deep blue (the radical cation form) and pale color after a subsequent reduction (the neutral form). Scheme 1.3. The simplicity of varying the substituents in the quaternary ammonium position means they can be chemically modified in a wide variety of manners, and therefore their properties such as solubility and color tuning. Other less widespread examples but that also have electrochromic properties are carbazole, dimethylteraphtalate, diacetyl benzene, biphenyl dicarboxylic acid diethyl ester and triphenylamine [68]. The benefits and

disadvantages of EC organic molecules are very similar to metal complexes. The color change of the species can easily be tuned by modifying the compounds with functional groups of a more electron-donor or electro-withdrawing nature. Ideal chromic properties are shown by EC organic molecules such as good color contrast, fast responses, and robustness. However, processability is the limiting factor of using single EC organic molecules and requires the development of strategies for implementation in factual applications (e.g. entrapment in matrices, polymerization on conductive substrates, etc.)

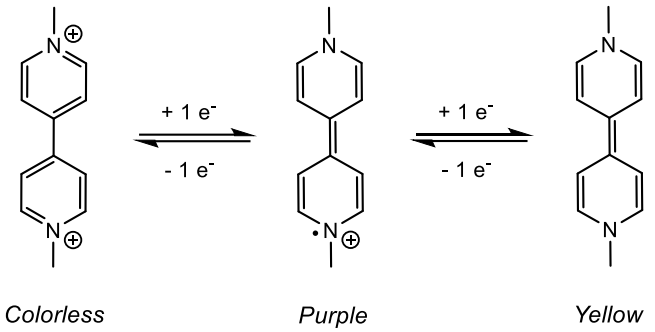

Scheme 1.3. Electrochemical reduction and reversible oxidation of 4,4'-bipyridinium dications and its corresponding color changes.

Prussian Blue (PB): $Fe_4^{III}[Fe^{II}(CN)_6]_3 \cdot nH_2O$ (n = 14-16), is the most popular cyanometallate system and is considered one of the first synthetic pigments, having been produced in 1704 by H. Diesbach [69]. Initially, PB was widely used as a pigment in paints and inks because of its intense blue coloration. However, little was known about its electrochromic properties, and nothing was published about them until 1978 [70]. The structure of PB consists of a 3D lattice containing mixed valence iron atoms (Fe^{2+} in 0.75 ratio to Fe^{3+}) in a face-centered cubic structure whose cavities are 3.2 Å. Potassium cations and water molecules are known to be present within the pores of the framework and it has been demonstrated that the electrochromic properties of PB are caused by the insertion/depletion of K^+ in the cavities. The intense blue color of PB arises from the intervalence charge transfer (IVCT) between the mixed-valence iron atoms (Fe^{2+} and Fe^{3+}), which generates a large absorption band located at 690 nm. The color changes when a reduction potential is applied and causes the incorporation in the structure of four extra K^+ atoms per unitary cell. In this case, the color drastically bleaches giving rise to a colorless Prussian White (PW) structure (colorless). However, when oxidizing PB, a palette color from green to yellow is presented. At initial potentials around zero, the color is green because of the partial electrochemical oxidation of the PB. At larger potential values, the structure establishes neutrality through the oxidation of all iron atoms to Fe^{3+}

and the depletion of all K^+ ions. In this case, the color turns yellow due to the formation of the Berlin Green (BG) structure and the absorption spectra reveals a peak at 425 nm with a substantially lower molar extinction coefficient [71]. Figure 1.6. depicts the electrochemical process involved and the structure of PB.

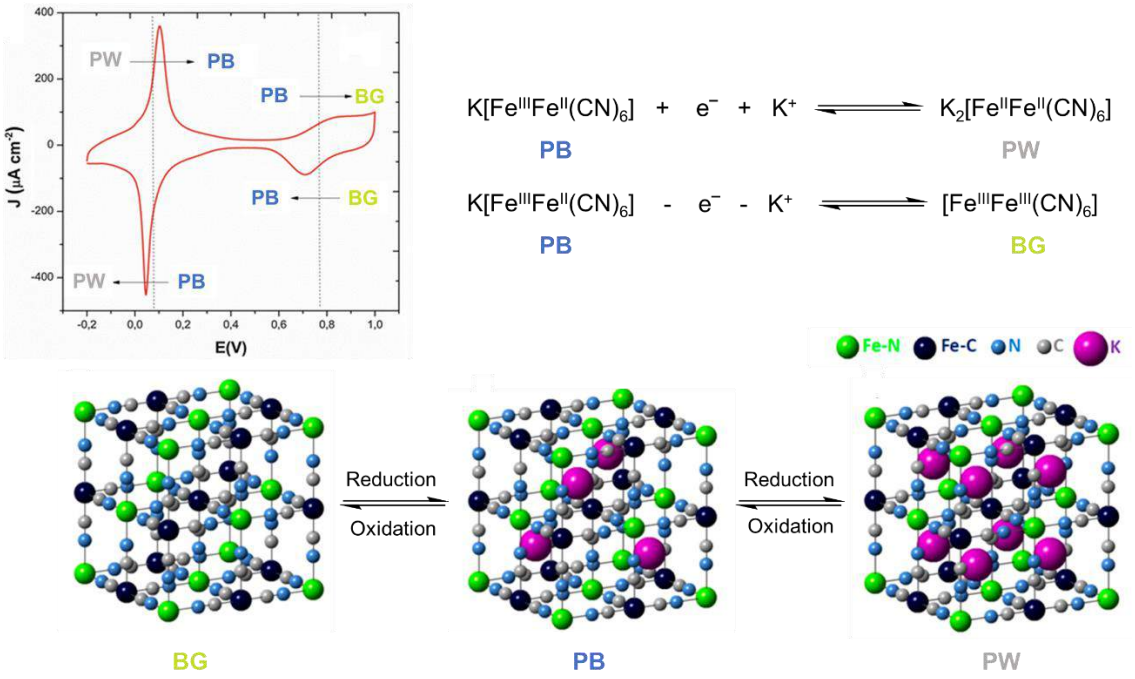

Figure 1.6. On the top left, cyclic voltammetry of PB in the cathodic scan (reversible reduction of PB to PW) and the anodic scan (reversible oxidation of PB to BG). Adapted with permission from ref.[72] On the top right, electrochemical reactions**.** At the bottom, BG, PG and PW structures respectively. Adapted with permission from ref.[73]. Copyright 2022 American Chemical Society.

Currently, significant progress is being made in the use of PB for different types of applications such including catalysis in the reduction of O_2 and H_2O_2 for the advancement of solar fuel production [74], storage of H_2 for energy production [75], production of cathodes for sodium batteries [76] and in photochemistry given the photoinduced magnetism of PB [77]. However, there is a field in which the use of PB particularly stands out, namely its function as an electron-transfer mediator in biosensors. PB acts as a redox species that enables communication between biomolecules and the electrode surface. This property has been exploited not only in the development of 1st generation oxidase-based electrochemical biosensors but also for the development of optical biosensors given the high contrast color produced after the reduction of PB to PW [62]. For this reason, the use of PB as a sensing compound boosted the design and production of electrodes modified

with this material [78]. As it will be specified in the following sections, in this doctoral thesis PB has been used as an electrochromic transducer in the design of a self-powered electrochromic display.

Conjugated electrochromic polymers (ECP): The electrochromic compounds discussed above have been especially useful for developing electrochromic devices since they work at low voltages, are robust and have good color contrast. However, one of the bottleneck factors of their use is that they do not permit color tuning or address the entire spectrum of possible colors. Electrochromic polymers emerged in response to this limitation, which are also known for their low production cost.

Examples of electrochromic polymers are polyaniline (PANI), poly-pyrrole (PPy, conducting polymers) and polythiophenes (PThs), among others.

Typically, polymers with electrochromic properties exhibit an extensive conjugation of π bonds in their structure. This enables resonance stabilization when they are oxidized (anodically coloring polymers) or reduced (cathodically coloring polymers) and in their oxidized or reduced state the charge is balanced with counterions. The energetic bandgap between the VB and the CB of the neutral form determines the intrinsic optical features. In this field, synthetic polymer chemists are able to fine-tune the pi-electron nature of molecules, which in turn allows for the modification of the energy gap and thus the color tuning.

Of particular note relevance among the studies on electrochromic polymers are those by the Reynolds' group, who are pioneers in the synthesis of a whole range of ECPs (poly(dioxythiophene)s, poly(3,4-dioxypyrrole)s, polyfluorenes and their analogues), thereby covering all colors and demonstrating that it is possible to have control over the color of the material [35,79,80]. Figure 1.7. Synthesized polymers are also highly processable, which solves is one of the main issues of problems the technology has had to face. Until now, the vast majority of ECPs were only applicable to devices if they could be electropolymerized on the surface of the electrode to form thin-films. It is now possible to use compounds formulated in such a way that they dissolve in organic or aqueous solvents. Hence, they can be deposited using different techniques such as spray coating, inkjet, doctor blading, etc. to print large areas for the manufacture of ECD.

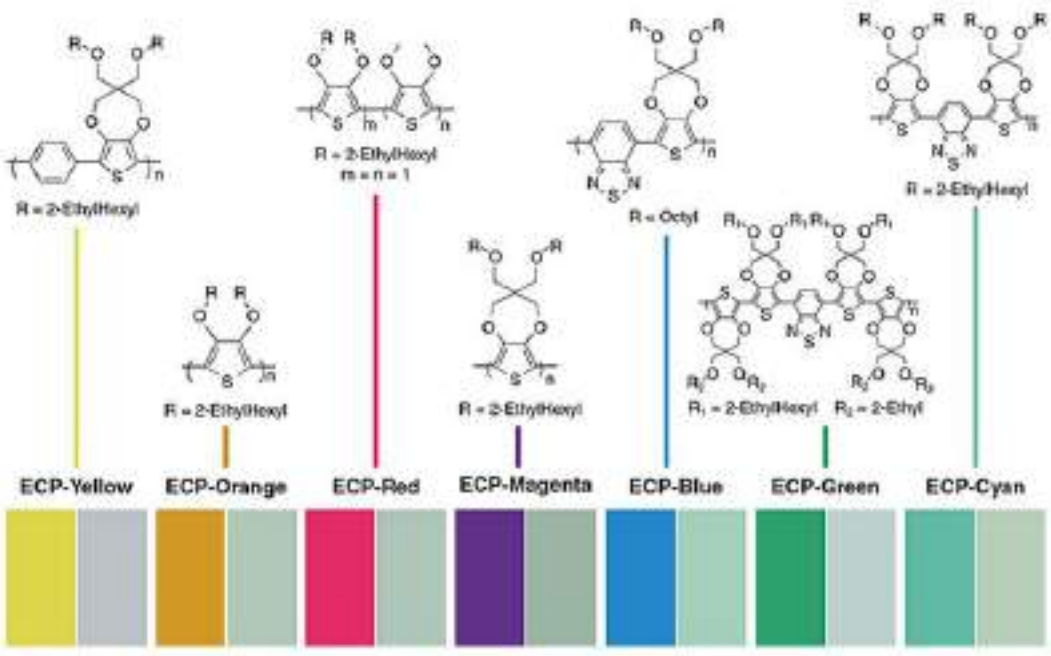

Figure 1.7. PXDOT type polymer derivatives with electrochromic properties designed by Adapted with permission from ref.[81] Copyright 2011 American Chemical Society.

The electrochromic characteristics of poly(3,4-(propylenedioxy)thiophene (PProDOT), an ECP with a chemical structure that is very similar to the traditional PEDOT, have been investigated in this PhD thesis.

The difference lies in the fact that the alkylene bridge of PProDOT ishas one more carbon larger. This increase in the bridge length impacts the electrochromic properties of the compounds since, it has been already demonstrated that It was discovered that this bridge plays a key role in the electrochromic properties. It is specifically known that the increase of the steric bulk of the dioxepane ring results in better color efficiencies [82].

1.2.2. ***Electrochromism with' Memory': Molecular Switches (MS)***

Molecular switches (MSs) are organic molecules or supramolecular systems able to modulate an output signal in response to an input stimulation. Thus, a molecular switch exists in two stable (or metastable) states (state 0 '*ON*') and state 1 (*'OFF'*)) that reversibly interconvert each other by means of specific stimuli (*e.g.,* light, electricity, heat, pH, etc.). In the case of electrochromic molecular switches, it is possible to have fine control of their UV-Vis spectroscopic properties through the application of an electric potential [83]. Figure 1.8.

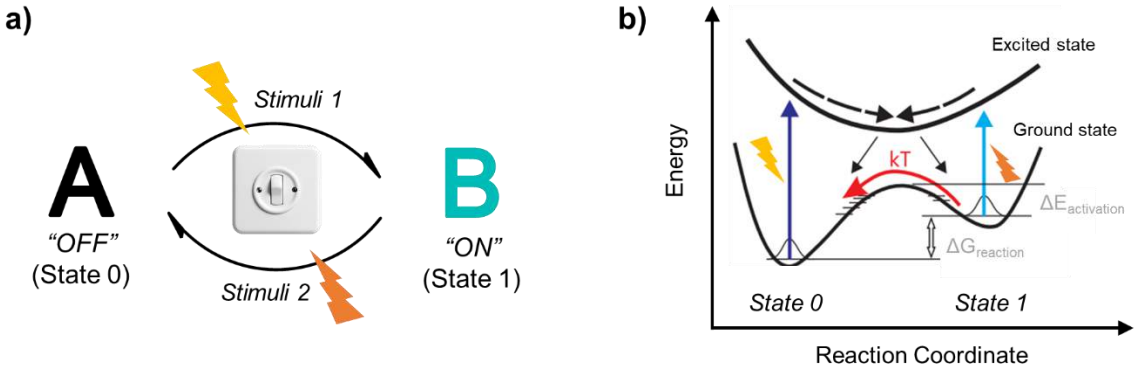

Figure 1.8 a) Schematic representation of a two-state molecular switch interconversion under an external stimulus. b) Potential energy of a bistate molecular switch that exhibits metastable states on the ground and excited state that can be accessed when an external input is applied.

The many different designs of MSs over the years offer the possibility of operating in a wide range of ways [84].

The impact of these compounds on the scientific community has been significant, to the extent that J. Fraser Stoddart, Bernard L. Feringa, and Jean Pierre Sauvage were honored with the Nobel Prize in Chemistry in 2016 for their work on the design and manufacture of molecular switches whose input yields regulate motion [85].

The advancement of knowledge in this area led to a new era in the construction of intelligent materials and molecular machines that can be classified into three main categories i) single molecules, which are based on their structural rearrangements, ii) supramolecular switches, which are based on reversible non-covalent interactions between two or more units, and iii) mechanically interlocked switches, where two or more structures are entrapped to each other by means of loops, whereby interlocked broken

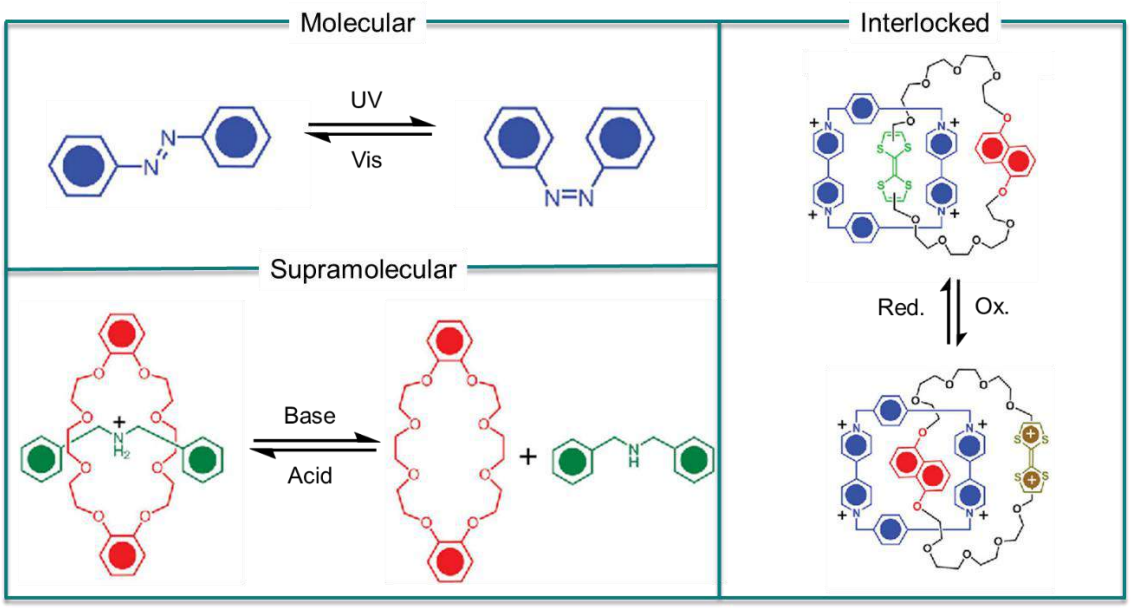

Figure 1.9. Types of MSs: molecules (example showing azobenzene *cis-trans* isomerization upon UV and visible light), supramolecular (complexation of dibenzylamine with dibenzo[24]crown-8 by means of pH modification) and interlocked structures (macrocycle formed by polyethene, TTF and DNP interlocked with a $CBPQT^{4+}$), The oxidation of TTF to TTF^{2+} leads to a change in the stabilization of subunit. Figure adapted with the permission of reference [86].

molecules cannot be separated. Figure 1.9 a).

The contributions of J. P. Sauvage in 1980 enabled the synthesis of first interlocked molecules by template-driven strategies (template-assisted route), which occurs with suitable functionalization of monomeric building blocks. A prominent example is phenanthroline -linked with ethylene glycol in the presence of a metal chelation that is needed to preorganize the monomer segments and facilitate interlocking. The afforded supramolecular structure is the so-called catenane [87].

Subsequent studies led by J. F. Stoddard in 1988 achieved a synthetic route under free-metal conditions for obtaining catenane structures. In this instance, the reaction was directed by the non-covalent interactions of functional groups that were intentionally incorporated in the molecule. An electron-withdrawing 4'4-bipyridinium moiety and a crown ether with electron-donor aromatic substituents resulted in C–H···π and C–H···O non-covalent interactions that enabled the strategic, preorganization, and stabilization and approximation of the monomeric segments, obtaining high synthetic yields. Nowadays, it is not only possible to synthetize a [2]-catenane (one crown ether interlocked with one bis-bipyridinium macrocyle) but also [5]-catenane and [7]-catenane with five and seven macrocycles respectively interlocked in series [88]. Following the same

donor-acceptor driven strategy, it is possible to obtain molecular architectures known as rotaxanes, where a macrocycle is threaded around a linear-shaped molecule as an axis. Rotaxanes can be synthetized with different interactive sites in order to enable the macrocycle shifting to different sites in a controlled way by incorporating functional groups. When exposed to a specific input (e.g., pH, electric potential or light), a change in the binding affinities occurs between the macrocycle and axis that produces a molecular motion [89]. Figure 1.9 b) and c). At this point, the change of state that can be reached for a dynamic molecular system (e.g., from state '0' to state '1' and *vice versa*) was defined for the first time, driven by an external stimulus in a controlled manner, giving rise to the new concept of 'Molecular Switch'.

Other research was inspired by the molecular motors existing in living systems, which are essential in most biological processes. A particular example is the protein complex of ATPase enzyme, which transforms the energy coming from a pH gradient concentration into a rotary motion that enables synthesis of ATP molecules. [90] Similarly, B. Feringa et al. developed the first generation of light-driven chiral molecules to consider the rotation of one half of the molecule over the other half. Achievement of motion requires unidirectional rotation and an intermediate with a low energy conformational state. In this regard, high sterically-hindered chiral alkenes are good candidates for presenting these properties and led to the subsequent synthesis of light-driven molecular motors [84,91].

It is crucial for molecular switches to respond to trigger elements precisely at the molecular level, while also maintaining their directionality and reversibility. Furthermore, the bistability of both states, which may be achieved after the application of a stimulus, is required for this to occur. Moreover, depending on the application, reversibility to the initial state must be generated by a second distinct stimulus of different nature rather than occurring spontaneously (or the reverse process must be slow enough) [83,92].

Given the potentiality of MS in numerous applications (optoelectronics, smart materials, molecular sensing, photo-controlled biological systems, control of molecular self-assembly, logic gates, storage systems, etc.), there are many compounds that have been developed over time to provide them with a variety of functionalities [93–95].

The most popular examples of MSs include photochromic molecules. The result of their exposure to light is the generation of different changes at the molecular level, such as cis/trans isomerization [96–98], a structural change due to the formation or breaking of bonds (e.g., cyclization/opening of the molecule skeleton) [99–101]. This

makes it possible the transition into a new state with significant different chemical and physical properties.

Figure 1.10. shows the main families of photochromic MSs according to the isomerization mechanism followed.

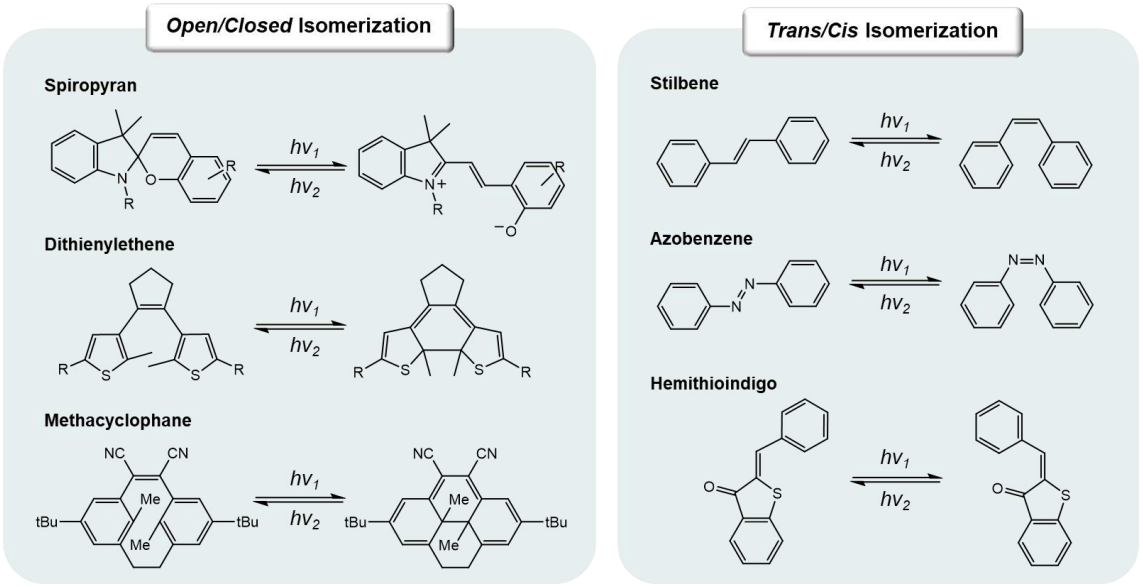

Figure 1.10. Main families of photochromic MSs. On the left, main MSs whose photochromic properties are caused by a ring-opening or closing of their skeleton. On the right, molecules undergo a color change through trans/cis isomerization.

Comparatively, while MSs are organic compounds, molecules with real electrochromism can be either organic or inorganic compounds that undergo a color switch because of a change in the oxidation state when applying a suitable electrical potential. 'Real' EC present several advantages: first, they present simplicity of the reactions since no structural reconfigurations occur which improves their reversibility. They also show a lower reduction potential, that requires lower electrical energies for the coloring process to occur. However, they have other limitations, such as the fact that their color change is limited to the application of a single type of stimulus (electricity) and a single response (color change). In this regard, MSs can offer more than one type of response to different stimuli such as pH, temperature, light, or electricity, conferring multifunctionality to the material. In some cases, such as the family of spiropyran-type and diarylethene MSs, it has been found that it is possible to induce a switch between the states not only through light but also through electrical stimuli.

For this reason, of among all categories of MS, the focus of this thesis is focused on spiropyrans and diarylethene derivatives, which are described below.

1.2.3. Spiropyrans-based MS

Spiropyran-type compounds are a family of MSs whose chemical structure consists of a benzopyranic moiety and an indole entity that are perpendicularly oriented and linked through a spiro carbon. This type of structure is what gives it numerous properties. However, the versatility that is known today, as well as its photochromic properties, whereas not evident at the time it was synthesized by Decker in 1908, who coined the term 'spiropyran' to refer to courmarin derivatives that present a chiral center of double pyran moieties. However, the photochromic properties had yet to be discovered at that time [102]. Since then, many modifications have been made to its structure with various substituents to provide new functionality such as responses to various stimuli such as pH or temperature. It was in 1952 when Fischer and Hirschberg discovered for the first time the photochromic properties of spiropyrans synthetized by condensation of simple Fischer bases with salicylaldehyde [103].

Since then, there has been huge interest in the photochromic characteristics of spiropyran derivatives. Many derivatizations of the molecule were also investigated to improve their photochromic responses.

Irradiation with UV light (λ_{exc} = 365 nm) of spiropyran - initially in the ring-closed or spirocyclic (SP) form - gives rise to the open isomer or merocyanine form (MC), which presents very intense coloration. It has been demonstrated that the substitution of spiropyran with an electrowithdrawing group (EWG) in the 6' position, such as a nitro group in the benzopyran moiety, is crucial for the stabilization of the phenolate group of the MC form and its half-life. As a result, in the case of spiropyran compounds with an EWG, such as a nitro group in 6' position (1',3'-dihydro-1'3',3'-trimethyl-6-nitrospiro[2H-1-benzospyran-2-2'-(2H)-indole] (NO_2BIPS)), the ring-opening, and hence the change in color, is preferred, to improveing their photochromic characteristics [104–106].

Ring-opening and closing has been extensively studied by computational and spectrochemical studies. The first stage involves the cleavage of C_{spiro}-O, obtaining the *cis*-MC structure. Next, the skeleton rotates through the central C-C bond, leading to the formation of *trans*-MC isomer. Figure 1.11.

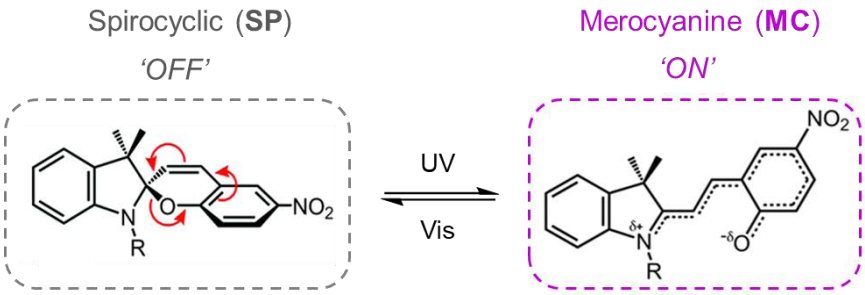

Figure 1.11. Mechanism of photochemical and thermal isomerization of NO_2BIPS spiropyran derivative.

The ring-opening process can be described either as a heterocyclic C-O bond cleavage or as having a 6π electrocyclic ring-opening. The result is the formation of a zwitterionic or quinoidal resonance structure that corresponds to the hybrid MC structure. The eventual MC structure presents an extended π-conjugation between the two moieties. Thus, a new absorbance band that has shifted to the visible region appears, with λ_{max} = 550-600 nm in most non-polar media.

Spiropyran molecules have attracted huge interest and their use has been widespread for to various applications, mainly because the structures that are accessed, the SP and MC forms, present vastly different physical and chemical properties. First, in comparison to SP, the charge separation of the MC form confers a large dipole moment (4-6 D for SP and 14-18 D for MC). Second, the ring-opening leads to significant structural changes, such the elongation of MC in comparison to the SP structure, which occupies less volume. Third, the opening of the structure through the C_{spiro}-O bond leads to the formation of a phenolate moiety whose pH is more basic than the closed SP form. In addition, due to the exposure of phenolate and amine substituents to MC structures, their affinity to ionic metal or other zwitterion species increases. Finally, one of the most remarkable and popular properties of spiropyran is the change in the absorbance spectra. While SP is transparent in the visible region, MC absorbs strongly at λ_{max} = 550-600 nm leading to a very intense pink to blue coloration.

Thus, due to the much-differentiated behavior of spiropyran and the capability of switching '*ON*' and '*OFF'* in response to an external stimulus, it has become one of the most exploited MSs in recent the last decades.

Another characteristic that makes spiropyran-type MS unique is the fact that apart from light (photochromism) and temperature (thermochromism), that not only is possible to access the SP and MC states through light (photochromism) or temperature

(thermochromism), but they are also sensitive to through a wide variety of stimuli such as solvent polarity (solvatochromism), pH variations (halochromism) and redox potential (electrochromism).

However, electrochromism has been one of the least explored properties due to the complexity of the electrochemical mechanism.

Previous reports have demonstrated the possibility of triggering the state shift of molecular switches that accompany the variation of the ring opening or closing between two states, not only by light but also by electrons. Therefore, the derivatization of a molecule with an electroactive group could pave the way for the introduction of electrons (or abstraction in the case of an oxidation process) to the structure of the molecule when an electric potential is applied. In this regard, nitro substituent is particularly intriguing since it not only improves the photochromic properties of the compounds, while but also causes enabling the molecule to be their reductioned on the electrode surface at relatively low potentials. In other words, oxidation or reduction of molecular switches can also induce a structural change to the molecule, resulting in the same color-changing effect [107–111].

Part of this doctoral thesis has focused on examining the electrochemical mechanism for the NO_2BIPS compound. The main electrochemical properties found for NO_2BIPS are summarized below.

i. Electrochromism of nitrospiropyran (NO_2BIPS) MS

The electrochromism of spiropyran derivatives, on the other hand, is almost unexplored in the literature [112–117]. In 1993, studies using EPR spectroscopy reported for the very first time that the electrochemical reduction of naphtospiropyran was fully reversible [118]. Subsequently, Fujishima et al. found that the electrochemical reduction of NO_2BIPS was accompanied by a color change. In this case, they postulated an electrochemical isomerization reaction from the SP (colorless) to the MC (colored) form by means of two consecutive electric inputs (1st reduction, 2nd oxidation). It was observed that the electrochemical reduction of NO_2BIPS (initially in the SP form) led to the formation of the corresponding radical anion ($SP^{\bullet -}$) whereby, after subsequent oxidation, the open and colored structure of the compound (MC) was obtained.

However, the electrochromism of NO_2BIPS was only observed under -42 ºC in DMF. Besides, it was also noted by cyclic voltammetry that the current intensity ratio between reduction and the oxidation peaks (corresponding to the oxidation of $SP^{\bullet-}$) shifts away from 1 as the scan rate goes down. This indicates that the reduction of SP implies a second process that is part of the formation of ($SP^{\bullet-}$)[115,116]. Scheme 1.4.

However, the mechanism was only described under very low temperatures, there still being some controversy regarding the electrochemical ring-opening., As a result, leaving the electrochromic properties of spiropyrans remained unexploited for more than 15 years.

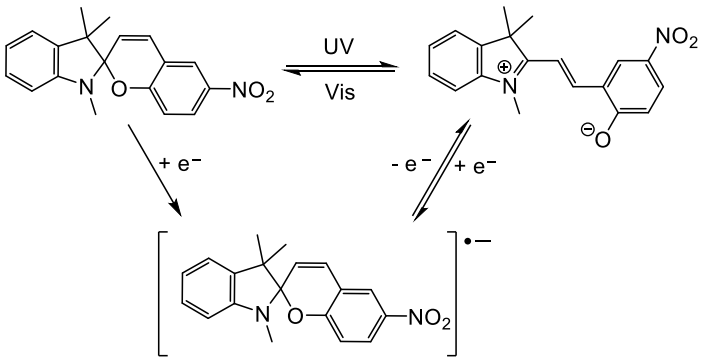

Scheme 1.4. Photoelectrochemical system found for NO_2BIPS in DMF at -70 ºC [119].

In more recent studies, the response of NO_2BIPS to an oxidation input was also investigated. Initially, studies carried out by Giordani et al. discovered that the cross-coupling reaction mediated by Cu(II) ions in mild conditions led to the dimerization of spiropyran through a C-C coupling [120]. Subsequently, Ivansheko *et al.* synthesized and isolated the electrochemical oxidation product of NO_2BIPS after having applied an oxidation potential greater than 1 V. They postulated that the oxidation takes place through the amine group of the indole entity, obtaining the corresponding radical cation stabilized in the *para* position. Thus, the resulting dimer consists of two monomers linked by a C-C bond in the *para* position of the indole. Furthermore, by means of cyclic voltammetry studies, they determined that if the corresponding *para* position coupling is blocked, electron transfer is fully reversible, indicating that dimerization does not occur [121]. The new dimeric spiropyran species were found to present different photochromic properties, paving the way towards new possibilities.

On the other hand, recent articles have described the spontaneous opening of the structure at room temperature via electrochemical oxidation of the molecule for

disubstituted spiropyrans with *t*-butyl groups in *orto* and *para* positions in the benzopyran moiety plus a chlorine located in the *para* position of the indoline part. It seems that the corresponding radical cation is stabilized in the indole moiety due to the chloride blocking in the *para* position that prevents an aryl-aryl coupling reaction. The study also shows that there is a reversal of the relative stabilization of SP and MC states, as well as a low barrier. This leads to a new oxidative gate to induce the ring-opening structure of the spiropyran that is accompanied by a color change [107].

Overall, given the major versatility of properties and stimuli that can be used to modulate the properties of spiropyrans, they are currently being used in applications in very diverse fields. Examples include biomedical applications such as fluorescent imaging or photo-induced drug delivery [122,123], bio- and chemosensing applications (detection of ions, pH variation...)[124] and even their use as rewritable optical storage memories [125].

Despite the promising photo-electrochemical properties of NO_2BIPS compounds, as well as their numerous advantages (e.g., good switchability, fast responses times, large color contrast, the possibility of acquisition at a low cost and manufacture of devices at a commercial level), these possibilities are not being exploited due to a lack of understanding of the exact mechanistic process.

This thesis, therefore, intends to improve our understanding of the electrochemical mechanism that takes place for in derivatives of the NO_2BIPS type for potential use in different applications.

1.2.4. Dithienylethene-based MS

Dithienylethene (DTE) molecules are a type of MS that were synthetized for the first time by Irie's group in the late 1980s. Since then, DTE have received special attention over other classes of MS in part due to their excellent photochromic properties [126].

DTE chromophore are molecules formed by the association of two types of structures: aromatic thienyl groups and hexatriene subunit. Under irradiation at a specific wavelength, MS based on photochromic DTE can undergo reversible 6π-photocyclization between their unconjugated open-ring isomer (DTE_O) and conjugated closed-ring isomer (DTE_C).

In the DTE_O state, molecules can have two structural isomers: anti-parallel and parallel conformations, as shown in Figure 1.12.

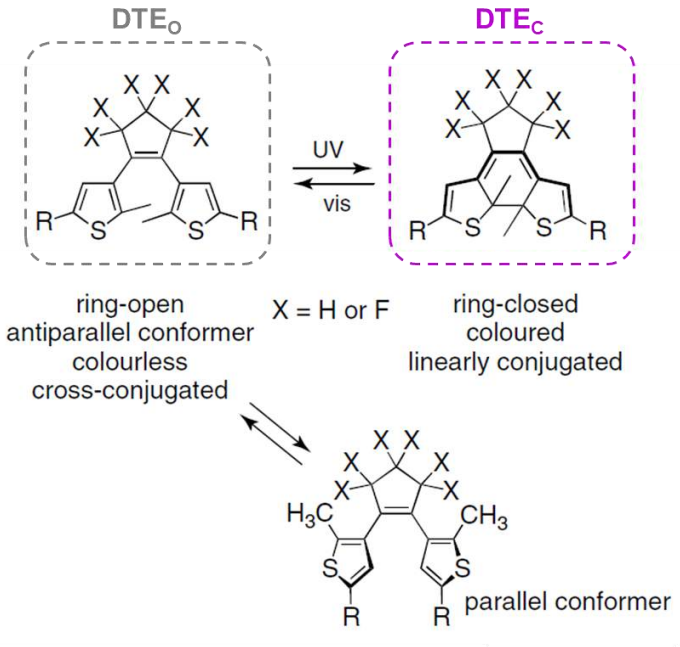

Figure 1.12. Reversible photochemical conversion of DTE through a 6π electrocyclation.

When exposed to UV light, only the anti-parallel conformer undergoes photocyclization, showing that the anti-parallel conformation is photoactive, while the parallel conformation is photochemically inert. As a result, the cyclization reaction's quantum yield is determined by the ratio of these conformations[127,128]. The introduction of bulky isopropyl groups in the 2- and 2'- position of benzothiophene aryl groups was shown to increase the proportion of antiparallel conformation and therefore, to increase quantum yields [129]. Importantly, the photoisomerization of DTE molecules permits access to two markedly different isomers. From the change in color from transparent (DTE_O) to pink color (DTE_C) -which is the most exploited feature- there is also a change in the electronic properties. The isomerization-induced wide gap between the HOMO-LUMO is predicted to profoundly alter the conductance of the molecule. While DTE_O is more isolating, the extensive π-conjugation of DTE_C improves the electrical conduction, making these compounds excellent components in organic electronics such as molecular wires [130].

Unlike other MSs, DTEs have outstanding ring-closing and ring-opening photoreactions, which are particularly attractive because their high symmetry means

they present and good fatigue-resistance. Besides, they present P-type photochromism, so they do not undergo thermal back isomerization.

In addition, because of their reversible photoinduced transformations that alter electrical conductivity, as well as their excellent thermal stability and resistance to photocyclization, they offer considerable potential as artificial photoelectronic switching molecules [131,132].

Another distinguishing aspect is their ability to undergo ring-closing and/or ring opening by means of an electric stimulus displaying a dual photo-electrochromic mode. Several studies in the literature have fully described the electrochemical mechanism for DTE ring-opening/closing, hence part of this thesis discusses the use of DTE as a mediator (photo)electrochrome in the development of electrochromic biosensors. What follows is a more in-depth discussion of electrochromic studies related to DTE-based molecules.

i. Electrochromism of DTE based MS

It has been found that some DTE molecules undergo cyclation and cycloreversion under redox potential providing a pathway to bypass the ground-state isomerization barrier.

In a previous study, Fox and Hurst described for the first time the electrochemical ring-closing (cyclation) reaction of fulgide [133], while Kawai et al. reported the electrochemical ring-opening (cycloreversion) reaction of DTE. They suggested that electrochemical ring-closing and ring-opening is typical in 6π-conjugated systems.

When applying an oxidation potential greater than 1 V to the DTE_O form with non-substituted 2- and 2' positions, the oxidation becomes irreversible due to an electropolymerization that creates a linearly conjugated π-system. However, the oxidation of DTE_C becomes reversible and can take place at lower potentials (often 400-700 mV less positive) due to the linear π-system in the molecule as a consequence of cyclation. Similarly, reduction of DTE_C is also less negative compared to DTE_O analogues. The differences in electrochemical behavior between both isomers indicate that DTE molecules can present different electrochemical mechanisms. For example, the difference in redox potential between isomers can be useful to modulate the use of DTE as quenchers or redox mediators when exposed to UV/Vis light that photoinduces the closed or the open isomer [134,135].

Further studies revealed derivatization of the molecule at the 2- and 2' positions, enables the reversible ring-opening or ring-closing when a convenient oxidation or reduction potential is applied. For instance, some derivatives undergo photocyclization to the formation of DTE_C when exposing the DTE_O isomer to UV light. Subsequently, when applying the appropriate oxidation potential, the reverse reaction ($DTE_C \rightarrow DTE_O$) is triggered. The oxidation of DTE_C leads to the formation of the corresponding radical cation, which is unstable, and the molecule backbone opens spontaneously, forming the DTE_O isomer.

Unlike the well-known matter of photochromism, there is more controversy about the intermediates involved in the electrochromic process. For example, the Branda, Launay, and Irie groups found that oxidative ring opening and closing reactions are mediated by radical cations [136–138] , whereas the Feringa group proposed that the reactions are mediated by dicationic species as mediators[139].

To disclose the factual electrochromic mechanism, several investigations focused on the electroinduced ring-opening/closing of a series of DTE compounds by cyclic voltammetry and UV-Vis spectroelectrochemistry.

On the one hand, spectroscopic measurements demonstrated that rates for isomerization of the key intermediates ($DTE_C^{\bullet+} \rightarrow DTE_O^{\bullet+}$) are favored by electrondonor groups (EDG) attached to aryl rings such as phenyl derivates. Mechanistic studies of a battery of DTE derivates with phenyl substituents of different electrondonor characteristics help to understand the process. The phenomenon is explained in the light of the computed spin density of broken C-C bonds that exists between the two thiophene rings. The C-C bond of $DTE_C^{\bullet+}$ presents a singly occupied molecular orbital (SOMO) with an interaction of its bonding orbital so that, when the spin density is smaller, the probability for ring opening increases. This effect is clearly observed when substituting DTE molecules with EDG such as methoxyphenyl groups, since the unpaired electrons are delocalized, leading to faster ring-opening. However, even though the ring-opening through the radical cations intermediates is faster in the case of DTE substituted with EDG, the overall reaction ($DTE_C \rightarrow DTE_C^{\bullet+} \rightarrow DTE_O^{\bullet+} \rightarrow DTE_O$) is the slowest. A thermal back isomerization ($DTE_O^{\bullet+} \rightarrow DTE_C^{\bullet+}$) seems to become dominant and a reduction electron transfer ($DTE_O^{\bullet+} \rightarrow DTE_O$) is less favored because it shows larger reduction potentials when an EDG is present, making the overall process slower [140].

On the other hand, thanks to voltammetric studies, it has been possible to complement and broaden our knowledge of the possible mechanisms involved in the

electrochromism process of DTE compounds. In this case, further derivatization of perfluoro or perhydro DTE with substituents ranging from EDG to EWG (e.g., chlorine, iodine, trimethylsilyl, phenylthio, aldehyde, carboxylic acid, and ethynylanisyl) enabled more precise description of the mechanisms involved. It was determined that the DTE_O form has two-electron irreversible oxidation waves, but its corresponding $DTE_O^{\bullet+}$ can undergo different mechanisms: dimerization, detected in the case of halogen or EDG derivates, or ring closure, which happens in the case of phenylthio-substituted molecules.

In addition, electrochromism is also observed for in the DTE_C form. In this case, electrochromism is favored when the molecule is functionalized with EWG and the color change becomes irreversible. On the other hand, in the case of DTE_C modified with EDG, consecutive oxidation-reduction cycles enable reversible color change because generation of the corresponding radical cation or neutral form, respectively. This is because the oxidation occurs at the cationic level and does not lead to structural changes [136].

Thus, the nature of DTE substituents strongly determines the final ring-opening/closure pathway for each case, making this type of molecule extremely versatile.

Given the benefits of DTE derivatives and the present state of knowledge regarding their electrochromic characteristics, it was determined that this thesis should employ and explore the use of this molecule as a colorimetric redox mediator in biosensor applications, as will be discussed in the next chapter.

1.3. Towards the Fabrication of Solid and Ecofriendly Platforms with Smart Functionalities

The appearance of SMs, among them the classic EC ('true' electrochromism) and MSs ((photo)electrochromes with 'memory'), has meant driven a major revolution in the technological world, and numerous commercial applications are intended to be developed based on these materials. For this reason, over the years, new methods and procedures have been established to adapt these compounds for their use in appealing applications and processes. One of the limiting aspects of their use is that, in many cases, the compounds present their (photo)electrochromic properties in solution., Hence, the need to look for an alternative or a strategy whereby the phase can be changed to the solid state without affecting its properties is necessary for many

applications. Secondly, there may also be cases in which the compounds are in a solid state, but for many of them the processability is complex and makes the manufacturing process difficult.

It should also be noted that the development and production of devices with 'smart' functionalities is also currently strongly determined by the social and environmental context in which we live. A clear example is the new demands for more "exotic" technologies such as the design of flexible devices, which have a direct impact on manufacturing procedures.

Besides, all these developments must be framed within the research and innovation of more sustainable chemical processes and compounds, considering the climate crisis of recent years. For this reason, another bottleneck is the type of process necessary for their production in terms of waste generation, toxicity, simplicity and affordability.

In particular, this thesis is focused on the use of different SMs with (photo)electrochromic properties to manufacture both electrochromic displays and sensor devices that change color as chemical signal transducers. Therefore, the main processes used today for the manufacture of these applications will be described, as well as the main factors that determine the type of process to follow within a sustainable and ecofriendly framework.

1.3.1. The Green Deal and its impact on the development of new materials

Climate change and environmental degradation are the main threats facing humanity, not only today, but also in the coming years. By the end of 2019, the European Commission had established a series of proposals included in the so-called Green Deal, hoping to make Europe a zero emissions community, in order to protect natural habitats and species, human beings, the planet, and the economy. For this propose, the EU's policies and regulations were to be applied in eight different areas: sustainable transportation, sustainable agriculture, clean energy, climate action, sustainable industry, environmental biodiversity preservation, investment in ecofriendly projects and innovative strategies and research. Figure 1.13. These actions are expected to reduce greenhouse gas emissions by 55% by 2030 compared with 1990 and reach climate neutrality by 2050 [141].

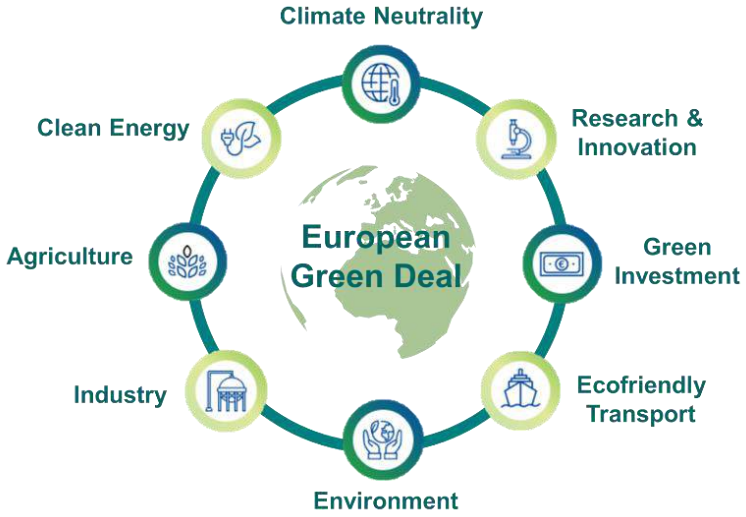

Figure 1.13 Illustration of the eight areas in which the regulations and policies of the Green Deal are being applied.

It is not surprising then that the climate problem that the planet is facing has direct implications for the development of the next-generation technologies, materials, and systems. In this regard, investment in research and innovation has a key role to play in boosting new projects within a more sustainable framework.

As it is known, chemicals are currently everywhere in our daily lives, since they play a fundamental role in most of our activities, forming part of all the devices that are useful to ensure our well-being, protecting our health and safety, and meeting new challenges through innovation. Hence, one of the measures being applied is the investment in the development of chemical components that are zero contaminants and/or are harmless to both the environment and the health of living beings. This set of proposals aims to promote more ecofriendly chemicals for the green transition.

Academic research has become paramount to transfer knowledge to society, industry, and business. This has had a direct impact on raising global awareness of what is already a current problem. Investment in research into more sustainable chemical products and processes has, therefore, increased considerably in recent years. This has been possible, among other measures, thanks to funding schemes from such as those from the European Commission, i.e. programs as the European Union's H2020 and Horizon Europe Programme, projects that support research projects focused on greener technologies that are free of toxic chemicals.

Improvements in synthetic processes and as well as in the technologies used, the use of green solvents, the implementation of zero-waste processes, the atoms economy, the reuse of compounds and the circular economy, as well as the synthesis of high added value products, are just a few examples of strategies pursued in chemical research and innovation to mitigate the consequences of human activity on the environment.

1.3.2. Processes for the Manufacture of Platforms

Since the discovery of the first chromic compounds, the scientific community has acquired extensive knowledge about their spectroscopic properties, producing objective and quantitative information based on their color change. Studies of soluble compounds are carried out at early stages in solution to understand the intrinsic chromic characteristics of the material and find its application fields. However, at the practical level, the use of compounds in solution is not appealing for factual applications because of liquid leakage, solvent evaporation and thus, efficiency loss. As a result, many methods have been implemented, all of which are appropriate depending on the nature of the substance to be deposited, as well as the surface or substrate onto which the coating will be implemented. Figure 1.14.

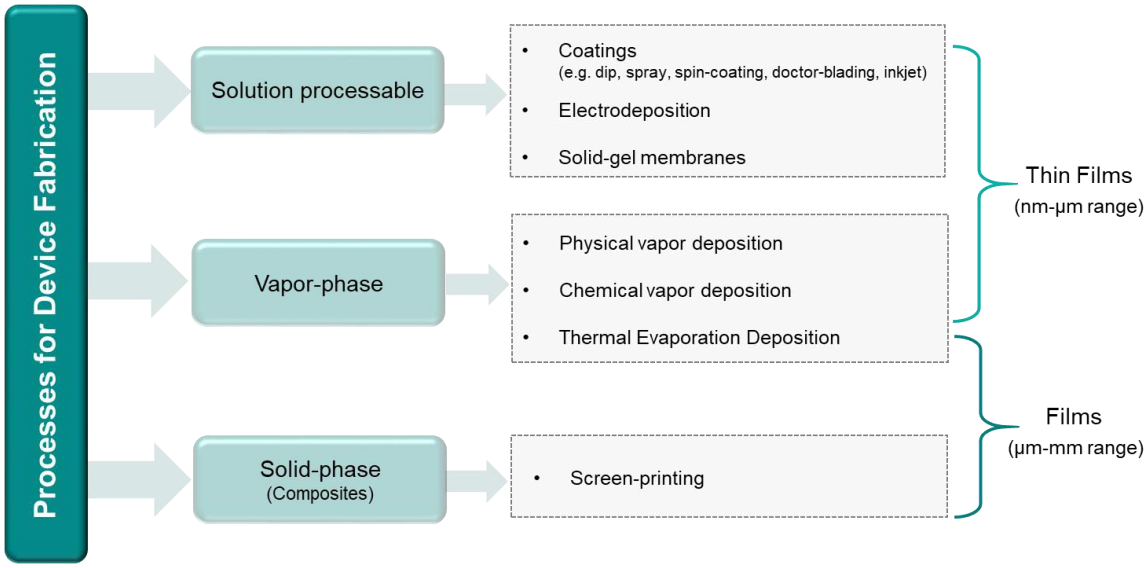

Figure 1.14. Types of processes used to produce chromic displays

Thus, the choice of production process depends on the substrate, but also on the nature of the active molecule, that will also determine the coating process.

On the one hand, some processes such as dip coating, spray coating and spin-coating require solubilization beforehand of components in solvents, generally organic solvents. The implementation of these techniques enables deposition over a wide range of substrates that can undergo deformations (e.g. stretching, twisting, bending, etc.), while keeping their functionalities.

These coating techniques have mainly been used for in polymeric coatings, being the reason why the solvent processability of several polymers has been extensively explored. Especial attention in this field should be paid to the group led by Prof. J. Reynolds, whose finding proved that the derivatization of the 3-position of polythiophenes plays a key role in controlling the solubility, and that regioregularity is directly related to their solvent-processability [142,143].

Meanwhile, electrodeposition or electropolymerization is an affordable, fast, and versatile method not only for producing metal or metal oxide coatings (e.g. Ag, Au, TiO_2, NiO, WO_3, ZnO, Co_3O_4, or V_2O_3) on conductive substrates but also for enabling the deposition of polymeric films. This technique also requires the solubilization of metal oxide precursors or monomers for film formation on conductive substrates. There are many advantages of this method: it does not require a high vacuum or temperature and it also enables fine control tuning the thickness and morphology of the nanostructure by modifying the electrochemical parameters. [144–146]

Another strategy consists of the entrapment or functionalization of EC in gels. This is interesting in that it is possible to use a wide variety of both organic and inorganic compounds, if they are soluble in the medium. Moreover, the use of conductive surfaces is not necessary as in the previous case. This makes it possible to prepare layers that are functionalized with compounds that do not necessarily have to present electrical properties, such as electrochromic compounds, and expands the variety of films with other properties that may be prepared, such as thermochromic, photochromic, halochromic, etc.

Several gels have already been modified with chromic chemicals that are responsive to various stimuli such as redox, light, temperature, or ions. Current examples include photochromic gels made with modified matrices (poly(vinylalcohol)) with TiO_2 and methylene blue (MB). Light irradiation causes the excitation of TiO_2, which has a photocatalytic effect and leads to the reduction of MB to its bleached form. The

subsequent oxidation with ambient oxygen causes it to return to its initial form, allowing it to act as a colorimetric oxygen sensor.[147] Other studies use water-based matrices like alginate membranes, which immobilize enzymes or chromic molecules for the development of biosensors or colorimetric labels for food quality control [148,149].

In contrast, the insolubility of a wide range of compounds such as oxides or metals boosted the implementation of technologies for the production of active layers of chromic devices. Clear examples are the thin-films produced by physical vapor deposition (PVD), chemical vapor deposition (CVD) or thermal deposition, where the precursor material is in the solid state and is evaporated in different ways, depending on the technique, and isbeing subsequently transported and deposited on to the target material surface. Such processes have been successfully used to deposit certain oxides such as WO_3 or V_2O_5, which have electrochromic properties, and enable the formation of robust thin coatings on large surfaces such as glass. However, the process is restricted to coating of oxides and inorganic compounds due to the high deposition temperatures, which would degrade organic compounds. For theis same reason, one of the main limitations of CVD and PVD is the complexity of using organic substrates such as plastics, which would make the final device more flexible [150].

One strategy whereby devices or systems can be manufactured using non-soluble electrochromes is through the formulation of composites or hybrid materials. The pioneers in making the first composites with electrochromic properties included Coleman et al. who, in general terms, performed the modification of conducting particles such as ATO-TiO_2, ITO-TiO_2 with PB [151,152]. Once the modification is done, the particles are dispersed in a resin or polymeric binder, such as fluoroelastomers, hydroxyethylcellulose or acrylics, which provides strength, flexibility and chemical resistance to the final material. The result is a paste or ink that changes the color in response to specific environmental stimuli, depending on the nature of the chromic compound. The rheological properties of the final ink is ideal for the production of low-cost applications using screen-printing, which enables fast, simple and large-scale manufacturing of devices. It also paves the way for the use of both inorganic and also organic compounds with chromic properties. Further, examples have formulated similar hybrid materials using in situ polymerization of polyaniline on nanocellulose, which presents high electrochromic responses (1.5 s for bleaching and 1.0 s for coloring)[153]. Meanwhile, others have managed to provide multifunctionality to these hybrid materials [154].

All these advances have revolutionized the field of device manufacture, leading to novel formulations with advanced functions, sparkling interest not only in the scientific world but also in the industrial sector. Some examples are shown in Figure 1.15. Novel attributes such as flexibility, stretchability and bending are much more appealing for 'futuristic' applications like wearables, which would be impossible to obtain had with classical manufacturing technologies not improved. But apart from creating the possibility of producing flexible devices with more attractive properties, manufacturing costs will drop dramatically due to the simplicity of the processing and the affordability of the materials.

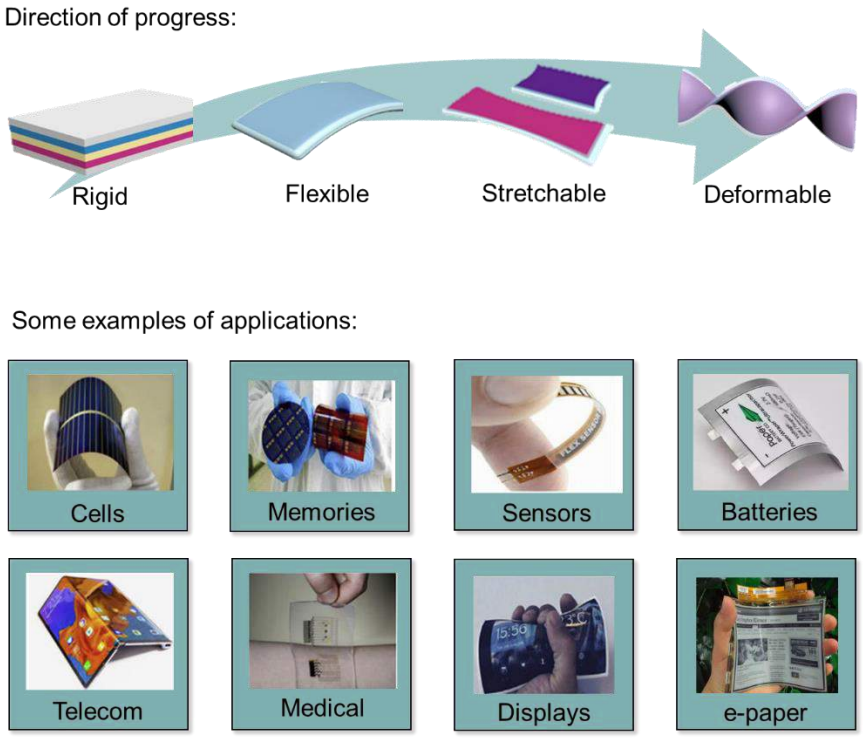

Figure 1.15. Directionality of future devices with advanced properties (twisting, bending, etc.) and some applications where they are applied. Examples of applications were adapted with permission from ref.[155] Copyright 2019. The Chinese Ceramic Society.

The production smart materials of for a wide range of applications is being attempted at the industrial level, from solar cells, memories, sensors and flexible batteries to mobile phones. However, in many cases, they are still under development, the goal being to improve their performance to compete with commercially available technologies.

This doctoral thesis has particularly sought to develop materials with electrochromic properties as a common factor, and in some cases multifunctional features. To do so, as will be detailed in the results and discussion sections, electrochromic inks or gels and membranes modified with different chromic compounds have been designed. In all cases, the objective of these formulations is not only to obtain a material with the desired functionalities, but also with potential rheological properties to facilitate handling and printing with simple techniques, whereby these materials could be implemented in future displays and devices.

1.3.3. Novel Approaches for the Development of Devices and Platforms for Electrochromic Applications

The construction and configuration of devices or systems that change of color in response to an external input is directly determined by the intended final application.

As a result, the building alternatives are many and diverse. Given that the materials developed in this doctoral thesis have two specific objectives, we shall exclusively focus on the components required for these two scenarios: their application as potential displays or as colorimetric biosensors.

i. Electrochromic displays

In the case of electrochromic displays, there are two types of configurations. The most traditional model is the one based on a 'sandwich' mode configuration, in which the two electrodes are facing each other and the rest of the components, i.e., the ion storage layer and the electrolyte, are arranged layer-by-layer between them. Figure 1.16 a). Although the electrical resistance for this configuration is usually good because of the electrode arrangement, on the other at least one of the two electrodes must be transparent, such as PEDOT:PSS [156], or tin-oxide derivatives such as ITO or FTO [157] to observe the color change, which in turn are less electric conducting compared to other materials such as carbon graphite, silver, copper...

The second configuration, shows a coplanar or interdigitated structure, in which the electrodes are arranged on the same horizontal plane. A layer of electrochromic material is placed on top of these electrodes, and finally the electrolyte on top it Figure 1.16. b). In this case, the electric field is applied laterally, producing a color change that starts at

one end of the layer and progresses horizontally to the end that is in contact with the counter electrode [151].

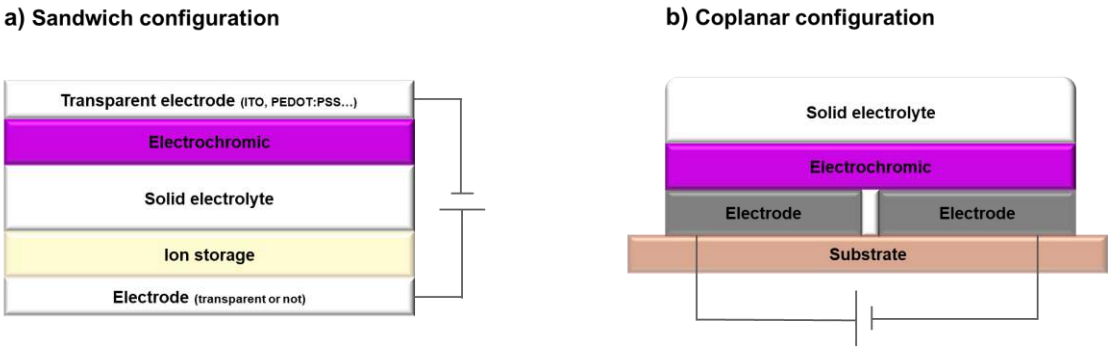

Figure 1.16. Types of architectures for electrochromic devices a) Sandwich configuration b) Coplanar configuration.

In both configurations, in addition to the electrochromic compounds and the two electrodes used for applying the potential, require an electrolyte layer. This component plays a key role in the efficiency and performance of the electrochromic device since it responsible to provide the necessary ionic conductivity, and also to enables charge compensation when the electrodes polarization.

In this type of application, for the reasons mentioned above, it is essential for these elements to be implemented in a solid-state configuration

For this reason, polymer electrolytes have become a viable alternative to liquid electrolytes that have to deal with poor mechanical properties and such safety issues as associated to liquid leakage, among others. Apart from mechanical strength, polymer electrolytes present other interesting properties such as flexibility and stretchability. However, as main disadvantage, polymers are generally poor ion solvents (due to their low dielectric constant and high viscosities). Hence, in many cases, solid-state electrolytes based on polymers frequently contain strongly solvating groups such, as carbonyl, ether oxygen and nitrile.

In this regard, solid polymer electrolytes present many benefits over liquid electrolytes, including mechanical resistance and in some cases flexibility and stretchability. Moreover, their composition prevents dendrite growth, which is the main cause of deterioration of electronic devices that require the use of electrolytes.

Various polymer hosts have been created and characterized to date, including poly(ethylene oxide), (PEO), poly(propylene oxide), (PPO), poly(acrylonitrile) (PAN),

poly(methyl methacrylate), (PMMA), poly(vinyl chloride) (PVC), poly(vinylidene fluoride) (PVdF), and poly(vinylidene fluoride-hexafluoro propylene) (PVdF-*co*-HFP).

Despite all the advantages of the use of electrochemical devices, one of the main drawbacks is still their low ionic conductivities (10^{-4} S·cm^{-2} - 10^{-5} S·cm^{-2}), which that greatly limit their performance. However, many approaches have been developed to tackle this issue.

Among all other polymer electrolytes, ionogels (IG) are taking a principal position for one candidate that meets all presenting the prerequisites the ideal properties for more futuristic applications such as the production of most advanced devices, i.e., wearables, e-paper, labels and flexible batteries, are ionogels (IG). Part of this thesis is devoted to the optimization of IG formulations and their use in electrochromic applications. Hence, a more detailed description of IG is provided in the following subsection.

ii. Ionogels (IGs) as solid and flexible electrolyte.

The advent of IGs ten years ago revolutionized research in the field of solid electrolytes. These are hybrid materials based on ionic liquids (ILs) whose ionic species are entrapped in the cavities of a polymeric matrix. Figure 1.17 a). As a result, a promising family of solid electrolytes membranes has been achieved that offer both the advantages of ILs and ideal rheological properties that provide access to novel all-solid devices [158,159]. The versatility of IGs is so varied that there is an unprecedented variety of options for their use, from solid electrolyte membranes to sensors, in drug delivery and in the optics field due to their high transparency. Figure 1.17 b).

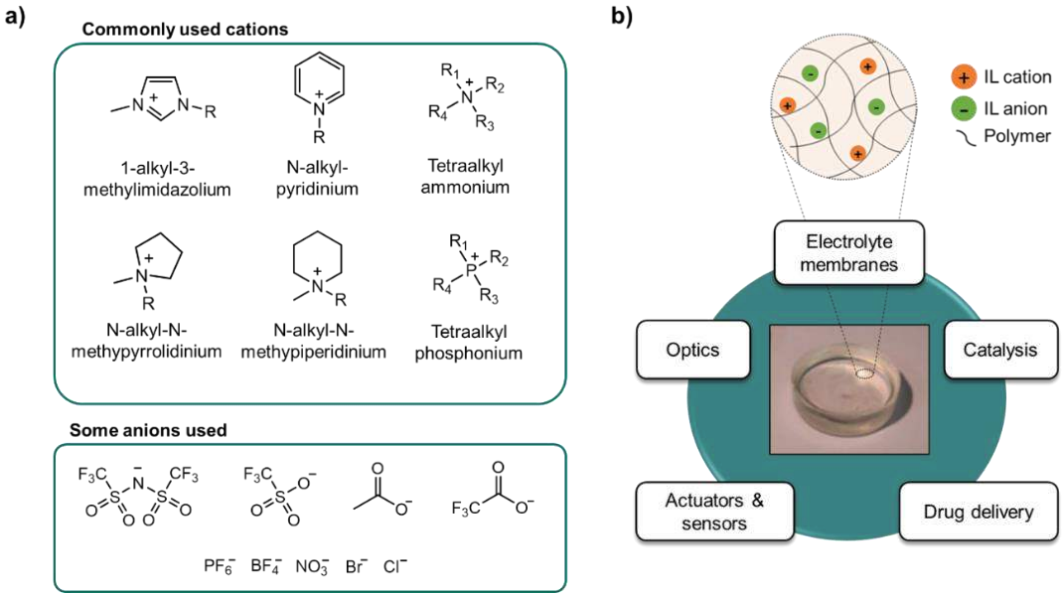

Figure 1.17. a) Typical cations and anions used for the synthesis of ILs. b) Formulation of IG and their field of application.

IGs, therefore, maintain the properties of ILs, such as high ionic conductivities (within 10^{-4} to $8{\cdot}10^{-2}$ $S{\cdot}cm^{-1}$ at room temperature), wide electrochemical window (5.7 V between Pt electrodes), capacity to solve a broad range of species, large thermal and chemical stability, low toxicity, and volatility [160]. Specially, these latter advantages have led them to be addressed as green solvent and to enable the production of more sustainable devices, which has been one of the main goals in recent years of the H2020 and HE framework. Moreover, the physicochemical properties of IGs can easily be tuned by modifying the cation-anion pair of the IL Figure 1.17 a), thus generating millions of options and endowing the final membrane with further properties (e.g., photochromism, or electrochemical response, biocompatibility, targeted biological properties)[161,162].

While presenting unique chemical properties, the solid-like appearance of IGs due to their hybridization with a polymer matrix leads to easy shaping and cut-stick properties, and simple processability that broadens the array range of applications with the particularity that they also present the ideal rheological properties for future applications.

In addition to the wide variety of ILs available for use in the formulation of IGs, the matrix where the ions are incorporated can also be used to tune the properties of final membranes. The options are varied and one way to categorize them is based on the nature of the solid-like network, as detailed below.

- **Inorganic IGs.** These include examples such as 'Bucky gels' which are obtained by grinding or sonicating carbon nanotubes (CNTs) in imidazolium-based ILs. The final material presents the properties of gels. Also by using polymerizable ILs, these gels are transformed into conductive polymeric materials [163]. A second group of inorganic IGs is based on the confinement of ILs within a silica network [164].
- **Organic IGs**. These IGs can either be low molecular weight gelators (LMWGs) or polymer gels. For LMWGs, organic molecules such as L-glutamic acids, carbohydrates[165] , cholesterol [166] or cyclo(dipeptides) [167] are mixed with ILs, heated to high temperatures, and after they cool down, interactions such as hydrogen bonds, π-π stacking or electrostatic interactions enable self-assembly and thus, gel formation. In the second case, polymers are used to immobilize IL in the form of free-standing membranes, endowing the final membrane with the flexibility of the polymer and high ionic conductivity. These membranes are typically used in displays due to their flexibility and good electrochemical properties. They are commonly prepared by mixing polymer and ionic liquid with a co-solvent that is eventually evaporated. Finally, the membrane is formed by swelling the polymer in an ILs. Typical polymers used thusin this case are poly(methylmethacrylate) (PMMA), poly(ethylene oxide) (PEO), Nafion®, poly(vinylidene fluoride-*co*-hexafluoropropylene (P(VdF-*co*-HFP)), and biopolymers such as chitosan, agarose, cellulose and starch [168–171].

This capability of immobilizing substances opens new avenues for designing advanced materials, especially (bio)catalytic membranes, sensors and drug release systems.

Specifically, this doctoral thesis uses IG formulated with PVdF-*co*-HFP and IL of distinct kinds in two different ways.

1) *Layered type*. In this approach the electrolyte is used as an independent layer that is differentiated from the remaining components (i.e., the electrochromic active layer and the ion storage layer). In this configuration, the EC is directly attached to the electrode surface. The other components are arranged depending on whether the ECD follows a sandwich or coplanar configuration.

2) *All-in-one layer*. In this case, both the main electrochrome and the redox mediator are dissolved in the electrolyte, that is, they are both in a single layer. If the ECD is manufactured in a sandwich configuration, the IG membrane is placed between two conductive electrodes. Otherwise, if the configuration is coplanar, it is directly placed in a single layer on the top of both electrodes. Although the manufacture

of ECD following this strategy is limited to EC materials that are soluble in electrolytic media (e.g., viologens), this design could provide a broad variety of color and simplify the production process, making them more appealing from an industrial standpoint.

iii. Electrochromic biosensors

Biosensors are defined as an analytical device that translate a biochemical reaction mediated by enzymes, immune systems, tissues, organelles or cells into a measurable signal [172], generally from the electrical domain.

Basic components of biosensors are: 1) detection interface, 2) transducer and 3) output system, and they are classified depending either on the type of biomolecule implied in the biochemical reaction, also known as recognition elements, and on the type of signal transducer, e.g., electrochemical, optical, thermal, etc. Figure 1.18.

More specifically, in this section, colorimetric biosensors will be examined in greater depth, as this is a possible potential application for which many of chromic chemicals can be employed.

Up to now, the construction of high-performance biosensors has attracted considerable attention because of their good selectivity and sensitivity, but among them it is worth highlighting the benefits that colorimetric biosensors present compared to classic electrochemical, optical or electronic systems, including the fact that colorimetric systems enable simple naked-eye determination without the need for external instruments (very well aligned with the RE-ASSURED criteria for detection systems for resources-limited environments), fast detection without needing sophisticated instruments and cost-effectiveness [173,174]. Therefore, colorimetric sensors have been used for the detection of DNA, proteins, viruses and small molecules of clinical interest or ions such as glucose, urea and, lactate and chloride or ions, among others [174–176].

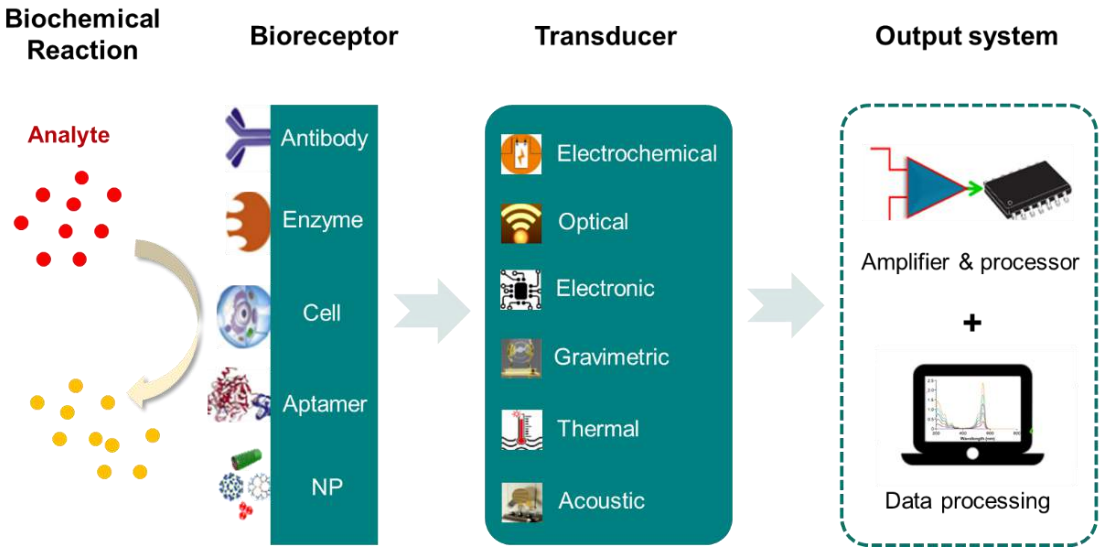

Figure 1.18. Parts of biosensors and types depending on the bioreceptor used or the transductor.

One of the most common strategies for colorimetric biosensors is the use of immune-aggregation of antibodies functionalized with gold NPs on a lateral flow format. In lateral flow, the sample is dispensed on the surface of a devices fabricated on a low-cost substrate with capillarity. The sample is then flowing through the substrate while reacting with non-attached antibodies functionalized with gold NPs that selectively recognize the target molecule of interest until reaching the detection area. In the detection area, the target molecule is recognized by a second antibody anchored to the surface that concentrates the gold NPs in a point. For instance, the presence of analytes in an NP-based biosensor causes the aggregation of NPs in the detection area, and thus the emergence of a clear color change visually detectable due to the surface plasmon resonance (SPR) [177]. Figure 1.19.

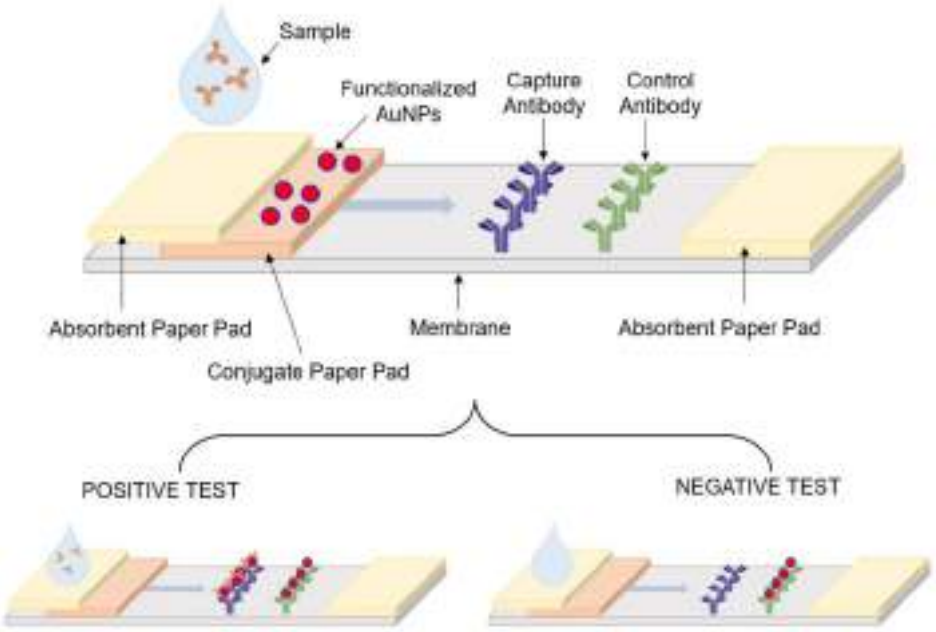

Figure 1.19. Example of a lateral flow based on functionalized gold NPs (AuNPs). The sample is absorbed in the first paper pad and flows through the membrane by capillarity.

Along the years, many approaches have been developed aiming to improve the detection capacity of lateral flow systems, particularly their sensitivity and quantification capacity. Highly relevant are those approaches based on the use second strategy consists of the functionalization of 2D materials such as graphene. The large specific surface area of graphene oxide (GO) improves the adsorption of biomolecules, NPs and chromic molecules, resulting in enhanced colorimetric sensor sensitivity [178,179].

Apart from plasmonics, other optical properties have been used to produce observable color changes in the production of colorimetric biosensors. One example is the use of photonic crystal biosensor (PC): PC is a kind of material whose observed color is dependent on the different structural arrangements that result in a different coloration. Thus, the coloration in this case is a consequence of the effect of Bragg diffraction. In sensor applications, the reaction of target molecules with PC substrates triggers changes in the refractive index or diffracting plan spacing. As a result, a color change is observed and may be reversibly converted to the initial form [180].

In contrast, in other systems when it is also possible to couple the biochemical recognition reaction between an analyte and a target biomolecule, a secondary reaction is promoted, leading to a color change in molecule color. This strategy is very common in enzymatic biosensors, where for example, an enzymatic catalytic activity is mediated

by enzymes (e.g., oxido-reductasesase or catalase) that generates H_2O_2 that subsequently oxidizes an electrochromic molecule such as 3,3',5,5'-tetramethylbenzidine (TMB), resulting in a color change that can be observed with the naked-eye. The combination of two enzymatic activities in cascade reactions, e.g. oxidoreductases to produce H_2O_2 and peroxidase to transform the previous molecule into oxygen and water, with electrochromic molecules is also very common in this case. This strategy has proved useful for the construction of various colorimetric sensors for small molecules and metallic ions [181]. In other examples, the color change is due to fluorescent organic dyes that in the presence of analyte react with the fluorescent probe, thereby behaving like an '*ON*'-'*OFF*' switch [182].

However, one of the main problems with biosensors is the immobilization of bioreceptors, which directly affects proper device operation. Various strategies exist to address the problem, each with their benefits and drawbacks. The most common methods for the immobilization of bioreceptors are entrapment in 3D matrices (e.g. electropolymerization, sol-gel process, polysaccharide-based gel, etc.), adsorption on solid supports (e.g. physical or electrostatic), cross-linking, covalent immobilization to supports (activation of carboxylic groups or amino groups, chemisorption) and affinity, based on oriented and site-specific immobilization of bioreceptors (biotin-(strept)avidin, metal ion-chelator, lectin-carbohydrate). Figure 1.20.

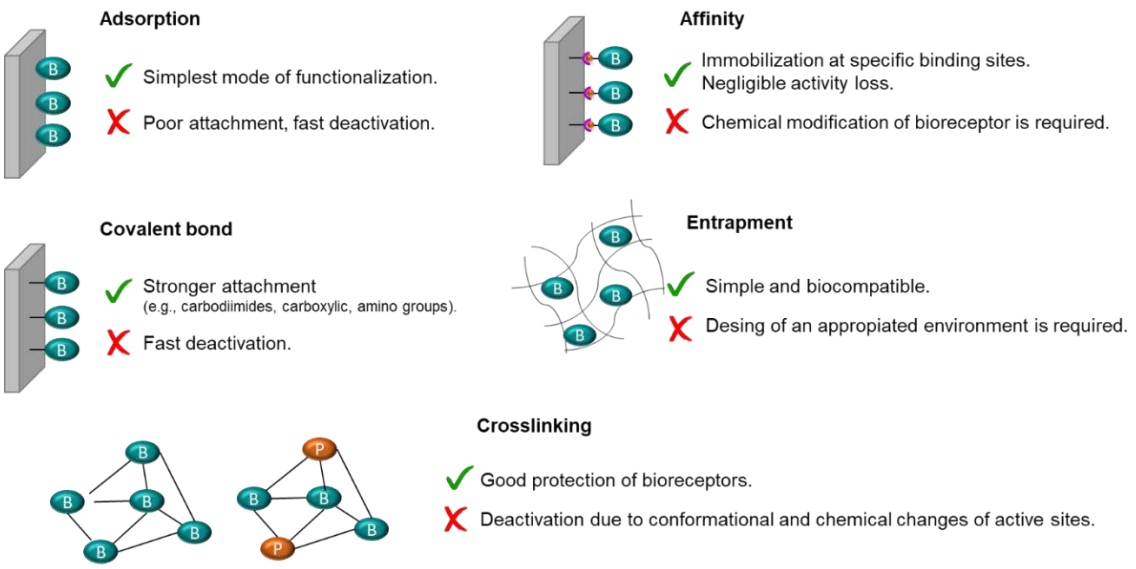

Figure 1.20. Schematic representation of strategies for immobilization of bioreceptors (e.g., enzymes, antibodies, NPs, etc.) and the advantages and drawbacks of their use. B: bioreceptor, P: inert protein

The choice of the most suitable approach depends on the biomarker characteristics, the transducer and the mode of detection. Of these, entrapment of biomolecules as enzymes has been deemed an accurate approach to the immobilization of enzymatic biosensors due to its simplicity and biocompatibility. Moreover, and similar to electrochromic displays, most new-era biosensors are endowed with flexible, stretchable properties for the next generation of wearable biosensors. Hence, the entrapment of biomolecules in biocompatible membranes that preserve the structure and function of the biomolecules and commonly present the same ideal rheological properties is also appealing for wearable applications.

In this case, enzymes are entrapped in three-dimensional matrices, such as an electropolymerized film, an amphiphilic network composed of polydimethylsiloxane (PDMS), a photopolymer, a silica gel, a polysaccharide or a carbon paste. Biopolymer-based hydrogels and membranes are currently gaining popularity due to their inherent biocompatibility and biodegradability. Hyaluronate, alginate, agarose, starch, gelatin, cellulose, chitosan, and their derivatives have commonly been used to make various biopolymer hydrogels. Table 1.2 summarizes the most relevant colorimetric biosensors to have been developed employing biopolymer matrices.

Table 1.2. Typical biopolymers used for enzyme immobilization and some examples of applications in which they are used.

Biopolymer	Composition	Source	Some biosensors examples
Alginate	Salts of Ca^{2+}, Mg^{2+} or Na^{+} of alginic acid	Cell walls of brown algae	Urea [183], DNA[184]
Chitosan and chitin	glucosamine (dea cetylated monomer) and N-acetyl-glucosamine (acetylated monomer) monomers linked through β-,4 glycosidic bonds	Shells of crustaceans, fish scales, fungi, insects…	Cholesterol[185], glucose[186], uric acid[187]
Collagen	Three left-handed helix by interaction of glycine, proline and hydroxyproline units	Found in connective tissue, skin, tendons, bonds and cartilage	Glucose [188], pathogens and toxins [189]
Cellulose	Polysaccharide formed by β-1,4-linked glucose units	Plant cell walls.	Kanamycin[190], glucose[191], lactate[192]
Starch	Polysaccharide formed by α-1,4-linked glucose units	Corn, potatoes, wheat…	Ochratoxin A [193], phenylketonuria [193].

As mentioned above, there are numerous options to immobilize biomolecules. However, many of these require laborious processes and/or the microenvironment is not suitable, meaning that biomolecules such as enzymes lose their activity in short periods of times.

In this regard, it has been proven that silk fibroin (SF) presents a unique structure that enables major enzymatic stabilization. Thus, part of this thesis attempted to use SF from *Bombyx Mori* cocoons for the immobilization and development of colorimetric and enzymatic biosensors.

iv. Physicochemical Properties of Silk Fibroin (SF) as Biomaterials

SF has been considered a very promising material for medical devices, drug delivery platforms, tissue-engineering scaffolds, and platforms for enzyme stabilization because of the combination of such unique properties as outstanding mechanical resistance, biodegradability, biocompatibility, excellent optical and electronic properties, and diversity of structural re-adjustments [194–198].

Raw silk, derived from native *Bombyx Mori* silkworm fibers, is mainly composed of two SF fibers (~ 75 %) stuck together by an adhesive protein called sericin (~ 25 %) that is removed after a degumming process by boiling the cocoons in sodium carbonate [199]. SF is a semi-crystalline material that confers both stiffness and strength. Figure 1.21 a).

SF have a light (L) chain protein (~ 26 kDa) which is hydrophilic, and a heavy (H) chain polypeptide (~ 390 kDa) which is hydrophobic. These are bound together by a disulfide bond at the C-terminus of the H-chain, forming the H-L complex. At the same time, glycoprotein P25 present in SF binds the resulting H–L complex by hydrophobic interactions [200,201]. Figure 1.21 b).

The amino composition hydrophobic domain (H-chain) is a repetitive hexapeptide sequence of Gly-Ala-Gly-Ala-Gly-Ser and repeats of Gly-Ala/Ser/Tyr dipeptides whose intermolecular forces (hydrogen bonds, van der Waals and hydrophobic interactions) form anti-parallel β-sheet structures that confer crystallinity to SF and good mechanical properties to the material, including major rigidity and tensile strength. In addition, tyrosine is present to ~ 5% and provides certain reactivity to the material. In turn, hydrophilic domains (L-chain) are non-repetitive and have an amorphous structure, so they are relatively more elastic [202–204].

The specific arrangement of amino acids results in the formation of different crystalline structures, silk I and silk II. While silk II is formed by folded β-sheets (nanocrystals) as a consequence of intermolecular interactions, silk I forms a zigzag conformation because it is composed of a β-sheet, α-helix and random coil. The more ordered silk II structure can be induced from silk I after a water annealing process or via methanol or potassium phosphate treatment [197,205,206].

The silk-III structure is also possible, but is less stable and is only formed in regenerated SF [207].

Depending on the treatment, SF solution can be processed to confer fine control over its properties and structures, from the micro scale to the macroscopic level. Examples include the sponges, microspheres, hydrogels, films and nanofibers produced by electrospun, Figure 1.21 c).

The scope of applications of silk-based materials has expanded in recent years. Current applications range from tissue engineering scaffolds[208,209], drug delivery[210] and biosensor devices [211,212]. Recently, due to its mechanical and optical properties, SF has also been used in the manufacture of flexible electronics[213] and photonic displays [214]. This material's robustness, flexibility, non-toxicity, biocompatibility and biodegradability make it suitable for the development of next-generation devices [215].

As mentioned above, SF has been used in this thesis to stabilize enzymes and electrochromic molecules used as reaction mediators for the development of long-term glucose colorimetric biosensors. It has been demonstrated that the assembly of SF leads to nanoscale 'pockets' where enzymes can be stably entrapped. SF is also exceptionally stable under changes in humidity and temperature, as well as being mechanically durable thanks to its large network resulting from physical cross-links. Furthermore, the processing of silk-based materials does not require harsh chemicals and can be carried out in ambient conditions in aqueous media without affecting the bioactivity and/or structure of the enzymes. Overall, previous studies have demonstrated that SF is a suitable biomaterial for the immobilization of enzymes such as glucose oxidase (GOx) or peroxidase, and which remains 90% active for more than 84 months [196,216–218].

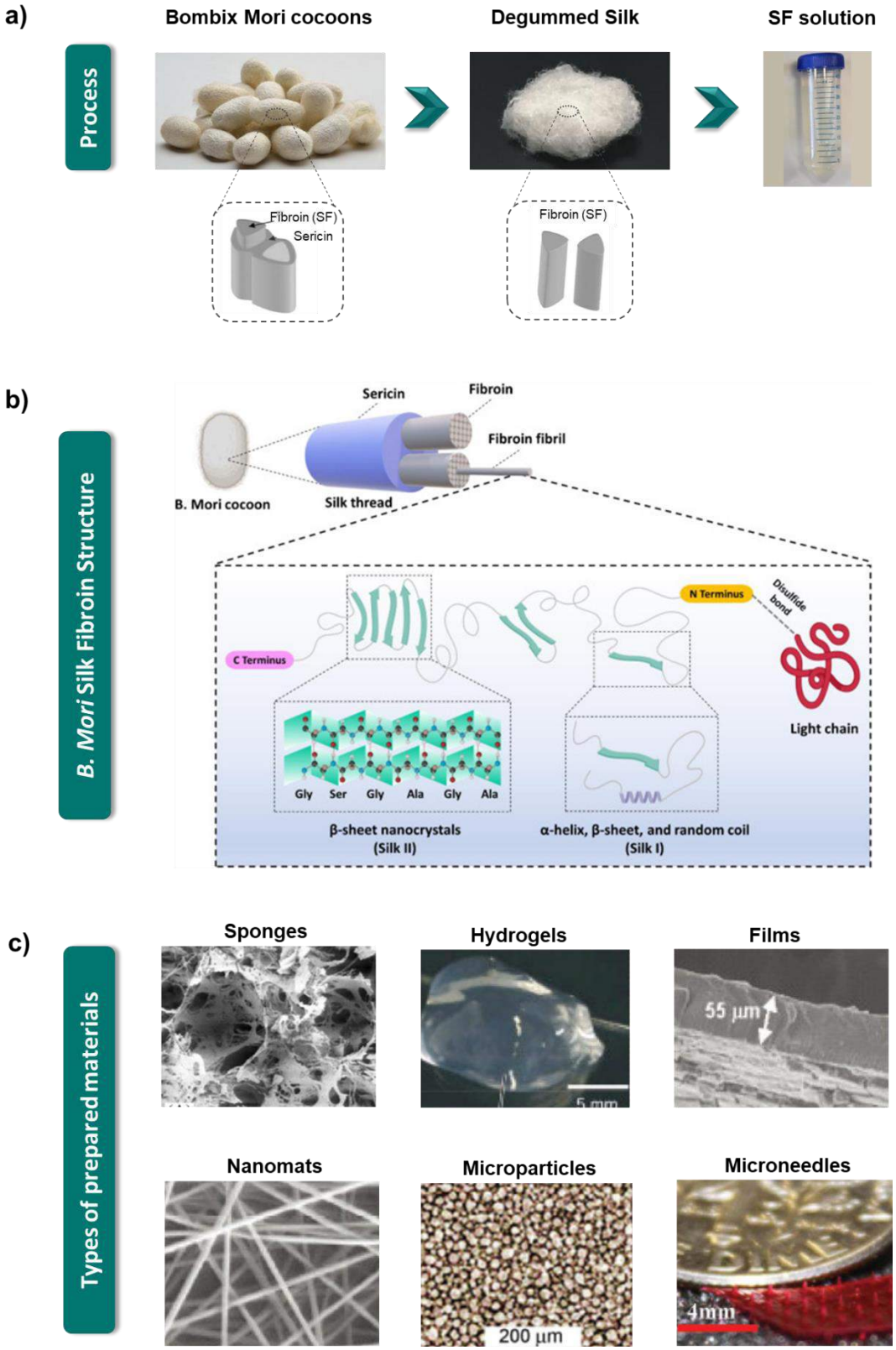

Figure 1.21. a) Raw silk consists of two fibroin fibers held together with a layer of sericin. After degumming, sericin is removed and the fibroin fibers are dissolved in lithium bromide solution. After that, the solution is dialyzed against ultrapure water [199]. b) Schematic representation of silk microstructure. c) Examples of materials formed using SF solution.

1.4. References

(1) Teyssier, J.; Saenko, S. V.; van der Marel, D.; Milinkovitch, M. C. Photonic Crystals Cause Active Colour Change in Chameleons. *Nature Communications* **2015**, *6* (1), 6368. https://doi.org/10.1038/ncomms7368.

(2) Yura, T.; Nagai, H.; Mori, H. REGULATION OF THE HEAT-SHOCK RESPONSE IN BACTERIA. *Annual Review of Microbiology* **1993**, *47* (1), 321–350. https://doi.org/10.1146/annurev.mi.47.100193.001541.

(3) Dawson, C.; Vincent, J. F. V.; Rocca, A.-M. How Pine Cones Open. *Nature* **1997**, *390* (6661), 668–668. https://doi.org/10.1038/37745.

(4) Chortos, A.; Liu, J.; Bao, Z. Pursuing Prosthetic Electronic Skin. *Nature Materials* **2016**, *15* (9), 937–950. https://doi.org/10.1038/nmat4671.

(5) Mathôt, S. Pupillometry: Psychology, Physiology, and Function. *Journal of Cognition* **2018**, *1* (1). https://doi.org/10.5334/joc.18.

(6) Runnerstrom, E. L.; Llordés, A.; Lounis, S. D.; Milliron, D. J. Nanostructured Electrochromic Smart Windows: Traditional Materials and NIR-Selective Plasmonic Nanocrystals. *Chem. Commun.* **2014**, *50* (73), 10555–10572. https://doi.org/10.1039/C4CC03109A.

(7) Kang, J.; Tok, J. B.-H.; Bao, Z. Self-Healing Soft Electronics. *Nature Electronics* **2019**, *2* (4), 144–150. https://doi.org/10.1038/s41928-019-0235-0.

(8) Vatankhah-Varnosfaderani, M.; Daniel, W. F. M.; Everhart, M. H.; Pandya, A. A.; Liang, H.; Matyjaszewski, K.; Dobrynin, A. V.; Sheiko, S. S. Mimicking Biological Stress–Strain Behaviour with Synthetic Elastomers. *Nature* **2017**, *549* (7673), 497–501. https://doi.org/10.1038/nature23673.

(9) Giachino, J. M. Smart Sensors. *Sensors and Actuators* **1986**, *10* (3–4), 239–248. https://doi.org/10.1016/0250-6874(86)80048-8.

(10) Bahl, S.; Nagar, H.; Singh, I.; Sehgal, S. Smart Materials Types, Properties and Applications: A Review. *Materials Today: Proceedings* **2020**, *28*, 1302–1306. https://doi.org/10.1016/j.matpr.2020.04.505.

(11) Bahl, S.; Nagar, H.; Singh, I.; Sehgal, S. Smart Materials Types, Properties and Applications: A Review. *Materials Today: Proceedings* **2020**, *28*, 1302–1306. https://doi.org/10.1016/j.matpr.2020.04.505.

(12) Kim, J.; Kim, M.; Lee, M.-S.; Kim, K.; Ji, S.; Kim, Y.-T.; Park, J.; Na, K.; Bae, K.-H.; Kyun Kim, H.; Bien, F.; Young Lee, C.; Park, J.-U. Wearable Smart Sensor Systems Integrated on Soft Contact Lenses for Wireless Ocular Diagnostics. *Nature Communications* **2017**, *8* (1), 14997. https://doi.org/10.1038/ncomms14997.

(13) Mirfakhrai, T.; Madden, J. D. W.; Baughman, R. H. Polymer Artificial Muscles. *Materials Today* **2007**, *10* (4), 30–38. https://doi.org/10.1016/S1369-7021(07)70048-2.

(14) Soto, F.; Wang, J.; Ahmed, R.; Demirci, U. Medical Micro/Nanorobots in Precision Medicine. *Advanced Science* **2020**, *7* (21), 2002203. https://doi.org/10.1002/advs.202002203.

(15) Khan, A.; Jawaid, M.; Abdullah, M.; Ahmed, A. *Self-Healing Composite Materials. From Design to Applications*; Elsevier, 2020. https://doi.org/10.1016/C2018-0-02118-0.

(16) Manouras, T.; Vamvakaki, M. Field Responsive Materials: Photo-, Electro-, Magnetic- and Ultrasound-Sensitive Polymers. *Polymer Chemistry* **2017**, *8* (1), 74–96. https://doi.org/10.1039/C6PY01455K.

(17) Crespy, D.; Rossi, R. M. Temperature-Responsive Polymers with LCST in the Physiological Range and Their Applications in Textiles. *Polymer International* **2007**, *56* (12), 1461–1468. https://doi.org/10.1002/pi.2277.

(18) Yoshihara, E.; Sasaki, M.; Nabil, A.; Iijima, M.; Ebara, M. Temperature Responsive Polymer Conjugate Prepared by “Grafting from” Proteins toward the Adsorption and Removal of Uremic Toxin. *Molecules* **2022**, *27* (3), 1051. https://doi.org/10.3390/molecules27031051.

(19) Kamila, S. Introduction, Classification and Applications of Smart Materials: An Overview. *American Journal of Applied Sciences* **2013**, *10* (8), 876–880. https://doi.org/10.3844/ajassp.2013.876.880.

(20) Behl, M.; Lendlein, A. Shape-Memory Polymers. *Materials Today* **2007**, *10* (4), 20–28. https://doi.org/10.1016/S1369-7021(07)70047-0.

(21) Huang, W. M.; Ding, Z.; Wang, C. C.; Wei, J.; Zhao, Y.; Purnawali, H. Shape Memory Materials. *Materials Today* **2010**, *13* (7–8), 54–61. https://doi.org/10.1016/S1369-7021(10)70128-0.

(22) Mahapatra, S. Das; Mohapatra, P. C.; Aria, A. I.; Christie, G.; Mishra, Y. K.; Hofmann, S.; Thakur, V. K. Piezoelectric Materials for Energy Harvesting and Sensing Applications: Roadmap for Future Smart Materials. *Advanced Science* **2021**, *8* (17), 2100864. https://doi.org/10.1002/advs.202100864.

(23) Ivaneyko, D.; Toshchevikov, V.; Saphiannikova, M.; Heinrich, G. Mechanical Properties of Magneto-Sensitive Elastomers: Unification of the Continuum-Mechanics and Microscopic Theoretical Approaches. *Soft Matter* **2013**, *10* (13), 2213–2225. https://doi.org/10.1039/C3SM52440J.

(24) Chen, L.; Gong, X. L.; Li, W. H. Microstructures and Viscoelastic Properties of Anisotropic Magnetorheological Elastomers. *Smart Materials and Structures* **2007**, *16* (6), 2645–2650. https://doi.org/10.1088/0964-1726/16/6/069.

(25) Xu, Y.; Gong, X.; Xuan, S. Soft Magnetorheological Polymer Gels with Controllable Rheological Properties. *Smart Materials and Structures* **2013**, *22* (7), 075029. https://doi.org/10.1088/0964-1726/22/7/075029.

(26) Sliwa, M.; Mouton, N.; Ruckebusch, C.; Aloïse, S.; Poizat, O.; Buntinx, G.; Métivier, R.; Nakatani, K.; Masuhara, H.; Asahi, T. Comparative Investigation of Ultrafast Photoinduced Processes in Salicylidene-Aminopyridine in Solution and Solid State. *The Journal of Physical Chemistry C* **2009**, *113* (27), 11959–11968. https://doi.org/10.1021/jp901849a.

(27) Mitra, S.; Tamai, N. A Combined Experimental and Theoretical Study on the Photochromism of Aromatic Anils. *Chemical Physics* **1999**, *246* (1–3), 463–475. https://doi.org/10.1016/S0301-0104(99)00178-0.

(28) Ding, J.; Zheng, C.; Wang, L.; Lu, C.; Zhang, B.; Chen, Y.; Li, M.; Zhai, G.; Zhuang, X. Viologen-Inspired Functional Materials: Synthetic Strategies and Applications. *Journal of Materials Chemistry A* **2019**, *7* (41), 23337–23360. https://doi.org/10.1039/C9TA01724K.

(29) Patrick Sullivan, B. Large Solvatochromism of Metal-to-Ligand Charge-Transfer Transitions in Organometallic Complexes of Rhenium(I). *The Journal of Chemical Physics* **1989**, *93* (1), 24–26.

(30) Vik, M.; Prince Periyasamy, A. *Chromic Materials. Fundamentals, Measurements, and Applications*; Viková, M., Ed.; Apple Academic Press, 2019.

(31) Deng, Y.; Li, S.-Q.; Yang, Q.; Luo, Z.-W.; Xie, H.-L. High-Efficiency Responsive Smart Windows Fabricated by Carbon Nanotubes Modified by Liquid Crystalline Polymers. *Crystals (Basel)* **2021**, *11* (4), 440. https://doi.org/10.3390/cryst11040440.

(32) Chen, P.-W.; Chang, C.-T.; Ko, T.-F.; Hsu, S.-C.; Li, K.-D.; Wu, J.-Y. Fast Response of Complementary Electrochromic Device Based on WO3/NiO Electrodes. *Scientific Reports* **2020**, *10* (1), 8430. https://doi.org/10.1038/s41598-020-65191-x.

(33) Bhattacharyya, S.; Chowdhury, A.; Saha, R.; Mukherjee, P. S. Multifunctional Self-Assembled Macrocycles with Enhanced Emission and Reversible Photochromic Behavior. *Inorganic Chemistry* **2019**, *58* (6), 3968–3981. https://doi.org/10.1021/acs.inorgchem.9b00039.

(34) Helmy, S.; Leibfarth, F. A.; Oh, S.; Poelma, J. E.; Hawker, C. J.; Read de Alaniz, J. Photoswitching Using Visible Light: A New Class of Organic Photochromic Molecules. *J Am Chem Soc* **2014**, *136* (23), 8169–8172. https://doi.org/10.1021/ja503016b.

(35) Mortimer, R. J.; Dyer, A. L.; Reynolds, J. R. Electrochromic Organic and Polymeric Materials for Display Applications. *Displays* **2006**, *27* (1), 2–18. https://doi.org/10.1016/j.displa.2005.03.003.

(36) Martins, P.; Correia, V.; Lanceros-Mendez, S. Additive Manufacturing of Multifunctional Materials. In *Advanced Lightweight Multifunctional Materials*; Elsevier, 2021; pp 25–42. https://doi.org/10.1016/B978-0-12-818501-8.00011-1.

(37) Levy, D. Photochromic Sol−Gel Materials. *Chemistry of Materials* **1997**, *9* (12), 2666–2670. https://doi.org/10.1021/cm970355q.

(38) Qi, Q.; Fang, X.; Liu, Y.; Zhou, P.; Zhang, Y.; Yang, B.; Tian, W.; Zhang, S. X.-A. A TPE-Oxazoline Molecular Switch with Tunable Multi-Emission in Both Solution and Solid State. *RSC Advances* **2013**, *3* (38), 16986. https://doi.org/10.1039/c3ra43357a.

(39) Julià-López, A.; Ruiz-Molina, D.; Hernando, J.; Roscini, C. Solid Materials with Tunable Reverse Photochromism. *ACS Applied Materials & Interfaces* **2019**, *11* (12), 11884–11892. https://doi.org/10.1021/acsami.8b22335.

(40) Sonmez, G.; Sonmez, H. B. Polymeric Electrochromics for Data Storage. *Journal of Materials Chemistry* **2006**, *16* (25), 2473. https://doi.org/10.1039/b600053c.

(41) Rosseinsky, D. R.; Mortimer, R. J. Electrochromic Systems and the Prospects for Devices. *Advanced Materials* **2001**, *13* (11), 783–793. https://doi.org/10.1002/1521-4095(200106)13:11<783::AID-ADMA783>3.0.CO;2-D.

(42) *Gentex Corporation*. https://www.gentex.com/ (accessed 2020-04-17).

(43) Österholm, A. M.; Shen, D. E.; Kerszulis, J. A.; Bulloch, R. H.; Kuepfert, M.; Dyer, A. L.; Reynolds, J. R. Four Shades of Brown: Tuning of Electrochromic Polymer Blends Toward High-Contrast Eyewear. *ACS Applied Materials & Interfaces* **2015**, *7* (3), 1413–1421. https://doi.org/10.1021/am507063d.

(44) Ishiba, K.; Morikawa, M.; Chikara, C.; Yamada, T.; Iwase, K.; Kawakita, M.; Kimizuka, N. Photoliquefiable Ionic Crystals: A Phase Crossover Approach for Photon Energy Storage Materials with Functional Multiplicity. *Angewandte Chemie International Edition* **2015**, *54* (5), 1532–1536. https://doi.org/10.1002/anie.201410184.

(45) *SageGlass*. https://www.sageglass.com/en (accessed 2020-04-17).

(46) Liu, D.; Yang, F.; Xiong, F.; Gu, N. The Smart Drug Delivery System and Its Clinical Potential. *Theranostics* **2016**, *6* (9), 1306–1323. https://doi.org/10.7150/thno.14858.

(47) Son, S.; Shin, E.; Kim, B.-S. Light-Responsive Micelles of Spiropyran Initiated Hyperbranched Polyglycerol for Smart Drug Delivery. *Biomacromolecules* **2014**, *15* (2), 628–634. https://doi.org/10.1021/bm401670t.

(48) Guo, X.; Shao, B.; Zhou, S.; Aprahamian, I.; Chen, Z. Visualizing Intracellular Particles and Precise Control of Drug Release Using an Emissive Hydrazone Photochrome. *Chemical Science* **2020**, *11* (11), 3016–3021. https://doi.org/10.1039/C9SC05321B.

(49) Cheng, Y.; Zhang, X.; Fang, C.; Chen, J.; Wang, Z. Discoloration Mechanism, Structures and Recent Applications of Thermochromic Materials via Different Methods: A Review. *Journal of Materials Science & Technology* **2018**, *34* (12), 2225–2234. https://doi.org/10.1016/j.jmst.2018.05.016.

(50) Dussault, J.-M.; Gosselin, L.; Galstian, T. Integration of Smart Windows into Building Design for Reduction of Yearly Overall Energy Consumption and Peak Loads. *Solar Energy* **2012**, *86* (11), 3405–3416. https://doi.org/10.1016/j.solener.2012.07.016.

(51) Kho, Y.-M.; Shin, E. Spiropyran-Isoquinoline Dyad as a Dual Chemosensor for Co(II) and In(III) Detection. *Molecules* **2017**, *22* (9), 1569. https://doi.org/10.3390/molecules22091569.

(52) Fries, K.; Samanta, S.; Orski, S.; Locklin, J. Reversible Colorimetric Ion Sensors Based on Surface Initiated Polymerization of Photochromic Polymers. *Chemical Communications* **2008**, No. 47, 6288. https://doi.org/10.1039/b818042c.

(53) Platt, J. R. Electrochromism, a Possible Change of Color Producible in Dyes by an Electric Field. *The Journal of Chemical Physics* **1961**, *34* (3), 862–863. https://doi.org/10.1063/1.1731686.

(54) Berzelius, J. Försök till Ett Rent Kemiskt Mineralsystem. *Afhandlingar i fysik, kemi och mineralogi* **1815**, *4*, 1–147.

(55) Wang, Y.; Chen, B.; Zhu, Y.; Fu, L.; Wu, Y.; van Ree, T. Metal Oxides in Energy-Saving Smart Windows. In *Metal Oxides in Energy Technologies*; Elsevier, 2018; pp 341–360. https://doi.org/10.1016/B978-0-12-811167-3.00013-4.

(56) Takada, K.; Sakamoto, R.; Yi, S.-T.; Katagiri, S.; Kambe, T.; Nishihara, H. Electrochromic Bis(Terpyridine)Metal Complex Nanosheets. *J Am Chem Soc* **2015**, *137* (14), 4681–4689. https://doi.org/10.1021/ja510788b.

(57) Banasz, R.; Wałęsa-Chorab, M. Polymeric Complexes of Transition Metal Ions as Electrochromic Materials: Synthesis and Properties. *Coordination Chemistry Reviews* **2019**, *389*, 1–18. https://doi.org/10.1016/j.ccr.2019.03.009.

(58) Jennings, J. R.; Lim, W. Y.; Zakeeruddin, S. M.; Grätzel, M.; Wang, Q. A Redox-Flow Electrochromic Window. *ACS Applied Materials & Interfaces* **2015**, *7* (4), 2827–2832. https://doi.org/10.1021/am508086u.

(59) Moreira, T.; Maia, M.; Parola, A. J.; Zangoli, M.; Di Maria, F.; Laia, C. A. T. Ink-Jet-Printed Semiconductor Electrochromic Nanoparticles: Development and Applications in Electrochromism. In *Chemical Solution Synthesis for Materials Design and Thin Film Device Applications*; Elsevier, 2021; pp 407–437. https://doi.org/10.1016/B978-0-12-819718-9.00021-2.

(60) Hoshino, K.; Okuma, M.; Terashima, K. Electrochromic Properties of Metal Oxide Nanoparticles/Viologen Composite Film Electrodes. *The Journal of Physical Chemistry C* **2018**, *122* (39), 22577–22587. https://doi.org/10.1021/acs.jpcc.8b06898.

(61) Aller-Pellitero, M.; Fremeau, J.; Villa, R.; Guirado, G.; Lakard, B.; Hihn, J.-Y.; del Campo, F. J. Electrochromic Biosensors Based on Screen-Printed Prussian Blue Electrodes. *Sensors and Actuators B: Chemical* **2019**, *290*, 591–597. https://doi.org/10.1016/j.snb.2019.03.100.

(62) Karyakin, A. A.; Gitelmacher, O. V.; Karyakina, E. E. Prussian Blue-Based First-Generation Biosensor. A Sensitive Amperometric Electrode for Glucose. *Analytical Chemistry* **1995**, *67* (14), 2419–2423. https://doi.org/10.1021/ac00110a016.

(63) Koncki, R.; Lenarczuk, T.; Radomska, A.; Głąb, S. Optical Biosensors Based on Prussian Blue Films. *Analyst* **2001**, *126* (7), 1080–1085. https://doi.org/10.1039/b103044m.

(64) Howard, E. L.; Österholm, A. M.; Shen, D. E.; Panchumarti, L. P.; Pinheiro, C.; Reynolds, J. R. Cost-Effective, Flexible, and Colorful Dynamic Displays: Removing Underlying Conducting Layers from Polymer-Based Electrochromic Devices. *ACS Applied Materials & Interfaces* **2021**, *13* (14), 16732–16743. https://doi.org/10.1021/acsami.1c00463.

(65) Dautremont-Smith, W. C. Transition Metal Oxide Electrochromic Materials and Displays: A Review. *Displays* **1982**, *3* (2), 67–80. https://doi.org/10.1016/0141-9382(82)90100-7.

(66) Gillaspie, D. T.; Tenent, R. C.; Dillon, A. C. Metal-Oxide Films for Electrochromic Applications: Present Technology and Future Directions. *Journal of Materials Chemistry* **2010**, *20* (43), 9585. https://doi.org/10.1039/c0jm00604a.

(67) Demir, F.; Bıyıklıoğlu, Z.; Koca, A. Electrochromism of Electropolymerized Metallophthalocyanines. *Journal of The Electrochemical Society* **2014**, *161* (3), G1–G6. https://doi.org/10.1149/2.002403jes.

(68) Monk, P. M. S. *The Viologens: Physicochemical Properties, Synthesis and Applications of the Salts of 4,4'-Bipyridine*; John Wiley & Sons, Inc: Chichester, 1998.

(69) Diesbach. No Title. *Handbuch der Anorganischen Chemie* **1704**, *59*.

(70) Neff, V. D. Electrochemical Oxidation and Reduction of Thin Films of Prussian Blue. *Journal of The Electrochemical Society* **1978**, *125* (6), 886–887. https://doi.org/10.1149/1.2131575.

(71) Mortimer, R. J. Electrochromic Materials. *Annu. Rev. Mater.* **2011**, *41* (1), 241–268. https://doi.org/10.1016/0921-5107(89)90200-6.

(72) Salazar, P.; Martín, M.; O'Neill, R. D.; González-Mora, J. L. In Vivo Biosensor Based on Prussian Blue for Brain Chemistry Monitoring : Methodological Review and Biological Applications; 2017; pp 155–179. https://doi.org/10.1007/978-1-4939-6490-1_8.

(73) Simone, F.; Galán-Mascarós, J.; López, N. A Database of the Structural and Electronic Properties of Prussian Blue, Prussian White, and Berlin Green Compounds through Density Functional Theory. *Inorganic Chemistry* **2016**, *55* (24), 12851–12862.

(74) Pintado, S.; Goberna-Ferrón, S.; Escudero-Adán, E. C.; Galán-Mascarós, J. R. Fast and Persistent Electrocatalytic Water Oxidation by Co–Fe Prussian Blue Coordination Polymers. *J Am Chem Soc* **2013**, *135* (36), 13270–13273. https://doi.org/10.1021/ja406242y.

(75) Jiménez-Gallegos, J.; Rodríguez-Hernández, J.; Yee-Madeira, H.; Reguera, E. Structure of Porous Copper Prussian Blue Analogues: Nature of Their High H 2 Storage Capacity. *The Journal of Physical Chemistry C* **2010**, *114* (11), 5043–5048. https://doi.org/10.1021/jp910544j.

(76) Chen, R.; Huang, Y.; Xie, M.; Wang, Z.; Ye, Y.; Li, L.; Wu, F. Chemical Inhibition Method to Synthesize Highly Crystalline Prussian Blue Analogs for Sodium-Ion Battery Cathodes. *ACS Applied Materials & Interfaces* **2016**, *8* (46), 31669–31676. https://doi.org/10.1021/acsami.6b10884.

(77) Pajerowski, D. M.; Gardner, J. E.; Frye, F. A.; Andrus, M. J.; Dumont, M. F.; Knowles, E. S.; Meisel, M. W.; Talham, D. R. Photoinduced Magnetism in a Series of Prussian Blue Analogue Heterostructures. *Chemistry of Materials* **2011**, *23* (12), 3045–3053. https://doi.org/10.1021/cm2003337.

(78) Ricci, F.; Amine, A.; Palleschi, G.; Moscone, D. Prussian Blue Based Screen Printed Biosensors with Improved Characteristics of Long-Term Lifetime and PH Stability. *Biosensors and Bioelectronics* **2003**, *18* (2–3), 165–174. https://doi.org/10.1016/S0956-5663(02)00169-0.

(79) Beaujuge, P. M.; Reynolds, J. R. Color Control in π-Conjugated Organic Polymers for Use in Electrochromic Devices. *Chemical Reviews* **2010**, *110* (1), 268–320. https://doi.org/10.1021/cr900129a.

(80) Dyer, A. L.; Thompson, E. J.; Reynolds, J. R. Completing the Color Palette with Spray-Processable Polymer Electrochromics. *ACS Applied Materials and Interfaces* **2011**, *3* (6), 1787–1795. https://doi.org/10.1021/am200040p.

(81) Dyer, A. L.; Thompson, E. J.; Reynolds, J. R. Completing the Color Palette with Spray-Processable Polymer Electrochromics. *ACS Applied Materials & Interfaces* **2011**, *3* (6), 1787–1795. https://doi.org/10.1021/am200040p.

(82) Argun, A. A.; Aubert, P. H.; Thompson, B. C.; Schwendeman, I.; Gaupp, C. L.; Hwang, J.; Pinto, N. J.; Tanner, D. B.; MacDiarmid, A. G.; Reynolds, J. R. Multicolored Electrochromisin in Polymers: Structures and Devices. *Chemistry of Materials* **2004**, *16* (23), 4401–4412. https://doi.org/10.1021/cm049669l.

(83) Feringa, B. L.; Browne, W. R. *Molecular Switches*, Second.; Feringa, B. L., Browne, W. R., Eds.; WILEY-VCH, 2011.

(84) Feringa, B. L. The Art of Building Small: From Molecular Switches to Motors (Nobel Lecture). *Angewandte Chemie - International Edition* **2017**, *56* (37), 11060–11078. https://doi.org/10.1002/anie.201702979.

(85) Jayaraman, N. 2016 Nobel Prize in Chemistry: Conferring Molecular Machines as Engines of Creativity. *Resonance* **2017**, *22* (9), 835–845. https://doi.org/10.1007/s12045-017-0538-2.

(86) Fahrenbach, A. C.; Warren, S. C.; Incorvati, J. T.; Avestro, A.-J.; Barnes, J. C.; Stoddart, J. F.; Grzybowski, B. A. Organic Switches for Surfaces and Devices. *Advanced Materials* **2013**, *25* (3), 331–348. https://doi.org/10.1002/adma.201201912.

(87) Dietrich-Buchecker, C. O.; Sauvage, J. P.; Kern, J. M. Templated Synthesis of Interlocked Macrocyclic Ligands: The Catenands. *J Am Chem Soc* **1984**, *106*, 3043–3045. https://doi.org/10.1021/ja00322a055.

(88) Amabilino, D. B.; Ashton, P. R.; Reder, A. S.; Spencer, N.; Stoddart, J. F. Olympiadane. *Angewandte Chemie International Edition in English* **1994**, *33*, 1286–1290. https://doi.org/10.1002/anie.199412861.

(89) Ashton, P. R.; Ballardini, R.; Balzani, V.; Bělohradský, M.; Gandolfi, M. T.; Philp, D.; Prodi, L.; Raymo, F. M.; Reddington, M. V.; Spencer, N.; Stoddart, J. F.; Venturi, M.; Williams, D. J. Self-Assembly, Spectroscopic, and Electrochemical Properties of [n]Rotaxanes 1. *J Am Chem Soc* **1996**, *118* (21), 4931–4951. https://doi.org/10.1021/ja954334d.

(90) Skou, J. C. The Identification of the Sodium-Potassium Pump (Nobel Lecture). *Angewandte Chemie International Edition* **1998**, *37* (17), 2320–2328. https://doi.org/10.1002/(SICI)1521-3773(19980918)37:17<2320::AID-ANIE2320>3.0.CO;2-2.

(91) Koumura, N.; Zijlstra, R. W. J.; van Delden, R. A.; Harada, N.; Feringa, B. L. Light-Driven Monodirectional Molecular Rotor. *Nature* **1999**, *401* (6749), 152–155. https://doi.org/10.1038/43646.

(92) Saha, S.; Stoddart, J. F. Photo-Driven Molecular Devices. *Chemical Society Reviews* **2007**, *36*, 77–92. https://doi.org/10.1039/b607187b.

(93) Khattab, T. A. From Chromic Switchable Hydrazones to Smart Materials. *Materials Chemistry and Physics* **2020**, *254*, 123456. https://doi.org/10.1016/j.matchemphys.2020.123456.

(94) Erbas-Cakmak, S.; Kolemen, S.; Sedgwick, A. C.; Gunnlaugsson, T.; James, T. D.; Yoon, J.; Akkaya, E. U. Molecular Logic Gates: The Past, Present and Future. *Chemical Society Reviews* **2018**, *47* (7), 2228–2248. https://doi.org/10.1039/C7CS00491E.

(95) Li, H.; Qu, D.-H. Recent Advances in New-Type Molecular Switches. *Science China Chemistry* **2015**, *58* (6), 916–921. https://doi.org/10.1007/s11426-015-5417-7.

(96) Hartley, G. S. The Cis-Form of Azobenzene. *Nature* **1937**, *140*, 281. https://doi.org/10.1038/140281a0.

(97) Yu, J. K.; Bannwarth, C.; Liang, R.; Hohenstein, E. G.; Martínez, T. J. Nonadiabatic Dynamics Simulation of the Wavelength-Dependent Photochemistry of Azobenzene Excited to the Nπ* and Ππ* Excited States. *J Am Chem Soc* **2020**, *142* (49), 20680–20690. https://doi.org/10.1021/jacs.0c09056.

(98) Wiedbrauk, S.; Dube, H. Hemithioindigo—an Emerging Photoswitch. *Tetrahedron Letters* **2015**, *56* (29), 4266–4274. https://doi.org/10.1016/j.tetlet.2015.05.022.

(99) Klajn, R. Spiropyran-Based Dynamic Materials. *Chemical Society Reviews* **2014**, *43* (1), 148–184. https://doi.org/10.1039/c3cs60181a.

(100) Irie, M.; Fukaminato, T.; Matsuda, K.; Kobatake, S. Photochromism of Diarylethene Molecules and Crystals: Memories, Switches, and Actuators. *Chemical Reviews* **2014**, *114* (24), 12174–12277. https://doi.org/10.1021/cr500249p.

(101) Schönborn, J. B.; Koslowski, A.; Thiel, W.; Hartke, B. Photochemical Dynamics of E-IPr-Furylfulgide. *Physical Chemistry Chemical Physics* **2012**, *14* (35), 12193. https://doi.org/10.1039/c2cp41817g.

(102) Decker, H.; Felser, H. NoÜber Cyclische Oxoniumsalze Aus Dicumarketon Und Über Spiropyranderivate. *Berichte der Deutschen Chemischen Gesellschaft* **1908**, *41*, 2993–3007.

(103) Hirshberg, Y.; Fischer, E. Photochromism and Reversible Multiple Internal Transitions in Some Spiropyrans at Low Temperatures. Part I. *Journal of the Chemical Society (Resumed)* **1954**, 297. https://doi.org/10.1039/jr9540000297.

(104) Berman, E.; Fox, R. E.; Thomson, F. D. Photochromic Spiropyrans. I. The Effect of Substituents on the Rate of Ring Closure. *J Am Chem Soc* **1959**, *81* (21), 5605–5608. https://doi.org/10.1021/ja01530a021.

(105) Brügner, O.; Reichenbach, T.; Sommer, M.; Walter, M. Substituent Correlations Characterized by Hammett Constants in the Spiropyran-Merocyanine Transition. *Journal of Physical Chemistry A* **2017**, *121* (13), 2683–2687. https://doi.org/10.1021/acs.jpca.7b01248.

(106) Chibisov, A. K.; Görner, H. Photoprocesses in Spiropyran-Derived Merocyanines. *Journal of Physical Chemistry A* **1997**, *101* (24), 4305–4312. https://doi.org/10.1021/jp962569l.

(107) Steen, J. D.; Duijnstee, D. R.; Sardjan, A. S.; Martinelli, J.; Kortekaas, L.; Jacquemin, D.; Browne, W. R. Electrochemical Ring-Opening and -Closing of a Spiropyran. *Journal of Physical Chemistry A* **2021**, *125* (16), 3355–3361. https://doi.org/10.1021/acs.jpca.1c01142.

(108) Coudret, C.; Guirado, G.; Hortholary, C.; Launay, J.; Klein, H.; Dumas, P.; Coudret, C.; Guirado, G.; Hortholary, C.; Launay, J.; Battaglini, N. " Electrical " Behaviour of Photochromic Compounds To Cite This Version : HAL Id : Hal-01770312. **2018**.

(109) Peters, A.; Branda, N. R. Electrochemically Induced Ring-Closing of Photochromic Electrochromism Is Observed for Two 1 , 2-Bis (Dithienyl) Cyclo-. *Chem. Commun.* **2003**, 954–955.

(110) Peters, A.; Branda, N. R. Electrochromism in Photochromic Dithienylcyclopentenes. *J Am Chem Soc* **2003**, *125* (12), 3404–3405. https://doi.org/10.1021/ja028764x.

(111) Mitchell, R. H.; Brkic, Z.; Sauro, V. A.; Berg, D. J. A Photochromic, Electrochromic, Thermochromic Ru Complexed Benzannulene: An Organometallic Example of the Dimethyldihydropyrene-Metacyclophanediene Valence Isomerization. *J Am Chem Soc* **2003**, *125* (25), 7581–7585. https://doi.org/10.1021/ja034807d.

(112) Preigh, M. J.; Stauffer, M. T.; Lin, F.-T.; Weber, S. G. Anodic Oxidation Mechanism of a Spiropyran. *Journal of the Chemical Society, Faraday Transactions* **1996**, *92* (20), 3991. https://doi.org/10.1039/ft9969203991.

(113) Browne, W. R.; Ivashenko, O.; Feringa, B. L.; Rudolf, P.; van Herpt, J. T. Oxidative Electrochemical Aryl C–C Coupling of Spiropyrans. *Chemical Communications* **2013**, *49* (60), 6737. https://doi.org/10.1039/c3cc42396d.

(114) Kortekaas, L.; Ivashenko, O.; Van Herpt, J. T.; Browne, W. R. A Remarkable Multitasking Double Spiropyran: Bidirectional Visible-Light Switching of Polymer-Coated Surfaces with Dual Redox and Proton Gating. *J Am Chem Soc* **2016**, *138* (4), 1301–1312. https://doi.org/10.1021/jacs.5b11604.

(115) Jin Fang Zhi; Baba, R.; Hashimoto, K.; Fujishima, A. Photoelectrochromic Properties of a Spirobenzopyran Derivative. *Journal of Photochemistry and Photobiology, A: Chemistry* **1995**, *92* (1–2), 91–97. https://doi.org/10.1016/1010-6030(95)04167-0.

(116) Zhi, J. F.; Baba, R.; Fujishima, A. An Electrochemical Study of Some Spirobenzopyran Derivatives in Dimethylformamide. *Berichte der Bunsengesellschaft/Physical Chemistry Chemical Physics* **1996**, *100* (11), 1802–1807. https://doi.org/10.1002/bbpc.19961001108.

(117) Ivashenko, O.; Van Herpt, J. T.; Feringa, B. L.; Rudolf, P.; Browne, W. R. Electrochemical Write and Read Functionality through Oxidative Dimerization of Spiropyran Self-Assembled Monolayers on Gold. *Journal of Physical Chemistry C* **2013**, *117* (36), 18567–18577. https://doi.org/10.1021/jp406458a.

(118) Campredon, M.; Giusti, G.; Guglielmetti, R.; Samat, A.; Gronchi, G.; Alberti, A.; Benaglia, M. Radical Ions and Germyloxyaminoxyls from Nitrospiro[Indoline-Naphthopyrans]. A Combined Electrochemical and EPR Study. *Journal of the Chemical Society, Perkin Transactions 2* **1993**, No. 11, 2089. https://doi.org/10.1039/p29930002089.

(119) Jin Fang Zhi; Baba, R.; Hashimoto, K.; Fujishima, A. Photoelectrochromic Properties of a Spirobenzopyran Derivative. *Journal of Photochemistry and Photobiology, A: Chemistry* **1995**, *92* (1–2), 91–97. https://doi.org/10.1016/1010-6030(95)04167-0.

(120) Natali, M.; Giordani, S. Interaction Studies between Photochromic Spiropyrans and Transition Metal Cations: The Curious Case of Copper. *Org. Biomol. Chem.* **2012**, *10* (6), 1162–1171. https://doi.org/10.1039/C1OB06375H.

(121) Ivashenko, O.; van Herpt, J. T.; Rudolf, P.; Feringa, B. L.; Browne, W. R. Oxidative Electrochemical Aryl C–C Coupling of Spiropyrans. *Chemical Communications* **2013**, *49* (60), 6737. https://doi.org/10.1039/c3cc42396d.

(122) Zhu, M.-Q.; Zhang, G.-F.; Hu, Z.; Aldred, M. P.; Li, C.; Gong, W.-L.; Chen, T.; Huang, Z.-L.; Liu, S. Reversible Fluorescence Switching of Spiropyran-Conjugated Biodegradable Nanoparticles for Super-Resolution Fluorescence Imaging. *Macromolecules* **2014**, *47* (5), 1543–1552. https://doi.org/10.1021/ma5001157.

(123) Cardano, F.; Del Canto, E.; Giordani, S. Spiropyrans for Light-Controlled Drug Delivery. *Dalton Transactions* **2019**, *48* (41), 15537–15544. https://doi.org/10.1039/C9DT02092F.

(124) Ali, A. A.; Kharbash, R.; Kim, Y. Chemo- and Biosensing Applications of Spiropyran and Its Derivatives - A Review. *Analytica Chimica Acta* **2020**, *1110*, 199–223. https://doi.org/10.1016/j.aca.2020.01.057.

(125) Petriashvili, G.; De Santo, M. P.; Devadze, L.; Zurabishvili, T.; Sepashvili, N.; Gary, R.; Barberi, R. Rewritable Optical Storage with a Spiropyran Doped Liquid Crystal Polymer Film. *Macromolecular Rapid Communications* **2016**, *37* (6), 500–505. https://doi.org/10.1002/marc.201500626.

(126) Feringa, B. L.; Browne, W. R. *Molecular Switches*; Feringa, B. L., Browne, W. R., Eds.; Wiley-VCH Verlag GmbH & Co. KGaA: Weinheim, Germany, 2011. https://doi.org/10.1002/9783527634408.

(127) Irie, M. Diarylethenes for Memories and Switches. *Chemical Reviews* **2000**, *100* (5), 1685–1716. https://doi.org/10.1021/cr980069d.

(128) Takeshita, M.; Yamada, M.; Kato, N.; Irie, M. Photochromism of Dithienylethene-Bis(Trimethylammonium) Iodide in Cyclodextrin Cavities. *Journal of the Chemical Society, Perkin Transactions 2* **2000**, No. 4, 619–622. https://doi.org/10.1039/b000117l.

(129) Uchida, K.; Tsuchida, E.; Aoi, Y.; Nakamura, S.; Irie, M. Substitution Effect on the Coloration Quantum Yield of a Photochromic Bisbenzothienylethene. *Chemistry Letters* **1999**, *28* (1), 63–64. https://doi.org/10.1246/cl.1999.63.

(130) van der Molen, S. J.; Liao, J.; Kudernac, T.; Agustsson, J. S.; Bernard, L.; Calame, M.; van Wees, B. J.; Feringa, B. L.; Schönenberger, C. Light-Controlled Conductance Switching of Ordered Metal−Molecule−Metal Devices. *Nano Letters* **2009**, *9* (1), 76–80. https://doi.org/10.1021/nl802487j.

(131) He, J.; Chen, F.; Liddell, P. A.; Andréasson, J.; Straight, S. D.; Gust, D.; Moore, T. A.; Moore, A. L.; Li, J.; Sankey, O. F.; Lindsay, S. M. Switching of a Photochromic Molecule on Gold Electrodes: Single-Molecule Measurements. *Nanotechnology* **2005**, *16* (6), 695–702. https://doi.org/10.1088/0957-4484/16/6/012.

(132) Fraysse, S.; Coudret, C.; Launay, J.-P. Synthesis and Properties of Dinuclear Complexes with a Photochromic Bridge: An Intervalence Electron Transfer Switching “On” and “Off.” *European Journal of Inorganic Chemistry* **2000**, *2000* (7), 1581–1590. https://doi.org/10.1002/1099-0682(200007)2000:7<1581::AID-EJIC1581>3.0.CO;2-2.

(133) Fox, M. A.; Hurst, J. R. Electrochemically Induced Pericyclic Reactions. A Radical Anionic Cyclization. *J Am Chem Soc* **1984**, *106* (24), 7626–7627. https://doi.org/10.1021/ja00336a055.

(134) Odo, Y.; Fukaminato, T.; Irie, M. Photoswitching of Fluorescence Based on Intramolecular Electron Transfer. *Chemistry Letters* **2007**, *36* (2), 240–241. https://doi.org/10.1246/cl.2007.240.

(135) Márquez, A.; Santiago, S.; Domínguez, C.; Muñoz-Berbel, X.; Guirado, G. Photoelectro-Enzymatic Glucose Reusable Biosensor by Using Dithienylethene Mediators. *Chemistry – A European Journal* **2020**, *26* (40), 8714–8719. https://doi.org/10.1002/chem.202000865.

(136) Guirado, G.; Coudret, C.; Hliwa, M.; Launay, J. P. Understanding Electrochromic Processes Initiated by Dithienylcyclopentene Cation-Radicals. *Journal of Physical Chemistry B* **2005**, *109* (37), 17445–17459. https://doi.org/10.1021/jp052459r.

(137) Moriyama, Y.; Matsuda, K.; Tanifuji, N.; Irie, S.; Irie, M. Electrochemical Cyclization/Cycloreversion Reactions of Diarylethenes. *Organic Letters* **2005**, *7* (15), 3315–3318. https://doi.org/10.1021/ol051149o.

(138) Gorodetsky, B.; Branda, N. R. Bidirectional Ring-Opening and Ring-Closing of Cationic 1,2-Dithienylcyclopentene Molecular Switches Triggered with Light or Electricity. *Advanced Functional Materials* **2007**, *17* (5), 786–796. https://doi.org/10.1002/adfm.200600902.

(139) Browne, W. R.; de Jong, J. J. D.; Kudernac, T.; Walko, M.; Lucas, L. N.; Uchida, K.; van Esch, J. H.; Feringa, B. L. Oxidative Electrochemical Switching in Dithienylcyclopentenes, Part 2: Effect of Substitution and Asymmetry on the Efficiency and Direction of Molecular Switching and Redox Stability. *Chemistry - A European Journal* **2005**, *11* (21), 6430–6441. https://doi.org/10.1002/chem.200500163.

(140) Lee, S.; You, Y.; Ohkubo, K.; Fukuzumi, S.; Nam, W. Mechanism and Fluorescence Application of Electrochromism in Photochromic Dithienylcyclopentene. *Organic Letters* **2012**, *14* (9), 2238–2241. https://doi.org/10.1021/ol300604n.

(141) European Commission. Resource.Html. **2019**.

(142) Reeves, B. D.; Grenier, C. R. G.; Argun, A. A.; Cirpan, A.; McCarley, T. D.; Reynolds, J. R. Spray Coatable Electrochromic Dioxythiophene Polymers with High Coloration Efficiencies. *Macromolecules* **2004**, *37* (20), 7559–7569. https://doi.org/10.1021/ma049222y.

(143) Amb, C. M.; Dyer, A. L.; Reynolds, J. R. Navigating the Color Palette of Solution-Processable Electrochromic Polymers. *Chemistry of Materials* **2011**, *23* (3), 397–415. https://doi.org/10.1021/cm1021245.

(144) Bayat, M.; Izadan, H.; Santiago, S.; Estrany, F.; Dinari, M.; Semnani, D.; Alemán, C.; Guirado, G. Study on the Electrochromic Properties of Polypyrrole Layers Doped with Different Dye Molecules. *Journal of Electroanalytical Chemistry* **2021**, *886*, 115113. https://doi.org/10.1016/j.jelechem.2021.115113.

(145) Tsuboi, A.; Nakamura, K.; Kobayashi, N. Multicolor Electrochromism Showing Three Primary Color States (Cyan–Magenta–Yellow) Based on Size- and Shape-Controlled

Silver Nanoparticles. *Chemistry of Materials* **2014**, *26* (22), 6477–6485. https://doi.org/10.1021/cm5039039.

(146) Baggio, B.; Vicente, C.; Pelegrini, S.; Plá Cid, C.; Brandt, I.; Tumelero, M.; Pasa, A. Morphology and Structure of Electrodeposited Prussian Blue and Prussian White Thin Films. *Materials* **2019**, *12* (7), 1103. https://doi.org/10.3390/ma12071103.

(147) Gao, Z.; Liu, L.; Tian, Z.; Feng, Z.; Jiang, B.; Wang, W. Fast-Response Flexible Photochromic Gels for Self-Erasing Rewritable Media and Colorimetric Oxygen Indicator Applications. *ACS Applied Materials and Interfaces* **2018**, *10* (39), 33423–33433. https://doi.org/10.1021/acsami.8b09825.

(148) Sutthasupa, S.; Padungkit, C.; Suriyong, S. Colorimetric Ammonia (NH3) Sensor Based on an Alginate-Methylcellulose Blend Hydrogel and the Potential Opportunity for the Development of a Minced Pork Spoilage Indicator. *Food Chemistry* **2021**, *362*, 130151. https://doi.org/10.1016/j.foodchem.2021.130151.

(149) Márquez, A.; Jiménez-Jorquera, C.; Domínguez, C.; Muñoz-Berbel, X. Electrodepositable Alginate Membranes for Enzymatic Sensors: An Amperometric Glucose Biosensor for Whole Blood Analysis. *Biosensors and Bioelectronics* **2017**, *97*, 136–142. https://doi.org/10.1016/j.bios.2017.05.051.

(150) Park, S.-I.; Quan, Y.-J.; Kim, S.-H.; Kim, H.; Kim, S.; Chun, D.-M.; Lee, C. S.; Taya, M.; Chu, W.-S.; Ahn, S.-H. A Review on Fabrication Processes for Electrochromic Devices. *International Journal of Precision Engineering and Manufacturing-Green Technology* **2016**, *3* (4), 397–421. https://doi.org/10.1007/s40684-016-0049-8.

(151) Coleman, J. P.; Lynch, A. T.; Madhukar, P.; Wagenknecht, J. H. Printed, Flexible Electrochromic Displays Using Interdigitated Electrodes. *Solar Energy Materials and Solar Cells* **1999**, *56* (3–4), 395–418. https://doi.org/10.1016/S0927-0248(98)00144-5.

(152) Coleman, J. P.; Lynch, A. T.; Madhukar, P.; Wagenknecht, J. H. Antimony-Doped Tin Oxide Powders: Electrochromic Materials for Printed Displays. *Solar Energy Materials and Solar Cells* **1999**, *56* (3–4), 375–394. https://doi.org/10.1016/S0927-0248(98)00143-3.

(153) Zhang, S.; Sun, G.; He, Y.; Fu, R.; Gu, Y.; Chen, S. Preparation, Characterization, and Electrochromic Properties of Nanocellulose-Based Polyaniline Nanocomposite Films. *ACS Applied Materials and Interfaces* **2017**, *9* (19), 16426–16434. https://doi.org/10.1021/acsami.7b02794.

(154) Julià-López, A.; Ruiz-Molina, D.; Hernando, J.; Roscini, C. Solid Materials with Tunable Reverse Photochromism. *ACS Applied Materials & Interfaces* **2019**, *11* (12), 11884–11892. https://doi.org/10.1021/acsami.8b22335.

(155) Gao, W.; Zhu, Y.; Wang, Y.; Yuan, G.; Liu, J.-M. A Review of Flexible Perovskite Oxide Ferroelectric Films and Their Application. *Journal of Materiomics* **2020**, *6* (1), 1–16. https://doi.org/10.1016/j.jmat.2019.11.001.

(156) Singh, R.; Tharion, J.; Murugan, S.; Kumar, A. ITO-Free Solution-Processed Flexible Electrochromic Devices Based on PEDOT:PSS as Transparent Conducting Electrode. *ACS Applied Materials & Interfaces* **2017**, *9* (23), 19427–19435. https://doi.org/10.1021/acsami.6b09476.

(157) Kumar, A.; Zhou, C. The Race To Replace Tin-Doped Indium Oxide: Which Material Will Win? *ACS Nano* **2010**, *4* (1), 11–14. https://doi.org/10.1021/nn901903b.

(158) Jana, S.; Parthiban, A.; Chai, C. L. L. Transparent, Flexible and Highly Conductive Ion Gels from Ionic Liquid Compatible Cyclic Carbonate Network. *Chemical Communications* **2010**, *46* (9), 1488. https://doi.org/10.1039/b921517d.

(159) Le Bideau, J.; Viau, L.; Vioux, A. Ionogels, Ionic Liquid Based Hybrid Materials. *Chemical Society Reviews* **2011**, *40* (2), 907–925. https://doi.org/10.1039/c0cs00059k.

(160) Lei, Z.; Chen, B.; Koo, Y.-M.; MacFarlane, D. R. Introduction: Ionic Liquids. *Chemical Reviews* **2017**, *117* (10), 6633–6635. https://doi.org/10.1021/acs.chemrev.7b00246.

(161) Branco, L. C.; Pina, F. Intrinsically Photochromic Ionic Liquids. *Chemical Communications* **2009**, No. 41, 6204. https://doi.org/10.1039/b907672g.

(162) Hough, W. L.; Smiglak, M.; Rodríguez, H.; Swatloski, R. P.; Spear, S. K.; Daly, D. T.; Pernak, J.; Grisel, J. E.; Carliss, R. D.; Soutullo, M. D.; Davis, Jr., J. H.; Rogers, R. D. The Third Evolution of Ionic Liquids: Active Pharmaceutical Ingredients. *New Journal of Chemistry* **2007**, *31* (8), 1429. https://doi.org/10.1039/b706677p.

(163) Lee, J.; Aida, T. “Bucky Gels” for Tailoring Electroactive Materials and Devices: The Composites of Carbon Materials with Ionic Liquids. *Chemical Communications* **2011**, *47* (24), 6757. https://doi.org/10.1039/c1cc00043h.

(164) Néouze, M.-A.; Le Bideau, J.; Gaveau, P.; Bellayer, S.; Vioux, A. Ionogels, New Materials Arising from the Confinement of Ionic Liquids within Silica-Derived Networks. *Chemistry of Materials* **2006**, *18* (17), 3931–3936. https://doi.org/10.1021/cm060656c.

(165) Kimizuka, N.; Nakashima, T. Spontaneous Self-Assembly of Glycolipid Bilayer Membranes in Sugar-Philic Ionic Liquids and Formation of Ionogels. *Langmuir* **2001**, *17* (22), 6759–6761. https://doi.org/10.1021/la015523e.

(166) Ikeda, A.; Sonoda, K.; Ayabe, M.; Tamaru, S.; Nakashima, T.; Kimizuka, N.; Shinkai, S. Gelation of Ionic Liquids with a Low Molecular-Weight Gelator Showing T Gel above 100 °C. *Chemistry Letters* **2001**, *30* (11), 1154–1155. https://doi.org/10.1246/cl.2001.1154.

(167) Kubo, W.; Kambe, S.; Nakade, S.; Kitamura, T.; Hanabusa, K.; Wada, Y.; Yanagida, S. Photocurrent-Determining Processes in Quasi-Solid-State Dye-Sensitized Solar Cells Using Ionic Gel Electrolytes. *The Journal of Physical Chemistry B* **2003**, *107* (18), 4374–4381. https://doi.org/10.1021/jp034248x.

(168) Lu, J.; Yan, F.; Texter, J. Advanced Applications of Ionic Liquids in Polymer Science. *Progress in Polymer Science* **2009**, *34* (5), 431–448. https://doi.org/10.1016/j.progpolymsci.2008.12.001.

(169) Shi, Y.; Wang, Y.; Gu, Y.; Zheng, L.; Ma, S.; Xu, X. Self-Healable and Stretchable Ionogels Serve as Electrolytes and Substrates for Integrated All-in-One Micro-Supercapacitors. *Chemical Engineering Journal* **2020**, *392*, 123645. https://doi.org/10.1016/j.cej.2019.123645.

(170) Singh, P. K.; Bhattacharya, B.; Nagarale, R. K.; Kim, K.-W.; Rhee, H.-W. Synthesis, Characterization and Application of Biopolymer-Ionic Liquid Composite Membranes.

Synthetic Metals **2010**, *160* (1–2), 139–142. https://doi.org/10.1016/j.synthmet.2009.10.021.

(171) Singh, T.; Trivedi, T. J.; Kumar, A. Dissolution, Regeneration and Ion-Gel Formation of Agarose in Room-Temperature Ionic Liquids. *Green Chemistry* **2010**, *12* (6), 1029. https://doi.org/10.1039/b927589d.

(172) Nagel, B.; Dellweg, H.; Gierasch, L. M. Glossary for Chemists of Terms Used in Biotechnology (IUPAC Recommendations 1992). *Pure and Applied Chemistry* **1992**, *64* (1), 143–168. https://doi.org/10.1351/pac199264010143.

(173) Choi, Y.; Hwang, J. H.; Lee, S. Y. Recent Trends in Nanomaterials-Based Colorimetric Detection of Pathogenic Bacteria and Viruses. *Small Methods* **2018**, *2* (4), 1700351. https://doi.org/10.1002/smtd.201700351.

(174) Wongkaew, N.; Simsek, M.; Griesche, C.; Baeumner, A. J. Functional Nanomaterials and Nanostructures Enhancing Electrochemical Biosensors and Lab-on-a-Chip Performances: Recent Progress, Applications, and Future Perspective. *Chemical Reviews* **2019**, *119* (1), 120–194. https://doi.org/10.1021/acs.chemrev.8b00172.

(175) Liu, G.; Lu, M.; Huang, X.; Li, T.; Xu, D. Application of Gold-Nanoparticle Colorimetric Sensing to Rapid Food Safety Screening. *Sensors* **2018**, *18* (12), 4166. https://doi.org/10.3390/s18124166.

(176) Piriya V.S, A.; Joseph, P.; Daniel S.C.G., K.; Lakshmanan, S.; Kinoshita, T.; Muthusamy, S. Colorimetric Sensors for Rapid Detection of Various Analytes. *Materials Science and Engineering C* **2017**, *78*, 1231–1245. https://doi.org/10.1016/j.msec.2017.05.018.

(177) Liu, B.; Zhuang, J.; Wei, G. Recent Advances in the Design of Colorimetric Sensors for Environmental Monitoring. *Environmental Science: Nano* **2020**, *7* (8), 2195–2213. https://doi.org/10.1039/D0EN00449A.

(178) Govindhan, M.; Amiri, M.; Chen, A. Au Nanoparticle/Graphene Nanocomposite as a Platform for the Sensitive Detection of NADH in Human Urine. *Biosensors and Bioelectronics* **2015**, *66*, 474–480. https://doi.org/10.1016/j.bios.2014.12.012.

(179) Zhu, D.; Liu, B.; Wei, G. Two-Dimensional Material-Based Colorimetric Biosensors: A Review. *Biosensors (Basel)* **2021**, *11* (8), 259. https://doi.org/10.3390/bios11080259.

(180) Wang, H.; Zhang, K.-Q. Photonic Crystal Structures with Tunable Structure Color as Colorimetric Sensors. *Sensors* **2013**, *13* (4), 4192–4213. https://doi.org/10.3390/s130404192.

(181) Zhao, L.; Wu, Z.; Liu, G.; Lu, H.; Gao, Y.; Liu, F.; Wang, C.; Cui, J.; Lu, G. High-Activity Mo, S Co-Doped Carbon Quantum Dot Nanozyme-Based Cascade Colorimetric Biosensor for Sensitive Detection of Cholesterol. *Journal of Materials Chemistry B* **2019**, *7* (44), 7042–7051. https://doi.org/10.1039/C9TB01731C.

(182) Huang, S.; Qiu, H.; Zhu, F.; Lu, S.; Xiao, Q. Graphene Quantum Dots as On-off-on Fluorescent Probes for Chromium(VI) and Ascorbic Acid. *Microchimica Acta* **2015**, *182* (9–10), 1723–1731. https://doi.org/10.1007/s00604-015-1508-6.

(183) Khattab, T. A.; Fouda, M. M. G.; Abdelrahman, M. S.; Othman, S. I.; Bin-Jumah, M.; Alqaraawi, M. A.; Al Fassam, H.; Allam, A. A. Co-Encapsulation of Enzyme and

Tricyanofuran Hydrazone into Alginate Microcapsules Incorporated onto Cotton Fabric as a Biosensor for Colorimetric Recognition of Urea. *Reactive and Functional Polymers* **2019**, *142*, 199–206. https://doi.org/10.1016/j.reactfunctpolym.2019.06.016.

(184) Lin, Y.; Sun, Y.; Dai, Y.; Sun, W.; Zhu, X.; Liu, H.; Han, R.; Gao, D.; Luo, C.; Wang, X. A "Signal-on" Chemiluminescence Biosensor for Thrombin Detection Based on DNA Functionalized Magnetic Sodium Alginate Hydrogel and Metalloporphyrinic Metal-Organic Framework Nanosheets. *Talanta* **2020**, *207*, 120300. https://doi.org/10.1016/j.talanta.2019.120300.

(185) Dhawane, M.; Deshpande, A.; Jain, R.; Dandekar, P. Colorimetric Point-of-Care Detection of Cholesterol Using Chitosan Nanofibers. *Sensors and Actuators B: Chemical* **2019**, *281*, 72–79. https://doi.org/10.1016/j.snb.2018.10.060.

(186) Maruthupandy, M.; Rajivgandhi, G.; Muneeswaran, T.; Vennila, T.; Quero, F.; Song, J.-M. Chitosan/Silver Nanocomposites for Colorimetric Detection of Glucose Molecules. *International Journal of Biological Macromolecules* **2019**, *121*, 822–828. https://doi.org/10.1016/j.ijbiomac.2018.10.063.

(187) Gabriel, E. F. M.; Garcia, P. T.; Cardoso, T. M. G.; Lopes, F. M.; Martins, F. T.; Coltro, W. K. T. Highly Sensitive Colorimetric Detection of Glucose and Uric Acid in Biological Fluids Using Chitosan-Modified Paper Microfluidic Devices. *Analyst* **2016**, *141* (15), 4749–4756. https://doi.org/10.1039/C6AN00430J.

(188) Unser, S.; Holcomb, S.; Cary, R.; Sagle, L. Collagen-Gold Nanoparticle Conjugates for Versatile Biosensing. *Sensors* **2017**, *17* (2), 378. https://doi.org/10.3390/s17020378.

(189) Banerjee, P.; Lenz, D.; Robinson, J. P.; Rickus, J. L.; Bhunia, A. K. A Novel and Simple Cell-Based Detection System with a Collagen-Encapsulated B-Lymphocyte Cell Line as a Biosensor for Rapid Detection of Pathogens and Toxins. *Laboratory Investigation* **2008**, *88* (2), 196–206. https://doi.org/10.1038/labinvest.3700703.

(190) Abedalwafa, M. A.; Tang, Z.; Qiao, Y.; Mei, Q.; Yang, G.; Li, Y.; Wang, L. An Aptasensor Strip-Based Colorimetric Determination Method for Kanamycin Using Cellulose Acetate Nanofibers Decorated DNA–Gold Nanoparticle Bioconjugates. *Microchimica Acta* **2020**, *187* (6), 360. https://doi.org/10.1007/s00604-020-04348-x.

(191) Luo, X.; Xia, J.; Jiang, X.; Yang, M.; Liu, S. Cellulose-Based Strips Designed Based on a Sensitive Enzyme Colorimetric Assay for the Low Concentration of Glucose Detection. *Analytical Chemistry* **2019**, *91* (24), 15461–15468. https://doi.org/10.1021/acs.analchem.9b03180.

(192) Dai, G.; Hu, J.; Zhao, X.; Wang, P. A Colorimetric Paper Sensor for Lactate Assay Using a Cellulose-Binding Recombinant Enzyme. *Sensors and Actuators B: Chemical* **2017**, *238*, 138–144. https://doi.org/10.1016/j.snb.2016.07.008.

(193) Suea-Ngam, A.; Deck, L.-T.; Howes, P. D.; DeMello, A. J. An Ultrasensitive Non-Noble Metal Colorimetric Assay Using Starch-Iodide Complexation for Ochratoxin A Detection. *Analytica Chimica Acta* **2020**, *1135*, 29–37. https://doi.org/10.1016/j.aca.2020.08.028.

(194) Tomeh, M. A.; Hadianamrei, R.; Zhao, X. Silk Fibroin as a Functional Biomaterial for Drug and Gene Delivery. *Pharmaceutics* **2019**, *11* (10), 494. https://doi.org/10.3390/pharmaceutics11100494.

(195) Kasoju, N.; Bora, U. Silk Fibroin in Tissue Engineering. *Advanced Healthcare Materials* **2012**, *1* (4), 393–412. https://doi.org/10.1002/adhm.201200097.

(196) Lu, S.; Wang, X.; Lu, Q.; Hu, X.; Uppal, N.; Omenetto, F. G.; Kaplan, D. L. Stabilization of Enzymes in Silk Films. *Biomacromolecules* **2009**, *10* (5), 1032–1042. https://doi.org/10.1021/bm800956n.

(197) Fan, S.; Zhang, Y.; Huang, X.; Geng, L.; Shao, H.; Hu, X.; Zhang, Y. Silk Materials for Medical, Electronic and Optical Applications. *Science China Technological Sciences* **2019**, *62* (6), 903–918. https://doi.org/10.1007/s11431-018-9403-8.

(198) Vepari, C.; Kaplan, D. L. Silk as a Biomaterial. *Progress in Polymer Science* **2007**, *32* (8–9), 991–1007. https://doi.org/10.1016/j.progpolymsci.2007.05.013.

(199) Rockwood, D. N.; Preda, R. C.; Yücel, T.; Wang, X.; Lovett, M. L.; Kaplan, D. L. Materials Fabrication from Bombyx Mori Silk Fibroin. *Nature Protocols* **2011**, *6* (10), 1612–1631. https://doi.org/10.1038/nprot.2011.379.

(200) Yamaguchi, K.; Kikuchi, Y.; Takagi, T.; Kikuchi, A.; Oyama, F.; Shimura, K.; Mizuno, S. Primary Structure of the Silk Fibroin Light Chain Determined by CDNA Sequencing and Peptide Analysis. *Journal of Molecular Biology* **1989**, *210* (1), 127–139. https://doi.org/10.1016/0022-2836(89)90295-7.

(201) Zhou, C.-Z. Fine Organization of Bombyx Mori Fibroin Heavy Chain Gene. *Nucleic Acids Research* **2000**, *28* (12), 2413–2419. https://doi.org/10.1093/nar/28.12.2413.

(202) Inoue, S.; Tanaka, K.; Arisaka, F.; Kimura, S.; Ohtomo, K.; Mizuno, S. Silk Fibroin of Bombyx Mori Is Secreted, Assembling a High Molecular Mass Elementary Unit Consisting of H-Chain, L-Chain, and P25, with a 6:6:1 Molar Ratio. *Journal of Biological Chemistry* **2000**, *275* (51), 40517–40528. https://doi.org/10.1074/jbc.M006897200.

(203) Tanaka, K.; Inoue, S.; Mizuno, S. Hydrophobic Interaction of P25, Containing Asn-Linked Oligosaccharide Chains, with the H-L Complex of Silk Fibroin Produced by Bombyx Mori. *Insect Biochemistry and Molecular Biology* **1999**, *29* (3), 269–276. https://doi.org/10.1016/S0965-1748(98)00135-0.

(204) Mori, K.; Tanaka, K.; Kikuchi, Y.; Waga, M.; Waga, S.; Mizuno, S. Production of a Chimeric Fibroin Light-Chain Polypeptide in a Fibroin Secretion-Deficient Naked Pupa Mutant of the SilkwormBombyx Mori. *Journal of Molecular Biology* **1995**, *251* (2), 217–228. https://doi.org/10.1006/jmbi.1995.0429.

(205) Drummy, L. F.; Phillips, D. M.; Stone, M. O.; Farmer, B. L.; Naik, R. R. Thermally Induced α-Helix to β-Sheet Transition in Regenerated Silk Fibers and Films. *Biomacromolecules* **2005**, *6* (6), 3328–3333. https://doi.org/10.1021/bm0503524.

(206) Qi, Y.; Wang, H.; Wei, K.; Yang, Y.; Zheng, R.-Y.; Kim, I.; Zhang, K.-Q. A Review of Structure Construction of Silk Fibroin Biomaterials from Single Structures to Multi-Level Structures. *International Journal of Molecular Sciences* **2017**, *18* (3), 237. https://doi.org/10.3390/ijms18030237.

(207) Valluzzi, R.; Gido, S. P.; Muller, W.; Kaplan, D. L. Orientation of Silk III at the Air-Water Interface. *International Journal of Biological Macromolecules* **1999**, *24* (2–3), 237–242. https://doi.org/10.1016/S0141-8130(99)00002-1.

(208) Rodriguez, M. J.; Brown, J.; Giordano, J.; Lin, S. J.; Omenetto, F. G.; Kaplan, D. L. Silk Based Bioinks for Soft Tissue Reconstruction Using 3-Dimensional (3D) Printing with in Vitro and in Vivo Assessments. *Biomaterials* **2017**, *117*, 105–115. https://doi.org/10.1016/j.biomaterials.2016.11.046.

(209) Perrone, G. S.; Leisk, G. G.; Lo, T. J.; Moreau, J. E.; Haas, D. S.; Papenburg, B. J.; Golden, E. B.; Partlow, B. P.; Fox, S. E.; Ibrahim, A. M. S.; Lin, S. J.; Kaplan, D. L. The Use of Silk-Based Devices for Fracture Fixation. *Nature Communications* **2014**, *5* (1), 3385. https://doi.org/10.1038/ncomms4385.

(210) Mottaghitalab, F.; Farokhi, M.; Shokrgozar, M. A.; Atyabi, F.; Hosseinkhani, H. Silk Fibroin Nanoparticle as a Novel Drug Delivery System. *Journal of Controlled Release* **2015**, *206*, 161–176. https://doi.org/10.1016/j.jconrel.2015.03.020.

(211) You, X.; Pak, J. J. Graphene-Based Field Effect Transistor Enzymatic Glucose Biosensor Using Silk Protein for Enzyme Immobilization and Device Substrate. *Sensors and Actuators B: Chemical* **2014**, *202*, 1357–1365. https://doi.org/10.1016/j.snb.2014.04.079.

(212) Huang, W.; Tarakanova, A.; Dinjaski, N.; Wang, Q.; Xia, X.; Chen, Y.; Wong, J. Y.; Buehler, M. J.; Kaplan, D. L. Design of Multistimuli Responsive Hydrogels Using Integrated Modeling and Genetically Engineered Silk–Elastin-Like Proteins. *Advanced Functional Materials* **2016**, *26* (23), 4113–4123. https://doi.org/10.1002/adfm.201600236.

(213) Wang, H.; Zhu, B.; Wang, H.; Ma, X.; Hao, Y.; Chen, X. Ultra-Lightweight Resistive Switching Memory Devices Based on Silk Fibroin. *Small* **2016**, *12* (25), 3360–3365. https://doi.org/10.1002/smll.201600893.

(214) Zhou, Z.; Shi, Z.; Cai, X.; Zhang, S.; Corder, S. G.; Li, X.; Zhang, Y.; Zhang, G.; Chen, L.; Liu, M.; Kaplan, D. L.; Omenetto, F. G.; Mao, Y.; Tao, Z.; Tao, T. H. The Use of Functionalized Silk Fibroin Films as a Platform for Optical Diffraction-Based Sensing Applications. *Advanced Materials* **2017**, *29* (15), 1605471. https://doi.org/10.1002/adma.201605471.

(215) Fan, S.; Zhang, Y.; Huang, X.; Geng, L.; Shao, H.; Hu, X.; Zhang, Y. Silk Materials for Medical, Electronic and Optical Applications. *Science China Technological Sciences* **2019**, *62* (6), 903–918. https://doi.org/10.1007/s11431-018-9403-8.

(216) Demura, M.; Asakura, T.; Kuroo, T. Immobilization of Biocatalysts with Bombyx Mori Silk Fibroin by Several Kinds of Physical Treatment and Its Application to Glucose Sensors. *Biosensors (Basel)* **1989**, *4* (6), 361–372. https://doi.org/10.1016/0265-928X(89)80002-1.

(217) Lu, S.; Wang, X.; Uppal, N.; Kaplan, D. L.; Li, M. Stabilization of Horseradish Peroxidase in Silk Materials. *Frontiers of Materials Science in China* **2009**, *3* (4), 367–373. https://doi.org/10.1007/s11706-009-0058-4.

(218) Acharya, C.; Kumar, V.; Sen, R.; Kundu, S. C. Performance Evaluation of a Silk Protein-Based Matrix for the Enzymatic Conversion of Tyrosine ToL-DOPA. *Biotechnology Journal* **2008**, *3* (2), 226–233. https://doi.org/10.1002/biot.200700120.

CHAPTER 2. OBJECTIVES

2. Objectives

The main objective of this PhD thesis is the development of novel (photo)electrochromic solid-state displays and sensors that need to be tailored to society's changing demands and the present environmental conditions. The aim is, therefore, to develop these applications in a framework that requires the use of more ecofriendly materials and newer qualities such as multifunctionality, flexibility and stretchability to meet the demands of future market applications.

To achieve this goal, the following specific objectives have been envisioned:

- To acquire preliminary knowledge about the intrinsic properties of compounds with 'True Electrochromism' or 'Electrochromism with Memory'. The objective is to gain a broader understanding of the (photo)electrochromic mechanisms that occur and to assess their chromic properties, such as response times, coloration efficiency, color contrast and fatigue resistance. A further intention is to gain an in-depth understanding of other possible stimuli that can be used to modulate the color change response (e.g., light, pH, temperature).

- Development and optimization of ecofriendly solid matrices for use as platforms in the manufacture of (photo)electrochromic devices and sensors. To this end, the aim is to produce and optimize ionogel-type membranes with sufficient ionic and flexible conductivity. Secondly, to seek to produce biocompatible silk fibroin membranes in which biocatalytic reactions can occur.

- Design of formulations and subsequent spectroelectrochemical, electrochemical and/or optical characterization of hybrid materials that combine (photo)electrochromic compounds in (bio)polymeric matrices.

- Ultimately, the objective is to integrate the aforesaid concepts in the development of specific application-specific platformss, such as:

    - Electrochromic inks to manufacture low-power electrochromic devices by using low-cost printing techniques.
    - Development / improvement of the efficiency of self-powered electrochromic biosensors
    - Development of a new reversible optical enzymatic biosensor based on silk and modified with photoelectrochromic mediators for the detection of glucose.

CHAPTER 3. RESULTS & DISCUSSION

3. Results and Discussion

In this section a discussion of the results related to the development of novel electrochromic and multifunctional solid materials and their use in displays and sensors is presented.

The results referring to this chapter are published in different scientific journals and available in the following scientific report.

[1] Santiago, S.; Aller, M.; Campo, F. J.; Guirado, G. Screen-printable Electrochromic Polymer Inks and Ion Gel Electrolytes for the Design of Low-power, Flexible Electrochromic Devices. *Electroanalysis* **2019**, *31*, 1664–1671. https://doi.org/10.1002/elan.201900154.

[2] Santiago, S.; Muñoz-Berbel, X.; Guirado, G. Study of P(VDF-Co-HFP)-Ionic Liquid Based Ionogels for Designing Flexible Displays. *J. Mol. Liq.* **2020**, *318*, 114033. https://doi.org/10.1016/j.molliq.2020.114033.

[3] Santiago-Malagón, S.; Río-Colín, D.; Azizkhani, H.; Aller-Pellitero, M.; Guirado, G.; del Campo, F. J. A Self-Powered Skin-Patch Electrochromic Biosensor. *Biosens. Bioelectron.* **2021**, *175*, 112879. https://doi.org/10.1016/j.bios.2020.112879.

[4] Santiago, S.; Giménez-Gómez, P.; Muñoz-Berbel, X.; Hernando, J.; Guirado, G. Solid Multiresponsive Materials Based on Nitrospiropyran-Doped Ionogels. *ACS Appl. Mater. Interfaces* **2021**, *13*, 26461–26471. https://doi.org/10.1021/acsami.1c04159.

[5] Santiago, S.; Richart, C.; Mena, S.; Gallardo, I.; Hernando, J.; Guirado, G. Electrocarboxylation of Spiropyran Switches through Carbon-Bromide Bond Cleavage Reaction. *ChemElectroChem* **2022**, *9*. https://doi.org/10.1002/celc.202101559.

In addition to the articles listed above, this doctoral thesis will also explain experimental results related to future scientific publications. At the beginning of each corresponding section, the content that has not yet been published will be specified.

3.1. Optimization and Formulation of Ionogels for its use in electrochromic applications

The results discussed in this section correspond to the following publication: *J. Mol. Liq.* **2020**, *318*, 114033.

Currently, ionogels (IG) are preferred over other solid electrolytes, basically because their formulation with ionic liquids avoids problems such as liquid leakage or solvent evaporation. Moreover, they are less toxic than other electrolytes and their versatile formulation allows infinite combinations such as the production of IGs with hybrid properties, as it will be discussed in the following chapters. However, most recent popularity of these materials relies on their rheological properties (elasticity, flexibility, and highly optical transparency), and particularly on their excellent electrochemical properties (i.e., high ionic conductivity and very wide electrochemical window), one of the most limiting constrains of solid electrolytes [1,2].

One of the most common strategies to produce IG is the combination of mechanically resistant and transparent polymers with ionic liquids (IL) that confer them ionic conductivity. Regarding to the polymer, many examples of IGs formulated with polymeric matrices of different composition have been already reported in the recent years. Among them, P(VDF-co-HFP) has been selected in this work due to its chemical stability and mechanical strength.

The doping of the polymeric matrix with IL has a major impact on the properties of the final IG. For this reason, in this work the IG properties and how they are affected by both, the content and the type of IL, have been deeply studied. Figure 3.1. shows the IL and the polymer matrix used in this study.

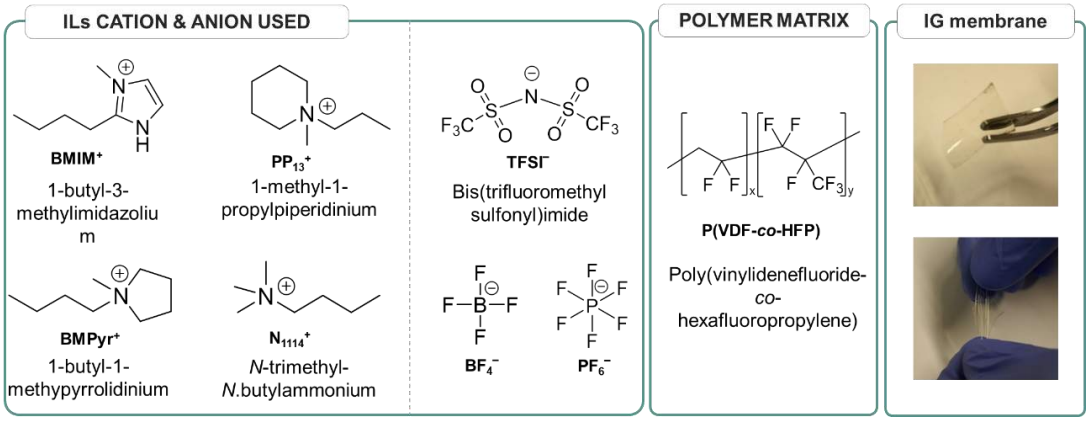

Figure 3.1 Chemical structure of cations and anions present in the IL used in this study. The structure of the polymer and the appearance of final IG membranes are also illustrated

Initial studies were conducted to determine the effect of the IL content in the electrical and rheological properties of the formulation of IG membranes using P(VDF-*co*-HFP) as polymer matrix and and BMIMF TFSI as model IL, IG membranes were prepared containing between 0% and 90% w/w. of BMIM.TFSI. Images of the membranes are included in Figure 3.2. The thickness of each one depended on the IL content and ranged between 100-700 µm.

The rheological properties of membranes were evaluated qualitatively. Membranes prepared without IL (0% w/w BMIM TFSI content), were opaque (transmittance % (ΔT %) = 14.8%), while the transparency increased with the concentration of IL up to a ΔT % = 83.2% for samples containing 83.3% w/w BMIM TFSI. Mechanical properties also changed significantly, from rigid and poorly elastic membranes when containing small content of BMIM TFSI to highly flexible and stretchable ones, when the content was high. This improvement in the elasticity and stretchability of the membranes when increasing IL content is associated to two aspects: (i) the swelling of the polymer in presence of IL, and (ii) the plasticizer capacity of ILs, which enables sliding between the polymer chains, thus generating flexibility. It is important to note that BMIM TFSI contents above 83.3% w/w resulted in IL leakage from the IG membrane, as well as an important loss of membrane consistency. This loss of consistency suggested a change in the morphology of the polymer chain. To investigate this morphological change, the previous membranes were analyzed by FT-IR. As a result, the peaks related to the crystal structure of P(VDF-*co*-HFP) (non-polar α-phase; $\nu = 796$ cm^{-1} (CF_3 sym. stretching) and $\nu = 760$ cm^{-1} (-CH_2 bending)) clearly decrease when increasing the percentage of BMIM TFSI in the membrane, while those corresponding to the amorphous polar β-phase ($\nu = 1404$ cm^{-1} (-CH_2 ant. stretching) and $\nu = 876$ cm^{-1} (CF_2 and C-C sym. stretching) were more pronounced. This confirmed the morphological change of the IG, which completely lost the crystalline structure above an IL concentration of 83.3% w/w.

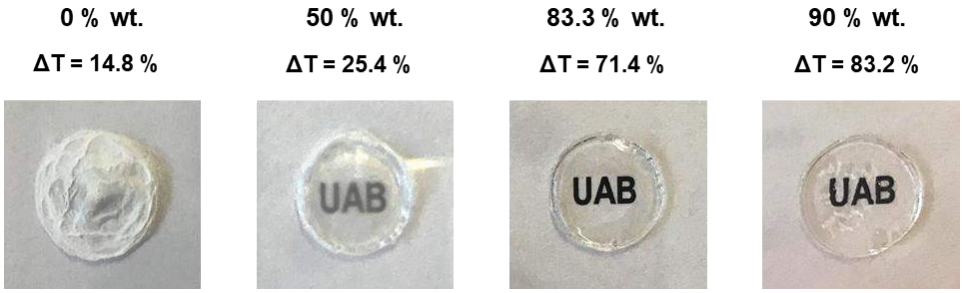

Figure 3.2. IG prepared using different BMIM TSI contents (expressed in weight ratio percentage % wt.) and the corresponding transmittance value measured in the visible range. Qualitatively, it can clearly be observed that there is a change in the aspect and transparency from more rigid, rough and opaque to more flexible, smooth and transparent as the content in IL increases. Note that the membrane prepared at 90% wt. presents a loss in consistency due to an excess of BMIM TFSI in its formulation

In addition to the rheological properties, the content of BMIM TFSI in the membrane also influenced its ionic conductivity (σ). Conductivities were estimated by determining the resistance associated with the ionic mobility of the charges in the membrane through electrochemical impedance spectroscopy (EIS). This ionic resistance appeared at high frequencies (> 10^5 Hz) and its magnitude could be determined as either the radius of the semicircle in the Nyquist plot or the frequency-independent impedance modulus above 10^5 Hz in the Bode plot, both of them providing directly the resistance magnitude in ohms. For a more precise determination, the full impedance spectra could be fit with the corresponding equivalent circuit. However, in this case it was not necessary by the simplicity of the equivalent circuit. Conductivity values from the resistance magnitude were obtained by applying eq (1):

$$\sigma = \frac{l}{A} x \frac{1}{R} \qquad \text{eq.(1)}$$

where σ is the ionic conductivity (in S), R is the resistance obtained from EIS analysis (in ohm) and $\frac{l}{A}$ is the cell constant (in cm^{-1}) where *l* is the distance between electrodes and A is the electrode area. In this case, the cell constant was determined experimentally by measuring the R magnitude of several KCl solutions of known conductivity by EIS. The cell constant value corresponded to the slope of σ versus R representation, and the value obtained was 0.60 cm^{-1}.

Impedance studies of the membranes indicated that the ionic conductivity of the IG was directly proportional to the BMIM TFSI content Figure 3.3. Apart from an increasing number of free ions by the presence of BMIM TFSI, the IL also produced a

change on P(VDF-*co*-HFP) structure from crystalline to amorphous that may facilitate ionic motility in the membrane. Loadings above 83.3% w/w in BMIM TFSI resulted in conductivities similar to those of the IL alone. This confirmed that above this value the IL could not be retained in the polymer matrix cavities and leaked, and thus, only free IL was measured by impedance.

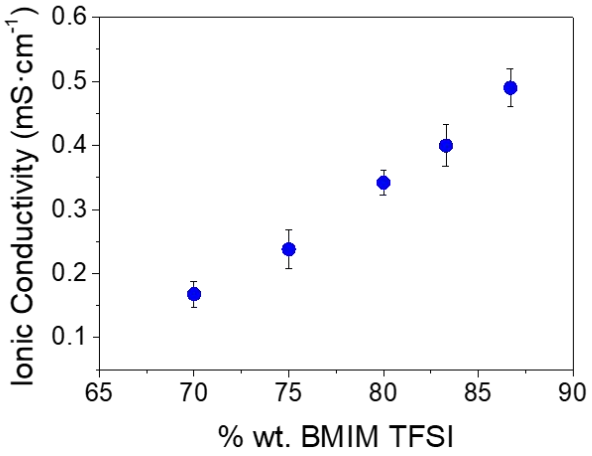

Figure 3.3. Representation of conductivity values measured by EIS for IG membranes prepared at different % wt. of BMIM TFSI. Note that membrane prepared at 90% wt. BMIM TFSI is not shown since the IL leakage interferes with the result. For IG e at 90% wt. BMIM TFSI wt. BMIM TFSI soared up to 1.06 $mS \cdot cm^{-1}$, which is a value close to those obtained for the pure IL

Based on these results, the IG membranes containing 83.3% w/w of BMIM TFSI in P(VDF-*co*-HFP) were considered optimal since presenting high conductivities, i.e., 0.40 mS/cm, in agreement with those provided by the IL alone at room temperature (3.60 mS/cm), flexibility, elasticity and transparency.

In a second step, the influence of using IL of different formulations was evaluated. IG containing P(VDF-*co*-HFP) and ILs at the same molar ratio were produced using EMIM TFSI, PP_{13} TFSI, BMPyr TFSI, N_{1114}TFSI, BMIM BF_4 and BMIM PF_6, and compared.

Considering rheological properties, it was observed that the membranes containing BMPyr TFSI and BMIM BF_4 were more rigid and less transparent (ΔT % < 40.0%). Regarding to the former, this may be due to the worse plasticizing effect of $BMPyr^+$ cation when compared to $BMIM^+$. In the second case, the use of larger anions ($TFSI^- < PF_6^- < BF_4^-$) may disorder the polymer arrangements, hindering the formation of crystalline domains and resulting in less plastic and more opaque membranes. Figure 3.4.

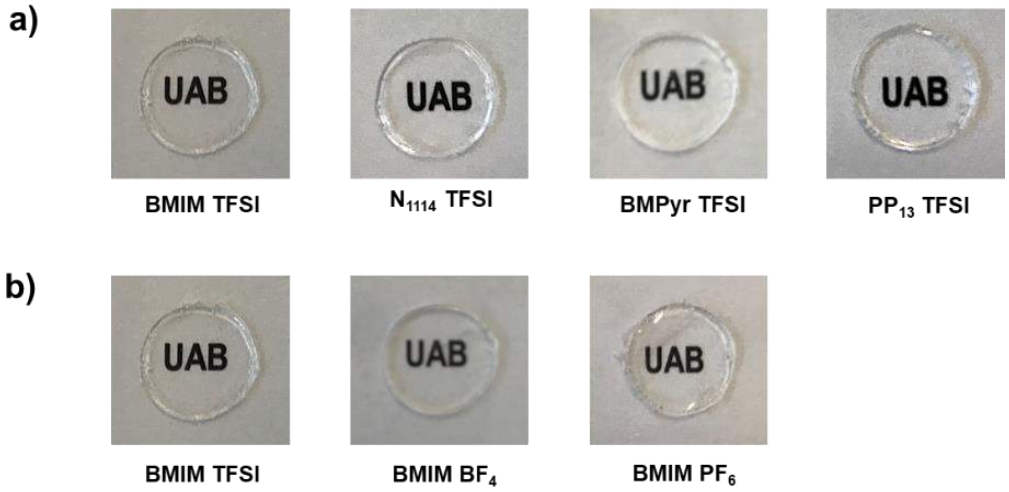

Figure 3.4. Appearance of the different membranes prepared using IL of different chemical nature. a) the Il used have the same anion ($TFSI^-$) but different cations. b) the effect of changing the anion is observed when $BMIM^+$ is used as a common cation**.**

Electrochemical studies of the membranes showed wide electrochemical windows between 2.72-3.20 V in all cases. The largest electrochemical window was recorded in the case of N_{1114}TFSI (3.20 V), probably by the higher reduction potential required by the N_{1114}^+ cation due to its poor electron-withdrawing effect. In the anions case, the oxidation potential was very similar since presenting very similar electron-donor characters.

Regarding conductivities, all membranes presented conductivities in the range between 0.215 and 0.846 mS/cm that made them suitable to produce low power solid and flexible electrochemical applications. Membrane conductivity was very influenced by the size of the counterions in the membrane. In general, smaller counterions presented faster mobility rates, resulting in larger conductivity values. This correlation was very evident in the case of cations, which presented a descending conductivity in the following order $BMIM^+ > N_{1114}^+ > BMPyr^+ > PP_{13}^+$, in accordance with the size of the countercation. The tendency was less evident in the case of anions, where only BMIM BF_4 presented a remarkable increase in conductivity due to their small size.

Table 3.1. summarizes the most relevant properties obtained for the IG membranes prepared with IL of different nature. Considering the overall properties of the membranes, IG formulated with N_{1114} TFSI at 79% wt. were selected for presenting the best electrochemical window, high transparency, and large ionic conductivity.

Table 3.1. Values of UV-vis transmittance in the range of 400-700 nm using different ILs in the preparation of IG at the same molar concentration. Ionic conductivity estimated from resistance values obtained by A.C. EIS measurements and electrochemical windows recorded by CV.

Sample	ΔT (%)	σ (mS/cm)	E_{pc} (V)	E_{pa} (V)	Electrochemical Window (V)
BMIM TFSI	71.3	0.295	-1.33	1.43	2.76
BMIM PF_6	69.9	0.393	-1.26	1.47	2.73
BMIM BF_4	38.4	0.846	-1.32	1.40	2.72
N_{1114}TFSI	72.8	0.303	-2.00	1.20	3.20
BMPyr TFSI	35.9	0.295	-1.73	1.20	2.93
PP_{13} TFSI	65.6	0.215	-1.73	1.10	2.83

This preliminary study established the basis for the formulation and the characterization of IG-type electrolytes, as well as the procedures to determine their rheological and electrochemical properties. The results obtained in this section were used in the production of electrochromic devices (ECD) and multicolored-sensing materials based on IG, as it will be described in the following sections.

In addition, the study on different formulations of IG and its properties that was carried out in this PhD thesis, also led to contributions in other publications: *Nano Letters* **2020**, *20* (5), 3528–3537 and *2D Materials* **2020**, *7* (2), 025046. IG were used as gates to control the crosstalk in graphene solution-gated field effect-transistors (g-SGFETs) aimed to spatially map the electrophysiological signals in brain. This technology eliminates the need of switches, simplifying the technical complexity. Besides it was demonstrated the possibility of printing IG electrolytes by inkjet which pave the way for upscaling the fabrication of g-SGFETs.

3.2. Production of Low-Power Electrochromic Devices

Electrochromic devices (ECD), in general, pursue the design of materials and architectures able to operate at low applied potentials. The properties observed for IGs make them ideal candidates in the production of ECD since, if necessary, they can work at higher potentials than other electrolytes thanks to their wide electrochemical window. Additionally, IGs present high ionic conductivities, which (i) minimizes the ohmic drop,

(ii) prevents operation at high potentials responsible for components degradation and (iii) enables the construction of more efficient ECD with faster color switching. Moreover, its high transparency would enable clear observation of the color contrast of the electrochromic compound.

IGs can be used as a solid electrolyte in different ways. The most common and simple is the layer-by-layer configuration. In this case, each component of the ECD is implemented as an independent layer with a discrete function in the full system. In this architecture, the electrolyte layer simply provides charge neutrality during the electrochemical coloring or bleaching.

Alternatively, a second approach consists of producing integrated ECD where all components are implemented in a single layer. In this case, the IG membrane is doped with the necessary ionic species (IL), electrochromic compounds and, in some cases, redox mediators, to produce a single membrane ECD.

In this thesis, both approaches are explored. Below, the different processes and strategies are described according to the type of device, as well as the characterization of their electrochromic properties.

3.2.1. Low power electrochromic material based on ECP-Magenta

The findings covered in this section are detailed in the following article: *Electroanalysis* **2019**, *31* (9), 1664–1671.

As previously commented, one of the main objectives when designing an ECD is to be able to operate it at low applied potentials, ideally around 1 V, to minimize energy costs and performance inefficiencies associated to the use of high voltage.

The need for high voltages in ECD is the consequence of diverse factors, namely: *i*) an overpotential caused by the high resistance of the medium; *ii*) a high oxidation or reduction potential of the electrochromic compound due to its chemical nature; or *iii*) the use of unsuitable redox mediators in electrochromic systems based on two electrodes.

To minimize previous factors, IGs were used as electrolyte of the developed ECDs since presenting high ionic conductivities, which would reduce medium overpotential.

A broad range of conductive polymers with electrochromic capabilities has been developed in recent years because of their low oxidation and reduction potentials, and the possibility of customizing their physicochemical features, including color contrast,

switching time and switching stability, Among them, ProDOT polymer derivatives (poly(3,4-propylenedioxythiophene)) can be easily substituted on the propylene bridge with symmetrical alkyl groups, which enhances their solubility in organic solvents. Specifically, ProDOT substituted with the 2-ethylhexyl group is the one referred to us as ECP-Magenta and which is studied in this thesis. Figure 3.5.The electrochromic ink based on the electrochromic polymer (ECP) known as ECP-Magenta was kindly provided by Doctors Anna M. Österholm, Eric Shen and John R. Reynolds from Georgia Institute of Technology, Atlanta.

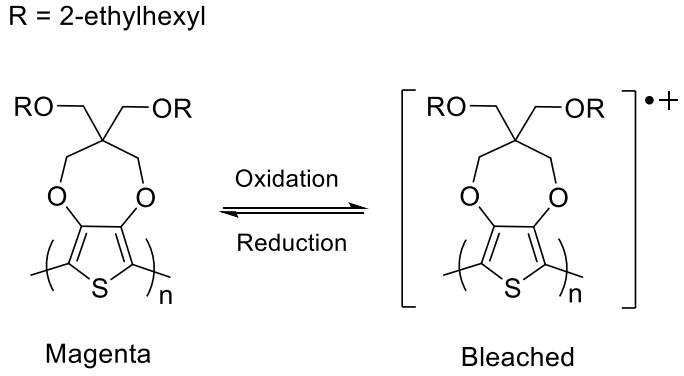

Figure 3.5. Chemical structure of ECP-Magenta and the switching color that takes place upon reversible electrochemical oxidation. R= 2-ethylhexy

In general, ECP-Magenta exhibits an intense coloration that can be efficiently bleached at low oxidation potentials around 0.5 V vs (Ag/AgCl), obtaining large color contrast values (> 60%). Main limitation of this compound is on its processability. Although its solubility has been improved through chemical modification, the production of electrochromic displays based on this type of ECP with low-cost and scalable technologies is still a challenge.

In that regard, it is one of the objectives of this thesis, to develop a new formulation for producing ECP-Magenta electrochromic inks compatible with screen-printing technologies. Apart from highly affordable and mass-production, this technology is very versatile, enables the production of components and systems in a wide range of substrates, e.g., flexible ones, and resolute, enabling to customize shapes and sharp edges up to micron range resolutions.

Electrochromic inks are composed of three key components: i) the electrochromic material ii) the conducting particles, and iii) the binder, when necessary, to provide proper consistency and viscosity [3–6]. Here, ECP-Magenta, ATO@TiO_2 microparticles and

dimethylpropylurea (DMPU) were selected as electrochromic material, conducting particle and binder, respectively. ATO@TiO_2 microparticles were chosen for their pale coloration and low cost, when compared to other conducting oxide particles such as indium-tin oxide NPs (ITO-NPs). The production of the ink involved the physical adsorption of ECP-Magenta on the ATO@TiO_2 microparticles by sonication, and the subsequent addition of the binder when the solvent was completely evaporated.

The ECP-Magenta@ATO@TiO_2 ink was used to produce screen-printed electrodes through the process illustrated in Figure 3.6. First, the pads and connections were screen-printed with Ag ink. Then, both the working electrode (WE) and the counter electrode (CE), were manufactured with graphite carbon ink, and the reference (Ref) with Ag/AgCl ink. The ECP-Magenta ink was then deposited on the WE surface, on top the graphite. Finally, the dielectric layer was deposited to protect the electrical connection and avoid short-circuits.

An IG membrane was placed on top of the three electrodes, i.e., WE, CE and Ref, covering all of them, and used to evaluate the electrochromic properties of the ink. The IG membrane containing 83.3% w/w BMIM TFSI on P(VDF-*co*-HFP) was chosen due to its high transparency (>80%, which enables to observe the color change of the ink), conductivity (0.40 mS/ cm) and large electrochemical window, suitable to oxidize the ECP-Magenta.

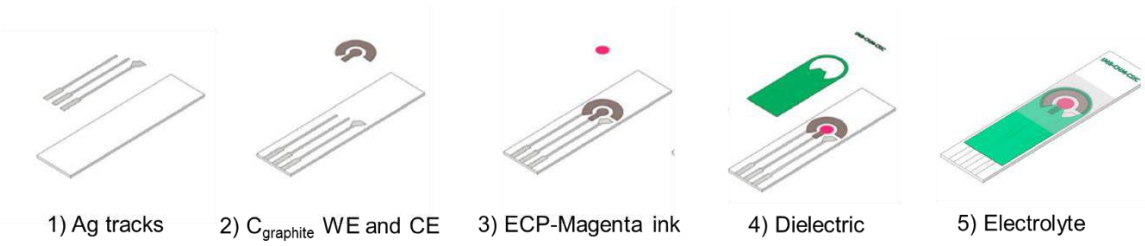

Figure 3.6. Step-by-step device manufacture by screen-printing. The system is used for the electrochemical and spectroelectrochemical characterization

CV studies of the ink revealed an oxidation peak at E_{pa} = 0.30 V vs Ag/AgCl, which associated to a reduction one at E_{pc} = 0.20 V vs Ag/AgCl (E^O = 0.25 V vs. Ag/AgCl). The electrochemical oxidation was completely reversible since similar intensity values were obtained for the anodic and cathodic peaks. This indicated that the compound presented 'real' electrochromism and could be completely converted into its neutral form after applying a low potential below 0.20 V. Figure 3.7. a).

In addition, the relationship between the anodic intensity peak vs the scan rate was calculated using a modification of the Randles-Sevick equation adapted to electroactive films or adsorbed species on the electrode surface [7]. The linear correlation obtained (Figure 3.7 b)) indicated that there were no free electroactive species in the medium and thus, the ink was well-adhered on the graphite surface.

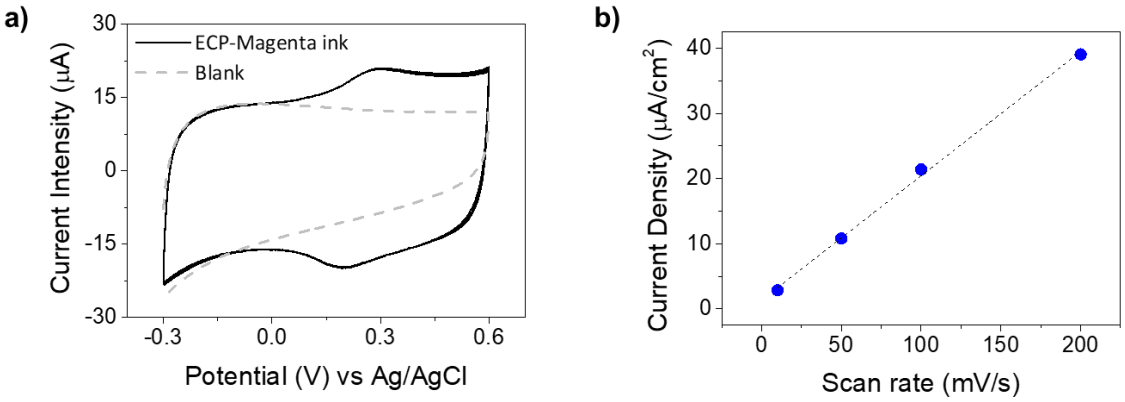

Figure 3.7. a) CV recorded at 50 mV/s in the anodic direction. Black dashed line corresponds to the voltammogram of handmade screen-printed electrodes without the ECP-Magenta using BMIM TFSI as electrolyte. Black solid line is the electrochemical response corresponding to the formulated ECP-Magenta ink. b) Representation of the anodic peak current density recorded at different scan rates (5 – 200 $mV \cdot s^{-1}$)

Spectroelectrochemical measurements, consisting of in situ UV-Vis spectroscopic measurements when applying an electric potential, were conducted aiming to correlate the previous electrochemical results with the ink color changes. Initially, the neutral form of ECP-Magenta ink presented an intense absorbance peak at λ_{max} = 528 nm associated to π-π* electronic transitions. After applying a potential above E_{pa} = 0.30 V, the molecule was oxidized, and its color was bleached. The reversibility to the colored form was achieved after applying a reduction potential of 0.00 V. Figure 3.8.

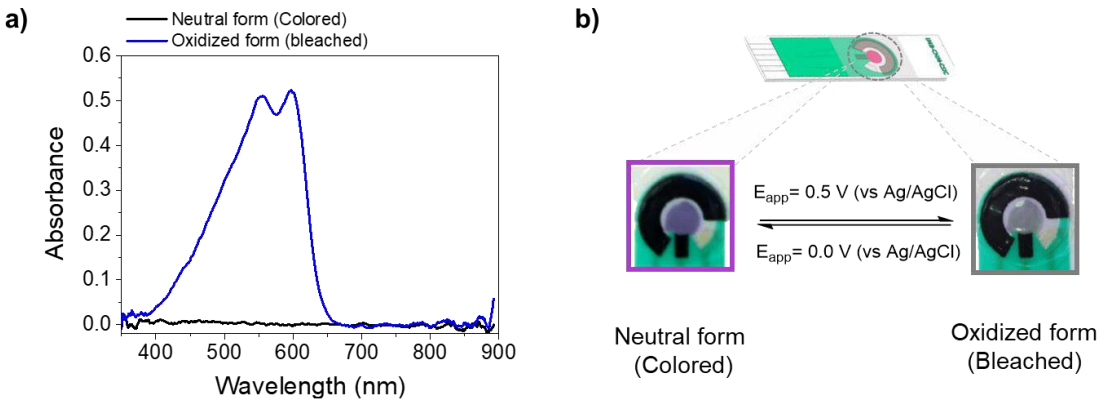

Figure 3.8. a) UV-Vis spectroscopy of ECP-Magenta ink using IG as electrolyte. The blue spectra represent the color exhibited when ECP-Magenta is in the initial neutral form. After oxidation, the color bleaches and the absorbance peak detected at 528 nm completely decreases. b) The image shows an amplification of the hand-made device manufactured by screen-printing and the color change observed by the naked eye when applying the corresponding oxidation potential at which the sample bleaches (E_{app} = 0.5 V (vs Ag/AgCl)) and the reverse electrochromic process when the reduction potential is applied (E_{app} = 0.0 V (vs Ag/AgCl)).

It is important to note here that ATO@TiO_2 microparticles also presented electrochromism, exhibiting a weak color change from pale to more intense green color when a reduction potential was applied. However, in this case, since ECP-Magenta was oxidized at a very low potential, the color change caused by the ATO@TiO_2 microparticles was insignificant and all electrochromic changes in the ink should be related to the ECP-Magenta.

Based on previous experiments, the switching color contrast, the switching time for bleaching and coloring, as well as the fatigue resistance were determined. Fatigue resistance was evaluated through consecutive cycles by applying 0.4 V and 0.1 V for 5 s in agreement with the CV results. Since it was possible to run the device at very low potential differences (below 1 V), it could be categorized as a low power electrochromic device. The following values were obtained after 4 cycles: 60% switching color contrast, τ_B = 2.1 s of bleaching time and τ_C = 2.2 s of coloring time. The coloration efficiency (CE), defined as the change in optical density (ΔOD) per unit of charge, was calculated to be 496 cm^2/C. This was consistent with previous studies that reported that only a small amount of charge was necessary to produce a detectable color change [8].

Some differences were observed in longer fatigue studies involving 500 cycles. Most important change was on the color contrast since ECP-Magenta ink exhibited a contrast loss of 20% after these cycles. This decay may be related to the narrow voltage window used to induce the color change. By increasing the potential, the color contrast

might increase. However, larger potentials may accelerate the degradation of the material because of side reactions and the loss of reversibility. On the other hand,the ink did not present significant differences on the switching time, providing values of τ_B = 2.04 s and τ_C = 2.04 s. This switching capacity met the requirements established by materials used as electrochromic displays (0.1 s – 10 s). Table 3.2. summarizes the electrochromic properties of the ink.

Table 3.2. Electrochromic parameters of ECP-Magenta ink using IG based on BMIM TFSI.

# Cycles	ΔT (%)	τ_a (s)	τ_C (s)	ΔOD	CE (cm^2/C)
1-4	60	2.10	2.20	0.190	496
496-500	40	2.04	2.04	0.130	-

Overall, the results prove that it is possible to produce screen-printable electrochromic inks based on ECP-Magenta formulated with conducting particles such as ATO@TiO_2. These inks presented interesting properties such as the possibility to operate at low voltages, to present large color contrasts, CE and short response times (~2 s), among others. Furthermore, the observed features were feasible thanks to the combination of the formulated inks with IG electrolytes, which provided an adequate ionic conductivity, while presenting high transparency that enabled color detection.

In the mid-term, these inks and material capable to operate at very low applied potentials and fully compatible with cost-effective and mass-production screen-printing technologies are envisioned as viable alternatives to produce the next generation of solid-state and low-cost electrochromic devices. Additionally, the strategy presented here paves the way to further ink formulations based on other organic electrochromic compounds.

3.2.2. Development of self-powered skin-patch electrochromic biosensor based on PB

The results corresponding to this subsection can be found in the following reference: *Biosens. Bioelectron.* **2021**, *175*, 112879.

In biosensing, lactate is an important target molecule involved in anaerobic metabolism. In sport, lactate levels have a direct relation to physical activity and fatigue. On the other hand, lactate is also relevant in healthcare, where used as an indicator of general health conditions related to pressure ischemia and insufficient oxidative metabolism. For this reason, many investigations are now focused on the development of lactate biosensors, and particularly wearable biosensors, for continuous monitoring of lactate levels either in blood, serum, interstitial liquid or sweat.

Electrochromic materials are excellent candidates for the development of sensors and biosensors since largely simplifying their manufacture and operation. Furthermore, with the right design, it is even possible to quantify the (bio)sensor response visually, without the need for external instrumentation [9–12].

Considering that, self-powered electrochromic patch biosensors enabling visual quantification of lactate in sweat were produced based on the strategy presented in the previous section. This time, Prussian Blue (PB) were used as electrochromic molecules, and ATO@TiO_2 were implemented as conducting particles.

In the production of the PB inks compatible with screen-printing [13], conducting particles were suspended under vigorous stirring in iron (II) sulfate aqueous solution. Then, a potassium ferricyanide solution was added dropwise to the solution and the precipitation reaction of $KFe[Fe(CN)_6]$ (PB) took place following equation (1).

$$FeSO_{4\,(aq)} + K_3[Fe(CN)_6]_{(aq)} \rightarrow KFe[Fe(CN)_6]_{(s)} \qquad \text{eq. (1)}$$

The resulting blue particles were centrifuged and washed with diluted HCl to remove the excess of non-reactant species, without compromising PB stability (PB is stable at acidic pH). After drying at 100 ºC, PB particles were physically adsorbed on ATO@TiO_2 surface. To improve the consistency and stability of the ink, the particles were finally mixed with a commercial binder (Viton ®).

As in the previous case, the electrochromic properties of the ink were evaluated with custom-made screen-printing electrodes containing graphite WE and CE and Ag/AgCl Ref, where the PB ink was deposited on the WE surface. CV and spectroelectrochemical were conducted in aqueous solutions of KNO_3 (0.1 M), which used as electrolyte.

CV showed an excellent electrochemical response of the PB ink. Figure 3.9 a). The cathodic voltammogram presented a peak at E_{pc} = 0.20 V vs Ag/AgCl corresponding to the reversible reduction of PB to Prussian White (PW). In the reverse scan, the oxidation of PW to PB was also observed at potentials above E_{pa} = 0.30 V vs Ag/AgCl. A second redox process was observed at more positive potentials of 0.90 V vs Ag/AgCl, which was related to the oxidation of PB to Berlin Green (BG). Since the device was designed to operate at low potentials between -0.10 V to 0.30 V, this second electrochemical process (i.e., PB → PG and *vice versa*) was not considered.

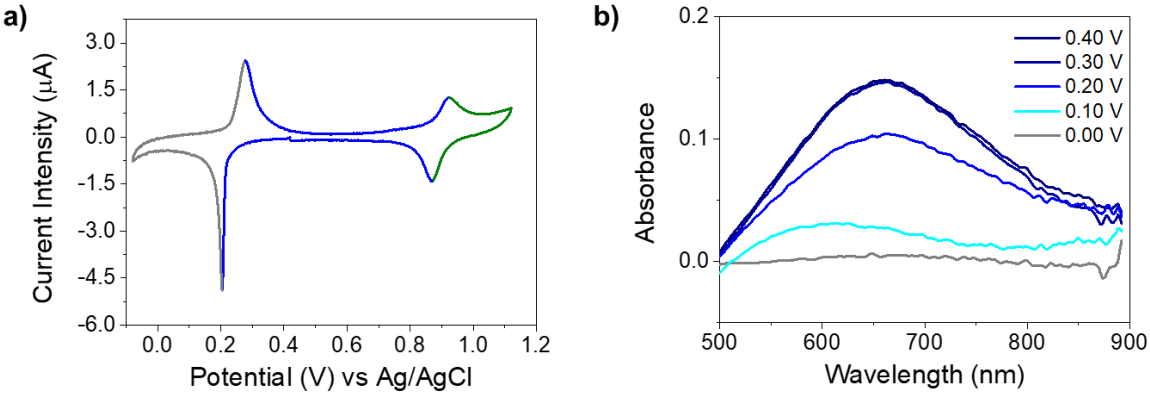

Figure 3.9. a) CV recorded at 5 $mV \cdot s^{-1}$ of PB pastes when printed over $C_{graphite}$ WE and using 0.1 M KNO_3 aqueous electrolyte. The potential region where PB is stable is outlined in blue. PW is shown in grey and BG in green. b) UV-Vis absorption spectra showing the reversible PB → PW electrochromic process on application of increasing reduction potential values (from 0.40 V to 0.0 V (vs Ag/AgCl)).

Regarding the spectroscopic response, the high absorbance of the PB ink at λ_{max} = 680 nm associated to its deep blue color decreased after applying reduction potentials below 0.20 V. The fully bleached state (PW) was obtained at 0.00 V vs Ag/AgCl, obtaining the highest color contrast around 30%. The electrochromic system presented good reversibility and recovered the initial PB state after applying oxidation potentials close to 0.40 V vs Ag/AgCl. Figure 3.9 b).

Lactate biosensing required the implementation of a crosslinked mixture containing lactate oxidase (LOx), poly(1-vinylimidazole) and a redox mediator Os(4,4'-dimethylbpy)$_2$Cl (PVI-dmeOs) [14]. The redox mediator presented low potentials, i.e., an oxidation peak at E_{pa} = 0.12 V vs Ag/AgCl (Os^{II}/Os^{III}) and the corresponding reduction peak at 0.19 V vs Ag/AgCl (Os^{III}/Os^{II}), which allow it to mediate the electron transference from the enzyme to the electrode. The presence of the mixture conferred the biosensor with capacity to detect lactate through the reaction cascade depicted in Figure 3.10 a).

Overall, the reaction started when lactate was present in the medium and the enzyme LOx oxidized it to pyruvate. The reduced form of the enzyme was then reoxidized by the redox mediator, PVI-dmeOs, which was reduced, at the same time, from to PVI-dmeOs (III) to PVI-dmeOs (II). The redox mediator is finally reoxidized on the electrode surface by applying the suitable potential. With this, and thanks to the cascade reaction, it is possible to produce an electron flow that is directly proportional to the lactate concentration in the sample.

The catalytic capacity of the PVI-dmeOs-LOx complex was assessed by drop-casting the mixture solution on $C_{graphite}$ WE screen-printed electrodes and incubate them with a solution containing lactate. When the mixture was placed on the electrode surface and dried, it remained adsorbed on the graphite carbon electrode by physical interactions. After lactate addition, the reversibility of the osmium mediator was lost, and a higher intensity irreversible peak was observed only in the cathodic sweep by the catalytic activity of the mixture when lactate was present. Figure 3.10. b).

In a second assay, the analytical performance of the lactate biosensor was evaluated. Current densities of the biosensor after incubation with PBS solutions containing lactate concentrations in the range between 0 and 12 mM were acquired by amperometric detection and plotted. Figure 3.10. c). A linear detection range between 0-4 mM lactate was obtained before biosensor saturation in the range between 4 and 12 mM.

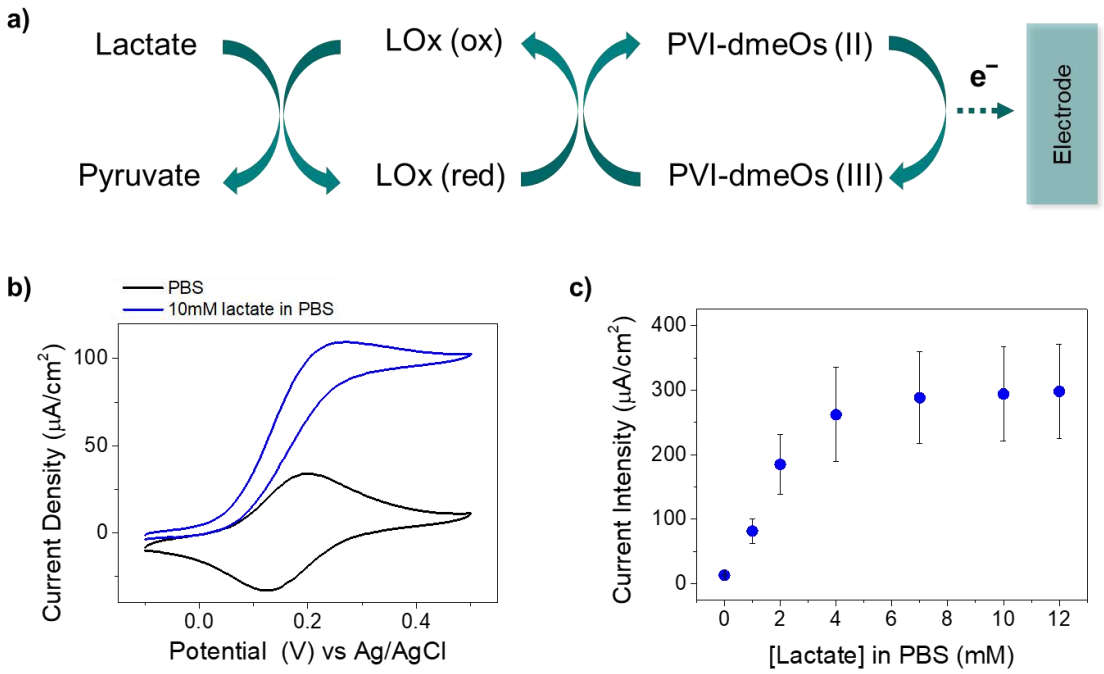

Figure 3.10. a) Reaction cascade produced when oxidizing the redox mediator PVI-dmeOs (II) on the electrode, which triggers the oxidation of lactate present in the sample. b) CV of dropcasted biosensor on $C_{graphite}$ screen-printed electrodes, using PBS as supporting electrolyte and scanned at 5 $mV \cdot s^{-1}$. A reversible wave corresponding to the redox response of PVI-dmeOs is observed. After the addition of lactate, a catalytic effect is detected. c) Current densities extracted from chronoamperometries at E_{app} = 0.30 V (vs Ag/AgCl) for various concentrations of lactate (0 – 12 mM) in PBS. The current density value for each case was taken when a constant current was achieved (after 120 s).

In the skin-patch configuration, the anode, i.e., the biosensor, was in a coplanar arrangement adjacent to the PB strip, which functioned as the cathode. Both anode and catode were printed on a conductive and transparent substrate of poly(3,4-ethylenedioxythiophene) polystyrene sulfonate (PEDOT:PSS).

Before the construction of the final device, the suitability of PEDOT:PSS electrodes as conductive supports was assessed. PEDOT:PSS is known to be much more affordable than others materials conventionally used in the production of transparent electrodes, e.g. indium tin oxide on polyethylene terephthalate (ITO-PET). However, its large electrical resistivity (400 $\Omega \cdot cm^{-1}$ vs 60-75 $\Omega \cdot cm^{-1}$ of ITO-PET), may limit its use in the development of electrochromic systems. A conventional strategy to overcome this limitation consists of increasing the thickness of the PEDOT:PSS layer. However, in the case of electrochromic displays and sensors this strategy may be not suitable since PEDOT:PSS also presents electrochromic properties and change its color when applying reduction/oxidation potentials. This limitation is particularly relevant in the case

of PB since both materials absorb at the same wavelength (λ_{max}=685 nm) and thus, PEDOT:PSS may mask PB color changes.

In order to achieve a proper compromise between conductivity and color change, the electrochromism of PB on PEDOT:PSS layers of different thickness was studied by UV-Vis spectroelectrochemistry and compared. As a result, clear readout with suitable perfomances were obtained when depositing a PB layer of 30 µm thick on two layers of PEDOT:PSS of 2 µm.

In general, the methods for extracting chemical information from electrochromic sensors varies from a hue color change [15], understood as a total color change between a colored and a colorless form generating a type of 'yes/no' response, to a gradual color change proportional to the concentration of analyte present in the sample. In this case, quantitative determination was necessary since variation of lactate levels may result in more or less critical pathological situations. Among other quantitative strategies, the final prototype in this section was designed based on the iR drop effect described by Pellitero et al. in the production of PB self-powered electrochromic displays. The iR drop effect takes benefit from the fact that, in a coplanar configuration, the internal resistance gradually increased with distance between the anode and the cathode [16]. Thanks to that, it is possible to relate the energy supplied by the redox reaction in the biosensor, which directly proportional to the analyte concentration, to the PB reduction. Since the internal resistance increases gradually, the conversion from PB to PW is easier and faster in those molecules situated closer to the anode. This produces the partial conversion of the cathode from PB to PW, with the particularity that the length of the colored region is directly proportional to the analyte concentration. This fact provided a very simple manner to quantify the target molecule, even with the bare eye.

Based on that, the anode (biosensor) and the cathode (electrochromic display) in the final prototype were printed on conducting PEDOT:PSS substrates and connected to form a galvanic system. Additionally, the system implemented an electrolyte layer composed of EMIM TFSI and potassium triflate (KTf) covering the cathode and the gap between cathode and anode. The role of the electrolyte layer was double. On the one hand, it was necessary to ensure the proper color change of the electrochromic layer of PB since the crystalline structure of PB required K^+ ions for bleaching to PW. On the other hand, the isolation of the cathode with the IG stabilized the response of the cathode while minimizing the influence of any interfering molecule in the sample. Figure 3.11. shows the steps followed to produce the electrochromic skin-patches.

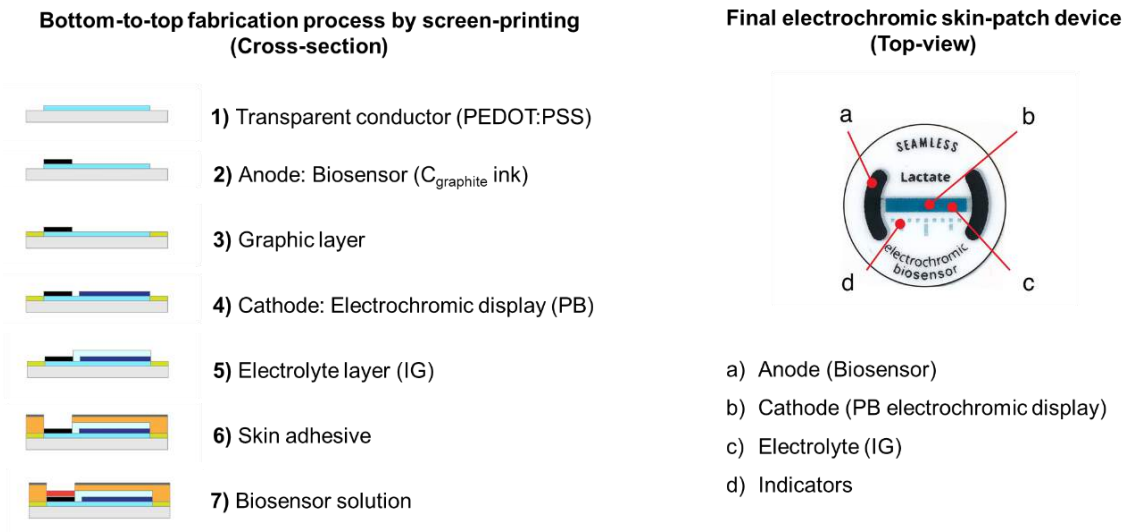

Figure 3.11. Steps followed to produce the device by screen-printing. A top view of the final appearance is shown on the right.

In self-powered systems, power is commonly the limiting factor that affects their operation, leading to limited performance. This problem was solved in the current prototype by using electrochromic displays, which provide visual information of the analyte concentration through a simple color change.

The electrochromic wearable was designed in a way that could operate, providing quantitative information, without the need for external instruments or power sources. It took advantage of the configuration of the electrochemical cell, containing an anode (biosensor) with a lower redox potential that the PB electrochromic cathode. Even when both cathode and anode were connected by a conductive layer, the redox reaction did not occur spontaneously due to the internal resistance that the device strategically presents [16], which conferred it with biosensing capacity. That this, color changes were only driven in the presence of lactate, which was the trigger that initiated the cascade of reactions. The reason was on the changes of cell potential with and without lactate. The cell potential of the current system was: $E_{cell} = E_{cat} – E_{an} – iR$. When lactate concentration was 0, $iR > E_{cat} – E_{an}$, and the system remained stable and at an OFF situation. When lactate concentration reached a value close to 1 mM, $iR < E_{cat} – E_{an}$ due to an increase in $E_{cat} – E_{an}$, which behaved in a Nernstian manner. According to this, higher lactate concentrations would increase E_{cell}, resulting in the reduction of PB molecules situated farther from the anode and thus, in a decrease of the colored length. The length of the colored PB region would be then proportionally to the lactate concentration for the range of concentrations studied and for the proposed design.

As an experimental demonstration of the sensor performance, Figure 3.12. a) shows the images of the devices before and after incubation with lactate concentrations between 1 and 13 mM. from As expected, the front color was proportional to the lactate concentration, reaching larger distances at higher concentrations (corresponding to higher E_{cell}). In absence of lactate, no color change was observed, confirming the selectivity of the device. Notably, the color distances did not return, probably because the sample volumes were large enough to maintain the electromotive force during the experiment.

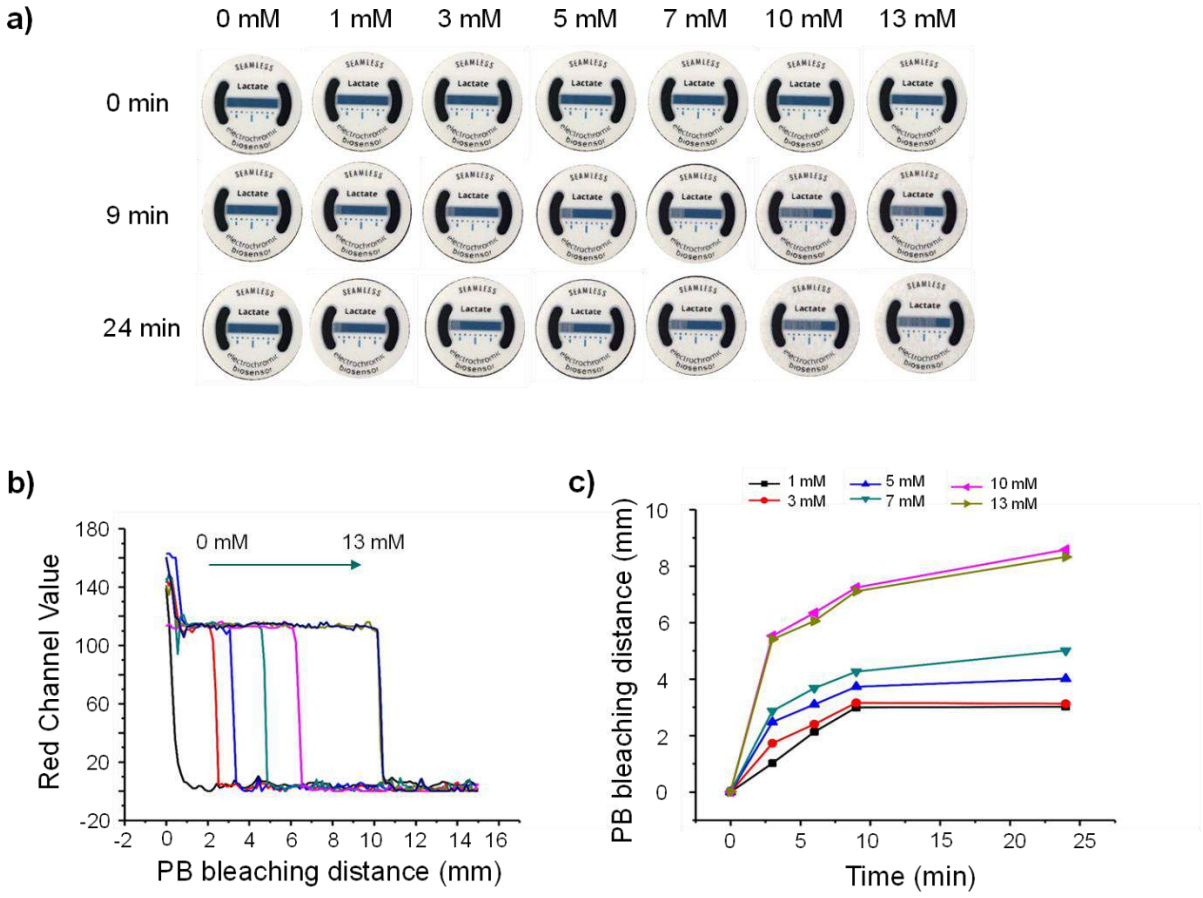

Figure 3.12. a) Images taken of the displays at various times and with different concentrations of lactate solutions in PBS. The bleaching distance in the electrochromic display (PB strip) is observed. b) Color analysis by ImageJ of PB strips. The bleaching distance is represented by analyzing the color intensity measured in the red channel to obtain better sensitivities. The distance was measured after 24 min when the steady color was reached. c) Representation of bleaching distance vs time is also plotted so that the time required to obtain a stable color readout (10 min) is determined.

Sensor images were processed with the ImageJ software. First, they were split into the three main colour using the RGB analysis function, and then the red channel (R) was selected for being the one providing best sensitivities. Figure 3.12. b) shows the

distances reached as a function of concentration at times until 24 min after the previous treatment. As shown, the sensors reached an end point after 24 min of incubation because the potential difference (E_{cat} – E_{an}) or electromotive force equaled the ohmic drop (i*R*). However, the 85% response was already obtained after 10 min of incubation, making the devices suitable for wearable applications. Figure 3.12 c).

In summary, the present study presents advances towards the development of self-powered wearable biosensors, simpler and more sustainable than current alternative, for potential use in resources-limited setting. Regarding the operation principle, the device is capable to report on lactate levels by simple visual inspection thanks to a configuration that correlates the level of analyte with the length of the PB colored regions. This configuration provides quantitative data without the need for external power sources or instruments. The electrochromic materials are here implemented in biosensors to create an electrochemical device able to perform three purposes in a single electrochemical cell: energy generation, sensing, and information display. The detection ranges of the device are in agreement with those obtained in blood, i.e. 1.5 mM before physical exercise to 10 mM after physical exercise, but still far from those reported in sweat, ranging from 20 and 70 mM after exercise. However, due to the simplicity and versatility of the sensor operation principle, it could be improved through future adaptation of the prototype, which would imply a promising approach to the non-invasive monitoring of biomarkers.

The advances described here is the result of a previous contribution in the following publication: Sensors and Actuators B: Chemical **2020**, 306, 127535.

In this study, a first version of the coplanar configuration proposed for the self-powered electrochromic biosensor was electrochemically characterized for the first time. As difference to the studies included in this thesis, the device was provided with electrical connections to connect it to a potentiostat and to analyze the color variation of the electrochromic display as a function of the system resistance and the generated current density. It was found that for the display built using IG as electrolyte, the maximum current density obtained was 35 $\mu A \cdot cm^{-2}$, which led to a blurred bleaching front. However, the design presented in this thesis was corrected and a better defined color front was observed.

3.3. All-in-one (photo)electrochromic systems

One of the main drawbacks of compounds with real electrochromism is the inability to induce a change of state, and color, by means of different stimuli. In opposition, MS are organic compounds many of them sensitive to multiple stimuli of different nature. When each stimulus induces a different color change, it is possible to reach multicolored states. In other cases, it is possible to make the transition from one colored state to the other using different stimulus, although the change of color is identical in all cases.

To implement the MSs in appealing applications, it would be necessary to incorporate them in solid-state systems. Unfortunately, this process is not straight forward since MSs need to perform important conformational changes, which are highly prevented in the solid state formats. It is one of the main objectives of the thesis to implement MSs in solid-state structures for the production of advanced devices. For this, the use of gel-solid consistency supports, i.e., IG, is considered in the processing and manufacture of the MS-containing devices.

3.3.1. ***Development of Multistimuli IG flexible materials based on Nitrospiropyran (NO_2BIPS)***

The study presented in this section was published in the following scientific journal: *Appl. Mater. Interfaces* **2021**, *13*, 26461–26471.

Spiropyran-like compounds are excellent candidates for a multitude of applications due to their ability to reversibly change between states with distinct features (e.g., color and polarity) in response to external stimuli. Although photo-isomerization between their colorless spirocyclic (SP) and colorful merocyanine (MC) isomers is their most exploited property, these compounds are able to respond to other external stimuli, including pH, presence of metal ions, solvent polarity, and redox potentials, among others. Considering that, IG membranes were doped with the derivative nitrospiropyran (NO_2BIPS), and the response of the solid-state material to the different stimuli was evaluated. The study of the responses of this material to different types of stimuli is presented below.

i. Photochromism of nitrospiropyran in IG membranes (NO_2BIPS@IG)

The photochromism of NO_2BIPS was investigated first in using N_{1114} TFSI solutions, and then after implementation in IG membranes (NO_2BIPS@IG) based on N_{1114} TFSI since it offers a broader electrochemical window.

As already reported [17,18], NO_2BIPS solutions presented a maximum absorbance peak in the UV range, i.e., at λ_{abs} = 346 nm, corresponding to its most thermally stable form, the closed-ring SP. After irradiation at λ_{exc} = 356 nm, SP is photo-isomerized into the MC open form, with an isomerization yield of 28% once the photostationary state (PSS) was reached. The ring opening isomerization involved the cleavage of a C-O_{spiro} bond, conferring the isomer a vivid purple color. In fact, MC form presented two absorption bands at $\lambda_{abs\ 1}$ = 376 nm and $\lambda_{abs\ 2}$ = 555 nm, the latter responsible of its coloration. The conversion could be totally reversed to the SP form by exposition to visible light. Figure 3.13.

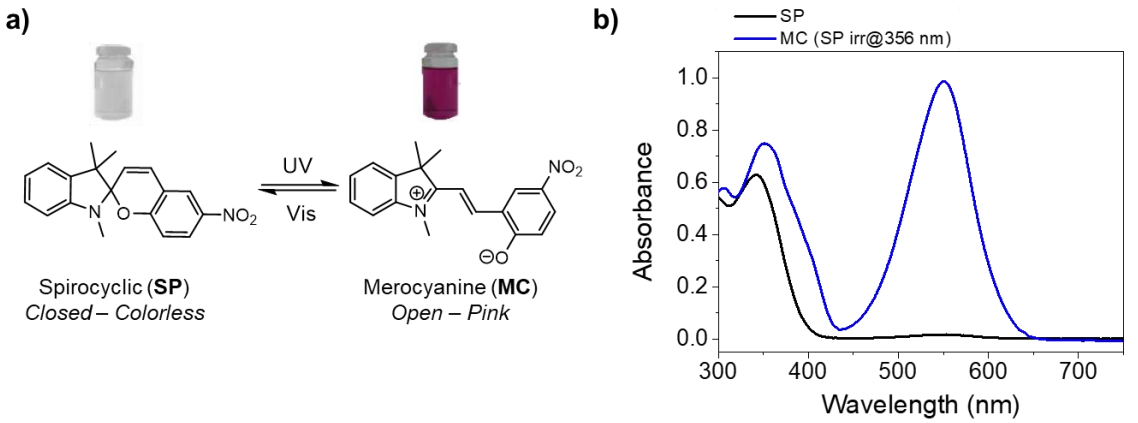

Figure 3.13. a) Reversible photochromic scheme of NO_2BIPS from the closed-ring or spirocyclic isomer (SP) to the open-ring merocyanine form (MC) under UV and visible light respectively. b) Absorbance UV-Vis spectra of 0.5 mM NO_2BIPS in N_{1114} TFSI after and before irradiation of the sample at λ_{exc} = 356 nm.

In the preparation of NO_2BIPS@IG membranes, the content of NO_2BIPS in the IG was one of the most critical points and two aspects should be considered. On the one hand, the NO_2BIPS content should be high enough to produce a good color contrast within the concentration range satisfying the Lambert-Beer law, thus enabling quantification. On the other hand, the compound should dissolve completely in the IL, and distribute homogeneously, to present suitable switching performance.

Taking in mind previous considerations, a number of membranes were prepared, which containing between 0.05-0.5 mg NO_2BIPS/g IG. Initial studies concluded that all

of them presented rheological properties similar to pristine IGs (elasticity, transparency, flexibility, etc.). This demonstrated that NO_2BIPS could be processed through a very simple manufacturing process only requiring a simple entrapment step. Additionally, once entrapped, NO_2BIPS@IG membranes could be shaped and cut very easily, which offered a myriad of possibilities for the design and production of smart devices.

Regarding their chromic properties, the closed SP form of NO_2BIPS was again the most stable in the IG membrane, making the films essentially transparent to the naked eye. After irradiating with UV light (λ_{exc} = 365 nm), it was possible to photo-isomerize the compound and to produce the intensely colored MC form. Figure 3.14. a). The spectral properties of both SP and MC forms in the membrane where completely comparable to those obtained in solution, either in N_{1114} TFSI or ACN. Figure 3.14. b). At the PSS, a total conversion of 22% for MC was obtained in the membrane, which quite similar to the 28% obtained in N_{1114} TFSI solutions. Additionally, the quantum yield in the membrane was found to be $\Phi_{SP\text{-}MC}$ = 0.15 ± 0.03, which was in agreement with the values reported by this compound in polar solvents such as ACN ($\Phi_{SP\text{-}MC}$ = 0.12) [18].

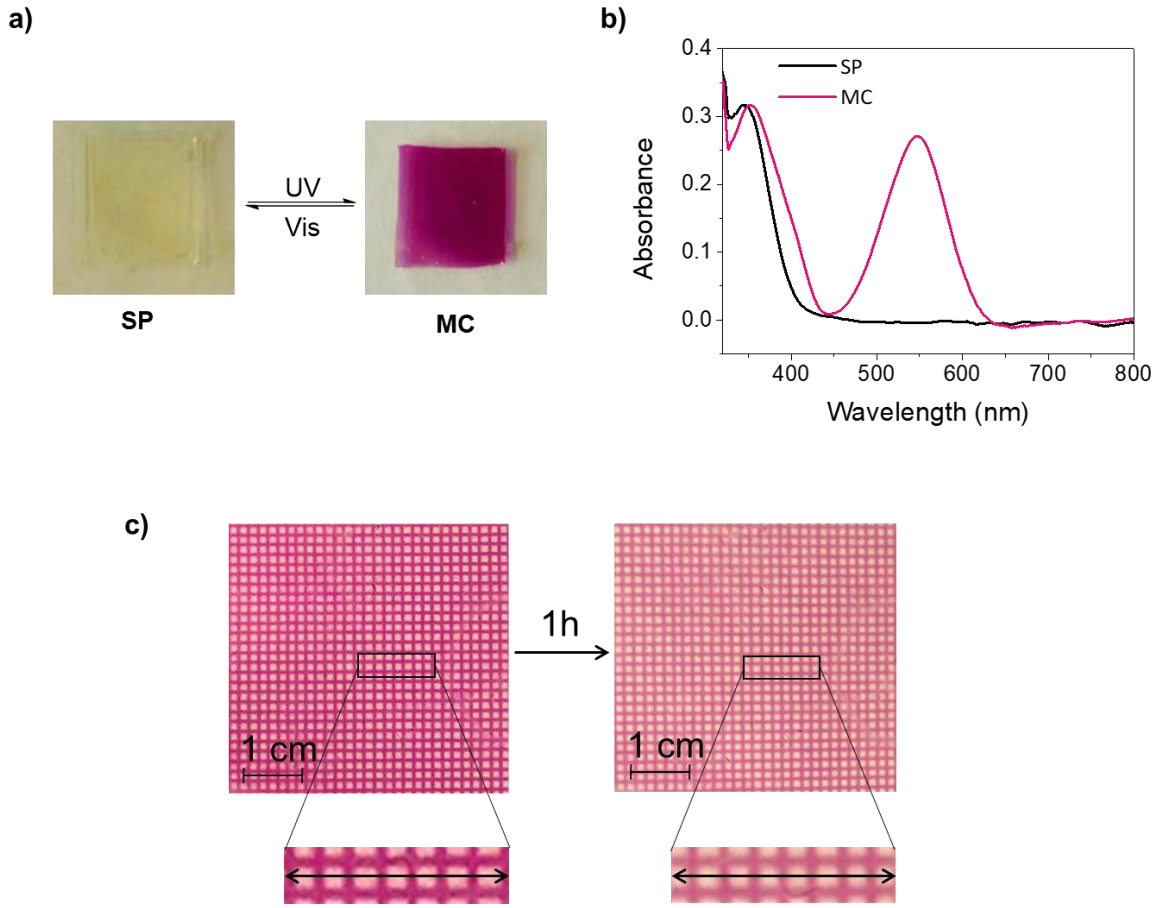

Figure 3.14. a) Photochromic characteristics of NO2BIPS@IG membranes. Exposure to UV light (λ_{exc} = 365 nm) resulted in a vivid pink coloring, while visible light resulted in a transparent membrane. b) Color change of NO_2BIPS@IG membranes is analyzed by UV-Vis absorbance spectroscopy. Initially, the membrane is completely transparent corresponding to the SP form as registered by UV-Vis spectra. After irradiation at λ_{exc} = 365 nm and the PSS is reached, the pink lined spectra is obtained, demonstrating that the MC form in IG membranes is conceivable. c) A patterned membrane was created with the use of a photomask by irradiating the open sections through the photomask at λ_{exc} = 365 nm. The region exposed to UV light became pink (MC), whereas the sections that were not exposed to UV light (squares) stayed clear (SP). After 1h in the dark, the patterning is maintained and a slight decrease in color intensity can be seen.

In reference to the reverse back-isomerization from MC to SP, spontaneous thermal back-isomerization was found to follow a first order kinetics at a constant rate $k_{MC\rightarrow SP}$ = 9.2 x 10^{-4} s^{-1} at 25 °C, which similar to the magnitude reported in solution by organic polar solvents (N_{1114} TFSI: $k_{MC\rightarrow SP}$ = 1.9 x 10^{-3} s^{-1}; ethanol: $k_{MC\rightarrow SP}$ = 9.2 x 10^{-4} s^{-1} at 25 °C). The process was slower than photo-isomerization and enabled the creation of patterns such as the one shown in Figure 3.14. c). The reason for that slow thermal reversion was associated to two factors: (i) the limited mobility of NO_2BIPS molecules inside the membranes and (ii) principally, the polarity of the solvent, i.e., N_{1114}TFSI, which stabilized

the MC form avoiding its fast reversion. Coversely, when irradiating the sample with visible light, the process was faster and the membrane was totally converted to the transparent SP form after short irradiation times (i.e, 2 s).

The switching process between SP and MC forms could be repeated several times without affecting the membrane properties thanks to its robust responsiveness. This confirmed that the photo-switching behavior from SP to MC and vice versa remained unalterable after the incorporation of NO_2BIPS in IG membranes. A plausible explanation of this fact may be that NO_2BIPS molecules in the membrane remained, in fact, dissolved in the ionic liquid phase of IG. This IL offered a soft, fluidic, and conductive environment to NO_2BIPS, which could switch in response to light, as they were in solution. After that observation, other stimuli were studied to evaluate the multi-response capacity of the NO_2BIPS@IG membranes to chemicals, electrical current or temperature, among others.

ii. Thermo and halochromism of NO_2BIPS@IG membranes

Apart from the well-described photochromism, thermochromism [19] (i.e., color change due to temperature changes) and halochromism [20,21] (i.e., chromic response to acid-base changes in polar solvents) have been also reported by NO_2BIPS in solution. Here, these two properties were investigated in NO_2BIPS@IG membranes

Halochromism of NO_2BIPS molecules is attributed to the basic behavior of the 4-nitrophenolate group of the MC form. After addition of a strong acid, i.e., H_2SO_4, in the dark, the SP structure opened to yield (*Z*)-MCH^+ with the 4-nitrophenolate group protonated. This produced transparent NO_2BIPS solutions and membranes, with an absorption band at $\lambda_{abs} < 350$ nm. In the membrane, the exact position of the band could not be determined since overlapping with the absorption band of the IG. When irradiating the compound with UV light at $\lambda_{exc} = 365$ nm, both the solution and the membrane become yellow with a clear absorption band close to $\lambda_{abs} = 400$ nm. This color was associated to the isomerization of (*Z*)-MCH^+ to (*E*)-MCH^+, which corroborated the formation of the (*Z*)-MCH^+ isomer in acid conditions. The yellow color could be reversibly converted to transparent after irradiation with visible light, $\lambda_{exc} = 445$ nm, which produced the transformation from (*E*)-MCH^+ to (*Z*)-MCH^+. Figure 3.15 a).

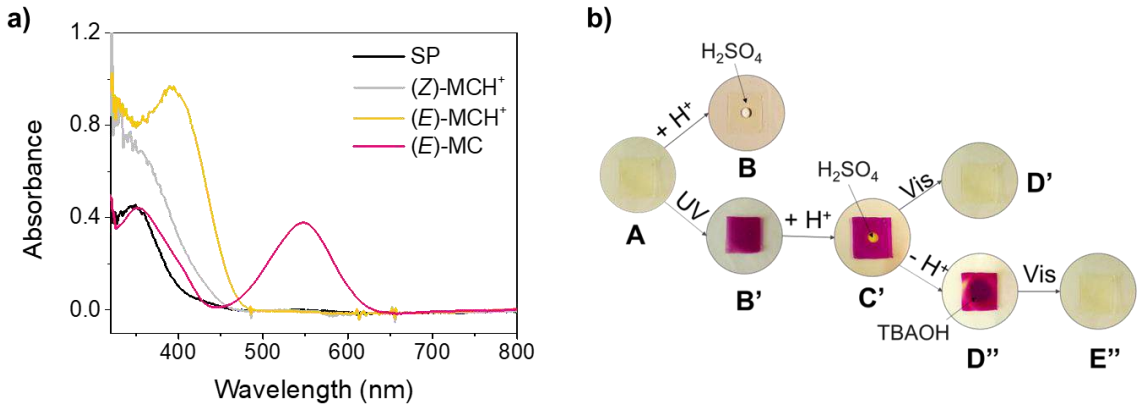

Figure 3.15. a) UV-Vis absorption spectra corresponding to NO_2BIPS@IG membranes under light and pH variations. b) Images of membranes after exposure to light, pH changes or combinations of both. A droplet of a diluted solution of H_2SO_4 (10 mM) was used to decrease the pH. Meanwhile, a diluted solution of tetrabutylammonium hydroxide (TBAOH, 10 mM) was prepared and used to recover pH neutrality.

An additional experiment was performed to confirm the previous mechanism qualitatively, which illustrated in Figure 3.15. b). As shown, the membrane was initially transparent (A), even after the addition of a droplet of diluted sulfuric acid solution (B) in the center. After irradiation with UV light, the membrane acquired an intense pink color (B'), except for the acid-contact region, which turned yellow (C'). The membrane returned to its initial transparent coloration either after direct irradiation with visible light (D') or after incubation with a basic solution (D'') and visible light irradiation (E''). It is important to remark that prolonged acid-base cycles led to the chemical degradation of the membranes, possibly due to a Hofmann elimination of the quaternary ammonium of N_{1114} TFSI.

On the other hand, the thermochromic behavior of NO_2BIPS molecules was also investigated in solution and in NO_2BIPS@IG membranes. When heating the compound above 29°C, a gradual color change was observed from colorless to intense pink colored, with absorptions bands close to λ_{abs}=550 nm. Concretely, NO_2BIPS@IG membranes presented an absorption band located at λ_{abs}=552 nm, which slightly differed from those obtained with the same sample after photoisomerization (λ_{abs}=548 nm). Figure 3.16. This discrepancy was associated to the formation of different stereoisomers through the two mechanisms.

Thermochromism reached a maximum absorption value at 45 °C, with thermochromic efficiencies of 4% and 5% in solution and in membranes, respectively. This result suggested a better stabilization of the MC isomer when induced by UV light.

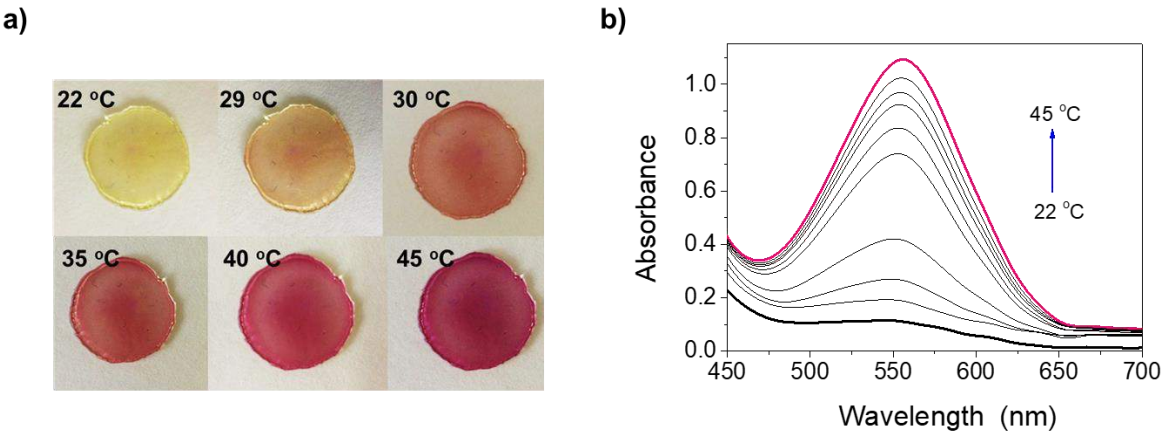

Figure 3.16. a) Images of NO_2BIPS@IG membranes at different temperatures. b) UV-Vis absorption spectra of NO_2BIPS@IG membranes. An increase at λ_{abs}=552 nm when increasing the temperature is observed due to the formation of MC isomer.

The reversibility of thermochromism was also demonstrated since the samples recovered their transparency after cooling down by the formation of the initial SP isomer. Thermal cycles also demonstrated the stability of the sample, without apparent degradation of either the NO_2BIPS compound or the IG membrane.

As a result, these resulted confirmed that it was possible to produce low-cost photo- halo- and thermochromic materials based on spiropyrans for smart sensing, labeling, and packaging, among other applications.

iii. Electrochromism of NO_2BIPS@IG membranes

Response upon oxidation potential

Although already demonstrated, the electrochromic properties of spiropyrans have received less attention than previous photo-, halo- or thermos-chromic properties. As a result, there is a lack of understanding of the electrochromic mechanisms of these compounds, which limits their implementation in redox-induced solid-state materials and systems.

Regarding to the latter, we explored the electrochromic and electrochemical characteristics of NO_2BIPS@IG membranes on the basis of previous results obtained by Browne et al. concerning NO_2BIPS redox-response in solution. According to them, electrochromic properties of NO_2BIPS resulted from the dimerization of the compound after oxidation [22–24].

The anodic response of NO_2BIPS@IG membranes after CV analysis is illustrated in Figure 3.17. a). The compound presented initially a peak at 0.95 V (vs Ag/AgCl), which decreased with the consecutives CV cycles, resulting in two new peaks at 0.77 and 1.10 V (vs Ag/AgCl). Based on the studies in solutions, the initial anodic peak at 0.95 V may be related to the electrochemical oxidation of the amino groups of the indoline moiety. The appearance of the two new oxidation peaks at 0.77 and 1.10 V (vs Ag/AgCl) may be associated with the dimerization reaction (Figure 3.17. b)) for two reasons. On the one hand, the peak positions agreed with the formation of the radical cation (0.77V) and the dication (1.10V) of the dimeric form, respectively. On the other hand, the oxidation signals magnitude was half of that recorded with the monomer, which coincided with what expected in a dimerization process.

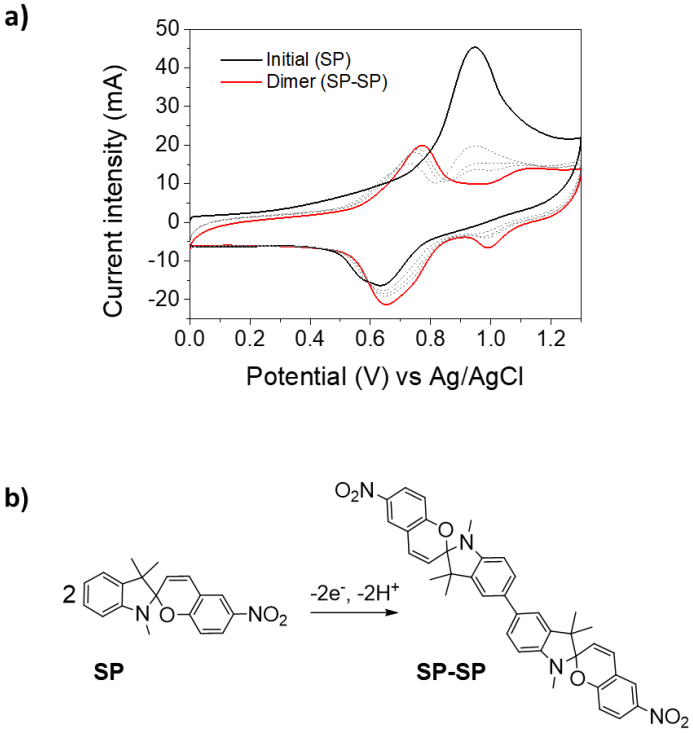

Figure 3.17. a) CV of NO_2BIPS@IG membranes recorded at 20 $mV \cdot s^{-1}$. After 30 consecutive cycles, the initial peak located at 0.95 V (vs Ag/AgCl) decreases (solid black line) and there are two new ones due to the formation of SP-SP (solid red line). Dashed lines correspond to the intermediate voltammograms. b) Dimerization reaction that occurs when the sample is oxidized.

These results confirmed the possibility to directly transfer the electrochemical features of NO_2BIPS from solution into solid-state materials. However, IG materials may promote SP electrodimerization in ways not possible in solution, which may benefit their electrical performance. Hence, two main processes may contribute to SP dimerization,

namely i) the decrease in NO_2BIPS diffusion into IG membranes, which may benefit the reactivity between neighboring SP radical cations; and ii) the increase in stability of radical cation species in the IG by solvation.

It is also worth noting that the electrochemical dimerization of NO_2BIPS in IG was accompanied by a color change resulting from the structural changes produced in NO_2BIPS molecules. Electrochromic properties of these membranes were studied using UV-Vis spectroelectrochemistry.

When applying 1.20 V (vs Ag/AgCl), the electrochemical dimerization of NO_2BIPS caused a noticeable color change to reddish-orange. This observation was associated to two different processes, taking place consecutively. First, the most thermodinamically stable form of NO_2BIPS, the SP isomer, was oxidized and dimerized in SP-SP molecules. In a second step, SP-SP molecules were overoxidized at high potential (>1.10 V vs Ag/AgCl) to the corresponding dication $[SP\text{-}SP]^{2+}$. The formation of the dication was confirmed spectroelectrochemically through the presence of two absorbance bands at λ_{abs}=416 and 500 nm when applying 1.20 V (vs Ag/AgCl), which corresponded to $[SP\text{-}SP]^{2+}$. The following parameters related to the electrochromism of the dimerization process were determined at λ_{abs}=500 nm: i) a large color contrast of ΔT = 90%; ii) a long response time of t_a = 125 s, most likely due to limited diffusion in membranes, which minimize molecular interactions required for dimerization; and iii) an electrochromic efficiency of η = 245.9 $cm^2 \cdot mC^{-1}$.

The dimerization process was irreversible, and a permanent coloration was observed in the membrane in the area where the electric potential was applied, as expected by a compound with electrochromism 'with memory'. However, the $[SP\text{-}SP]^{2+}$ dimer presented a reversible two-step reduction process, where it was reduced first to the corresponding radical cation $[SP\text{-}SP]^{\bullet+}$, and then to the neutral [SP-SP] form, when applying 0.2 V (vs Ag/AgCl). These reversible reductions revealed consecutive color changes from reddish ($[SP\text{-}SP]^{2+}$), orange ($[SP\text{-}SP]^{\bullet+}$) to yellow ([SP-SP]). This observation agreed with spectrochemical analysis, where the following absorption bands at λ_{abs} = 360 and 473 nm, corresponding to the $[SP\text{-}SP]^{\bullet+}$, and at λ_{abs} = 385 and 984 nm, associated to the [SP-SP], were obtained. The near-IR band may correspond to charge transfers with the dication and monocation species.

The color contrast estimated for the reduction of $[SP\text{-}SP]^{2+}$ to the neutral form [SP-SP] was ΔT = 47%, which lower than before by the overlapping of the absorbance peaks corresponding to $[SP\text{-}SP]^{2+}$ and [SP-SP] species. The reduction had a shorter

response time of t_c = 60.4 s since not requiring the interaction of different molecules. Figure 3.18. a). After subsequent cycles of oxidation (E_{app} = 1.20 V (vs Ag/AgCl)) and reduction (E_{app} = 0.20 V (vs Ag/AgCl)), the response remained fairly stable when measuring the absorbance at λ_{abs} = 500 nm. Figure 3.18. b).

It should be concluded that, although the dimerization process was irreversible and should be classified as electrochromism 'with memory', the dimer itself presented a reversible electrochromic response corresponding to 'true' electrochromism'.

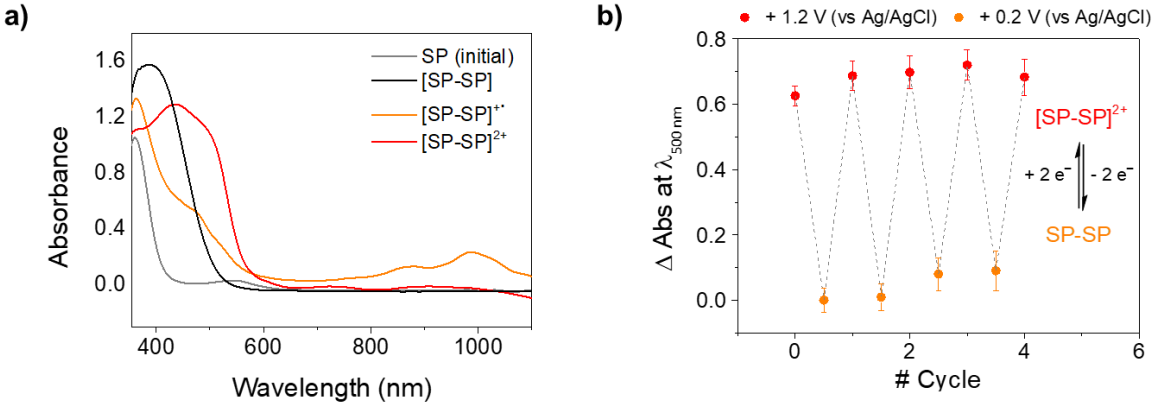

Figure 3.18. a) UV-Vis absorption spectra of initial SP monomer and the dimer in its various oxidation states: SP-SP, $[SP\text{-}SP]^{\bullet+}$, $[SP\text{-}SP]^{2+}$. b) Reversible electrochromism of the dimer upon consecutive oxidation (at 1.20 V (vs Ag/AgCl)) and reduction (at 0.20 V (vs Ag/AgCl)) cycles.

Response to reduction potential

Apart from the previous electrochromic response to oxidation potentials, spiropyran monomers are also susceptible to electrochemical reduction. The reduction potential is, in this case, very dependent on the donor character of the functional groups in the molecule, and in their positions. These groups also affect the stability of the reduction intermediates, giving rise to different reaction mechanisms. It is known, for example, that the substitution of spiropyrans with an electrowithdrawing group at the 6' position in the benzopyran moiety is crucial for the stabilization of the phenolate group of the MC form and its half-life. This is the case of NO_2BIPS, which presents a nitro electrowithdrawing group at the 6' position. In this case, the ring-opening and the formation of the colored MC form is the preferred reduction mechanism. This obviously improves the photoelectrochromic characteristics of the compound [25–27]. Moreover, the -NO_2 substituent is particularly interesting since it can be reduced at relatively low applied potentials.

Although it is known that NO_2BIPS derivatives can undergo ring-opening and access the MC form through electrical stimuli, the reduction mechanism is still controversial, which limits the use of these compounds in electrochromic applications. Considering that, a preliminary study in solution conducted aiming to clarify the process involved in the electrochromic response of NO_2BIPS molecules.

The electrochemical behavior of the compound was studied by CV. Figure 3.19. a). No faradaic currents were detected in the first anodic sweep recorded from 0.0 V to 0.60 V (vs SCE). Subsequent cathodic scan from 0.60 to -1.30 V (vs SCE) presented a reduction peak at relatively low potentials of $E_{pc,1}$ = -1.23 V vs SCE. This one-electrode pseudo reversible cathodic peak (ΔEp ≈ 56 mV) was associated to the reduction of the closed SP form, i.e., the most thermodynamically stable, to the [$SP^{\bullet -}$] radical anion. The reverse oxidation peak observed at $E_{pa,1}$= -1.10 V (vs SCE) corresponded to the oxidation of [$SP^{\bullet -}$] to SP. Apart from that, two new peaks appeared at $E_{pa,2}$= 0.19 and $E_{pa,3}$ = 0.47 V (vs SCE), which will be discussed above in this section.

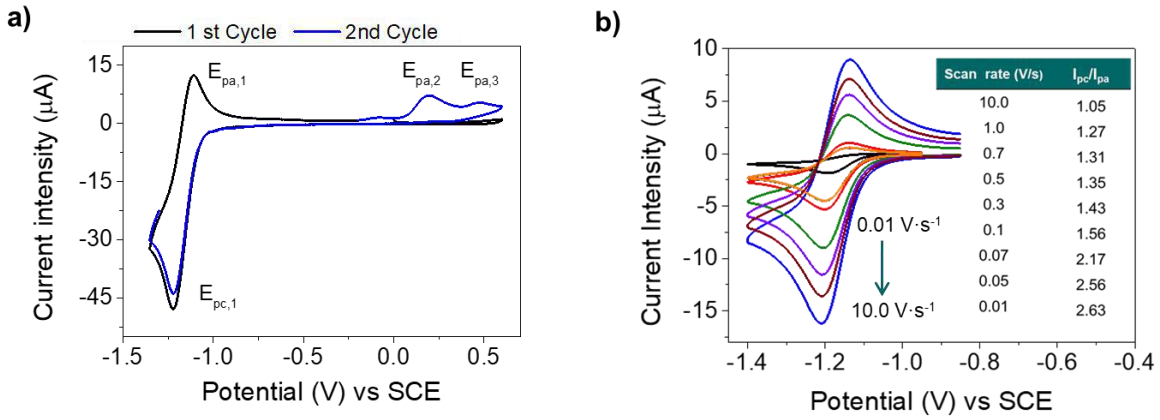

Figure 3.19. a) CV of 5 mM NO_2BIPS solution in acetonitrile (ACN) and 0.1 M of $TBAPF_6$ as supporting electrolyte. Scan rate 0.5 $V \cdot s^{-1}$. b) Study of the reduction peak at different scan rates (from 0.01 to 10 $V \cdot s^{-1}$).

The anodic and cathodic current intensities increased linearly with the square root of the scan, confirming that (i) the electrochemical reduction of NO_2BIPS was a diffusion-controlled process; and (ii) no adsorption occurred on the electrode surface. Figure 3.19 b). The reversibility of the oxidation-reduction process between SP and [$SP^{\bullet -}$] was determined by comparing the cathodic (I_{pc}) and the anodic peak current values (I_{pa}) at several scan rates. Results in Figure 3.19 b) show how the ratio I_{pc}/ I_{pa} ratio decreased when increasing the scan rate up to values close to 1 at scan rates above 10 $V \cdot s^{-1}$. Thus, the reduction electron transfer of NO_2BIPS became totally reversible at fast scan rates,

meaning that the $SP^{\bullet-}$ generated on the electrode surface was completely oxidized to SP in the reverse anodic scan. Considering the peak width ($\Delta Ep \approx 56$ mV) and the independence of the cathodic peak potential on the specie concentration, it was concluded that the electron transfer reaction was of first order. Based on these results, an EC mechanism with a fast one-electron transfer step (E) followed by a homogeneous and irreversible chemical reaction (C) was proposed for the electrochemical reduction of NO_2BIPS. Scheme 3.1. Considering that, it was possible to determine the value of the kinetic constant of the electron-transfer chemical reaction, obtaining a value of k = 0.003 s^{-1}.

In order to evaluate the viability of the proposed mechanism, theoretical calculations of the stability of the SP and MC neutral and radical anion forms were performed. As expected, the calculations revealed that the SP isomer was the most stable form in ACN (0.6 kcal mol^{-1}). Interestingly, the MC radical anion ($MC^{\bullet-}$) form was 3 kcal mol^{-1} more stable than the corresponding SP radical anion ($SP^{\bullet-}$). According to these results, it may be concluded that the most plausible mechanisms for the reduction reaction was an isomerization. Scheme 3.1.

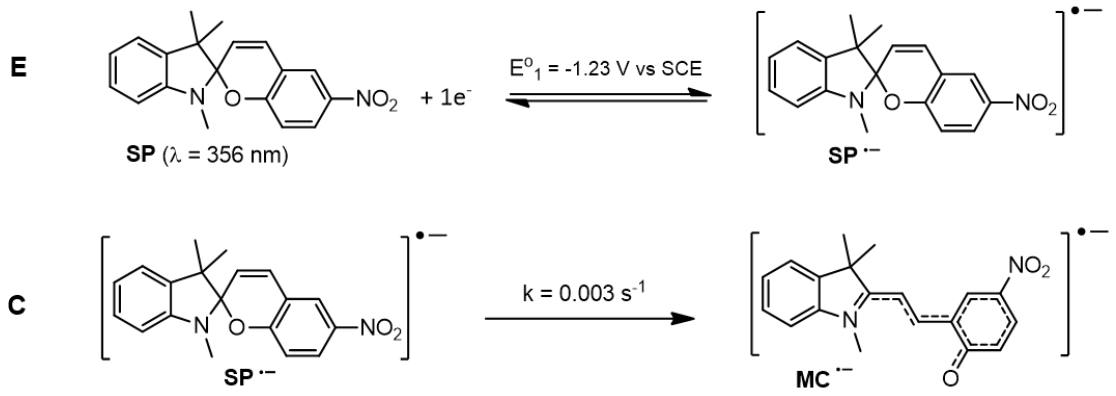

Scheme 3.1. Mechanism proposed for the electrochemical reduction of NO_2BIPS in solution.

Chemical analysis of the species involved in the reaction required the isolation and purification of the product. To this end, a 30 mM solution of the compound was electrolyzed at -1.30 V (versus SCE) in ACN 0.1 M $TBAPF_6$ and in an inert atmosphere. After the passage of 1 F, the electrochemical reaction was considered completed, and a dimeric product (P) was successfully isolated and analyzed by different chemical techniques, including CV, proton nuclear magnetic resonance spectroscopy (^{1}H-NMR); high-resolution electrospray ionization mass spectrometry (ESI-MS) and Attenuated Total Reflectance Infrared Spectroscopy (ATR-IR).

ATR-IR spectra corresponding to the starting reagent and the formed dimer (P) were comparable due the high structural similarity of both compounds. Main differences between them were: (i) in the 1657 cm^{-1} peak corresponding to the vibrational stretching of the olefinic carbons, which disappeared after the formation P; and (ii) in the 976 cm^{-1} corresponding to the O-C-N stretching mode peak, which shift in the P dimer due to the opening of the structure.

ESI-MS revealed the exact mass of the new chemical species, i.e., M^+ nNa= 669.2661, which was compatible with two NO_2BIPS units. This confirmed that the P was a dimer, where hydrogenated olefinic carbons due to the exposure of the sample to longer electrolysis times and large charge amounts.

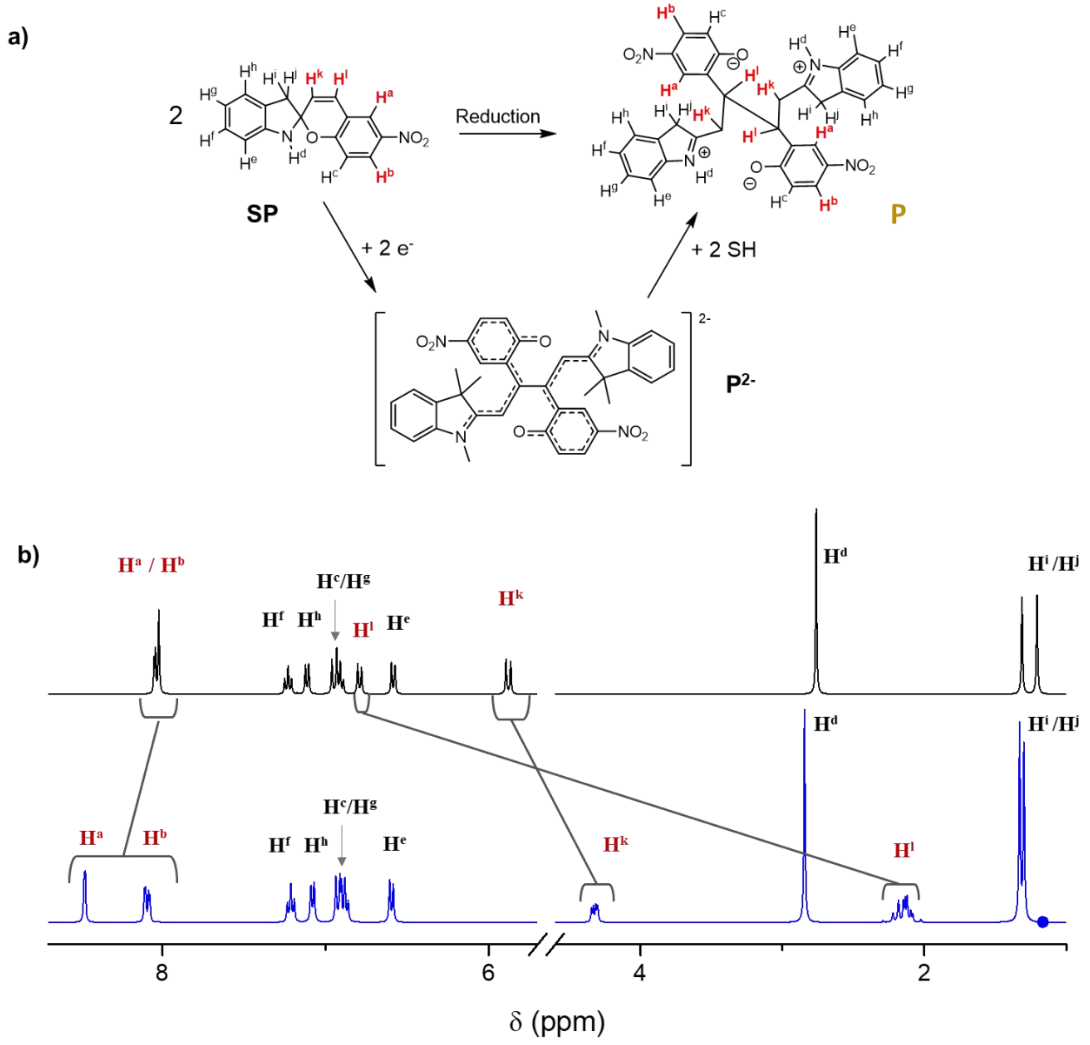

Figure 3.20. a) Mechanism of the electrochemical reduction proposed and the hypothetical intermediate b) ^{1}H NMR spectrum (360 MHz, in $CDCl_3$ of initial NO2BIPS in the SP form (black spectra) and product P electrochemically synthetized and purified (blue spectra). Labels in red correspond to proton signals that presented larger shifts before and after electrochemical reduction.

Regarding the electrochemical response of P, and as already observed by cyclic voltammetry, two new oxidation peaks located at $E_{pa,2}$= 0.19 and $E_{pa,3}$= 0.47 V (vs SCE) appeared during the electrosynthetic process, whereas the peak current value of the first reduction peak diminishes to 50% after the passage of 1 F ($C \cdot mol^{-1}$). Figure 3.21. The presence of the two new oxidation peaks at low potential was associated to the oxidation of a phenolate moiety, which supported the information previously detailed.

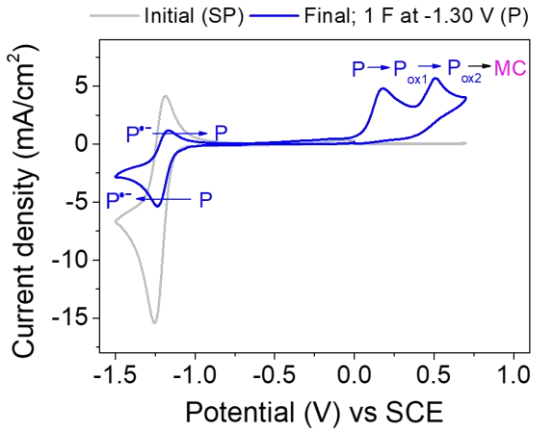

Figure 3.21. CV of a solution 30 mM of NO_2BIPS in its initial SP form and the dimeric product (P) obtained after the reduction of SP and purification. The CV was registered using ACN 0.1 M $TBAPF_6$ as solvent at a scan rate of 0.1 $V \cdot s^{-1}$

Spectroelectrochemical studies were performed aiming to resolve the electrochemical reduction mechanism and to confirm the existence of P. The latter was sustained on the fact that P was responsible for the anodic peaks at $E_{pa,2}$ = 0.19 and $E_{pa,3}$ = 0.47 V (vs SCE) after the ET of the SP form in the CVs..The results showed a significant increase in the absorbance at λ_{max} = 426 nm (yellow color) at reduction potentials slightly higher than $E_{pc,1}$ = - 1.23 V, (E_{app} = - 1.30 V (vs SCE)). The appearance of this band was in good agreement with the formation of a dimeric product, $P^{\bullet -}$, with an electronic resonance in the 4-nitrophenolate moiety (λ_{max} = 400 nm for 4-nitrophenolate) [28]. Considering that, the previous oxidation peaks at $E_{pa,2}$ = 0.19 and $E_{pa,3}$ = 0.47 V (vs SCE) was associated to the oxidation of the two phenolate moieties present in the P since similar to the electrochemical response of pure 4-nitrophenate derivatives in the same conditions [29,30]. Figure 3.22.

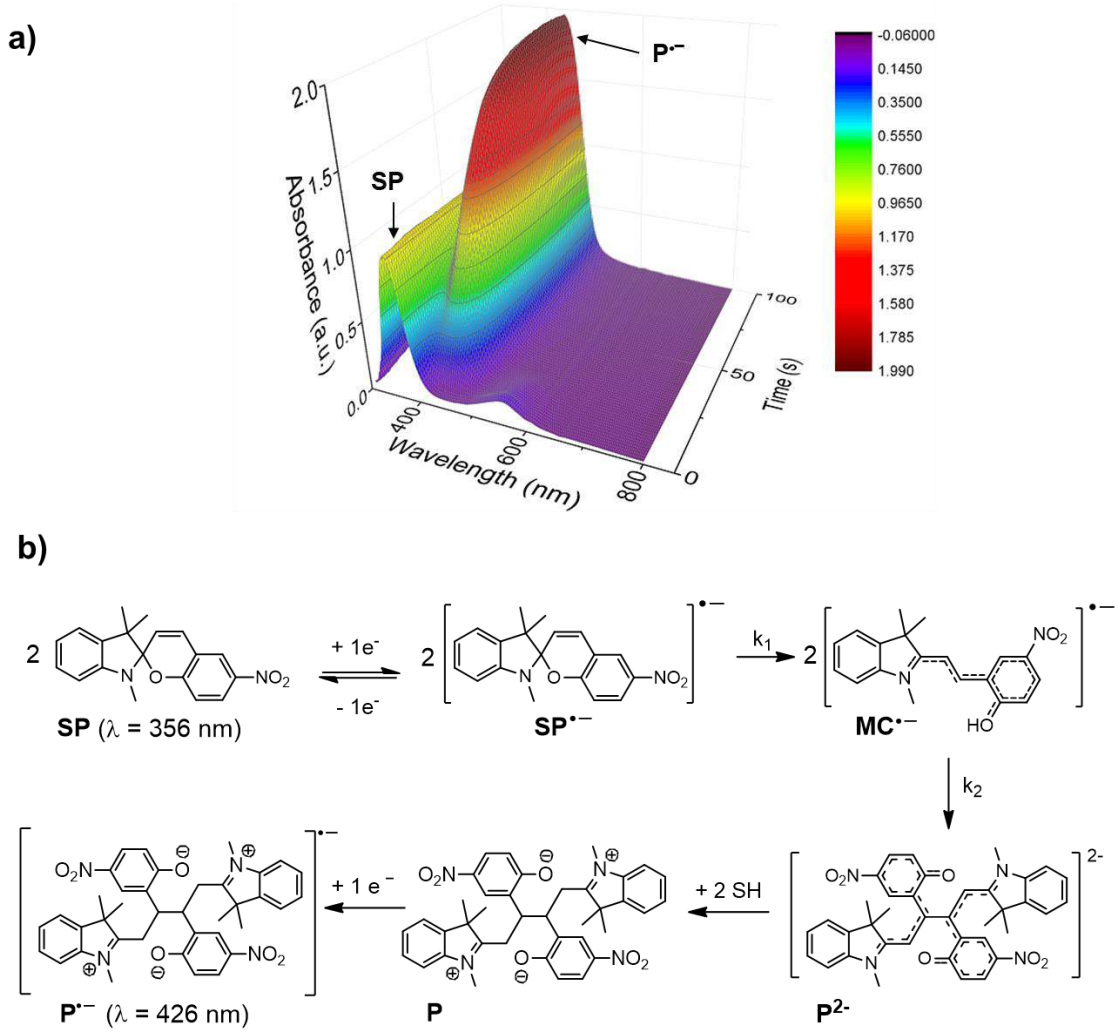

Figure 3.22. a) Spectroelectrochemistry of 0.5 mM NO_2BIPS solution in ACN 0.1 M $TBAPF_6$ in its initial form SP (λ_{max} = 346). Initially, no potential is applied but after 5 seconds there is a reduction potential of E_{app} = - 1.30 V (vs SCE), a large increase at λ_{max} = 426 nm because of the formation of $P^{\bullet-}$.

The previous results were confirmed by B3LYP-D3 calculations in ACN and at room temperature. The coupling reaction between the two spiropyran units at the merocyanine radical anion ($MC^{\bullet-}$) was favored by the spin density in the 6-carbon ring. Thus, the two open NO_2BIPS anion radical units (in the merocyaninic form) would couple by making a σ-bond in the olefinic C4, being separated by a distance of 3 Å. Thus, the reduction of SP provoked the $C_{(spiro)}$-O bond cleavage, leading to the formation of $MC^{\bullet-}$ that evolved to the formation of P^{2-}, which would present an open structure merocyanine-type isomer. This meant that, prior to dimerization, there was a ring-opening of the spiropyran units. Note that there were precedents in similar π-delocalized systems, where two radical anions reacted leading to a doubly charged σ-bonded dimeric species [31–33] After the

dimerization, the abstraction of a hydrogen atom from the solvent would take place, leading to the product P.

Spectroelectrochemical analyses were completed by coupling an oxidation reaction to the NO_2BIPS reduction. The study revealed the existence of a new compound, i.e., MC, with purple coloration and an absorption band at 555 nm that appeared when the $P^{\bullet -}$ was oxidized with positive potentials above 0.8 V. Figure 3.23 a). Conversely, no spectrochemical or electrochemical changes were observed when applying E_{app} = +0.30 V. To demonstrate the reversibility between states, 5 successive reduction-oxidation cycles were applied consisting of 20 s of reduction at -1.30 V followed by 30 s of oxidation at +0.8 V, while monitoring absorbance at λ_{abs} = 426 nm (corresponding to the maximum wavelength for the dimer $P^{\bullet -}$). Results presented in Figure 3.23. c). demonstrated the reversibility of the system in the conversion from $P^{\bullet -}$ to MC. It was also evident, therefore, that the direct conversion from SP to MC upon two-step electric input was not possible, but it required the formation of the yellow dimer intermediate (P).

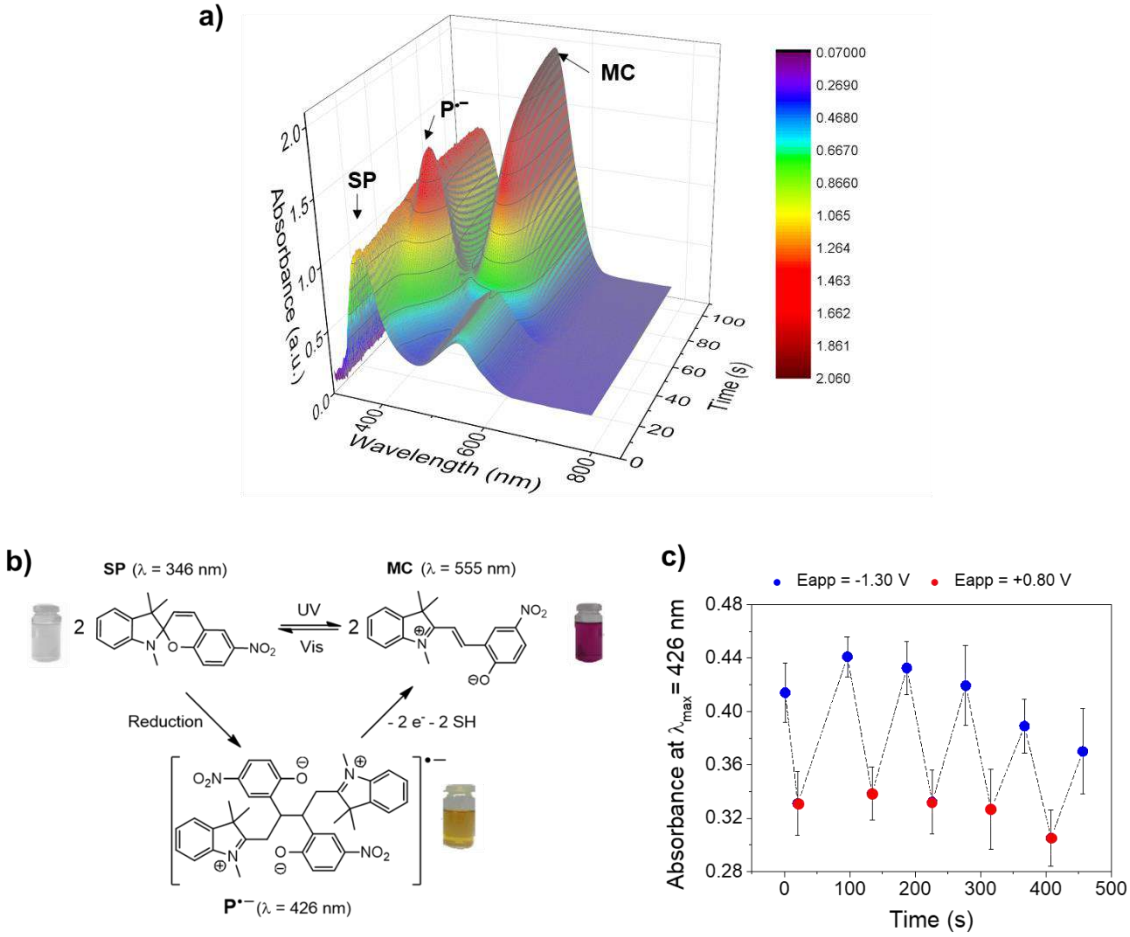

Figure 3.23. a) Spectroelectrochemistry of a 0.5 mM NO_2BIPS solution in ACN 0.1 M $TBAPF_6$ in its initial form SP (λ_{max} = 346). As previously demonstrated, after applying a constant potential of E_{app}= -1.30 V (vs SCE) an increase at λ_{abs}= 426 nm is observed as a result of the formation of P^{2-}. Next, an oxidation potential was applied, E_{app}= + 0.80 V (vs SCE), and an increase in absorption at λ_{abs}= 555 nm was recorded due to the formation of the MC form. b) Mechanisms proposed for the photoelectrochromic NO_2BIPS system in ACN. c) Fatigue resistance when applying successive potentials at E_{app}= -1.30 V and E_{app}= +0.80 V (vs SCE) for 40 s each

These results pave the way to the production of reversible photoelectrochemical devices based on one of the most studied SP compounds. To do so, the NO_2BIPS compound was incorporated into an IG matrix (NO_2BIPS@IG) and the spectroelectrochemical behavior of the solid-state system was compared with that initially observed in solution.

Analogously to what was observed in solution, the NO_2BIPS@IG membranes were initially transparent, with an absorbance band at the UV region, i.e., λ_{abs} = 358 nm. After applying a reduction potential of E_{app} = -1.30 V (vs SCE), the membrane became yellow

in the area in contact with the electrode, with an absorbance band at λ_{abs} = 440 nm that corresponded to the formation of the dimeric intermediate $P^{\bullet -}$. Figure 3.24.

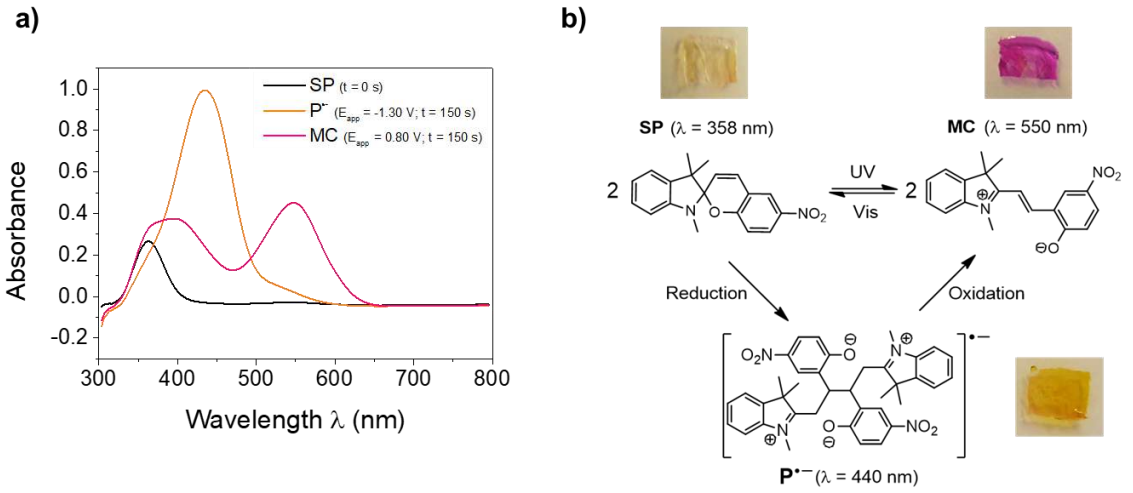

Figure 3.24. a) UV-Vis absorption spectra of NO_2BIPS@IG membranes corresponding to the different forms involved in the photoelectrochromic cycle (SP, MC and $P^{\bullet -}$). b) Photoelectrochromic reactions and the appearance of NO_2BIPS@IG membranes depending on the stimuli applied.

The subsequent oxidation of $P^{\bullet -}$ at E_{app} = 0.80 V (vs. SCE) for 150 s resulted in the emergence of a pink color with an absorbance band at λ_{abs} = 550 nm corresponding to the MC form. The membrane recovered its initial colorless state after exposition to visible light.

Overall, it can be concluded that apart from the photo- halo- and thermochromic properties of NO_2BIPS, a two-step electrical input (1st reduction, 2nd oxidation) can be used to access the ring-open structure (MC) of NO_2BIPS derivative either in solution or in IG membranes. The process is fully reversible since it is possible to obtain the initial isomer (SP) with light, closing the photoelectrochromic cycle. It has been also demonstrated that, with an oxidation input, it is possible to produce a dimer presenting electrochromism with memory, which, in turn, gives access to a new family of photoelectrochromes. Additionally, this isomer can be reversibly oxidized to structures with different oxidation states and therefore, presenting 'real' electrochromism. Figure 3.25. summarizes the different responsiveness of NO_2BIPS discovered in IG membranes.

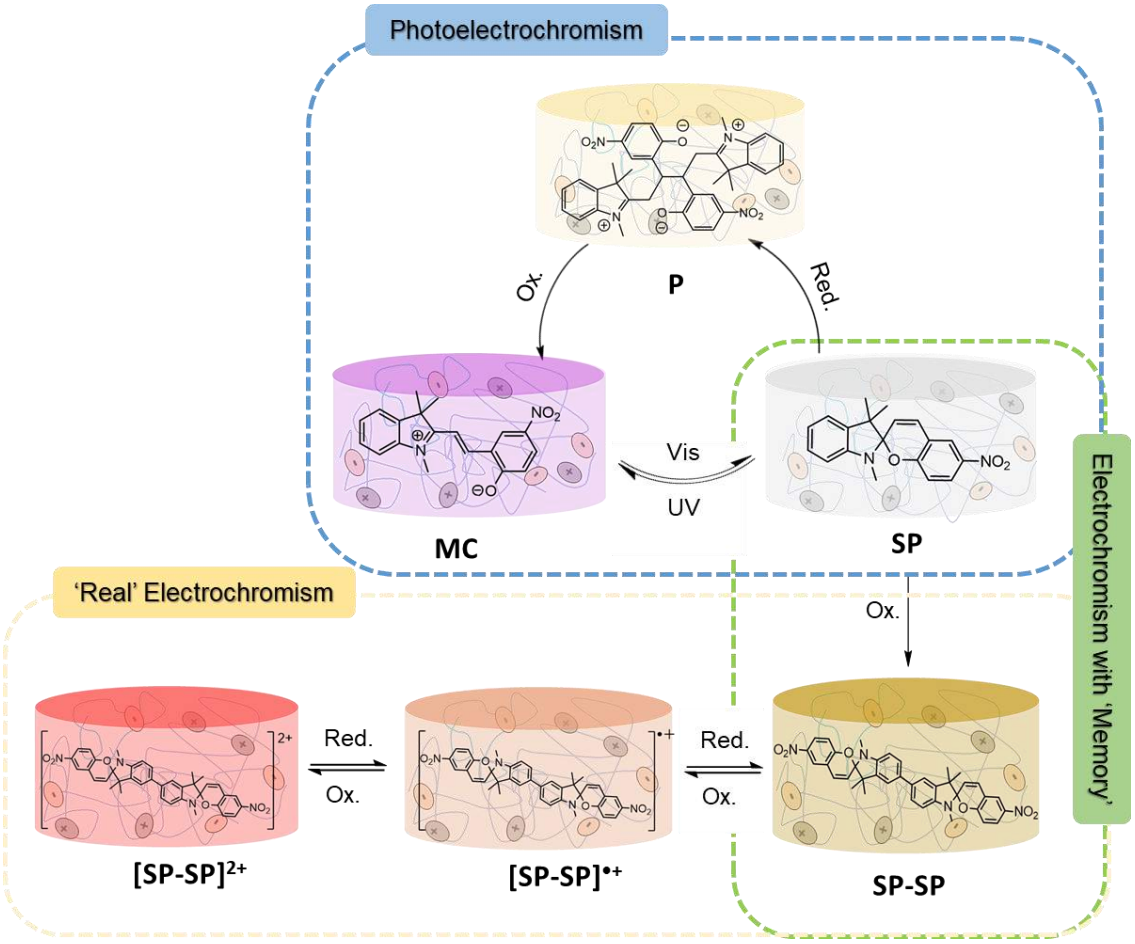

Figure 3.25. Summary of the responsiveness of NO_2BIPS@IG membranes obtained.

Despite the advantages offered by electrical stimuli, this property has not been fully exploited in the development of electrochromic devices. Considering that, electrochromic devices operating with electrical stimuli are presented below as a proof of concept, aiming to elucidate their potential for large-scale manufacture.

iv. Device production as proof-of concept

As proof of concept, a simple microfluidic system based on NO_2BIPS@IG membranes was constructed in order to demonstrate the feasibility of multi-responsiveness in practical applications. Figure 3.26. The devices consisted of four compartments where individual NO_2BIPS@IG membranes with complex shapes were implemented in a way that each membrane could be subjected to independent stimuli of different nature.

The 'U' shaped membrane was stimulated thermically by infusion of a hot liquid at T= 40 ºC, resulting in a change of color from uncolored to pink. The 'A' and the 'B' shaped membranes were stimulated optically with UV-light, but the first one was previously incubated with an acidic solution. After UV-light irradiation, 'A'- and the 'B'-shaped membranes developed yellow and pink colors, respectively. Additionally, a small square was cut to demonstrate the electrochromism of NO_2BIPS@IG. In this case, the membrane was placed on the Pt electrode and an irreversible reddish color was achieved after applying +1.0 V vs Pt. Figure 3.26. a).

A second device was manufactured to demonstrate the outstanding elastic and flexible properties of NO_2BIPS@IG membranes. In this case, the device consisted of a single compartment containing an ITO coated PET screen-printed electrode for electrochromic assays, and a fluidic channel, with the inlet and the outlet, for the infusion of solutions, in this case acid-base solutions to check halochromism or hot water for thermochromic analysis. With this device, it was possible to verify the response of the material to an oxidation stimulus, i.e., the formation of the dimer (SP-SP) and its different oxidation states ($[SP\text{-}SP]^{\bullet+}$ and $[SP\text{-}SP]^{2+}$), as well as the corresponding color changes (intense yellow, orange, red). Figure 3.26. b).

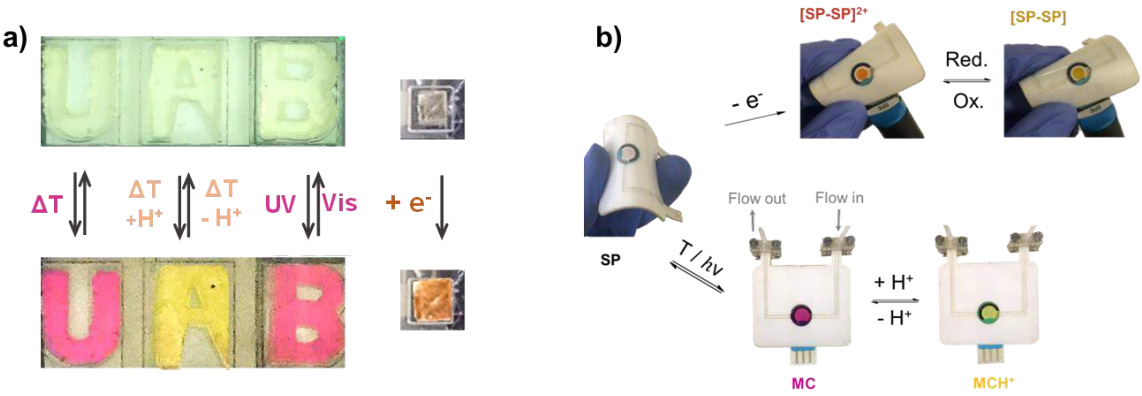

Figure 3.26. a) Multistimuli device with different compartments to compare the different responses to various stimuli (temperature, pH, light and electricity) b) Flexible display containing a three-electrode system and a channel to pass solutions of different acidity and temperature.

To test the photoelectrochromic properties through the application of a reduction potential to NO_2BIPS@IG membranes, a two-electrode system was constructed with transparent ITO-coated PET electrodes. The IG membrane containing NO_2BIPS was placed in between the electrodes for optimal electrical stimulus. Additionally, the IG membrane was doped with TEMPO (2,2,6,6-Tetramethylpiperidin-1-yl)oxyl), which used

as redox mediator to reduce the required redox potential of the system. TEMPO was uncolored and did not interfere the color change in the membrane caused by the NO_2BIPS molecules.

After the application of ΔE = 2 V, a color change was observed due to the reduction of SP and its subsequent oxidation by means of the TEMPO intermediate. Hence, when the right potential was applied, the MC form was obtained, which could be converted to the initial form through exposure with visible light. Figure 3.27

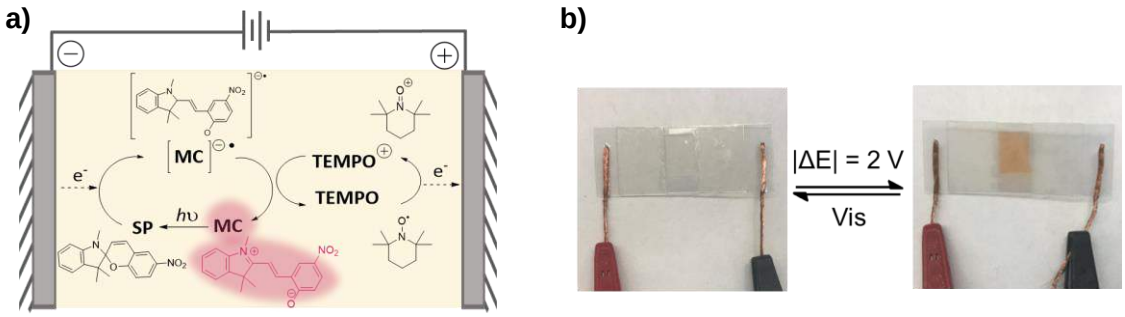

Figure 3.27. a) Schematic representation of the mode of operation and the reactions involved in the manufactured photoelectrochromic device. B) Photographs taken when the potential difference is applied (colored) and after irradiation with visible light (colorless).

3.3.2. Electrochemical carboxylation of bromo spiropyran (Br-BIPS)

The results discussed in this section correspond to our recent publication: *ChemElectroChem* **2022**, *9*.

Covalent bonding is a common method used in chemical functionalization of surfaces or materials to confer them or modify their intrinsic physic-chemical properties. Although this type of modification results in more stable and durable molecular immobilizations, covalent bonding is more complex and expensive than other alternatives. For example, the chemical incorporation of carboxylic functional groups or any of their derivatives (such as amides and esters), requires many synthetic steps, the use of multiple reagents, catalysts, organolithium compounds and mild-strong conditions, which results in moderate yields.

In an attempt to improve the reaction yields through a greener functionalization route, this section will explore an alternative mechanism for the functionalization of the spiropyran 1,3,3-trimethylindoline derivative, -6'-bromobenzopyrylospiran (Br-BIPS)

derived from previous experiences of the group on electrocarboxylation of aryl halide-type compounds.

One of the most used mechanisms for electrocarboxylation of organic compounds consists of the formation of a carbanion by electrochemical reduction of the compound, and the subsequent nucleophilic attack of this specie to a CO_2 molecule to produce the final carboxyl addition. Figure 3.28.

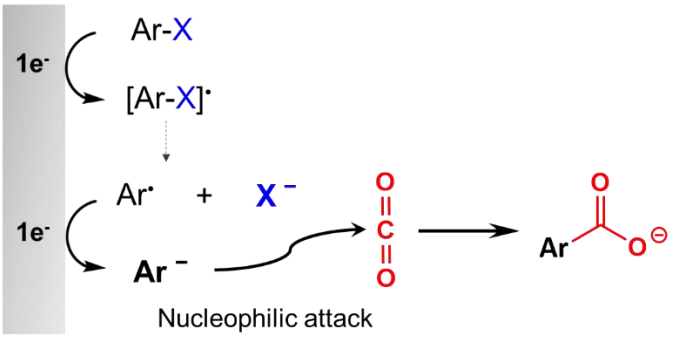

Figure 3.28. Schematic representation of generic electrocarboxylation processes in aryl halide organic compounds

The stability (lifetime) of the carbanion is essential to keep the reaction active and to obtain acceptable yields. Since carbanion stability is widely improved when applying low reduction potential, species with low reduction potentials, including aryl halides, are frequently chosen as first option. Alternatively, the use of various cathodes of materials with electrocatalytic properties like silver, also enables to reduce the applied potential.

Based on the previous statements, voltammetric studies of Br-BIPS in DMF and 0.1M $TBAPF_6$ were conducted using either glassy carbon (WE_C) or silver (WE_{Ag}) as WE to evaluate the electrochemical behavior of the compound. With WE_C, two ETs were observed at E_{pc} = -2.23 V (vs SCE) and E_{pc} = -2.47 V (vs SCE) related to the two-electron and one-electron reduction of Br-BIPS, respectively. Figure 3.29. a). In the case of WE_{Ag}, a single reduction peak at E_{pc} = -1.92 V (vs SCE), which shifted towards fewer negatives (280 mV) due to the electrocatalytic effect of the cathode. Figure 3.29. b).

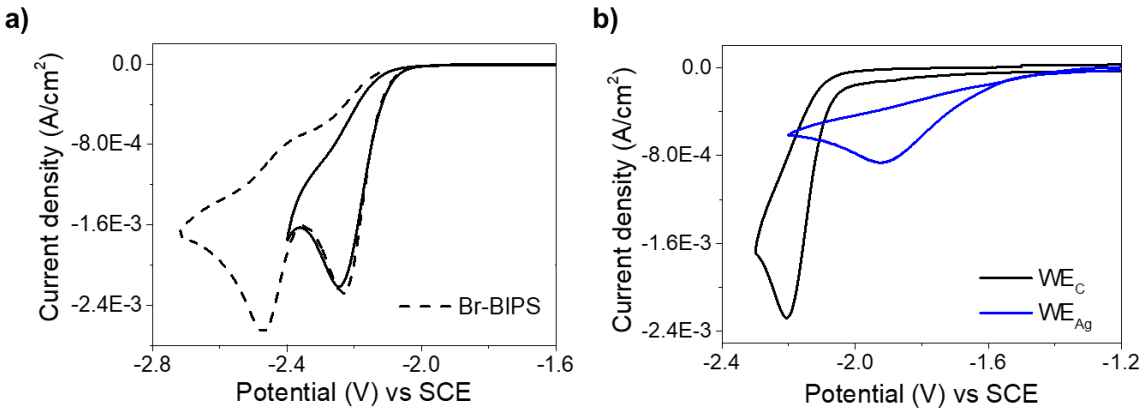

Figure 3.29. Voltammogram recorded at 0.1 $V \cdot s^{-1}$ for 5 mM Br-BIPS in DMF 0.1 M $TBAPF_6$. a) Comparative electrochemical behavior observed when using WE_C (solid black line) and WE_{Ag} (solid blue line). b) First and second ET recorded using WE_C

The irreversibility observed when using WE_C indicated the existence of a second chemical reaction coupled to the first ET. To evaluate that, voltammetric studies of this first ET were performed at different scan rates and concentrations. The experimental results showed that: i) it was a linear relationship between E_{pc} vs log v with a slope of 35 mV; and ii) the E_{pc} did not vary with the concentration. Both results confirmed that the reaction mechanism consisted of an electron transfer followed by a first kinetic order chemical reaction.

Besides, bulk electrolysis was performed under Ar at the applied potentials just before the first ET (E_{app} = -2.35 V for WE_C and -2.00 V for WE_{Ag} (vs SCE)) and monitored by CV to determine the nature of the chemical species generated after the first reduction. After the passage of 2 F, an anodic peak appeared and increased at E_{pa} ~ +0.70 V (vs SCE), which was associated to Br^- released during the debromination of Br-BIPS. After chemical analysis of the electrolysis products, it was concluded that the product corresponded to the debrominated spiropyran, BIPS, which obtained at 56% and 91% yields when using carbon graphite and silver cathode, respectively.

The one-electron reduction peak at -2.47 V (vs SCE) was then assigned to pure BIPS since matching the reduction peak of this compound (-2.50 V (vs SCE)) and the ET at -2.23 V vs (SCE) was ascribed to the C-Br breakage of Br-BIPS by means of an ECE mechanism. This mechanism involve the following steps: i) reduction of the Br-BIPS to the corresponding radical cation ($[Br\text{-}BIPS]^{\bullet -}$) (E); ii) first order chemical reaction related to the breakage of a C-Br bond (C), resulting in the formation of the neutral radical cation $[BIPS]^{\bullet}$ and free Br^-; iii) second reduction of the $[BIPS]^{\bullet}$ to produce the anionic form

$[BIPS]^-$ (E) thanks to the more positive potential of this second electron transfer reaction ($E_1^o < E_2^o$); iv) protonation of the $[BIPS]^-$, by subtracting the proton from either the solvent or the supporting electrolyte, to produce the final product, i.e., BIPS.

Once the mechanism was investigated and confirmed the generation of $[BIPS]^-$ during the reduction of Br-BIPS in an Ar atmosphere, the atmosphere was saturated with CO_2 and the same procedure was carried out to evaluate the electrocarboxylation of Br-BIPS compounds. The electrocarboxylation of Br-BIPS was studied under several experimental techniques.

With CV in DMF and in 0.1 M $TBAPF_6$ under a saturated atmosphere of CO_2, the electrochemical response of the compound was investigated. It was observed that the electrochemical behavior of Br-BIPS in CO_2 was similar to that observed in Ar when using WE_C: a two-electron reduction peak was detected at E_{pc} = -2.23 V. In the case of WE_{Ag}, the same catalytic effect observed in Ar atmosphere was replicated here, with an E_{pc} = -1.90 V, but a second reduction peak at E_{pc} = -2.60 V was also obtained, which was attributed to the electrochemical reduction of CO_2. Figure 3.30.

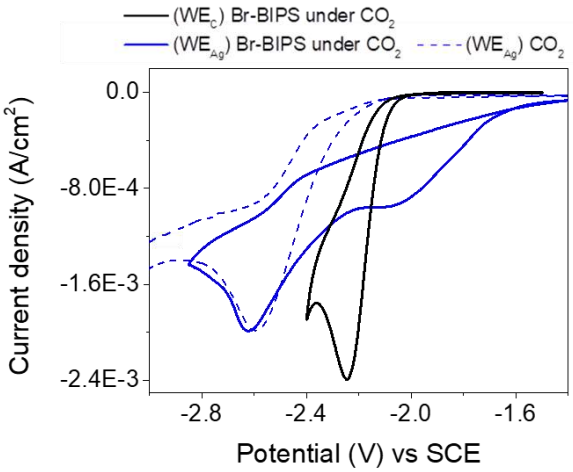

Figure 3.30. Voltammograms registered at a 0.1 V·s^{-1} scan rate for a 5 mM solution of Br-BIPS in DMF in presence of CO_2. The voltammograms were obtained using WE_C (solid black line) and WE_{Ag} (solid blue line). Dashed blue line represents the electrochemical reduction of a solution only containing CO_2 (no Br-BIPS was added in this case) and using WE_{Ag}.

Analogously, 2 F bulk electrolysis was also performed under CO_2 atmosphere in order to understand the nature of the final product. The reaction was performed using both WEs, i.e., WE_C (E_{app} = -2.35 V (vs SCE)) and WE_{Ag} (E_{app} = -2.00 V (vs SCE)), and monitored by CV, as before. In both cases voltammograms revealed the presence of two new oxidation peaks: i) one at E_{pa} ~ +0.70 V (vs SCE) associated to the Br^- anions

released after the reaction; ii) a second one at E_{pa} ~ +0.40 V (vs SCE), which not observed in electrolysis under Ar, which revealed the formation of a new product, probably the carboxylated form of the BIPS, i.e., BIPS-COO^-. This hypothesis was sustained on similar reaction mechanisms where the formation of a reactive nucleophilic anion such as $[BIPS]^-$ resulted in the nucleophilic attack of CO_2 molecules. The proposed mechanism for the electrocarboxylation of BIPS is presented in Scheme 3.2. and described below.

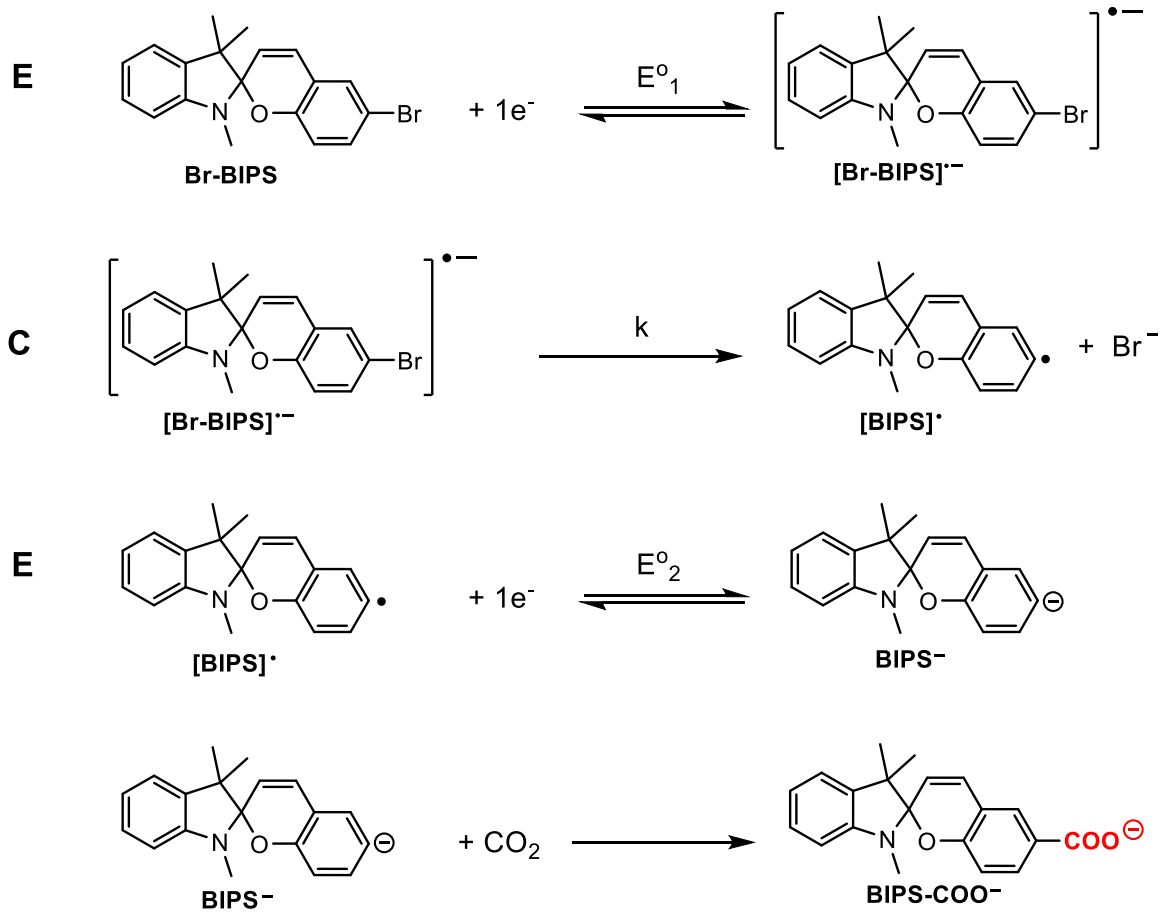

Scheme 3.2. Mechanism proposed for the electrochemical carboxylation of Br-BIPS. 'E' refers to the electron transfer and 'C' to the chemical reaction step.

First, a one-electron transfer took place (E), which led to the formation of the corresponding radical anion $[Br\text{-}BIPS]^{\bullet-}$. Then, the intermediate evolved to the neutral radical ($[BIPS]^{\bullet}$) due to the spontaneous C-X bond cleavage (C). A second electron reduced the intermediate to the anion $[BIPS]^-$ form because of $|E^o_2|<|E^o_1|$, (E). Finally, the $[BIPS]^-$ presented enough nucleophilic character to attack dissolved CO_2 molecules so that, the desired carboxylated compound was obtained $[COO\text{-}BIPS]^-$.

To confirm the formation of [COO-BIPS]$^-$, an excess of CH_3I was introduced into the crude reaction solution to isolate the product. Chemical analysis of the final product after purification confirmed that it was a carboxilated form of BIPS, namely BIPS-COOMe. This product was produced with a yield of 16% yield with WE_C and 35% with WE_{Ag}, while reaction byproducts were detected in 36% for WE_C and 30% for WE_{Ag} that mostly attributed to BIPS as a consequence of the competitive protonation reaction.

As a summary of the study, it demonstrated that electrochemical carboxylation is a valid strategy for the functionalization of aryl halide-type compounds such as Br-BIPS in a more sustainable manner. The use of catalyzers significantly improves the process, making it less energy-consuming and increasing the lifetime of carbanions to obtain better yields.

BIPS-COOMe produced in this reaction was then studied electrically and spectroscopically. It presented an electrochemical response different than that observed in BIPS or Br-BIPS due to a the electronwithdrawing effect of the ester substituent. The oxidation potential peak of BIPS-COOMe was less negative than those registered in BIPS-Br and BIPS. The difference between them was attributed to the different electron donor character of the substituents of these compounds (-COOMe, -Br and -H). Figure 3.31.Figure 1.1

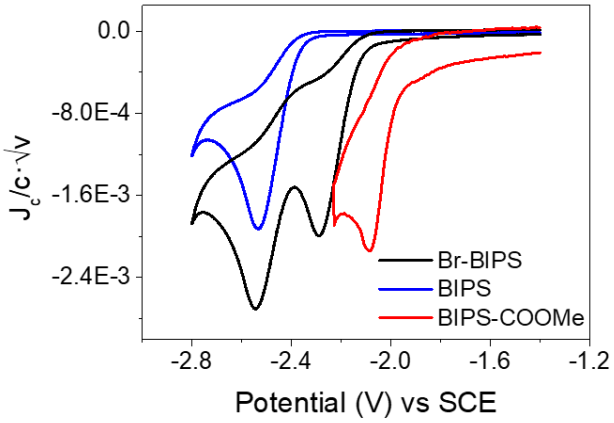

Figure 3.31. Cyclic voltammograms of the electrochemical behavior of Br-BIPS, BIPS and BIPS-COOMe

Based on previous results, the electrowithdrawing nature of the substituents was also expected to influence the photochromic properties of these BIPS-based molecules.

Solutions of BIPS, Br-BIPS and BIPS-COOMe were initially colorless due to the predominant presence of SP isomer, which absorbing in the UV region at λ_{abs}=293 nm with a molar absorption coefficient of ε = 3310 – 4586 M^{-1} cm^{-1}. UV-light irradiation at 312 nm of the closed SP structure produced its opening through C_{spiro}-O, leading to the formation of the MC isomer. MC isomer presented absorbance bands in the visible region in the three cases, with a clear hypsochromic shift associated to their composition and resulting in different color hues.

The photoreversibility of all three derivatives was assessed. Photoreversibility assays were performed in the presence of an ester or bromo substituent in the *para* position of the phenolate group of the MC isomer to confer it structural stabilization, to slow down the kinetic rates for the MC → SP return reaction, and to improve photoisomerization yields. It was possible to revert the previous reaction, getting access thus to a range of molecular switches with photochromic features. Figure X

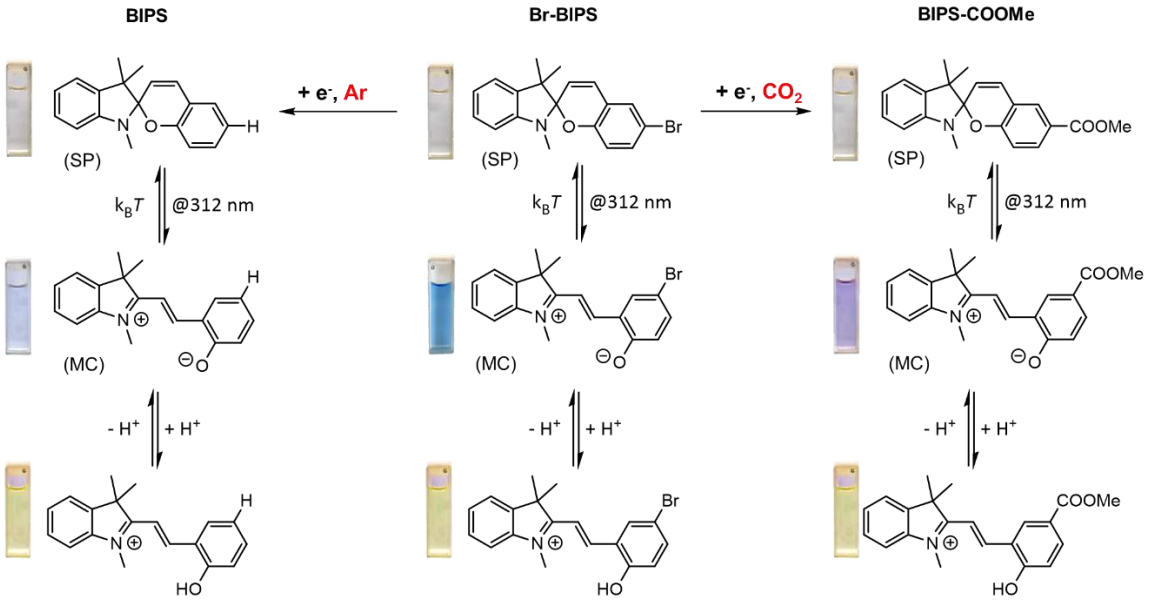

Figure 3.32. Photohalochromism of BIPS, Br-BIPS and BIPS-COOMe in DMSO. The switch from SP to MC can be reached by irradiating at λ_{exc} = 312 nm. The back isomerization reaction from MC to SP takes place spontaneously over time in the dark. When the pH of MC solutions is acidified, color turns yellow in all three cases. The color can be recovered by increasing the pH.

The responsiveness of these derivatives to pH changes was assessed in mild-acidic conditions. As expected, SP isomer was not protonated because of its low p*K*a. However, after exposure to UV light, the (*Z*)-MCH^+ conformation was formed, obtaining a yellow color solution with a λ_{abs}= 409-428 nm in all three cases. Figure 3.32.

Photochemical and electrochemical data extracted from cyclic voltammograms and UV-Vis spectra are included in Table 3.3.

Table 3.3. Photochemical and electrochemical parameters assessed for Br-BIPS, BIPS, BIPS-COOMe.

Name	State	λ_{max} ,nm (ε, $M^{-1}cm^{-1}$)	k (s^{-1}) (MC→SP)	$E_{p,c}$ (V)
Br-BIPS	SP	297, shoulder (6293)	0.01986	-2.23
	SPH^+	297		
	MC	601		
	MCH^+	428		
BIPS	SP	296 (8274)	0.0362	-2.53
	SPH^+	295		
	MC	585		
	MCH^+	418		
BIPS-COOMe	SP	292 (8719)	0.0186	-2.08
	SPH^+	286		
	MC	573		
	MCH^+	409		

Apart from the repercussion in terms of sustainability that the electrochemical carboxylation of organic compounds entails, chemical modification of these compounds provides greater reactivity to the molecule (e.g., coupling reactions with amines). In addition, the possibility of obtaining the corresponding anion (carboxylate) opens the door to its use as a counteranion in the preparation of the next generation of IL, which could present smart functionalities such as photo-halo-thermo and electrochromic responses. The following section presents a more advanced phase of the results related to the DTE compound, which used as counterion in the production of the next generation IL with smart functionalities.

3.3.3. DTE Ionic Liquids (DTE-IL). From solution to flexible IG

The following results are not part of the list of publications included in this doctoral thesis since being part of just submitted in a scientific journal. However, due to their relevance and relation with the previous results, they have been included as part of the present thesis for completeness.

DTE derivatives are well-known light-switchable MS that undergo reversible color changes thanks to the shift between their opened and closed isomers. Their most outstanding properties include an excellent photochromic fatigue-resistance, and their responsiveness to electric stimuli.

Given the smart functionalities of this compound, DTEs have recently gained interest from a technological point of view. However, their use in the liquid state is limited and their implementation at larger scales is mostly focused on their incorporation in scaffolds for the synthesis of IL.

In our research group, a simple synthetic route to produce DTE dicarboxylate has been already developed, which provides high yields and not involves cationic DTE derivatives (e.g., functionalization with pyridinium groups) that use to increase the complexity of the synthetic route [243–245].

ILs are liquid salts that can act as a solvent at room temperature, being hence considered a clean, efficient, and eco-friendly alternative to conventional organic solvents. Bearing in mind both concepts, in this study we propose the preparation of different IL based on DTE (DTE-ILs), which exhibiting smart functionalities such as photo and electro-responsiveness.

This study was conducted in collaboration with the LAQV-REQUIMTE group at University NOVA of Lisboa, which focused on synthesis of the respective DTE-ILs. Specifically, imidazolium and pyridinium type cations substituted with long alkyl chain cations were used in the preparation of the corresponding DTE based ILs (1:2 stoichiometry). The structure of the synthetized DTE-ILs is depicted in Figure 3.33. My contribution here was the spectroelectrochemical and electrochemical characterization of DTE-ILs, as well as the preparation of solid-state DTE-ILs-based materials with smart functionalities as proof-of-concept.

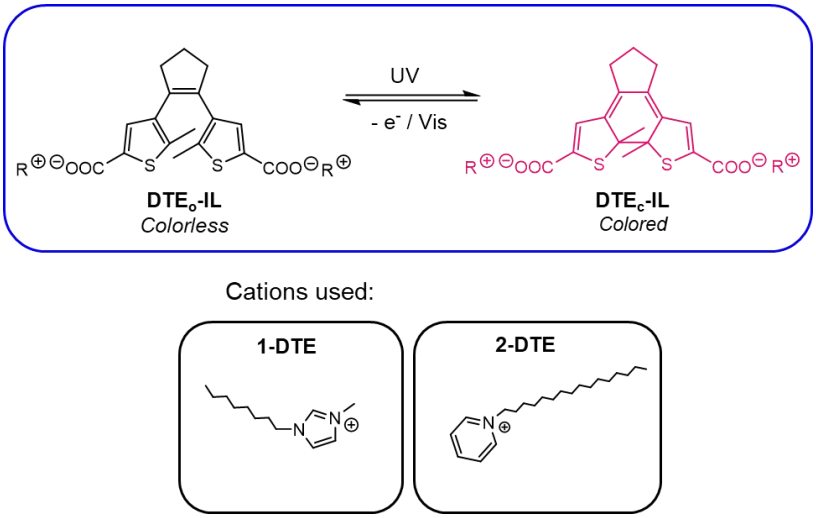

Figure 3.33. Chemical structures of DTE-ILs prepared in this study

The electrochemical behavior of the open state 1-DTE and 2-DTE was analyzed by CV. A two-electron and irreversible peak at E_{pa} = 1.32 and 1.34 V vs Ag/AgCl was observed in the anodic scan of 1-DTE and 2-DTE, respectively, which was ascribed to the oxidation of the DTE counteranion. After irradiation at λ_{exc} = 312 nm, the initially uncolored solution became deep purple, with a clear absorption band at λ_{abs} = 510 nm associated to the closed form of DTE. The electrochemical analysis of the closed form of both DTEs presented some differences. Both 1-DTE and 2-DTE presented a new one-electron oxidation peak at E_{pa} ~ 0.40 V vs Ag/AgCl. However, while in the 1-DTE case it was irreversible, probably due to the existence of a coupled chemical reaction, for 2-DTE_C it was slightly reversible. The latter indicated that the radical cation was more stable, probably due to a better solvation effect when using pyridinium. Additionally, the 2-DTE compound presented a second oxidation peak that may be associated to a further oxidation of the stabilized radical cation to the corresponding dication. Figure 3.34. CV of 1-DTE (a) and 2-DTE (b) performed in ACN 0.1 M $TBAPF_6$. The voltammograms were recorded before and after the irradiation of the solutions at λ_{exc} = 312 nm

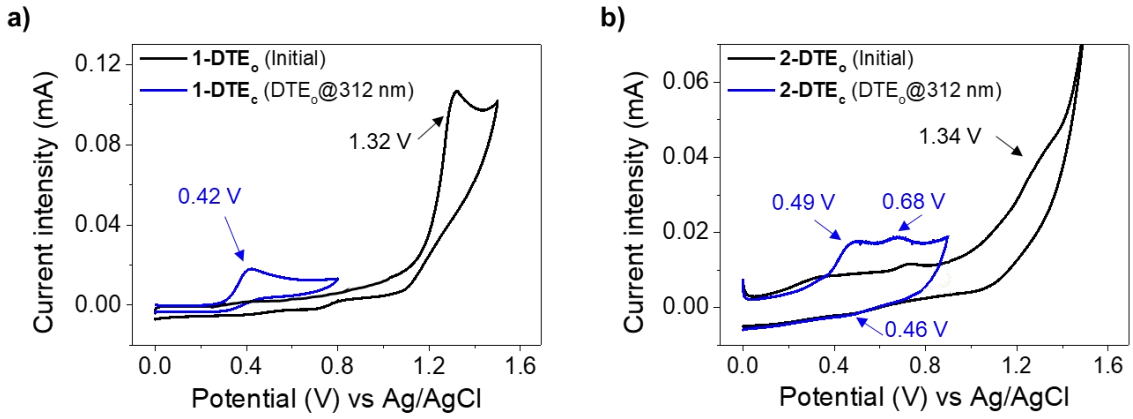

Figure 3.34. CV of 1-DTE (a) and 2-DTE (b) performed in ACN 0.1 M $TBAPF_6$. The voltammograms were recorded before and after the irradiation of the solutions at λ_{exc} = 312 nm

The oxidation mechanism of 1-DTE$_C$ and 2-DTE$_C$ was studied spectroelectrochemically in ACN solutions, aiming to establish the nature of the chemical reaction linked to the ET, as well as their electrochromic behavior. Figure 3.35.

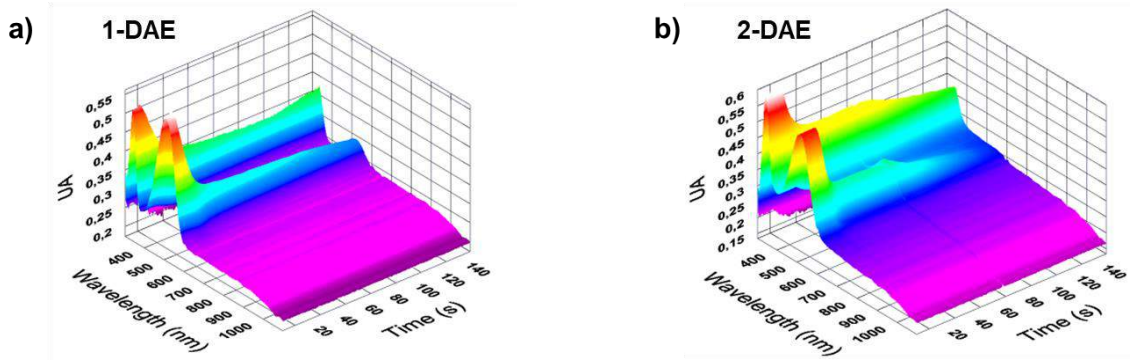

Figure 3.35. 3D spectroelectrochemical measurements performed for 0.5 mM solutions of 1-DTE (a) and 2-DTE (b) in ACN 0.1 M $TBAPF_6$. First, a constant potential of $E_{app,ox}$ = +1.20 V vs Ag/AgCl was applied for 140 s that led to a major decrement of the absorption band at ~510 nm, which indicates electroinduced isomerization of the DTE$_O$ isomer.

After irradiation at λ_{exc} = 312 nm and reaching the PSS, the ring-closing of DTE$_O$-IL to DTE$_C$-IL produced an increase in absorbance at λ_{abs} = 510 nm. When applying a potential E_{app} = +1.20 V vs Ag/AgCl for 140 s to selectively oxidize the DTE_C^{2-} anion, a clear decrease in the absorption band at λ_{abs} = 510 nm was observed, indicating the ring-opening of DTE_C^{2-} to DTE_O^{2-} isomer.

According to previous reports, the electrochemical ring-opening by oxidation of the 1-DTE involved, i) the formation of the radical cation, $[DTE_C\text{-IL}]^{+\bullet}$ by application of an

oxidation potential of E_{app} = +1.00 V vs Ag/AgCl; ii) the opening of the previous radical cation to its opened form $[DTE_O\text{-IL}]^{+\bullet}$; and iii) a homogeneous electron transfer from the $[DTE_O\text{-IL}]^{+\bullet}$ to DTE_O-IL, which occurred spontaneous thanks to the more oxidizing nature of the opened radical cation. Scheme 3.3. This reaction resulted in the complete and permanent discoloration of the sample, in a clear electrochromism with 'memory' process.

$$DTE_C - 1e^- \longrightarrow [DTE_C]^{\bullet+}$$

$$[DTE_C]^{\bullet+} \longrightarrow [DTE_O]^{\bullet+}$$

$$DTE_C + [DTE_O]^{\bullet+} \longrightarrow [DTE_C]^{\bullet+} + DTE_O$$

Scheme 3.3. Proposed electrochemical ring-opening mechanism for 1-DTE_C-IL in the closed form when an oxidation potential is applied (1st electron transfer).

However, 2-DTE followed a different electrochromic mechanism, which already noticed when analyzing the 3D UV-Vis spectra since: i) a plateau was reached between 20 and 80 s; and ii) the absorption peak located at 512 nm and corresponding to 2-DTE_C, drastically decreased when applying an oxidation potential of 1.00 V. These observations suggested that the process generated both the radical cation and the dication that may lead to ring-opening. The particularity in this case was on the reactivity of the radical cation. Thus, the generated radical cation may react with the starting material following a similar homogeneous redox reaction to that proposed for 2-DTE_C. In turn, in this redox reaction, open and closed radical cations were formed, the latter absorbing at 512 nm and keeping the absorption peak constant over the time of reaction. Scheme 3.4.

$$DTE_C - 2e^- \longrightarrow [DTE_C]^{2+}$$

$$[DTE_C]^{2+} \longrightarrow [DTE_O]^{2+}$$

$$DTE_C + [DTE_O]^{2+} \longrightarrow [DTE_C]^{\bullet+} + DTE_C^{\bullet+}$$

$$[DTE_C]^{\bullet+} \longrightarrow [DTE_O]^{\bullet+}$$

$$DTE_C + [DTE_O]^{\bullet+} \longrightarrow [DTE_C]^{\bullet+} + DTE_O$$

Scheme 3.4. Electrochromic mechanism proposed for the 2-DTE when applying an oxidation potential (1.00 V (vs Ag/AgCl)), after the second ET

These results were supported by the chemical and electrochemical analysis (CV, UV-Vis absorbance spectroscopy and thin-layer-chromatography) of the products

obtained after electrolysis of DTE_C-IL at a controlled potential, which confirmed that the only product obtained was the transparent form DTE_O-IL.

Given that the synthesized compounds were IL, this study evaluate their implementation in solid-state IG (DTE-IG) with photoelectrochromic properties.

As described in previous studies in solution, most of DTE implemeted in the IG was initially in its open form, DTE_O-IG, which presented an oxidation peak at high potentials (1.12 – 1.44 V (vs. Ag/AgCl)). After irradiation at λ_{exc} = 312 nm, a color change was observed as a consequence of the closure of the structure (DTE_C-IG). This structural change was accompanied by the appearance of a new peak at lower potentials (0.57 – 0.93 V (vs Ag/AgCl)) and a decrease in the initial one.

Next, the photochromic properties of both forms (open and closed) of the DTE^{2-} anion in the IGs were verified by UV-Vis absorption spectroscopy. The initially transparent membranes, with a single peak in the UV zone, became red-pink colored after irradiation at λ_{exc} = 312 nm, presenting an intense absorbance band between λmax = 506-527 nm by the formation of DTE_C-IG. The system was stable and did not return to its initial colorless DTE_O-IG form spontaneously, but required irradiation with visible light.

Finally, a spectroelectrochemical study was performed to check the photoelectrochromic properties of the prepared DTE-IG membranes. In the study, an oxidation potential of E_{app} = 1.20 V (vs Ag/AgCl) was applied to DTE_C-IG (colored) samples. The potential produced the ring-opening of the DTE-IG, resulting in an observable decoloration of the membrane in the region in contact with the electrode and a consequent decrease in the corresponding absorption peak. Figure 3.36.

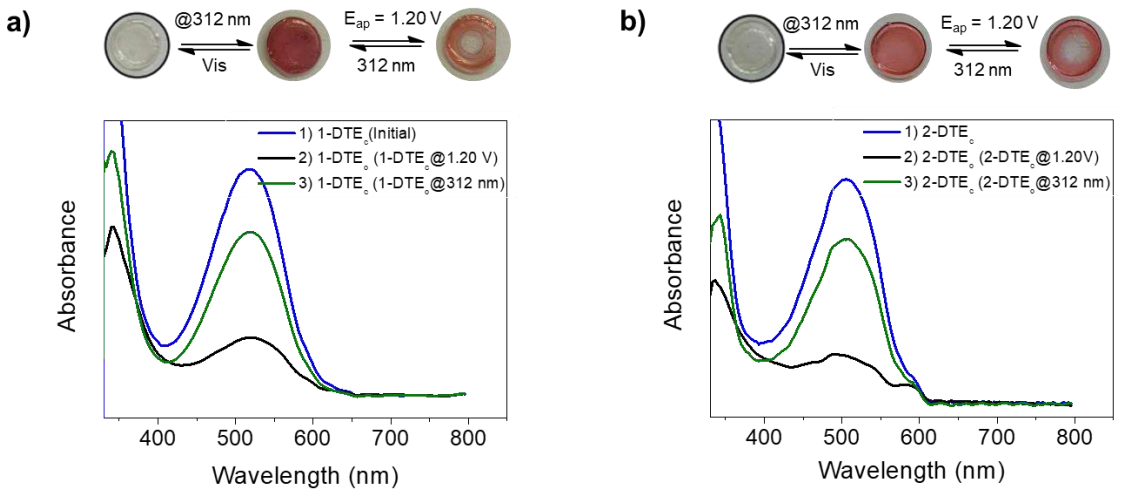

Figure 3.36. Absorbance spectra of (a) 1-DAE and (b) 2-DAE in ionogel membranes before (dark 280 line) and after irradiation (blue line) at 312 nm for 1 minute. The images in the inserts show the color change achieved this way for the IGs.

Table 3.4. collects all the electrochemical and spectroscopic data obtained for the DTE-IG membranes in their open and closed forms.

DTE-IG sample	Epa (V) vs Ag/AgCl	λ_{max} (nm)
1-DTE$_O$	1.12	349
1-DTE$_C$	0.77	527
2-DTE$_O$	1.44	340
2-DTE$_C$	0.95 / 0.57	506

Like with other electrochromic compounds, DTE-IG membranes were used to manufacture photoelectrochromic smart displays as proof of concept. Compared to other compounds, DTE had the advantage of not presenting thermal return. This property made DTE an ideal candidate in the construction of non-volatile memories since, once the stimulus that generated the change was removed, it remained constant over time.

Based on that, DTE-IG were used as logic gates in molecular memories, where each color change represents a 1 (colored shape) and a 0 (transparent) of the binary system. As a proof of concept, a flexible smart device was built susceptible to both electrical and light stimulation. Figure 3.37. a). Figure 3.37. b) collect all the responses, expressed as 0 and 1, obtained from the different stimuli (truth table). Finally, the logic

circuit corresponding to the triggered responses to different stimuli is depicted in Figure 3.37. c).

a)

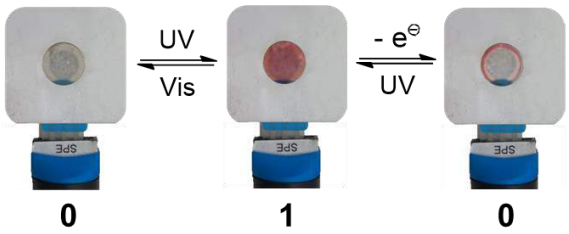

b)

In1 (UV)	In2 (Vis)	In3 (- e-)	Out (Absorbance at λ_{max} =512 nm)	Observed color
0	0	0	0	
1	0	0	1	
0	1	0	0	
0	0	1	0	
1	1	0	0	
1	0	1	0	
0	1	1	0	
1	1	1	0	

c)

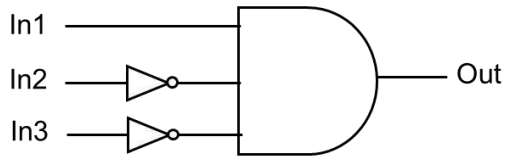

Figure 3.37. a) Photoelectrochromic display using DTE-IG as a smart material. The device is connected to a potentiostat and its surface is open to exposure of the material to UV or Vis light. b) Truth table with the responses obtained. 1 represents the presence of color or the application of a stimuli. 0 corresponds to the absence of color or stimuli. c) Logic gate constructed from the results obtained.

In addition to the study presented within the compendium requested for this doctoral thesis, the following publication was also contributed to it, which has a close relationship with the results presented in this subsection but which are not included within it: *Electrochem. Sci. Adv.* **2022**; e2100022.

In this case a multi-responsive photoelectrochromic salt was synthesized and spectroelectrochemically characterized. The salt was based on a DTE dicarboxylate, like the one studied in this thesis, which is colored to pink upon its exposure to UV light while bleached when applying an oxidation potential. The difference in this study relies on the fact that the countercation is a dimethyl bipyridinium cation which can be reduced with

an electrochemical potential and generate a deep purple coloration. These advances, together with those reported for this doctoral thesis, pave the way for the formulation of multi-responsive solid materials based on IG.

3.4. Fabrication of a Photo-patternable enzymatic optical biosensor based on DTE and SF

In previous studies performed in our group, initial results were obtained regarding the use of DTE as redox mediator in glucose sensors in solution[246]. It was observed that the close isomer of DTE selectively reacted with the peroxidase enzyme in presence of the substrate H_2O_2. This is based on the fact that only when DTE was in its closed (colored) DTE_C form after exposure to UV light at 312 nm, the E_{pa} potential was low enough to selectively react with the peroxidase enzyme. After the redox reaction of DTE_C with the peroxidase, the DTE_C compound was oxidized leading to a bleached intermediate $DTE^{\bullet}$. Figure 3.38.

Since the peroxidase reaction could be coupled to other oxidoreductases such as glucose oxidase (selective to glucose), lactate oxidase (selective to lactate) or ethanol oxidase (selective to ethanol) in a cascade reaction format, DTE could act as redox mediator in a wide variety of reactions and analytes.

Moreover, DTE could successfully play the role of an '*ON-OFF'* mediator in bioenzymatic reactions since their electrochemical properties were easily modulated by the application of light.

When coupling glucose oxidase and peroxidase activities, the presence of glucose in the medium produced the bleaching of the DTE mediator. It was observed in this case that the bleaching kinetics depended on the glucose concentration, being faster for higher glucose concentrations. There was a clear relationship between the DTE color and glucose concentration, enabling glucose quantification. The linear detection range for glucose was from 0 to 0.6 mM, which suitable for the detection of glucose in biological fluids such as serum, sweat or tears [38]. Thanks to the photo-electrochromic properties of DTE, the system could be regenerated 7 times for repetitive glucose measurements, maintaining the same sensibility and detection capacity. The modification of the biological system, e.g. by substituting glucose oxidase by other oxidoreductases, opened the door to the development of other biosensors based on the same detection principle.

However, appealing biosensing platforms require the immobilization of species. In this sense, there exists various strategies such as adsorption, covalent bond, affinity, crosslinking and entrapment of biomolecules, each one presenting advantages and disadvantages. The choice of one of them will rely, therefore, on the sort of system that is intended to be designed.

Entrapment of biomolecules is many times considered a first choice since enabled highly efficient and simple entrapment of molecules in matrices, although the stability of the biomolecule in the matrix will depend on the capacity to provide it a proper environment.

Until now, in this Doctoral Thesis we presented the use of IG, as organic membranes, which displayed two main roles: i) as pure electrolytes, using them as an independent layer from the rest of the components in electrochromic devices; ii) as a compatible matrix entrapping different MSs (NO_2BIPS and DTE). In the latter case, smart properties of MS were transferred to IG membranes, while they maintained their properties as electrolytes.

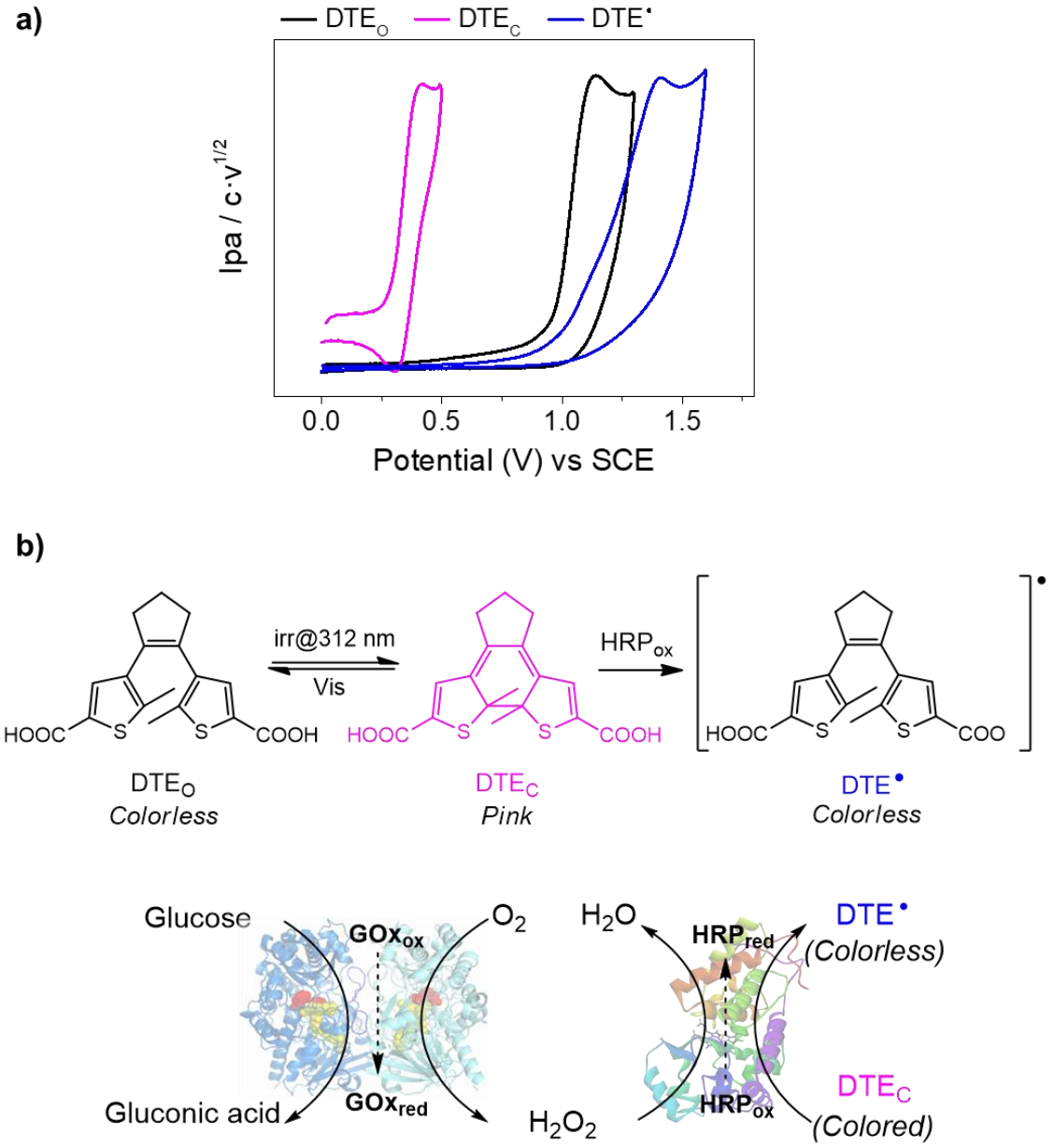

Figure 3.38. a) CV study of a solution of DTE in PBS in its initial open structure (DTE^O), after irradiation at 312 nm, closed structure (DTE^C) and after the catalytic reaction (DTE$^{\bullet}$). b) Bioenzymatic cascade reaction mediated by DTE.

However, the entrapment of biomacromolecules such as enzymes or antibodies presents the added requirement that these compounds should remain active after immobilization. That is, the entrapment process and the nature of the entrapment matrix should guarantee the structural stability and functionality of the molecules. Conventional IGs based on synthetic compounds do not provide a suitable environment in terms of biocompatibility, water content, etc., for the entrapment of biomolecules, resulting in a

fast and progressive deactivation of these bioreceptors and thus on the biosensing capacity of the system.

In this context, silk fibroin (SF) is a biopolymer that has been shown to maintain enzymatic activity for several months once the SF film is doped, even when stored at room temperature [39–41].

In addition to various enzymatic stability investigations carried out by various studies in our research group, excellent properties of this material have also been observed, such as:

- Great compatibility with biomolecules and solvation of different chemical compounds soluble or even insoluble in aqueous media such as dicarboxylate DTE derivatives.
- Large chemical and thermal stability.
- Good mechanical strength and flexibility.
- High transparency that makes them ideal candidates in optical sensor applications.
- High refractive index close to 1.6 that allows its use as light guiding or optical fibers.
- Ideal pore size that allows the filtration of components present in real samples of diagnostic interest such as the blood cell fraction, which contains red blood cells may interfere optical recordings.
- Unchanged enzyme activity after 10 months [42].

Thus, given the excellent properties of SF, part of this doctoral thesis focuses on the formulation of SF films doped with electrochromic compounds, such as DTE dicarboxylate, which act as colorimetric mediators in enzymatic reactions [43].

In this preliminary work, we successfully carried out a first enzymatic biosensing using a photoelectrochromic MS as a colorimetric mediator. The presented concept is particularly interesting because the amount of accessible mediator (DTEc) for the reaction may be controlled by UV irradiation. This finding is intriguing since it allows for the regulated consumption of a mediator throughout the reaction, enables subsequent analyte detections using the same enzymes, and restarts the system only with a UV pulse. Thus, DTE would be an ideal substitute to traditional end-point enzymatic mediators.

Bearing this concept in mind, next step was to immobilize the biosensing mixture to SF films aiming to develop a patternable SF film able to quantify glucose levels in biological fluids by simple visual inspection.

In the production of the SF films, the compositions employed in previous studies of the group for glucose biosensors development with SF films were considered were as starting point but enzyme and mediator concentrations were adjusted to adapt the sensor response to the detection range of interest, i.e., between 0 and 6 mM [43]. As a result, 25 $\mu g \cdot mL^{-1}$ GOx and 60 $\mu g \cdot mL^{-1}$ HRP in the 20% w/v SF was produced by direct dissolution of the enzymatic pellet on the SF aqueous solution. Due to its low solubility in water, a 1.2 mM saturated solution of DTE in 1:1 mixture of EtOH:H_2O (v/v) was prepared and mixed at a 1:1 v/v ratio with the previous SF solution containing the enzymes. The final precursor solution containing 0.3 mM DTE in 10% SF was drop-casted on a polystere Petri dish. SF films were produced in a two-step process involving: (i) solvent evaporation at 60 °C on a hot plate for 30 min; (ii) SF crystallization through water vacuum annealing in a saturated atmosphere of H_2O. The latter induced the formation of crystalline domains (β -sheet structures), which responsible for the stabilization of the enzymes and the hydrophobicity of the films. After 24 h, 20 µm-thick crystalline films were obtained and used for the production of biosensors. The formation of β -sheet structures was confirmed by ATR-IR spectroscopy. Figure 3.39.

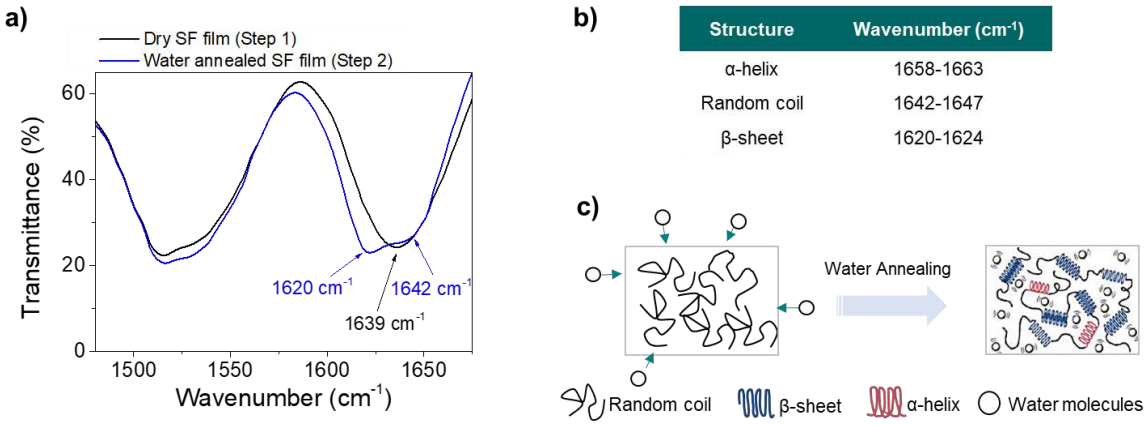

Figure 3.39, a) ATR-IR Transmittance spectroscopy of SF films after drying (step 1) and after the water annealing in vacuum (step 2). b) The table summarizes the most important peaks that allow to identify the crystallization of SF films. c) Schematic representation of the water annealing process.

For the production of the silk-based biosensors, photo-mask with 6 straight lines were produced by laser ablation and used to pattern SF films by photolithography. Concretely, the photo-mask was deposited on top of the SF film and irradiated. Only

those regions exposed were subjected to the photo-isomerization of the immobilized DTE molecules, resulting in pattern transference. Since photo-isomerization of DTE molecules is a dose-dependent process (i.e., the higher the dose, the larger the number of DTE molecules photo-isomerized), straight light with increasing color intensities were produced by exposing them during longer irradiation times (from 0 to 50 s), which corresponded to larger doses. As shown in Figure 3.40, it was a good linearity between the irradiation time and the color intensity, which confirmed that the exposition time was directly proportional to the amount of DTE_C generated. At higher times, however, this linearity is not maintained, which may be indicative of the photochemical degradation of the DTE. Note that irradiation times above 50 s did not increase color intensity and thus, this value was established as the maximum irradiation time. For quantitative analysis, color intensities were determined by image analysis with the ImageJ software after color intensity normalization. Figure 3.40.

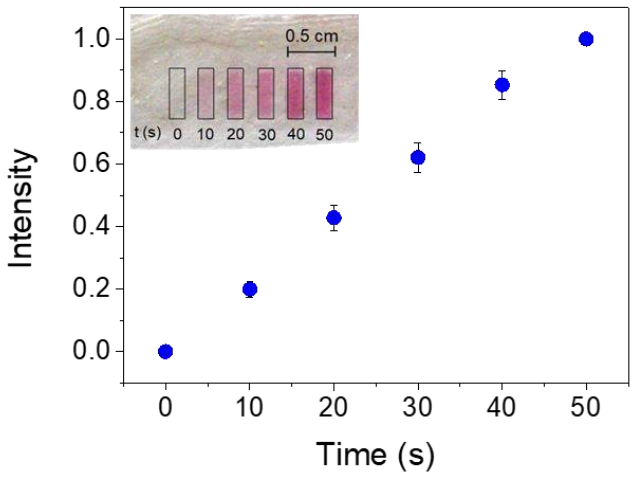

Figure 3.40. Color intensities measured for each line of doped SF films that were irradiated at 312 nm for different times (from 0 to 50 s)

In terms of operation, the silk-based biosensors were incubated with glucose samples. The presence of glucose started the cascade reaction that resulted in the oxidation and bleaching of DTE molecules. DTE discoloration was progressive over time and thus, regions with a weaker color intensity disappear first. The system was optimized in a way that glucose concentration could be determined by counting the number of bleached strips in the biosensor (numbered as L1 to L6) after 30 minutes of incubation. Four glucose concentration in PBS were studied, corresponding to the control (0 mM),

hypoglycemic (2 mM), normoglycemic (4mM) and hyperglycemic (6 mM) glucose levels. Figure 3.41 shows the color variation after 30 min. This was found to be optimal detection time.

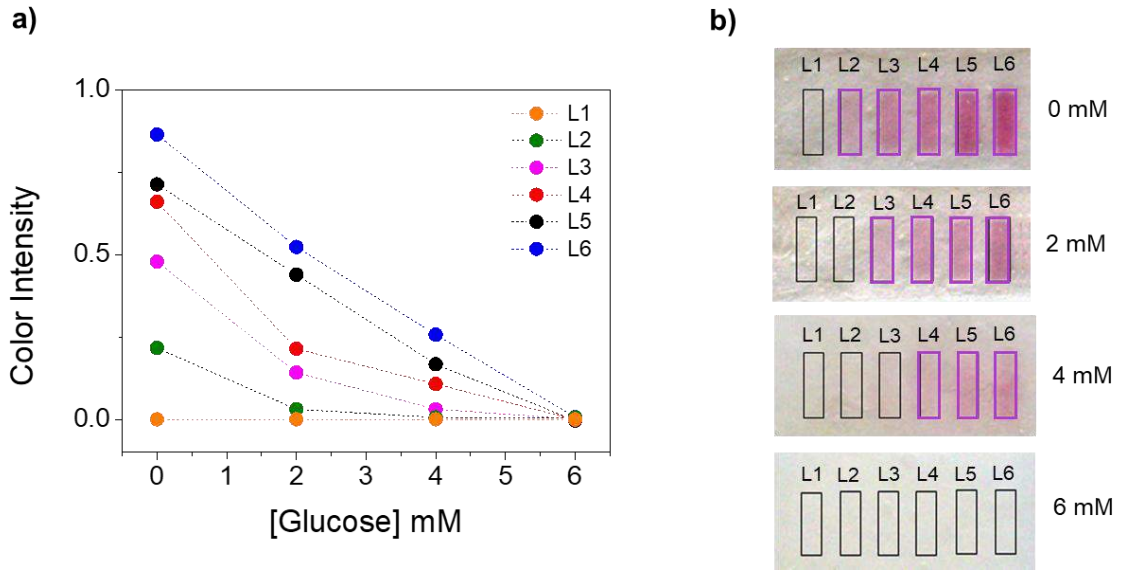

Figure 3.41. a) Change in color intensity monitored for each strip (L1-L6) at different concentration. b) Silk films after 30 min in contact with the corresponding glucose concentration (0- 6 mM).

Figure 3.41. shows that color bleaching only occurs when glucose is present, confirming the stability of the DTE mediator in the SF film. With glucose, the bleached kinetics depended on the glucose concentration in the sample, being faster by higher glucose concentrations. As a result, the number of bleached strips after an incubation time depended on the glucose concentration. After 30 minutes of incubation, only one strip (L2) was bleached in hypoglycemic levels, two (L2 and L3) for normoglycemic levels and five (from L2 to L6) for hyperglycemic levels, which allowed a precise glucose levels determination by simple visual inspection.

In addition, thanks to the small pore size observed in SF films, they behaved as size-exclusion filters being able to retain the cellular blood fraction in a region of the sensor, while pushing uncolored plasma through the SF film, thus minimizing blood inference in the optical analysis.

3.5. Final discussions

The present PhD thesis has as main objective the development of smart functional devices based on electrochemical compounds for the production of colorimetric displays and biosensors. Traditionally, the development of such devices has been mainly performed focusing on one of their two main components, namely the solid-gel electrolyte and the electrochromic molecules. The following aspects have been considered in the production of the next generation of electrochromic displays and (bio)sensors:

- High flexibility/elasticity of the device.
- Eco-friendliness of the materials and fabrication processes.
- Simplicity and low-cost of the manufacturing process for cost-effectiveness.
- Optimal electrochromic performance in solid-state.
- Multi-functionality and response capacity to several stimuli.

In the formulation of solid flexible materials with advanced functionalities for displays and/or biosensors, the use of IG has been a first choice due to their excellent optical properties, flexibility, and ionic conductivity. In recent years, important advances have been performed to improve the functionalities of these materials, including: (i) use of ILs as electrolyte to reduce the use of volatile and/or toxic organic solvent and thus their environmental fingerprint; (ii) improve electrochemical performance, e.g., enlarging the electrochemical window, by tuning the cation/anion composition of IL; (iii) an increase of ionic conductivity by doping the IG with additional salts, e.g. with lithium or potassium triflate salts; (iv) among other. To illustrate some relevant advances in terms of IG sustainability it was found that its eco-friendliness is improved by using biopolymers [44,45]. Some other studies revealed the importance of anion-cation interaction and their respective volume to provide high ionic condutivities, discovering that imidazolium based ionic ILs with bistrifliimide anion showed better conductivity values [46,47] . The present thesis has also contributed to improve the functionality of these materials in three main aspects, not previously reported.

First, the content and composition of IL in the IG matrix was optimized reaching a compromise between electrochemical performance (e.g., high ionic conductivities, large electrochemical windows) and rheological properties (e.g., liquid leakage, transparency, consistency and flexibility).

Second, silk-fibroin has been used for the very first time as polymeric matrix in the development of biosensors. Apart from an excellent rheological properties, i.e., high transparency in the visible range, elasticity, etc., biocompatibility and high thermal/mechanical/chemical stability, silk-fibroin membranes provided a more eco-friendly way to produce biosensors, in an all-water based methodology. The biosensors took also benefit from the small porosity of the membrane, that conferred it with capillary pumping capacity, and thus, enabled the measurement of real samples without external instrumentation, e.g. pumps or detection systems.

Third, novel electrochromic ink (material) formulation for mass-production and cost-effective devices by screen-printing was developed. Ink formulated with ATO@TiO_2 particles, a binder resin and the electrochome (PB and ECP-Magenta) provided the materials with (i) high electric conductivity that results in fast color switching (ii) adequate consistency that allows the fabrication of displays by screen-printing technology. The process showed simplicity and rapidity and enabled the fabrication of robust electrochromic systems.

Regarding the electrochromic molecules, over the last few years, noticeable advances have been obtained to fulfill the existent gap between the development of novel electrochromes with improved functionalities (photochromism, halochromism thermochromism…etc) and its implementation in the production of smart systems. Literature presents some examples illustrating the fancy qualities of molecules like spiropyrans or diaryletehenes derivatives among other molecular switches with such functionalities [48–50]. However, only few reports describes the implementation of this class of molecules in factual applications

In this sense, the present thesis assessed and differentiated the electrochromic behavior of the following chemical compounds: ECP-Magenta, PB, spiropyran and diarylethene derivatives. The found features were categorized as ‘Real’ electrochromism or electrochromism with ‘memory’ whether the color change is provoked as consequence of a change in the oxidation state or a structural rearrangement, respectively. Generally, this served to implement the compounds to one type of electrochromic application or another, since molecules with electrochromism with ‘memory’ usually exhibit responses to various types of stimuli (e.g., light, temperature, pH…etc.) that confers multifunctionality to the final material.

In this line, the advances obtained in both fields (development of IG/SF films and electrochromes) allowed the development of (i) low power electrochromic displays that

also allowed its implementation in self-powered electrochromic sensors. One of the main problems found in recent publications is the power consumption of self-powered electrochromic devices that many times results in the incorporation of batteries [51] and fuel cells [52] in the system which makes the fabrication process more complex and costly. In this thesis it is presented a potential combination of materials (electrochromes, electrolyte) and a design that allows the quantification of analytes such as glucose and lactose, (ii) multi-responsive applications upon light, pH, temperature and electric potential, that pave the way towards or renewable sensing applications that would contribute to more sustainable systems.

All the advances shown in this doctoral thesis demonstrate the great versatility offered by the electrochromic compounds studied and its formulations, which has allowed the design of a wide variety of applications as proof of concept with different objectives, from electrochromic displays to sensory applications. Figure 3.42. summarizes the work presented in this thesis.

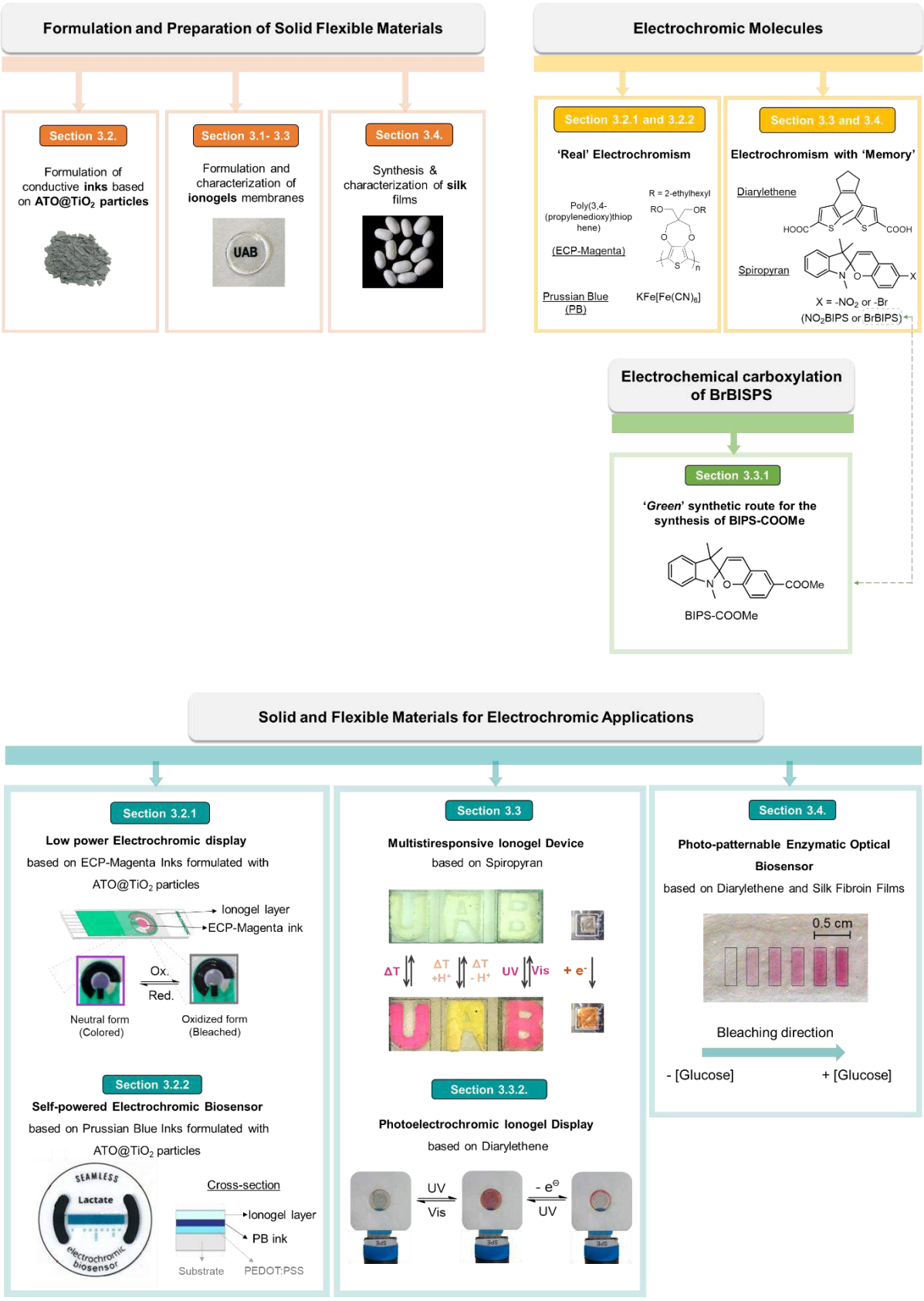

Figure 3.42. Summary of main work presented in the thesis and the sections where they are available.

3.6. References

(1) Le Bideau, J.; Viau, L.; Vioux, A. Ionogels, Ionic Liquid Based Hybrid Materials. *Chemical Society Reviews* **2011**, *40* (2), 907–925. https://doi.org/10.1039/c0cs00059k.

(2) Vioux, A.; Viau, L.; Volland, S.; Le, J. Use of Ionic Liquids in Sol-Gel ; Ionogels and Applications. *C.R. Chimie* **2010**, *13*, 242–255. https://doi.org/10.1016/j.crci.2009.07.002.

(3) Coleman, J. P.; Lynch, A. T.; Madhukar, P.; Wagenknecht, J. H. Antimony-Doped Tin Oxide Powders: *Solar Energy Materials and Solar Cells* **1999**, *56* (3–4), 375–394. https://doi.org/10.1016/S0927-0248(98)00143-3.

(4) Aller-Pellitero, M.; Fremeau, J.; Villa, R.; Guirado, G.; Lakard, B.; Hihn, J.-Y.; del Campo, F. J. Electrochromic Biosensors Based on Screen-Printed Prussian Blue Electrodes. *Sensors and Actuators B: Chemical* **2019**, *290*, 591–597. https://doi.org/10.1016/j.snb.2019.03.100.

(5) Aller-Pellitero, M.; Santiago-Malagón, S.; Ruiz, J.; Alonso, Y.; Lakard, B.; Hihn, J.-Y.; Guirado, G.; del Campo, F. J. Fully-Printed and Silicon Free Self-Powered Electrochromic Biosensors: Towards Naked Eye Quantification. *Sensors and Actuators B: Chemical* **2020**, *306*, 127535. https://doi.org/10.1016/j.snb.2019.127535.

(6) Liu, J.; Coleman, J. P. Nanostructured Metal Oxides for Printed Electrochromic Displays. *Materials Science and Engineering: A* **2000**, *286* (1), 144–148. https://doi.org/10.1016/S0921-5093(00)00719-X.

(7) AJ Bard, LR Faulkner, J Leddy, C. Z. *Electrochemical Methods: Fundamentals and Applications*, 2nd ed.; New York, 1980.

(8) Zhang, S.; Sun, G.; He, Y.; Fu, R.; Gu, Y.; Chen, S. Preparation, Characterization, and Electrochromic Properties of Nanocellulose-Based Polyaniline Nanocomposite Films. *ACS Applied Materials and Interfaces* **2017**, *9* (19), 16426–16434. https://doi.org/10.1021/acsami.7b02794.

(9) Aller-Pellitero, M.; Fremeau, J.; Villa, R.; Guirado, G.; Lakard, B.; Hihn, J.-Y.; del Campo, F. J. Electrochromic Biosensors Based on Screen-Printed Prussian Blue Electrodes. *Sensors and Actuators B: Chemical* **2019**, *290*, 591–597. https://doi.org/10.1016/j.snb.2019.03.100.

(10) Ellis, D.; Eckhoff, M.; Neff, V. D. Electrochromism in the Mixed-Valence Hexacyanides. 1. Voltammetric and Spectral Studies of the Oxidation and Reduction of Thin Films of Prussian Blue. *The Journal of Physical Chemistry* **1981**, *85* (9), 1225–1231. https://doi.org/10.1021/j150609a026.

(11) Farahmand Nejad, M. A.; Ranjbar, S.; Parolo, C.; Nguyen, E. P.; Álvarez-Diduk, R.; Hormozi-Nezhad, M. R.; Merkoçi, A. Electrochromism: An Emerging and Promising Approach in (Bio)Sensing Technology. *Materials Today* **2021**, *50*, 476–498. https://doi.org/10.1016/j.mattod.2021.06.015.

(12) Márquez, A.; Santiago, S.; Domínguez, C.; Muñoz-Berbel, X.; Guirado, G. Photoelectro-Enzymatic Glucose Reusable Biosensor by Using Dithienylethene Mediators. *Chemistry – A European Journal* **2020**, *26* (40), 8714–8719. https://doi.org/10.1002/chem.202000865.

(13) Coleman, J. P.; Lynch, A. T.; Madhukar, P.; Wagenknecht, J. H. Printed, Flexible Electrochromic Displays Using Interdigitated Electrodes. *Solar Energy Materials and Solar Cells* **1999**, *56* (3–4), 395–418. https://doi.org/10.1016/S0927-0248(98)00144-5.

(14) Ohara, T. J.; Rajagopalan, R.; Heller, A. "Wired" Enzyme Electrodes for Amperometric Determination of Glucose or Lactate in the Presence of Interfering Substances. *Analytical Chemistry* **1994**, *66* (15), 2451–2457. https://doi.org/10.1021/ac00087a008.

(15) Liana, D. D.; Raguse, B.; Gooding, J. J.; Chow, E. Toward Paper-Based Sensors: Turning Electrical Signals into an Optical Readout System. *ACS Applied Materials & Interfaces* **2015**, *7* (34), 19201–19209. https://doi.org/10.1021/acsami.5b04941.

(16) Aller Pellitero, M.; Guimerà, A.; Villa, R.; del Campo, F. J. IR Drop Effects in Self-Powered and Electrochromic Biosensors. *The Journal of Physical Chemistry C* **2018**, *122* (5), 2596–2607. https://doi.org/10.1021/acs.jpcc.7b11906.

(17) Lenoble, C.; Becker, R. S. Photophysics, Photochemistry, Kinetics, and Mechanism of the Photochromism of 6'-Nitroindolinospiropyran. *The Journal of Physical Chemistry* **1986**, *90* (1), 62–65. https://doi.org/10.1021/j100273a015.

(18) Görner, H. Photochromism of Nitrospiropyrans: Effects of Structure, Solvent and Temperature. *Physical Chemistry Chemical Physics* **2001**, *3* (3), 416–423. https://doi.org/10.1039/b007708i.

(19) Minkin, V. I. Photo-, Thermo-, Solvato-, and Electrochromic Spiroheterocyclic Compounds. *Chemical Reviews* **2004**, *104* (5), 2751–2776. https://doi.org/10.1021/cr020088u.

(20) Raymo, F. M.; Giordani, S. Signal Processing at the Molecular Level. *J Am Chem Soc* **2001**, *123* (19), 4651–4652. https://doi.org/10.1021/ja005699n.

(21) Wojtyk, J. T. C.; Wasey, A.; Xiao, N.-N.; Kazmaier, P. M.; Hoz, S.; Yu, C.; Lemieux, R. P.; Buncel, E. Elucidating the Mechanisms of Acidochromic Spiropyran-Merocyanine Interconversion. *The Journal of Physical Chemistry A* **2007**, *111* (13), 2511–2516. https://doi.org/10.1021/jp068575r.

(22) Preigh, M. J.; Stauffer, M. T.; Lin, F.-T.; Weber, S. G. Anodic Oxidation Mechanism of a Spiropyran. *Journal of the Chemical Society, Faraday Transactions* **1996**, *92* (20), 3991. https://doi.org/10.1039/ft9969203991.

(23) Kortekaas, L.; Ivashenko, O.; Van Herpt, J. T.; Browne, W. R. A Remarkable Multitasking Double Spiropyran: Bidirectional Visible-Light Switching of Polymer-Coated Surfaces with Dual Redox and Proton Gating. *J Am Chem Soc* **2016**, *138* (4), 1301–1312. https://doi.org/10.1021/jacs.5b11604.

(24) Browne, W. R.; Ivashenko, O.; Feringa, B. L.; Rudolf, P.; van Herpt, J. T. Oxidative Electrochemical Aryl C–C Coupling of Spiropyrans. *Chemical Communications* **2013**, *49* (60), 6737. https://doi.org/10.1039/c3cc42396d.

(25) Berman, E.; Fox, R. E.; Thomson, F. D. Photochromic Spiropyrans. I. The Effect of Substituents on the Rate of Ring Closure. *J Am Chem Soc* **1959**, *81* (21), 5605–5608. https://doi.org/10.1021/ja01530a021.

(26) Brügner, O.; Reichenbach, T.; Sommer, M.; Walter, M. Substituent Correlations Characterized by Hammett Constants in the Spiropyran-Merocyanine Transition. *Journal of Physical Chemistry A* **2017**, *121* (13), 2683–2687. https://doi.org/10.1021/acs.jpca.7b01248.

(27) Chibisov, A. K.; Görner, H. Photoprocesses in Spiropyran-Derived Merocyanines. *Journal of Physical Chemistry A* **1997**, *101* (24), 4305–4312. https://doi.org/10.1021/jp962569l.

(28) Saire-Saire, S.; Barbosa, E. C. M.; Garcia, D.; Andrade, L. H.; Garcia-Segura, S.; Camargo, P. H. C.; Alarcon, H. Green Synthesis of Au Decorated CoFe 2 O 4 Nanoparticles for Catalytic Reduction of 4-Nitrophenol and Dimethylphenylsilane Oxidation. *RSC Advances* **2019**, *9* (38), 22116–22123. https://doi.org/10.1039/C9RA04222A.

(29) Silvester, D. S.; Compton, R. G. Electrochemistry in Room Temperature Ionic Liquids: A Review and Some Possible Applications. *Zeitschrift für Physikalische Chemie* **2006**, *220* (10), 1247–1274. https://doi.org/10.1524/zpch.2006.220.10.1247.

(30) Forryan, C. L.; Lawrence, N. S.; Rees, N. v; Compton, R. G. Voltammetric Characterisation of the Radical Anions of 4-Nitrophenol, 2-Cyanophenol and 4-Cyanophenol in N,N-Dimethylformamide Electrogenerated at Gold Electrodes. *Journal of Electroanalytical Chemistry* **2004**, *561*, 53–65. https://doi.org/10.1016/j.jelechem.2003.07.001.

(31) Gallardo, I.; Guirado, G.; Marquet, J.; Vilà, N. Evidence for a π Dimer in the Electrochemical Reduction of 1,3,5-Trinitrobenzene: A Reversible N2-Fixation System. *Angewandte Chemie International Edition* **2007**, *46* (8), 1321–1325. https://doi.org/10.1002/anie.200602690.

(32) del Sesto, R. E.; Arif, A. M.; Novoa, J. J.; Anusiewicz, I.; Skurski, P.; Simons, J.; Dunn, B. C.; Eyring, E. M.; Miller, J. S. Chemical Reduction of 2,4,6-Tricyano-1,3,5-Triazine and 1,3,5-Tricyanobenzene. Formation of Novel 4,4‘,6,6‘-Tetracyano-2,2‘-Bitriazine and Its Radical Anion. *The Journal of Organic Chemistry* **2003**, *68* (9), 3367–3379. https://doi.org/10.1021/jo025833h.

(33) del Sesto, R. E.; Arif, A. M.; Miller, J. S. Formation of Different Framework Structured Dimeric Dianions Formed from the Reduction of 2,4,6-Tricyano-1,3,5-Triazine and 1,3,5-TricyanobenzeneDedicated to Michael Hanack on the Occasion of the 70th Birthday. *Chemical Communications* **2001**, No. 24, 2730–2731. https://doi.org/10.1039/b108297n.

(34) Guirado, G.; Coudret, C.; Hliwa, M.; Launay, J.-P. Understanding Electrochromic Processes Initiated by Dithienylcyclopentene Cation-Radicals. *The Journal of Physical Chemistry B* **2005**, *109* (37), 17445–17459. https://doi.org/10.1021/jp052459r.

(35) Lucas, L. N.; Jong, J. J. D. de; Esch, J. H. van; Kellogg, R. M.; Feringa, B. L. Syntheses of Dithienylcyclopentene Optical Molecular Switches. *European Journal of Organic Chemistry* **2003**, *2003* (1), 155–166. https://doi.org/10.1002/1099-0690(200301)2003:1<155::AID-EJOC155>3.0.CO;2-S.

(36) Hu, F.; Jiang, L.; Cao, M.; Xu, Z.; Huang, J.; Wu, D.; Yang, W.; Liu, S. H.; Yin, J. Cyanine-Based Dithienylethenes: Synthesis, Characterization, Photochromism and Biological

Imaging in Living Cells. *RSC Advances* **2015**, *5* (8), 5982–5987. https://doi.org/10.1039/C4RA12606H.

(37) Márquez, A.; Santiago, S.; Domínguez, C.; Muñoz-Berbel, X.; Guirado, G. Photoelectro-Enzymatic Glucose Reusable Biosensor by Using Dithienylethene Mediators. *Chemistry – A European Journal* **2020**, *26* (40), 8714–8719. https://doi.org/10.1002/chem.202000865.

(38) Witkowska Nery, E.; Kundys, M.; Jeleń, P. S.; Jönsson-Niedziółka, M. Electrochemical Glucose Sensing: Is There Still Room for Improvement? *Analytical Chemistry* **2016**, *88* (23), 11271–11282. https://doi.org/10.1021/acs.analchem.6b03151.

(39) Pritchard, E. M.; Dennis, P. B.; Omenetto, F.; Naik, R. R.; Kaplan, D. L. Physical and Chemical Aspects of Stabilization of Compounds in Silk. *Biopolymers* **2012**, *97* (6), 479–498. https://doi.org/10.1002/bip.22026.

(40) Lu, S.; Wang, X.; Lu, Q.; Hu, X.; Uppal, N.; Omenetto, F. G.; Kaplan, D. L. Stabilization of Enzymes in Silk Films. *Biomacromolecules* **2009**, *10* (5), 1032–1042. https://doi.org/10.1021/bm800956n.

(41) Thungon, P. D.; Kuri, P. R.; Bachu, V.; Goswami, P. Silk-Fibroin Film as Enzyme Stabilizing Material and Optical Signal Transducer for Developing Alcohol Oxidase-Based MPAD Methanol Biosensor. *Biosensors and Bioelectronics: X* **2022**, *11*, 100147. https://doi.org/10.1016/j.biosx.2022.100147.

(42) Márquez, A.; Santos, M. v.; Guirado, G.; Moreno, A.; Aznar-Cervantes, S. D.; Cenis, J. L.; Santagneli, S. H.; Domínguez, C.; Omenetto, F. G.; Muñoz-Berbel, X. Nanoporous Silk Films with Capillary Action and Size-Exclusion Capacity for Sensitive Glucose Determination in Whole Blood. *Lab on a Chip* **2021**, *21* (3), 608–615. https://doi.org/10.1039/D0LC00702A.

(43) Márquez, A.; Aznar-Cervantes, S. D.; Cenis, J. L.; Domínguez, C.; Muñoz-Berbel, X. Silk Fibroin Pads for Whole Blood Glucose Determination. In *EUROSENSORS 2018*; MDPI: Basel Switzerland, 2018; p 886. https://doi.org/10.3390/proceedings2130886.

(44) Kimizuka, N.; Nakashima, T. Spontaneous Self-Assembly of Glycolipid Bilayer Membranes in Sugar-Philic Ionic Liquids and Formation of Ionogels. *Langmuir* **2001**, *17* (22), 6759–6761. https://doi.org/10.1021/la015523e.

(45) Vidinha, P.; Lourenço, N. M. T.; Pinheiro, C.; Brás, A. R.; Carvalho, T.; Santos-Silva, T.; Mukhopadhyay, A.; Romão, M. J.; Parola, J.; Dionisio, M.; Cabral, J. M. S.; Afonso, C. A. M.; Barreiros, S. Ion Jelly: A Tailor-Made Conducting Material for Smart Electrochemical Devices. *Chemical Communications* **2008**, No. 44, 5842. https://doi.org/10.1039/b811647d.

(46) Xu, W.; Wang, L.-M.; Nieman, R. A.; Angell, C. A. Ionic Liquids of Chelated Orthoborates as Model Ionic Glassformers. *The Journal of Physical Chemistry B* **2003**, *107* (42), 11749–11756. https://doi.org/10.1021/jp034548e.

(47) Ding, Y.; Zhang, J.; Chang, L.; Zhang, X.; Liu, H.; Jiang, L. Preparation of High-Performance Ionogels with Excellent Transparency, Good Mechanical Strength, and High Conductivity. *Advanced Materials* **2017**, *29* (47), 1704253. https://doi.org/10.1002/adma.201704253.

(48) Kortekaas, L.; Chen, J.; Jacquemin, D.; Browne, W. R. Proton-Stabilized Photochemically Reversible *E* / *Z* Isomerization of Spiropyrans. *The Journal of Physical Chemistry B* **2018**, *122* (24), 6423–6430. https://doi.org/10.1021/acs.jpcb.8b03528.

(49) Steen, J. D.; Duijnstee, D. R.; Sardjan, A. S.; Martinelli, J.; Kortekaas, L.; Jacquemin, D.; Browne, W. R. Electrochemical Ring-Opening and -Closing of a Spiropyran. *The Journal of Physical Chemistry A* **2021**, *125* (16), 3355–3361. https://doi.org/10.1021/acs.jpca.1c01142.

(50) Peters, A.; Branda, N. R. Electrochromism in Photochromic Dithienylcyclopentenes. *J Am Chem Soc* **2003**, *125* (12), 3404–3405. https://doi.org/10.1021/ja028764x.

(51) Bandodkar, A. J.; Lee, S. P.; Huang, I.; Li, W.; Wang, S.; Su, C.-J.; Jeang, W. J.; Hang, T.; Mehta, S.; Nyberg, N.; Gutruf, P.; Choi, J.; Koo, J.; Reeder, J. T.; Tseng, R.; Ghaffari, R.; Rogers, J. A. Sweat-Activated Biocompatible Batteries for Epidermal Electronic and Microfluidic Systems. *Nature Electronics* **2020**, *3* (9), 554–562. https://doi.org/10.1038/s41928-020-0443-7.

(52) Jin, X.; Bandodkar, A. J.; Fratus, M.; Asadpour, R.; Rogers, J. A.; Alam, M. A. Modeling, Design Guidelines, and Detection Limits of Self-Powered Enzymatic Biofuel Cell-Based Sensors. *Biosensors and Bioelectronics* **2020**, *168*, 112493. https://doi.org/10.1016/j.bios.2020.112493.

CHAPTER 4. CONCLUSIONS

4. Conclusions

The main conclusions drawn from the results obtained in this doctoral thesis are detailed below.

- It has been shown that electrochromic properties can be classified into two differentitated groups: real electrochromism and memory electrochromism depending on whether the color change is due to a change in the oxidation state or due to a structural change in the molecule, respectively. As has been determined, the classic electrochromes (e.g. PB, ECP-Magenta) belong to the first group, while the MS (e.g. DTE and NO_2BIPS) belong to the second. It has been possible to determine that while the reversibility and fatigue resistance of electrochromic processes is better in compounds with real electrochromism, multifunctionality is only possible for compounds with memory electrochromism, that is, for MS. Meanwhile, they all presented high color contrasts and moderate coloration times (2-12 s) that would permit their use in different electrochromic applications.

- The formulation of electrochromic inks with conductive particles of ATO@TiO_2 and modified with electrochromic compounds such as ECP-Magenta and PB, has proven to be a valid strategy for the manufacture by screen-printing of electrochromic devices on a large scale and at a low cost. It has also been observed that the formulated electrochromic inks present good compatibility with IG-type electrolytes, which can also be screen-printed.

- ECP-Magenta ink has been found to have excellent electrochromic properties, good color contrast, ~2 s response time and good fatigue resistance. Also notable is its operation at low potential, which would improve the energy efficiency of future electrochromic displays.

- The formulation of PB inks has enabled the construction of a self-powered electrochromic glucose biosensor entirely by screen printing. The proposed coplanar configuration between a glucose biosensor (anode) and the electrochromic display of PB (cathode) has produced a self-powered biosensor. With future modifications to its prototyping, an easy quantitative readout could be

obtained by the naked eye of the analyte concentration in the PB display according to the distance of the color change reached in the electrochromic strip.

- It has been demonstrated that IG materials have outstanding qualities (elasticity, flexibility, transparency, and high ionic conductivity) and that they are relatively simple to modify to endow the material with new features. It has been observed that the IL that makes up the substance gives it the ability to function as both an electrolyte and a solvent for organic compounds like DTE and NO2BIPS. This creates the ideal environment for its properties to be maintained and to behave similarly to what is expected in solution.

- The spiropyran derivatives, NO2BIPS, have been shown to be MS with electrochromic properties that can be exploited for different electrochromic devices. It has also proven to be a highly versatile compound given its wide variety of responses to different stimuli. It has been observed that IG doped with NO2BIPS can be formulated, maintaining the same rheological properties as bare IG and the same photo-halo-thermo-electrochromic properties of NO2BIPS. Thanks to this strategy, large-scale manufacture of electrochromic applications based on NO_2BIPS@IG would be simplified.

- Similarly, DTE compounds have been incorporated into IG, in this case in the form of IL countercation. Furthermore, these materials have been shown to present a photo-electrochromic response. This strategy economizes the use of reagents, which would imply a lower manufacturing cost. It has been determined that this new formulation still exhibits photo-electrochromic properties.

- SF has been demonstrated to be a suitable biomaterial in which biocatalytic reactions can occur. The immobilization of DTE in SF, together with the other enzymes, has allowed the development of a light-induced and light-regenerable glucose optical biosensor that can easily be patterned on SF films.

CHAPTER 5. PUBLICATIONS

5. Publications

Journal of Molecular Liquids 318 (2020) 114033

Contents lists available at ScienceDirect

Journal of Molecular Liquids

journal homepage: www.elsevier.com/locate/molliq

Study of P(VDF-co-HFP)-ionic liquid based ionogels for designing flexible displays

Sara Santiago [a], Xavier Muñoz-Berbel [b], Gonzalo Guirado [a,*]

[a] Departament de Química, Universitat Autònoma de Barcelona, Bellaterra, Barcelona 08193, Spain
[b] Institut de Microelectrònica de Barcelona (IMB-CNM, CSIC), Bellaterra, Barcelona 08193, Spain

ARTICLE INFO

Article history:
Received 27 June 2020
Received in revised form 29 July 2020
Accepted 9 August 2020
Available online 18 August 2020

Keywords:
Ionic liquids
Ionogel
Flexible device
Photoelectrochromic devices

ABSTRACT

In flexible displays, solid electrolytes promote electron-transfer without compromising system integrity. Ionogels (IGs) are now preferred among other solid electrolytes, e.g. inorganic and hydrogel electrolytes, for being easier to produce than the former and showing excellent properties, including high ionic conductivities, broad electrochemical window, transparency, flexibility, and non-solvent volatility than the latter. IG properties widely depend on the composition and concentration of the ionic liquid (IL) in the polymeric matrix, affecting its transparency, integrity and flexibility. Here, we have investigated the loading and composition of the IL to produce P(VDF-co-HFP)-based IGs to be employed as substrates in the development of flexible photo-electrochromic displays. Single IG layers of P(VDF-co-HFP) loaded with 79% wt. of N_{1114}TFSI were optimal among the IGs formulations, reaching conductivity values up to 1.06 mS·cm^{-1}, showing high transparency (83% transmittance) and a large electrochemical window (3.2 V), while maintaining flexibility and integrity. The doping of the IG with the photo-electrochromic molecule spiropyran resulted in flexible displays with fast and reversible electrochromic and photochromic dynamics, not affecting the conformational changes of the molecule. These flexible photo-electrochromic displays, due to its simplicity, high-performance and low cost, are foreseen to impact in several fields, including smart windows, smart clothing or gas sensors, among others.

1. Introduction

Ionogels (IGs) are gel electrolytes with a liquid phase consisting of an ionic liquid (IL) that percolates the solid polymeric phase. These materials are now a first choice in the development of smart electrochemical devices for combining mechanical strength, durability, flexibility, elasticity and high ionic conductivities, something impossible to attain with stiff and brittle inorganic solid-state electrolytes or hydrogels susceptible to dehydration [1–12]. Especially remarkable is the application of IGs in electro-optic devices, e.g. advanced flexible displays, where their high transparency and ionic conductivities [13–16] is combined with their excellent mechanical features, i.e. flexibility and elasticity [17–20]. For this reason, the formulation of new IGs is still a reason for the continuous study, as their electrochemical and mechanical properties are entirely related to the chemical nature of the polymer matrix and the IL. In such formulation, the choice of a suitable polymer composition with the desired properties is crucial in the gel polymer electrolyte development [2,9,21–25]. Poly(vinylidene fluoride-co-hexafluoropropylene) (P(VDF-co-HFP)) polymers are now preferred due to their high thermal and chemical stability, flexibility, and large dielectric constants, which improve ionic dissociation [26–28]. Additionally, HFP units reduce polymer crystallinity while enhancing ionic conductivity [29–31]. However, ionic conductivities of such polymers are normally well below the 10^{-3} and 10^{-4} S/cm [32–35] required in conventional high-voltage electrochromic devices [36–38]. The introduction of IL as ionic charge in the P(VDF-co-HFP) formulation increases its ionic conductivity and expands the electrochemical windows of the material, much beyond traditional solid-gel electrolytes.

In previous reports, electrochromic molecules, such as bipyridinium salts, have been incorporated in IG electrolytes to produce flexible displays [14,15,32] in a single-step fabrication process, enabling large-scale production [39]. However, the influence of IGs composition in the design, fabrication, and performance of such devices is still controversial, and there are not general tips for a function-specific design.

This work presents an exhaustive study on P(VDF-co-HFP)-ionic liquid-based IG composition, and its influence on opto-electrochemical performance and mechanical properties. Several IG membranes at different IL loadings and modifications of the cation and/or the anion components were prepared and studied for optimization. Finally, the optimal material was employed in the development of an photo-electrochromic display, as proof-of-concept, namely a single electrolyte layer (1G)

* Corresponding author.
E-mail address: Gonzalo.Guirado@uab.cat (G. Guirado).

https://doi.org/10.1016/j.molliq.2020.114033
0167-7322/

doped with photoelectrochromic spiropyran derivatives with a wide range of applications from smart windows to gas sensors [40–48].

2. Experimental

2.1. Materials

Poly(vinylidene fluoride-co-hexafluoropropylene) (P(VDF-co-HFP), Mw 300,000 g·mol^{-1}), 1′,3′-Dihydro-1′,3′,3′-trimethyl-6-nitrospiro [2*H*-1-benzopyran-2,2′-(2*H*)-indole] (spiropyran, 98%), and anhydrous acetone for HPLC (>99.9%) were purchased from Sigma-Aldrich, and used as received.

Ionic liquids (ILs), 1-butyl-3-methylimidazolium bis (trifluoromethanesulfonyl)imide (BMIM TFSI), 1-butyl-3-methylimidazolium hexafluorophosphate (BMIM PF_6), 1-butyl-3-methylimidazolium tetrafluoroborate (BMIM BF_4), butyl-methyl-ammonium bis(trifluoromethanesulfonyl)imide ($N_{1,1,4}$ TFSI), 1-methyl-1-propylpiperidinium bis(trifluoromethanesulfonyl)imide ($PP_{1,3}$ TFSI), and 1-butyl-1-methylpyrrolidinium bis(trifluoromethanesulfonyl)imide (BMPyr TFSI) were purchased and dried with molecular sieves of 3 Å size under vacuum for 24 h to ensure a water content of <0.001%.

ITO-coated PET sheets, 60 Ω/sq. resistance, were acquired from Sigma-Aldrich. Screen-Printed electrodes for electrochemical and spectroelectrochemical measurements were purchased from DropSens.

2.2. IGs preparation

IGs were prepared by stirring the desired amount of IL, P(VDF-co-HFP), and acetone for 24 h in acetone under N_2 atmosphere at room temperature. For all IG compositions, the weight ratio P(VDF-co-HFP): Acetone of 1:20 was maintained. Once the solution was completely homogeneous, the same volume was casted in a mold and dried at room temperature for 24 h to ensure the total evaporation of acetone.

2.3. Photo-electrochromic display fabrication

The photo-electrochromic display was fabricated by preparing a solution containing spiropyran 2 mM and TEMPO 4 mM in BMIM TFSI. After this step, the desired volume of solution was weighed and mixed with P(VDF-co-HFP) (previously dissolved in acetone in 1:20 weight ratio), in order to obtain 83.3% BMIM TFSI loading. The resulting solution was casted on a glass ¿slide? and dried for 24 h. A 1.5 × 2 cm^2 IG area was then cut and placed between two ITO-coated PET electrodes and connected to a potentiostat.

2.4. Characterization techniques

Potentiostat CHinstrument 660E model was used to perform electrochemical impedance spectroscopy (EIS) to provide further insights into the electrochemical properties of IGs membranes. An A.C. impedance technique was used, and a small amplitude potential oscillation of 5 mV was applied in order to guarantee the measurements in the steady state, where no significant chemical changes were observed at a frequency range between 1 MHz and 1 Hz. The D.C. potential was set at open circuit potential (OCP). The resulting impedance spectra were fitted with Chi660e software, modeling the equivalent circuit model according to the physico-chemical processes that took place on the electrode surface.

Cyclic voltammetry (CV) measurements were made with the same potentiostat model in order to determine the electrochemical windows for each IG membrane. All electrochemical studies were performed using screen printed electrodes, where carbon electrodes were used as working and counter, and Ag/AgCl were used as pseudo-reference electrodes.

FTIR spectra of IG membranes were recorded using a FTIR Tensor 27 Bruker spectrophotometer, and the Specac Golden Gate accessory for the attenuated reflectance modality (ATR) in the range of 3300 to 650 cm^{-1}. OPUS 5.5 software was used for monitoring the spectra.

Spectroelectrochemistry studies were performed using a VSP100 model potentiostat and controlled by EC-Lab V9.51 software. The potentiostat was coupled to an LV10290 Hamamatsu spectrophotometer and controlled using BioKine 32 V4.46 software.

IG film thicknesses were examined using confocal imaging as a non-contact optical 3D profiling technique using Sensofar PLuNeox Microscopy and SensoSCAN software for monitoring.

Morphological studies of IG membranes at different percentages of BMIM TFSI were carried out using a MERLIN FE-SEM Scanning Electron Microscopy at a voltage of 1.0 kV. The samples were pre-treated by coating them with gold using Precision Etching Coating System (PECS™) sputtering.

3. Results

3.1. Influence of IL loading on optical and mechanical properties of IGs

In this study, the IG membranes presented in Fig. 1 were prepared and studied. They contained different cation-anion compositions, IL loading, and doping agents.

The effect of the IL content in the IG (weight percentage) was evaluated by loading different IL amounts in P(VDF-co-HFP) polymer matrices and comparing their optical, electrical and mechanical properties. The combination of $BMIM^+$ cation and $TFSI^-$ anion were used as model IL. Resulting IGs membranes presented clear aspect differences depending on the IL load (Fig. 2 **a**)), which corroborated by spectral analysis. At 50% (weight) of BMIM TFSI or below, IG membranes were opaque, with transmittance percentages (ΔT%) in the visible range below 25% (Fig. 2 **b**)) for 40 μm-thick membranes (thickness determined by optical profilometry) and too rigid to be used in flexible displays. The optical (i.e. transparency) and rheological properties (i.e. flexibility/elasticity) of the IGs improved when increasing the percentage of IL. Maximum light transmittance was obtained when incorporating 90% of IL (ΔT% = 83%), although IG membranes lost mechanical resistance when IL concentration exceeded 86.7%. Hence, optimal IL concentration in the IG was set at 83.3% for combining excellent optical and mechanical performances.

Although IL almost completely masked the polymer network and the factual membranes morphology, SEM images revealed evident morphological changes in the IGs at high IL concentrations that influenced the optical and mechanical properties (Fig. 3).

IL apparently reduced the porosity of the membrane, which may be partially responsible for its opacity, while contributing to polymer swelling, leading to less fragile and more flexible materials. More information was obtained from FTIR spectra (Fig. 4) where pristine IL and polymer were compared to IGs. Bond vibrations corresponding to BMIM TFSI IL were observed at 1465 cm^{-1} (CH_2 scissoring bending), 1350 cm^{-1} (SO_2 antisymmetric stretching + C-SO_2-N bonding), 1229 cm^{-1} (CF vibrational stretching), 1133 cm^{-1} (SO_2 symmetric stretching), 1048 cm^{-1} (S-N-S asymmetric stretching), 792 cm^{-1} (C-S + S-N stretching), and 739 cm^{-1} (CF_2 symmetric bending + C—S stretching). On the other hand, and due to its semi-crystalline nature resulting from the folding of polymer monomers on crystalline spherulite structures [49,50], P(VDF-co-HFP) presented two types of vibrational modes: amorphous polar β-phase vibrations at 1404 cm^{-1} (CF_2 antisymmetric stretching), 870 cm^{-1} (CF_2 and C—C symmetric stretching) and 838 cm^{-1} (CH_2 bonding), and crystalline non-polar α-phase signals at the wavelength of 796 cm^{-1} (CF_2 stretching) and 760 cm^{-1} (CH_2 bonding) [51,52]. In the IG membranes, the peaks coming from BMIM TFSI signals became more intense when increasing the IL content in the hosting P(VDF-co-HFP). In the case of vibrational modes associated with the polymer, those assigned to the β-phase remained present in the FTIR spectra, while those corresponding to the crystalline α-

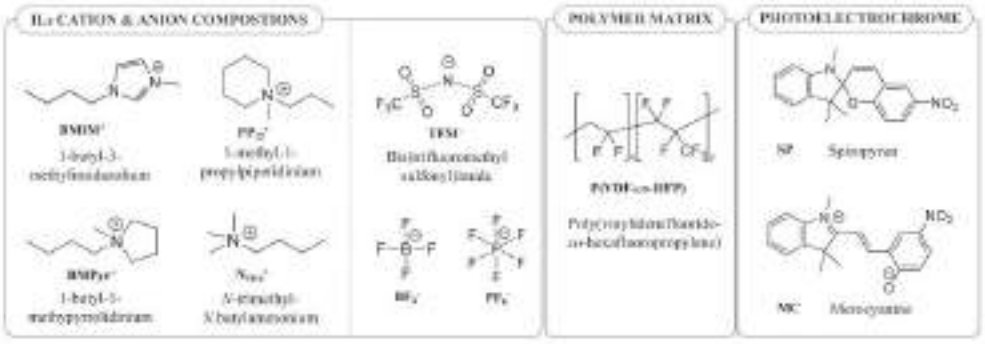

Fig. 1. Molecular structures of cation and anions of IL compositions, polymer matrix, and photoelectrochromic used in this study for IC film forming.

phase disappeared after addition of IL. This result suggested a change in the morphology of the P(VDF-co-HFP) matrix, losing part of its crystallinity and becoming more amorphous by the incorporation of IL molecules. In this sense, the addition of ILs may provoke voids or cavities among polymer chains so that spherulites were no longer formed, increasing the flexibility and elasticity of the polymer and reducing light scattering associated with these highly dispersive crystalline structures.

The ionic conductivity of the ICs was determined by EIS for its direct relationship with the electrochemical performance of the system. EIS spectra showed two consecutives semi-circles (Fig. 5a)) which associated to processes taking place in the electrode-membrane interface and membrane, respectively. Accordingly, EIS data were fitted with the equivalent circuit illustrated in Fig. 5 b), containing: parasite resistance associated to the contacts and the electrode material. R: the components of the electrode-IC interface (R_i and C_i for the interface resistance and capacitance, respectively); and the electrical parameters associated with the IC, namely the IC resistance (R_{IC}), the IC capacitance (C_{IC}) and constant phase element (CPE) associated to mass transport processes in the IC structure.

Ionic conductivity of ICs with different IL content (%wt. of BMIM TFSI; Fig. 6 **a**)) was estimated from R_{IC} impedance as detailed in previous report [53,54].

Ionic conductivity of gel electrolytes is commonly studied by EIS using standard electrochemical cells, where the samples are sandwiched between the electrodes. However, in some cases this experimental setup can modify the thickness of the material affecting final conductivity values. To avoid this problem, screen-printed electrodes are used, since samples are placed on the top of the electrodes. Prior their use, the corresponding cell constant was calculated for this system.

Fig. 6 **b**) shows a linear decay of the inverse of the IC conductivity (resistivity) with the IL content until reaching a value of 1.05 mS/cm at 90% IL in agreement with the expected conductivity of IL solutions (3.60 mS/cm) [55]. The increase of conductivity was associated to two main factors: i) the increase in the concentration of ionic species from the IL and ii) the decrease in the number of crystalline domains of P(VDF-co-HFP) polymer that hinder ion mobility and conductivity of the ICs. These processes, however, did not explain the high increase in conductivity observed in the samples between 86.7% and 90% of BMIM TFSI. In this case, an additional factor influenced conductivity which was the impossibility of the polymer matrix to retain more IL inside its cavities. Thus, the conductivity magnitude obtained in this last case could not be associated to the IC but to IL alone.

In summary, optimal ICs properties (i.e. optical, electrochemical and mechanical) were obtained after loading with 83.3% IL. This proportion was used in further optimizations of the IC formulation.

3.2. Influence of IL composition on optical, mechanical and electrochemical properties of ICs

The influence of the IL composition on IC properties was evaluated by combining different cation, i.e. BMIM, N_{1114}, BMPyr and PP_{13}, and anion molecules, i.e. TFSI, PF_6 and BF_4 (Fig. 7 a), all containing the same molar ratio compared to IC formulated at 83.3% of BMIM TFSI. Results are summarized in Fig. 7. There was a clear correlation between optical and mechanical properties since ICs with more opacity were also qualitatively more rigid and brittle. Two formulations showed a

b)

Sample (% wt. BMIM TFSI)	Transmittance (%)	Conductivity (mS/cm)
0.0	14.8	-
50.0	25.4	-
70.0	50.7	0.168
75.0	56.4	0.238
80.0	63.7	0.342
83.3	71.3	0.396
86.7	76.7	0.540
90.0	83.2	1.060

Fig. 2. a) ICs prepared at different weight ratios of BMIM TFSI, showing the transparency change upon the addition of BMIM TFSI. **b)** Collected data for the change in UV–vis transmittance in the range of 400–700 nm at different loadings of BMIM TFSI and conductivity values obtained by a.c. impedance measurements.

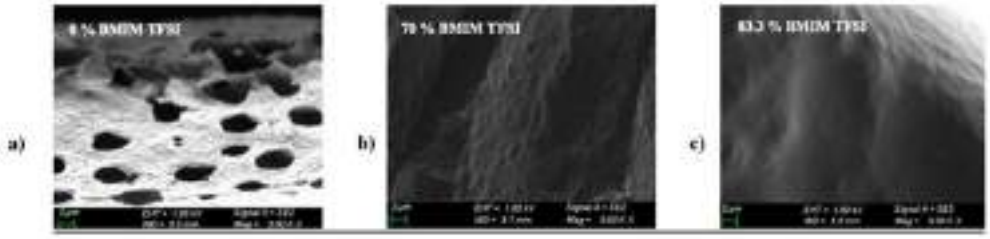

Fig. 3. Cross-sectional SEM images of a) pure P(VDF-co-HFP), b) BMIM TFSI and IGs at different weight loadings of BMIM TFSI (b) 70% and c) and 83.3%.

transmittance below 40% and some rigidity, i.e. BMPyr TFSI and BMIM BF_4. In the first case, BMPyr may have a poorer plasticizer effect than BMIM, used in the model IL, while the other cations presented similar properties. The differences were more evident and reasonable when changing the anion. The transparency increased with the anion size

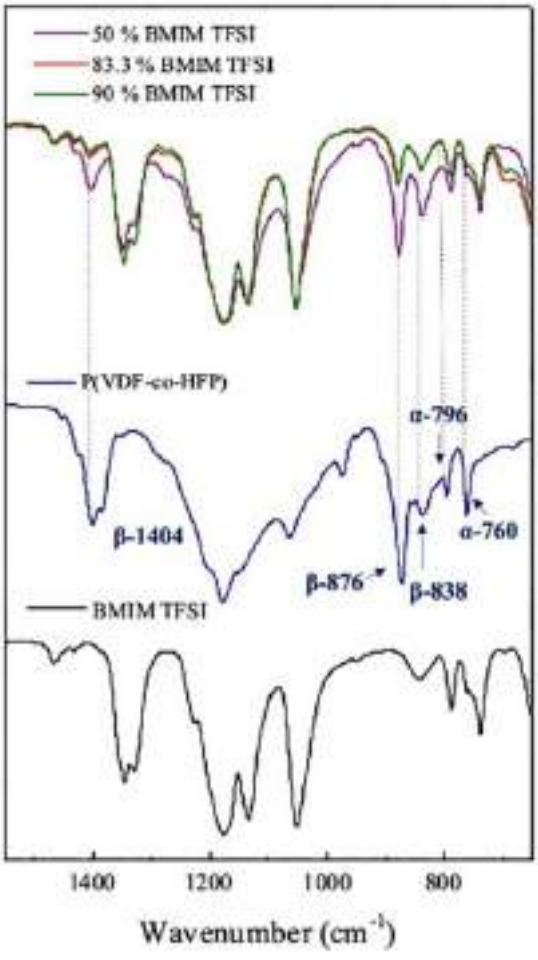

Fig. 4. FTIR spectra of pure BMIM TFSI, pure P(VDF-co-HFP), and IGs at different weight ratios of BMIM TFSI.

(TFSI < PF_6 < BF_4), which attributed to a loss of order in the polymer chain. Qualitatively, elasticity also improved along with the anion size. Large molecules incorporated in the polymeric matrix minimize polymer chain interactions and the formation of crystalline structures, reducing its rigidity and avoiding the formation of highly-dispersing particles responsible of polymer opacity. BF_4^- was too small to produce these structural changes, resulting in opaque and rigid IGs.

The different IL compositions also affected the electrochemical properties of the IG membranes, i.e. the electrochemical window. The electrochemical window was determined as the difference between the reduction and the oxidation potentials from CV at the scan rate of 10 mV/s (see Fig. S2 in supplementary information) that determines the maximum potential range of operation of the electrochromic system.

In IGs, the electrochemical window is limited by the reduction of the cations, and the oxidation of the anions of the ILs. Large electrochemical windows between 2.7 and 3.2 V vs Ag/AgCl were obtained in all cases thanks to the electrochemical stability of the used compounds. The oxidation limits similar values than the reduction ones due to the similarly low electron-donor character of fluorinated anions responsible of the oxidation potential (TFSI, BF_4^-, PF_6^-).

Regarding reduction potentials, when substituting the quaternary amines by alkyl chains (PP_{13}, BMPyr, N_{1114}) the electrochemical reduction significantly shifted to higher values and can be attributed to a poorer electron-withdrawing effect. The combination N_{1114} TFSI provided the largest redox potentials.

Conductivity values for the different IGs formulations were obtained from the inverse of the magnitude of the R_b. EIS spectra when changing anion and cation concentrations and the final conductivity magnitude are illustrated in Fig. 8. In general, all presented conductivities in the range between 0.215 mS/cm and 0.846 mS/cm, which suitable for all-solid and flexible electrochemical applications. The influence of the anion in IG conductivity was low, and only BF_4^- presented a noticeable increase in the conductivity magnitude which associated to its small size and high mobility in the IG matrix. In the case of cations, it was a clear correlation between the IG conductivity and that of the pristine ILs (BMIM > N_{1114} > BMPyr > PP_{13}). Thus, PP_{13}, the one with the largest size and less motility, presented lower conductivities.

Thus, the P(VDF-co-HFP)-based IG doped with 70% IL containing N_{1114} TFSI was selected as the optimal IG formulation in the production of flexible displays for presenting the highest transparency and electrochemical window, while maintaining an acceptable conductivity. Note that 70% of N_{1114} TFSI membranes contains same molar concentration than 83.3% of BMIM TFSI in IG.

3.2. Photo-electrochromic display fabrication

A low-cost two electrode display was prepared as a proof-of-concept by incorporating the well-known photo-electrochromic spiropyran molecule [41–44] on the previous IG. TEMPO molecule was also added as redox mediator to reduce de magnitude of the applied potential necessary to achieve the color change. To evaluate the photochromic and

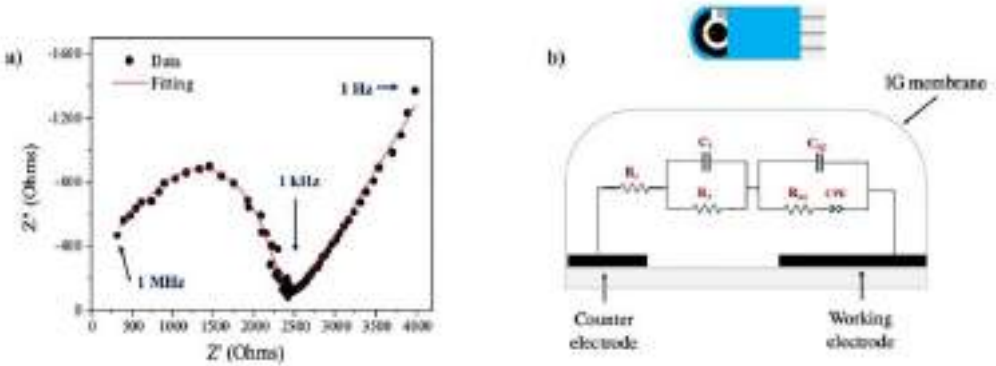

Fig. 5. a) Impedance spectra of IG at 80 wt% BMIM TFSI as an example of general interpretation of Nyquist plots. Experimental data is in black dots and fitted impedance curve is solid red line. b) Equivalent circuit model for impedance spectra of IGs measured using screen-printed electrodes.

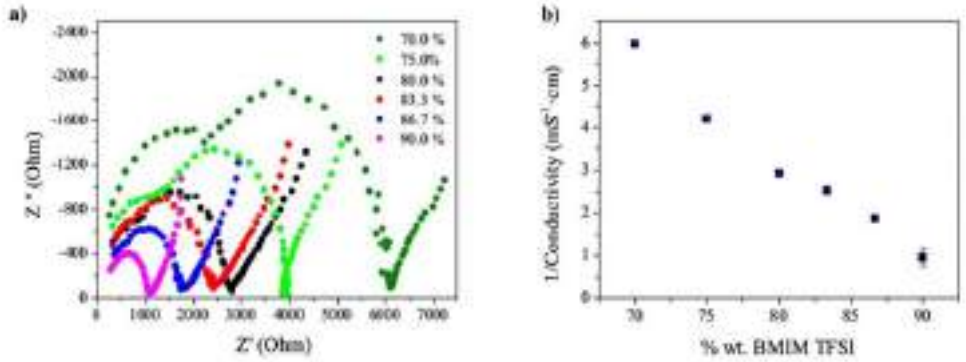

Fig. 6. a) Nyquist plot of IGs at different BMIM TFSI weight ratios. b) Linear relationship between the inverse of the ionic conductivity and % wt. of BMIM TFSI in IG membranes. Error bars were calculated from the standard deviation of fitted R_{ct}.

electrochromic capacity of the IG, it was placed between two flexible ITO-coated PET electrodes. An initial photochromic study demonstrated that spiropyran in the IG matrix responded to optical stimuli (UV light radiation) leading to the photo-isomerization from the spirocyclic form (colorless state, OFF, SP isomer) to its ring-open or merocyanine isomer (pink color, ON, MC isomer), and subsequent recovery after irradiation with visible light. Similarly, the electrochromism of the system was also explored and it was found that the application of a 2 V potential in a two electrodes system (based on the standard potential of spiropyran and TEMPO, (i.e. -1.2 V and 0.80 V vs Ag/AgCl, respectively), was needed to produce the change of color in the IG from transparent to pink-orange by the reduction of SP form and the subsequent electroinduced ring-opening to the MC form (Fig. 9). Mechanistically, the SP form is reduced on the cathode, leading to formation of the

a)

b)

Sample	Transmittance (%)	Conductivity (mS/cm)	Reduction Potential (V)	Oxidation Potential (V)	Electrochemical Window (V)
BMIM TFSI	71.3	0.396	-1.33	1.43	2.76
BMIM PF_6	69.9	0.395	-1.26	1.47	2.73
BMIM BF_4	18.4	0.846	-1.32	1.40	2.72
N_{444} TFSI	72.8	0.303	-2.00	1.20	3.20
BMPyr TFSI	35.9	0.295	-1.73	1.20	2.93
PP_{14} TFSI	65.6	0.215	-1.73	1.10	2.83

Fig. 7. a) IGs prepared with IL with different cations and anions. b) Change in UV–vis transmittance in the range of 400–700 nm using different ILs at the same molar concentration, ionic conductivity values obtained by a.c. impedance measurements and electrochemical windows recorded by CV.

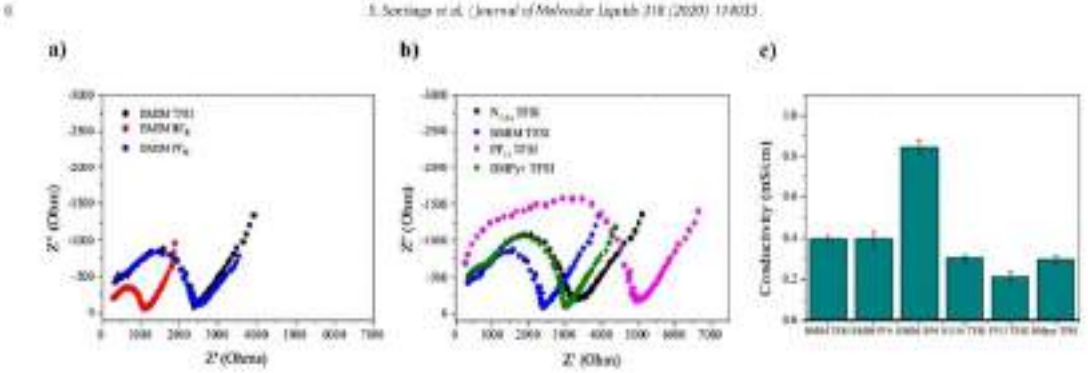

Fig. 8. Nyquist plot of the IGs when changing the a) anion or b) cation composition. c) Comparison of the conductivity magnitude from analysis of the previous EIS spectra. Error bars were calculated from the standard deviation of fitted R_{ct}.

open-ring radical anion, $[MC]^{\cdot-}$. Simultaneously, TEMPO was oxidized on the anode forming the corresponding cationic form, $TEMPO^{+}$. Both species, $[MC]^{\cdot-}$ and $TEMPO^{+}$, diffuse from the respective electrodes through the electrolyte layer to the bulk material. Eventually, $TEMPO^{+}$ was spontaneously regenerated due to the electron transfer reaction with $[MC]^{\cdot-}$. The oxidation of $[MC]^{\cdot-}$ after the homogenous electron transfer led to the open or merocyanine form MC, which resulted in an intense orange-pink coloration. The MC form was easily reconverted into the transparent state, SP form, upon irradiation of the material at 473 nm.

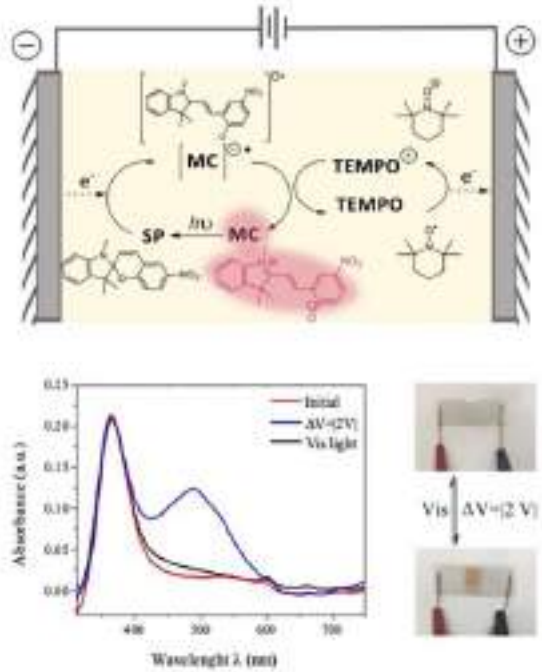

Fig. 9. a) Scheme of the electrochemical and photochemical reactions that take place in the IG membrane. b) UV–Vis absorbance spectra before and after the external inputs were applied. c) Photographs for transparent, when 0 V was applied or after visible light.

4. Conclusions

In summary, an exhaustive study is presented on P(VDF-co-HFP)-IL based IGs, in which their improved formulation perfectly overcome the main issues of typical solid electrolytes for electrochemical applications and more especially for opto-electrochemical devices. Firstly, proper formulations of IGs, particularly, based on BMIM TFSI (83.3% wt.) and $N_{1,1,1,4}$ TFSI achieved high ionic conductivities, a wide electrochemical window – for higher demanding electrochemical applications– and excellent rheological properties, such as good consistency, flexibility, transparency, and elasticity. On the other hand, we demonstrated that the possibility to easily change the IL composition owing to their good chemical compatibility allows their use for further applications to be expanded.

Eventually, we demonstrated the functionality of formulated IGs, showing the performance of an opto-electrochromic device constructed following simple fabrication steps. This proof of concept served to establish and test the compatibility of improved IG formulations with the well-known spiropyran organic photoelectrochrome.

CRediT authorship contribution statement

G.G. conceptualized the research topic, conceived and designed the experiments; S.S. perform the experiments, S.S., X.M-B. and G.G. analyzed and interpreted the results. S.S., X.M-B. and G.G. prepared the manuscript. All authors corrected the draft. G.G. obtained the funds for the research.

Declaration of competing interest

The authors declare no conflicts of interest.

Acknowledgments

The authors thank the Ministerio de Ciencia e Innovación of Spain for financial support though the projects CTQ 2015-65439-R and PID2019-106171RB-I00.

Appendix A. Supplementary data

Supplementary data to this article can be found online at https://doi.org/10.1016/j.molliq.2020.114033.

References

[1] T.P. Lodge, Materials science: a unique platform for materials design, Science (80-.). 321 (5885) (2008) 50–51. https://doi.org/10.1126/science.1156532.

[2] J. Le Bideau, L. Viau, A. Vioux, Ionogels, ionic liquid based hybrid materials, Chem. Soc. Rev. 40 (2) (2011) 907–925, https://doi.org/10.1039/c0cs00059k.

[3] J. Lai, Y. Xing, N. Chen, L. Li, F. Wu, R. Chen, Electrolytes for rechargeable lithium–air batteries, Angew. Chemie – Int. Ed. 59 (8) (2019) 2974–2997.

[4] N. Chen, H. Zhang, L. Li, R. Chen, S. Guo, Ionogel electrolytes for high-performance lithium batteries: a review, Adv. Energy Mater. 8 (32) (2018), 1702056https://doi.org/10.1002/aenm.201702056.

[5] M. Villalonga, M. Bezel, S. Mesa, R.O. Al-Kaysi, J. Hernando, G. Gonzalo, Multidimensional-responsive fluorescent switches based on spirocyclic merocyanine compounds: smart molecules for the Design of Optical Probes and Electrochromic Materials, J. Org. Chem. 83 (16) (2018) 9168–9177, https://doi.org/10.1021/acs.joc.8b01213.

[6] R. Sahraoui, A. Sklitiga, H. Razouq, T. Iqbal, S. Quiroz, PVDF based Ionogels: applications towards electrochemical devices and membrane separation processes, Polym 4 (11) (2018)https://doi.org/10.3390/polym4110647.

[7] M. Aller-Pellitero, S. Santiago-Malagón, J. Ruiz, Y. Alesanco, R. Lakard, J.Y. Hihn, G. Estrade, P.J. del Campo, Fully-printed and silicon free self-powered electrochromic biosensor: towards naked eye quantification, Sensors Actuators B Chem. 306 (December 2019) (2020), 127553https://doi.org/10.1016/j.snb.2019.127553.

[8] R. Garcia-Cortadella, N. Schäfer, J. Comelles-Fernandez, L. Bu, X. Illa, G. Schwesig, A. Mesa, S. Santiago, G. Gonzalo, R. Villa, A. Sirota, F. Serra-Graells, J.A. Garrido, A. Guimerà-Brunet, Switchless multiplexing of graphene active sensor arrays for brain mapping, Nano Lett. 20 (5) (2020) 3528–3537, https://doi.org/10.1021/acs.nanolett.0c00407.

[9] D.R. MacFarlane, M. Forsyth, P.C. Howlett, M. Kar, S. Passerini, J.M. Pringle, H. Ohno, M. Watanabe, F. Yan, W. Zheng, S. Zhang, J. Zhang, Ionic liquids and their solid-state analogues as materials for energy generation and storage, Nat. Rev. Mater. 1 (2) (2016)https://doi.org/10.1038/natrevmats.2015.5.

[10] M. Sahamanli, L. Robitaut, D. Mecerreyes, Polymeric ion gels: preparation methods, characterization and applications, in: A.A.J. Torriero (Ed.), Electrochemistry in Ionic Liquids 2015, pp. 283–315, https://doi.org/10.1007/978-3-319-13485-7_9.

[11] C.A. Giffin, Ionic liquid-based electrolytes for "beyond lithium" battery technologies, J. Mater. Chem. A 4 (35) (2016) 13378–13389, https://doi.org/10.1039/c6ta05300f.

[12] N. Gil-González, T. Aiyazi, A. Zuriaurregui, E. Castaño, F. Benito-Lopez, M.C. Morant-Miñana, Understanding the behavior of stimuli-responsive Ionogels for microfluidic applications, Procedia Eng. 168 (2016) 473–476, https://doi.org/10.1016/j.proeng.2016.11.132.

[13] J.M. Chem, A. Kavanagh, R. Copperthite, M. Dubitha, J. Owens, C. Mcdonagh, Photo-patternable hybrid ionogels for electrochromic applications, J. Mater. Chem. 21 (2011) 8687–8693, https://doi.org/10.1039/c1jm10304f.

[14] H.C. Moon, T.P. Lodge, C.D. Frisbie, Solution-processable electrochromic ion gels for flexible, low-voltage, emissive displays on plastic, J. Am. Chem. Soc. 3712 (2014)https://doi.org/10.1021/ja5062809.

[15] H.C. Moon, C. Kim, T.P. Lodge, C.D. Frisbie, Multicolored , low power , flexible electrochromic devices based on ion gels, ACS Appl. Mater. Interfaces 17 (2016) 6252–6262, https://doi.org/10.1021/acsami.6b01303.

[16] M.S. Kang, T.P. Lodge, Y. Gu, S. Zhang, K.H. Lee, C.D. Frisbie, "Lut and stick" rubbery ion gels as high capacitance gate dielectrics, Adv. Mater. 24 (32) (2012) 4457–4462, https://doi.org/10.1002/adma.201200550.

[17] T.P. Lodge, T. Ueki, Mechanically tunable, readily processable ion gels by self-assembly of block copolymers in ionic liquids, Acc. Chem. Res. 49 (2016) 2307–2314, https://doi.org/10.1021/acs.accounts.6b00308.

[18] C. Sanchez, B.J. Shea, S. Kitagawa, Hybrid materials themed issue, Chem. Soc. Rev. 40 (2011) 907–925, https://doi.org/10.1039/c0cs00059k.

[19] Z. Tang, L. Qi, G. Gao, Structural, thermal, and impedance properties of a gel polymer electrolyte containing ionic liquid, Polym. Adv. Technol. 21 (2010) 153–157, https://doi.org/10.1002/pat.1408.

[20] A.K. Tripathi, Y.L. Verma, R.K. Singh, Thermal, electrical and structural studies on ionic liquid confined in ordered mesoporous MCM-41, J. Mater. Chem. A 3 (2015) 23809–23820, https://doi.org/10.1039/c5ta03006a.

[21] A.I. Horowitz, M.J. Panzer, Poly(Dimethylsiloxane)-supported Ionogels with a high ionic liquid loading, Angew. Chemie Int. Ed. 53 (37) (2014) 9780–9783, https://doi.org/10.1002/anie.201405689.

[22] D.S. Ashby, H. Ryan, O. Block, L. Chen-Han, S. Christopher Patterniello, solution-processed Ionogels for thin-film lithium-ion electrolytes, Joule 1 (2) (2017) 344–358, https://doi.org/10.1016/j.joule.2017.08.012.

[23] X. Wang, H. Zhu, G.W. Greene, J. Li, N. Kumjoue, C. Gartner, J. Rang, M. Armand, M. Forsyth, J.M. Pringle, P.C. Howlett, Enhancement of ion dynamics in organic ionic plastic crystal/PVDF composite electrolytes prepared by co-electrospinning, J. Mater. Chem. A 4 (35) (2016) 8075–8080, https://doi.org/10.1039/c6ta02017a.

[24] N. Li, S. Li, H. Nah, J.J. Vlassak, Mechanical behavior of poly(methyl methacrylate)-based Ionogels, Soft Matter 10 (46) (2014) 7903, https://doi.org/10.1039/C4SM01466A.

[25] S. Thiemann, S.J. Sachnov, F. Pettersson, R. Bollström, R. Österbacka, P. Wasserscheid, J. Zaumseil, Cellulose-based Ionogels for paper electronics, Adv. Funct. Mater. 24 (35) (2013) 625–634, https://doi.org/10.1002/adfm.201302026.

[26] H. Bittar, et al. Use of polymer/ionic liquid plasticizers as gel electrolytes in electrochromic devices, J. Phys. Conf. Ser. 127 (2008)https://doi.org/10.1088/1742-6596/127/1/012015.

[27] Shalu, V.K. Singh, R.K. Singh, Development of ion conducting polymer gel electrolyte membranes based on polymer PVdF-HFP, BMIMTFSI ionic liquid and the Li-salt with improved electrical, thermal and structural properties, J. Mater. Chem. C 3 (2015) 7308–7318, https://doi.org/10.1039/c5tc00940k.

[28] S. Ahlstrand, J. Phend, D. Hilmas, J. Lindgren, J. Tegenfeldt, A. Wendsjö, Crystallinity and morphology of PVdF–HFP-based gel electrolytes, Polymer (Guildf). 42 (2001) 1407–1416, https://doi.org/10.1016/S0032-3861(00)00517-0.

[29] Y. Zhu, M.T. Otley, F. Alhabshi, A. Kumar, X. Zhang, O.M.B. Munangiru, M. Li, B.C. Arden, G.A. Sotzing, Electrochromic properties as a function of electrolyte on the performance of electrochromic devices consisting of a single-layer polymer, Org. Electron. 15 (2014) 1378–1386, https://doi.org/10.1016/j.orgel.2014.03.038.

[30] X. Tan, B. Zhu, Y.P. Xu, [VDF-Co-HFP] membrane for recovery of aroma compounds from aqueous solution by Pervaporation I. Ethyl acetate/water system, J. Membr. Sci. 248 (2005) 105–117, https://doi.org/10.1016/j.memsci.2004.10.003.

[31] S. Ramesh, S. Lu, Effect of lithium salt concentration on crystallinity of poly(Vinylidene fluoride-Co-Hexafluoropropylene)-based solid polymer electrolytes, J. Mol. Struct. 990 (2011) 403–408, https://doi.org/10.1016/j.molstruc.2011.03.005.

[32] E. Alesanco, F. Miranda, D. Schmidt, All-in-one gel-based electrochromic devices: strengths and recent developments, Materials (Basel). 11 (2018) 414, https://doi.org/10.3390/ma11030414.

[33] S.S. Sekhon, Deepa, S.A. Agnihotry, Solvent effect on gel electrolytes containing lithium salts, Solid State Ionics 136–137 (2000) 1189–1192, https://doi.org/10.1016/S0167-2738(00)00584-1.

[34] S.K. Chowdalla, A.L. Saraf, Shalu, V.K. Singh, A.K. Tripathi, A.K. Gupta, Y.L. Verma, R.K. Singh, Studies on structural, thermal and AC conductivity scaling of PEO-LiPF6 polymer electrolyte with added ionic liquid [BMIM]PF6, RSC Adv. 5 (2015), 077178https://doi.org/10.1063/1.4927698.

[35] J.H. Shin, W.A. Henderson, S. Passerini, PEO-based polymer electrolytes with ionic liquids and their use in lithium metal-polymer electrolyte batteries, J. Electrochem. Soc. 152 (2005) 978–983, https://doi.org/10.1149/1.1890701.

[36] J.M. Chem, Y. Ye, J. Rick, B. Hwang, Ionic liquid polymer electrolytes, J. Mater. Chem. A 1 (2013) 2719–2743, https://doi.org/10.1039/c2ta01268b.

[37] J. Fuller, A.C. Breda, R.T. Carlin, Ionic liquid-polymer gel electrolyte, J. Electrochem. Soc. 144 (1997) 8–11.

[38] A. Vioux, L. Viau, S. Volland, J. Le, Use of ionic liquids in sol-gel; ionogels and application, C.R. Chim. 13 (2010) 242–255, https://doi.org/10.1016/j.crci.2009.07.002.

[39] J. Jensen, F.C. Krebs, From the bottom up—flexible solid state electrochromic devices, Adv. Mater. 26 (2014) 7231–7234, https://doi.org/10.1002/adma.201402771.

[40] K. Straatsma, R. Birkjessen, Determining the photoconversion quantum yield of photoswitchable molecules in solution and in the solid state, Sci. Rep. 7 (December 2016) (2017) 1–8, https://doi.org/10.1038/srep41645.

[41] L. Kortekaas, W.R. Browne, The evolution of spiropyran: fundamentals and progress of an extraordinarily versatile photochromic, Chem. Soc. Rev. 48 (12) (2019) 3406–3424, https://doi.org/10.1039/c9cs00203k.

[42] M.J. Pringle, M.T. Stauffer, F.-T. Lin, S.C. Weber, Anodic oxidation mechanism of a spiropyran, J. Chem. Soc. Faraday Trans. 92 (20) (1996) 3991, https://doi.org/10.1039/ft9969203991.

[43] O. Kucharekko, J.T. Van Herpt, B.L. Feringa, P. Rudolf, W.R. Browne, Electrochemical write and read functionality through oxidative dimerization of spiropyran self-assembled monolayers on gold, J. Phys. Chem. C 117 (30) (2013) 15567–15577, https://doi.org/10.1021/jp404058a.

[44] S. Zhang, Q. Zhang, B. Ye, X. Li, X. Zhang, Y. Deng, Photochromism of spiropyran in ionic liquids: enhanced fluorescence and delayed thermal reversion, J. Phys. Chem. B 113 (17) (2009) 6012–6019, https://doi.org/10.1021/jp900218t.

[45] Jin Feng Zhi, R. Baba, K. Hashimoto, A. Fujishima, Photochromic properties of a spirobenzopyran derivative, J. Photochem. Photobiol. A Chem. 92 (1–2) (1995) 91–97, https://doi.org/10.1016/1010-6030(95)04167-0.

[46] M. Natali, S. Giordani, Interaction studies between photochromic spiropyrans and transition metal cations: the curious case of copper, Org. Biomol. Chem. 10 (6) (2012) 1162–1171, https://doi.org/10.1039/c1ob06379b.

[47] J.F. Zhi, R. Baba, A. Fujishima, An electrochemical study of some spirobenzopyran derivatives in dimethylformamide, Berichte der Bunsengesellschaft/Physical Chem. Chem. Phys. 100 (11) (1996) 1802–1807, https://doi.org/10.1002/bbpc.19961001108.

[48] Y.S. Nam, I. Yoo, O. Yarimaga, H.S. Park, D.H. Park, S. Song, J.M. Kim, C.W. Lee, Photochromic spiropyran-embedded PDMS for highly sensitive and tunable optochemical gas sensing, Chem. Commun. 50 (32) (2014) 4281–4284, https://doi.org/10.1039/c4cc00367h.

[49] N. Osaka, K. Yanagi, H. Saito, The optical transparency and structural change of quenched poly(vinylidene fluoride) caused by cold-drawing, Polym. J. 45 (2013) 1038–1042, https://doi.org/10.1038/pj.2013.26.

[50] I.M. Ward, J. Sweeney, Mechanical Properties of Solid Polymers, 3rd ed. John Wiley & Sons, Inc, 2012.

[51] R.P. Vijayakumar, D.V. Khakhar, A. Misra, Phase transformation and enhancement of roughness in polyvinylidene fluoride by cesium salts, J. Polym. Sci. Part B Polym. Phys. 49 (18) (2011) 1339–1344, https://doi.org/10.1002/polb.22303.

[52] V. Bermudez-Ortiz, R. Pogreb, O. Stanevsky, E. Bormashenko, Vibrational Spectrum of PVDF and its interpretation, Polym. Test. 23 (7) (2004) 791–796, https://doi.org/10.1016/j.polymertesting.2004.04.001.

[53] W. Choi, H.C. Shin, J.M. Kim, J.Y. Choi, W.S. Yoon, Modeling and applications of electrochemical impedance spectroscopy (Eis) for lithium-ion batteries, J. Electrochem. Sci. Technol. 11 (1) (2020) 1–13, https://doi.org/10.33961/jecst.2019.00528.

[54] N. Gil-González, T. Aiyazi, E. Castaño, F. Benito-Lopez, M.C. Morant-Miñana, Elucidating the role of the ionic liquid in the actuation behavior of thermo-responsive ionogels, Sensors Actuators B Chem. 260 (2018) 380–387, https://doi.org/10.1016/j.snb.2017.12.153.

[55] A. Seoppa, O. Zech, W. Kunz, R. Buchner, The conductivity of imidazolium-based ionic liquids from (−35 to 195) °C. A. Variation of cations alkyl chain, J. Chem. Eng. Data 55 (5) (2010) 1768–1773, https://doi.org/10.1021/je900781q.

Full Paper Wiley Online Library ELECTROANALYSIS

DOI: 10.1002/elan.201900154

Screen-Printable Electrochromic Polymer Inks and Ion Gel Electrolytes for the Design of Low-Power, Flexible Electrochromic Devices

Sara Santiago,[a] Miguel Aller,[b] F. Javier del Campo,[b] and Gonzalo Guirado*[a]

Abstract: We have developed electrochromic inks and electrolyte materials to enable mass production of flexible electrochromic displays (ECDs) and other optoelectronic devices by screen printing. Here we present a new screen-printable ink incorporating electrochromic polymer, poly (3,4-propylenedioxythiophene)bis(ethylhexyloxy), referred to here as ECP-Magenta, and antimony-doped tin oxide (ATO/TiO_2) particles to facilitate electron transport. Their dispersion in a P(VDF-co-HFP) binder leads to the formation of a new electrochromic ink that is suitable for screen printing. This strategy opens the door to the preparation of similar electrochromic inks based on other organic or polymeric compounds. This approach is scalable and can applied to different fields. Ion gels (IGs) composed of P(VDF-co-HFP) and room temperature ionic liquids (RTILs) are promising solid-state electrolytes with high ionic conductivity, flexibility, elasticity and eco-friendliness. The electrochemical features of different ion gels were analyzed as a function of composition and nature of the ionic liquid. Hence, new formulations of IGs were developed, evaluated by Electrochemical Impedance Spectroscopy, Cyclic Voltammetry, before being incorporated into ECDs. The electrochromic performance of ECP-Magenta ink combined with the RTIL-based IG was evaluated by terms of spectroelectrochemistry showing that fully flexible ECD operating at voltages below 1 V can be screen-printed.

Keywords: Electrochromism · ECP-Magenta · Ionogel · Screen-printing

1 Introduction

Electrochromic (EC) materials change colour upon the application of a current or voltage [1]. An increasing number of reports focuses on the development of electrochromic devices (ECD) such as display panels 2, EC smart windows [3,4] and sunglasses [5,6]. There is a large number of electrochromic materials that can be classified into three main groups: inorganic metal oxides, small organic molecules and polymeric materials. It is important to note that usually voltages between 2 and 3 V are needed in order to reach full contrast in electrochromic devices. The use of high voltages requires caution with pulse lengths to avoid degradation. Hence the design of low-power devices, which can be switched over a useful range of optical transmissions using voltages lower than 1 V is highly desirable. In this work, we report an electrochromic device based on polymeric materials where the switching voltage is considerable smaller than that required by other solid-state EC devices reported to date [7–9].

In this sense, conjugated polymers have been the subject of many studies in recent years as electrochromes as a result of the feasibility of customization of physicochemical properties such as colour control through steric and electronic effects, solubility in common solvents, reversibility, rapid switching times, and high colour contrast [10]. Among conjugated polymer electrochromes, poly(3,4-alkylenedioxythiophenes) have gained significant attention as a result of their ability to switch between vibrantly coloured states and highly transmissive states in seconds or less, and their long-term switching stability [11,12]. Poly(3,4-propylenedioxythiophene) derivatives can be regiosymmetrically disubstituted on the propylene bridge with a range of functional groups to afford high solubility in common organic solvents while still maintaining exceptional switching properties [13,14]. The electrochromic conducting material used in this work which, for convenience will be referred to as ECP-Magenta, belongs to this class (Figure 1). The polymer exhibits an intense and vibrant magenta colour in its as cast, neutral state and becomes transparent when it is oxidized. This results in a high colour contrast exceeding 60 % [12,15].

The construction of solid and flexible systems is a key current trend in the area of electrochromic devices, but processes for their mass production are scarce and costly [14,16–18]. Moreover, despite the efforts made to prepare soluble conjugated polymers that facilitate their process-

[a] S. Santiago, G. Guirado
Department de Química, Universitat Autònoma de Barcelona, C/ Til·lers s/n, 08193-Cerdanyola del Vallès, Barcelona, Spain
E-mail: gonzalo.guirado@uab.cat
[b] M. Aller, F. J. del Campo
Instituto de Microelectrónica de Barcelona, IMB-CNM-CSIC, Campus Universitat Autònoma de Barcelona, C/ Til·lers s/n, 08193-Cerdanyola del Vallès, Barcelona, Spain

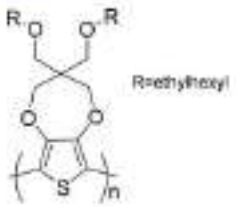

Neutral state

Fig. 1. Molecular structure of ECP-Magenta polymer.

ing and the development of electrochromic applications, simultaneously achieving adequate color properties, high performance and good solubility remains a challenge [19,20]. Besides, conjugated polymers can be synthetically modified to be highly soluble in a variety of organic solvents, but their rheologic properties are often unsuitable for coating techniques such as screen printing unless additives are used, which can adversely affect the electrochromism of the resulting coatings. Here we present a novel strategy to formulate screen-printable electrochromic inks, demonstrating this proof of concept using the conjugated polymer poly(3,4-propylenedioxythiophene) (ECP-Magenta), which maintains the native electrochromic properties of the original ECP-Magenta polymer. Screen-printing enables the design and integration of each of the components of an electrochromic device in a streamlined and cost-effective process that can be adapted to a wide variety of substrates. This method has been widely used for the construction of printed and patterned conjugated polymers for solar cells and light-emitting diodes [21–24]. In line with previous reports [25–29], we propose the use of carrier conductive metal oxide particles dispersed in a resin binder, with the novelty of incorporating the ECP-Magenta polymer as the electrochromic coating. We have investigated the use of antimony-doped tin oxide microparticles (ATO/TiO_2) as a conducting light-coloured material for use in spectroelectrochemistry [30]. This allows not only to observe the colour change of the electrochromic compounds, but also it is a less expensive material than other typical metal oxides as indium-tin oxide nanoparticles (ITO-NP's) commonly used. Despite the electrochromism that ATO microparticles can show, in this case, due to the low potential at which ECP-Magenta is oxidized, the change in color of ATO microparticles does not occur.

In addition to the electrochromic polymer, the electrolyte is another key device component providing a source of ions for charge-balancing and current transport purposes. Polymeric gel electrolytes are promising electrolyte materials due to their low cost, non-volatility, and long term chemical stability [31,32]. However, only few gel electrolytes show sufficiently high ionic conductivity, in the order of $mS\,cm^{-1}$. Among the possible candidates that can be used for flexible ECD, some of the most promising are ion gels (IGs) [33,34] since they show high conductivity and large electrochemical windows [35]. IGs are solid electrolytes composed of a copolymer and a room temperature ionic liquid (RTIL). RTILs have become the focus of many studies due to unique properties such as moderate ionic conductivity, non-toxicity, thermal stability up to 300 °C, electrochemical stability and low volatility. The resulting electrolytes exhibit suitable features for ECD fabrication such as: transparency, elasticity, flexibility and high ionic conductivity. IGs electrolytes can be cut and laminated on layers, but they can even be screen-printed. This enables a very easy, streamlined fabrication of ECDs where all components are flexible [36–38].

In the present work, we have synthesized IGs based on P(VDF-*co*-HFP) with sufficiently high ionic conductivity to serve as electrolytes in ECDs. Although the use altogether of P(VDF-*co*-HFP) with imidazolium ionic liquids is well-known, as far as we are aware this time where a systematic study of IGs electrochemical properties is function of the IL nature and concentration is performed. P(VDF-*co*-HFP) has a high dielectric constant that helps ionic dissociation, and we have explored the influence of using one of the following ILs (1-ethyl-3-methylimidazolium bis(trifluoromethylsulfonyl)imide ([EMIM][TFSI]), 1-butyl-3-methylimidazolium bis(trifluoromethylsulfonyl)imide ([BMIM][TFSI]), 1-butyl-3-methylimidazolium hexafluorophosphate bis(trifluoromethylsulfonyl)imide ([BMIM][PF_6]), and 1-butyl-3-methylimidazolium tetrafluroborate ([BMIM][BF_4]) at different weight ratios (from 1:1 to 1:5) on their conductivity and electrochemical window.

Through the use of the screen printable electrochromic ink formulation developed here, and the choice of an appropriate ion gel, we demonstrate the construction of a fully screen-printed and flexible electrochromic device. We believe this process can be further adapted to a wide variety of comparable conjugated polymers for various other electrochemical devices, which not only provides an inexpensive and rapid fabrication route to produce highly customized ECD in the laboratory, but which can also be transferred to higher volume production environments.

2 Results and Discussion

2.1 ECP-Magenta Ink Formulation and Structural Characterization

A dispersion was formed by sonicating 6 mL of a 30 mg/mL solution of ECP-Magenta and 1 g of ATO/TiO_2 particles in dichloromethane (CH_2Cl_2) for 15 minutes. The solvent was then allowed to evaporate at room temperature. The resulting solid (ECP-Magenta@ATO/TiO_2) was ground into a fine powder and then dispersed in a resin binder consisting of P(VDF-*co*-HFP) polymer dissolved at 15 % w.t. in dimethylpropylurea (DMPU). The ECP-Magenta@ATO/TiO_2-to-binder ratio was approximately 1:5. After thorough mixing, a smooth paste

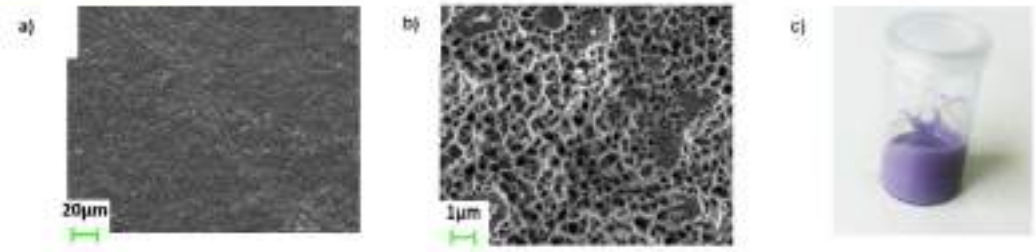

Fig. 2. a) b) SEM images of ECP-Magenta ink films. c) Sample of ECP-Magenta ink.

was obtained that had a suitable consistency to be used as ink for screen-printing with good elasticity and flexibility.

Figure 2 shows SEM images of stenciled films of ECP-Magenta ink. A homogeneous distribution of the ink components can be seen in Figure 2a. A closer look to the material reveals an amorphous and porous structure (Figure 2b). P(VDF-co-HFP) polymer leads to this porous morphology and facilitates ion diffusion through the electrochromic layer which may be related to the enhancement of its electrochromic properties.

2.2 Electrolyte Formulation and Electrochemical Characterization

Due to the low solubility of ECP-Magenta in water and in most organic solvents, the use of ion gel membranes (IGs), as electrolyte, seems to be very attractive. In our case the use of poly(vinylidenefluoride-co-hexafluoropropylene)/ionic liquid based ion gels is the best approach for building the electrochromic devices due to not only the chemical stability of the ECP-Magenta@ATO/TiO2 particles in the ion gel membrane but also the stability, chemical resistance and mechanical strength offer by it. Hence, a new approach based on using IGs and ECP-Magenta as electrolyte and electrochrom, respectively, is explored in other to design low power devices with high fatigue resistance properties.

Ionic conductivity of IGs. The physical and chemical properties of synthesized IGs facilitate the fabrication of EC devices by screen printing as well as a full construction of EC device in solid state. Conductivity of pure RTILs [EMIM][TFSI], [BMIM][TFSI], [BMIM][BF_4] and [BMIM][PF_6] as well as IGs prepared at different weight ratio of ILs mentioned above have previously been explored by EIS at room temperature using interdigitated electrodes. response of AC impedance of IGs using interdigitated electrodes with a simple equivalent circuit [39]. Here, conductivity of IGs has been determined comparing its AC impedance response at interdigitated gold microband electrodes [40]. The equivalent circuit consisted of a constant phase element (CPE) in series with a resistance, *Rs* representing the bulk electrolyte resistance, while the CPE represents the electrode/electrolyte interface. An additional CPE could be considered in parallel to Rs, related to the bulk electrolyte relaxation process [34], but this contribution was considered negligible in the experimental frequency range. The experimental and simulated data fits well indicating the validity of the proposed equivalent circuit (Figure 3).

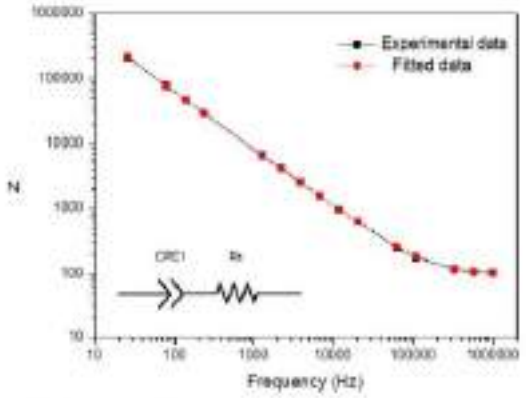

Fig. 3. Bode plot. General behaviour for studies electrolytes. Square symbols correspond to experimental data of IG P(VDF-co-HFP):[BMIM][TFSI] at a weight ratio of 1:5. Red circles corresponds to fitted data from the equivalent circuit.

The magnitude of the electrolyte resistance was estimated from the Bode plot at high AC frequencies, where the main impedance contribution corresponds to the electrolyte resistance, because |Z| does not depend on the frequency signal at high frequencies.

Results for each studied electrolyte are summarized in Table 1. When a RTIL is incorporated into the P(VDF-co-HFP) matrix, the conductivity of the resulting IGs gradually increase until they reach the ionic association point. Beyond this, conductivity decreases as more RTIL is added due to the saturation of ions at high concentrations. Nevertheless, there exists a compromise between their ionic conductivities and their rheological properties since low content of RTIL leads to a more crystalline electrolyte with low conductivity. When RTIL is added to the polymer the membrane becomes flexible and its conductivity increases. At higher amounts of RTIL, the resulting IG becomes less mechanically consistent.

Table 1. IGs formulation and conductivities.

Sample	P(VDF-co-HFP): IL weight ratio	Conductivity (mS/cm)
[EMIM][TFSI]	–	8,890
P(VDF-co-HFP) – [EMIM][TFSI]	1:1	0,102
P(VDF-co-HFP) – [EMIM][TFSI]	1:3.5	0,091
P(VDF-co-HFP) – [EMIM][TFSI]	1:5	0,052
[BMIM][TFSI]	–	3,900
P(VDF-co-HFP) – [BMIM][TFSI]	1:1	0,056
P(VDF-co-HFP) – [BMIM][TFSI]	1:3.5	0,085
P(VDF-co-HFP) – [BMIM][TFSI]	1:5	0,104
[BMIM][BF_4]	–	3,700
P(VDF-co-HFP) – [BMIM][BF_4]	1:1	0,057
P(VDF-co-HFP) – [BMIM][BF_4]	1:3.5	0,051
P(VDF-co-HFP) – [BMIM][BF_4]	1:5	0,046
[BMIM][PF_6]	-	2,200
P(VDF-co-HFP) – [BMIM][PF_6]	1:1	0,290
P(VDF-co-HFP) – [BMIM][PF_6]	1:3.5	0,136
P(VDF-co-HFP) – [BMIM][PF_6]	1:5	0,170

For this reason, the IG composed by P(VDF-co-HFP) – [BMIM][TFSI] at a weight ratio of 1:5 is the one used for the following spectroelectrochemical study since it shows a sufficient ionic conductivity, transparency, flexibility, and the possibility to be cut and stick or even screen-printed. This formulation allows us to screen print an electrolyte layer, leading to a simple fabrication process.

Electrochemical windows. IGs were explored by cyclic voltammetry to demonstrate that the electrolyte is electrochemically stable in the voltage window where many electrochromic polymers are switched. Figure 4 shows

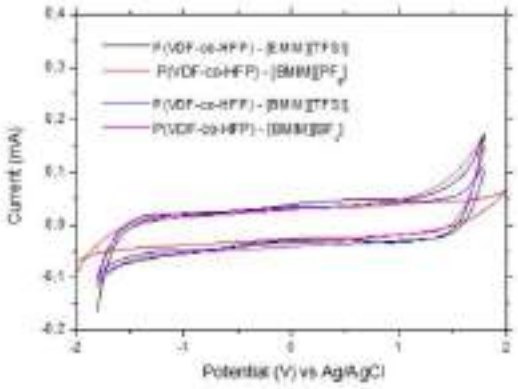

Fig. 4. Cyclic Voltammograms of several IGs at 50 mV/s. Scan Range: 0.00 V/−1.90 V/1.90 V/0.00 V.

cyclic voltammograms of IGs containing ILs at a weight ratio of 1:5 and at a scan rate of 50 mV/s. The electrochemical window of IGs spans from −2 V to +2 V vs SCE, bound by the reduction and oxidation of the RTIL anion and cation, respectively. The electrochemical window is wide enough to be used as electrolytes in the fabrication of ECDs. These results establish that the formulated IGs are electrochemically stable for this application, since the oxidation of ECP-Magenta occurs at ca. 0.3 V vs Ag/AgCl.

2.3 Electrochromic Properties of ECP-Magenta Ink Using P(VDF-co-HFP) – [BMIM][TFSI] at a Weight Ratio of 1:5 as Electrolyte

Handmade screen-printed electrodes were used to explore the performance of the electrochromic ECP-Magenta paste/ink using IG electrolyte. Fabrication and characterization of handmade screen-printed electrodes has been previously reported [41]. Electrochromic properties of formulated ECP-Magenta ink were explored using sample of [BMIM][TFSI] as IG electrolyte at a weight ratio of 1:5 (P(VDF-*co*-HFP):[BMIM][TFSI]) since it has shown one of the highest conductivities as well as good transparency and flexibility. Similar results were found for IG-[EMIM][TFSI], suggesting the possibility of using it as electrolyte indistinctly. For this study, the resulting ECP-Magenta ink was stenciled covering the working electrode, and the IG electrolyte was cut and placed covering the counter and working electrodes (Figure 5).

Cyclic Voltammetry Experiments. CV was used to determinate the redox potential at which ECP-Magenta ink switches between its two coloured states. Figure 6 shows CV curves of ECP-Magenta ink using IG-[BMIM][TFSI] as electrolyte at a scan rate of 50 mV/s. Hence, for all the experiments scan range used was from −0.30 V to 0.60 V vs Ag/AgCl, since ECP-Magenta shows a single reversible peak (E_{pa} = 0.30 V and E_{pc} = 0.20 V vs Ag/AgCl). Note that the electrochemical oxidation potential of ECP-Magenta ink in film using IG-[BMIM][TFSI] electrolyte is slightly shifted to 0.3 V due to its electron-rich character. Figure 6 b shows a linear relationship between the anodic peak current density and the scan rate from 5 mV/s to 200 mV/s. This is consistent with the fact

Fig. 5. Handmade electrode fabrication by screen-printing.

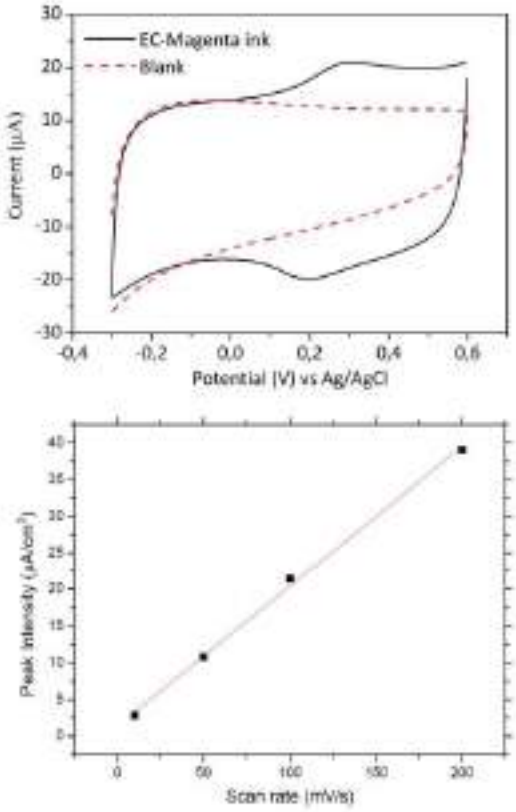

Fig. 6. a) Cyclic Voltammograms of EC-Magenta paste/ink using IG-[BMIM][TFSI] as electrolyte (solid black line) and blank (red dashed line) b) Current Intensity of anodic peaks as a function of the scan rate.

that the electroactive compound is fixed on the electrode surface, unable to diffuse, the Randles & Sevčik equation for diffusion-controlled systems is no longer valid. Thus, a modified equation for describing thin-film cyclic voltammetry processes is used. The relation between peak current and scan rate is given by equation 1:[42]

$$I_p = n^2F^2\Gamma v/4RT \quad (1)$$

where Γ is the total amount of active species initially present at the electrode surface. According to this equation, peak currents showing a linear dependence between peak current density and scan rate prove the formation of well adhered polymer films and non-diffusion controlled reversible redox processes in this scan rate range.

Spectroelectrochemical study of EC-Magenta ink using p(VDF-co-HFP)-[BMIM][TFSI] at a weight ratio of 1:5 as electrolyte. ECP-Magenta ink presents two stable states with different electrooptical properties resulting from the reversible redox reaction (Figure 7).

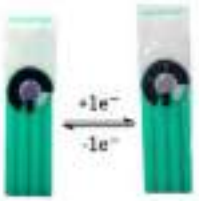

Fig. 7. Performance of ECP-Magenta using state using IG-[BMIM][TFSI] as electrolyte before (left) and after (right) applying 0.4 V.

The UV-vis spectra of neutral ECP-magenta ink shows an intense absorption band at $\lambda_{max} = 528$ nm (Figure 8), which is in good agreement with previous reported data [15]. This strong absorption in the visible range originates from the polymer's π–π^* transition. Electrochemical oxidation of ECP-Magenta leads to the formation of charged states along the backbone (cation radical and dication), where light absorption is transitioned to longer wavelengths, outside of the visible region, with a concurrent loss of absorption from the π–π^* transition. The minimum oxidation potential, E_{op}, at which the EC-Magenta is reversibly oxidized, was determined from the voltabsortogram shown in Figure 9. Voltabsortograms show the transient reflectance change at a specific wavelength in

response to a voltage sweep. From the voltabsortogram the maximum change in reflectance matches the anodic peak from the CV at 0.3 V vs Ag/AgCl. To evaluate the contrast and ensure complete conversion between the two states, the film was switched between 0.40 V vs Ag/AgCl (colorless) and 0.1 V vs Ag/AgCl (coloured). Color contrast was estimated by the difference in % between the reflectance value at λ_{max} of its neutral and oxidized state which in this case was 60 %.

The cycling stability (fatigue resistance) of ECP-Magenta ink performed using [BMIM][TFSI] IG as electrolyte, was evaluated by chronoamperometry (CA) measurements and recording its reflectance UV-vis spectra at 550 nm in situ. The electrochromic parameters are depicted in Table 2. Switching colour between the two ECP-Magenta states were explored by applying 0.4 V and 0.1 V for 5 s at each step. After switching 500 cycles colour contrast decreased approximately by 20 %. The

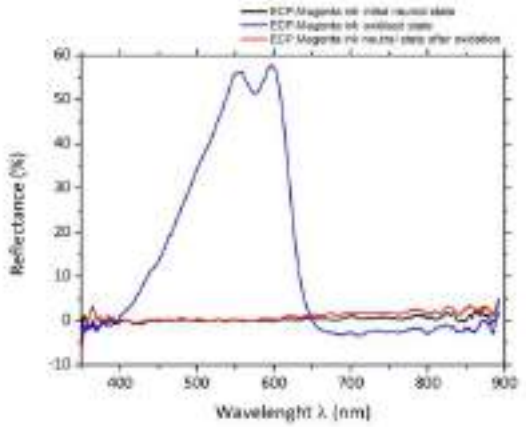

Fig. 8. UV-vis reflectance spectra of EC-Magenta paste/ink in its neutral and oxidized state using IG-[BMIM][TFSI] as electrolyte.

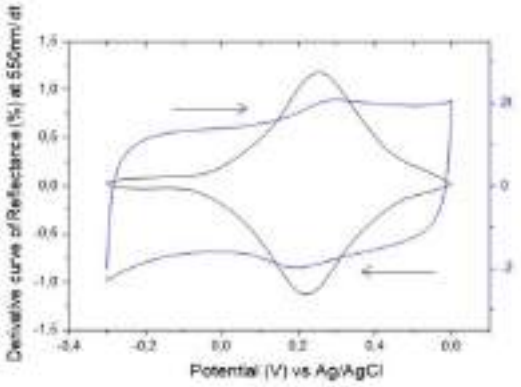

Fig. 9. Voltoabsortogram and overlayed cyclic voltammogram of ECP-Magenta ink using IG-[BMIM][TFSI] as electrolyte.

Table 2. Electrochromic parameters of EC-Magenta ink using IG-[BMIM][TFSI] as electrolyte.

Cycles	ΔT (%)	T_c (S)	T_b (S)	ΔOD	CE (cm^2/C)
1–4	60 %	2,1	2,2	0,190	496
496–500	40 %	2,04	2,04	0,13	–

aim is to select the minimum potential at which the color change occurs to ensure a final device that could work at a potential below 1 V or less. For this reason, the contrast decay may be related to the narrow voltage window we applied. The response time is defined as the time required for 90 % reflectance change in the bleaching process (τ_b) and colouring process (τ_c). The response time is about 2 s and there is no significant change on its value after and before 500 cycles; (Figure 10) which meets the requirement for most electrochromic devices (0.1 s–10 s).

Coloration efficiency (CE) is defined as the change in optical density (ΔOD) induced by unit charge density. CE is calculated from the equations 2 and 3, where *Tc* and *Tb* are the transmittance or reflection values of the colored and bleached states, respectively.

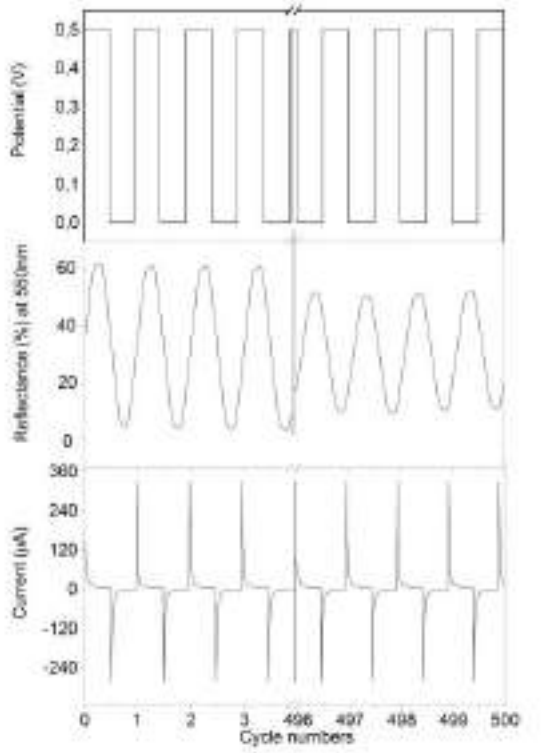

Fig. 10. Applied potential, chronoamperogram, and transmittance of EC-Magenta ink using IG-[BMIM][TFSI] as electrolyte.

$$CE = \frac{\Delta OD}{Q} \quad (2)$$

$$\Delta OD = \log\left(\frac{T_{\lambda}^{*}}{T_{\lambda}}\right) \quad (3)$$

The calculated CE values of EC-Magenta using IG-[BMIM][TFSI] as electrolyte is 496 cm^2/C which is in agreement with other studies and indicates that little charge is needed to produce a measurable color change [43]. These results suggest that these new materials perform well and are promising candidates for application in flexible ECD.

3 Conclusions

A novel screen-printable ink based on ECP-Magenta has been successfully formulated using ECP-Magenta, ATO/TiO_2 nanoparticles, and a P(VDF-co-HFP) binder. The ink films showed significant colour change at low potentials (0.3 V vs Ag/AgCl) in comparison with other electrochromic composite films or ink formulation. Besides, this new ECP-Magenta ink exhibits higher optical contrast values and coloration efficiency. Response time for bleaching and colouring is ~2 s which can be improved by optimizing the thickness of the film. Note that the formulation of the electrochromic ink is compatible with the use of "eco-friendly" flexible electrolytes, such as RTIL-IGs. Besides, this strategy will enable the formulation of further inks using different organic electrochromic compounds. All these features, specially its low potential at which the colour change occurs, enable to use this material in the fabrication of smart devices, such as flexible displays or sensors. In the case of sensors, thanks to this formulation, they can be totally manufactured using screen-printing technologies. Thus, the use of this low-cost, easy and reproducible methodology for a next generation of devices based on this material is potentially available.

4 Experimental Section

4.1 Materials

Poly(3,4-propylenedioxythiophene)bis(ethylhexyloxy) or EC-Magenta polymer of 15 kDa, was used as the EC material on the active layer and kindly provided by The Reynolds Research Group. EC-Magenta was synthesized according to previously reported procedure [14]. Toluene (99 %, Sigma-Aldrich) was used to dissolve EC-Magenta.

Poly(vinylidenefluoride-co-hexafluoropropylene), P(VDF-co-HFP), with Mw = 400000 g/mol was purchased from Sigma-Aldrich and used as received. Ionic liquids, [BMIM][TFSI], [EMIM][TFSI], were purchased from Solvionic and stored under dried conditions. Antimony-tin oxide particles (ZELEC 1610-S) were kindly provided by Milliken Chemical Company. Zelec materials by Milliken provide cost-effective, static-dissipative performance for coatings and polymers. They are non-volatile, non-corrosive, and resistant to heat, chemicals and humidity. Zelec enhances quality and durability by imparting resistivity throughout the lifetime of coatings, paints, and security inks and electronics products. ITO nanoparticles were purchased from Alfa Aesar (ITO Nanotek, ref. 44927).

Screen printed electrodes were homemade and used for the spectroelectrochemical and electrochemical characterization. Carbon ink (C2030519P4) was used for working and counter electrodes and silver/silver chloride (C61003P7) screen-printing paste for reference electrode (Gwent Electronic Materials Ltd., UK).

4.2 Preparation of EC-Magenta Ink

6 mL of a solution of EC-magenta polymer in dichloromethane at 30 mg/mL concentration was sonicated for 15 minutes with 1 g ATO/SiO2-NP's. Remaining dichloromethane was evaporated at room temperature and the resulting conductive powders were manually ground using a mortar and pestle. A resin binder is prepared by mixing P(VDF-co-HFP) at 15 % wt. in dimethylpropilurea (DMPU) and heated at 80 °C. Eventually, the dryed particles were mixed and dispersed in a resin binder in a pigment-to-binder weight ratio of 1:5. After thorough mixing, a smooth paste is obtained.

4.3 Preparation of Ion Gels (IGs)

All the chemicals used for the preparation of Ion Gels (IGs) were dry. A desired amount of and P(VDF-co-HFP) polymer was dissolved in anhydrous acetone under stirring at 50 °C until a homogeneous solution was obtained. Ionic Liquid (IL) was added then at different weight ratios on the previous solution (1:1/1:3/1:5; P(VDF-co-HFP):IL) and stirred again for 1 h. The resulting viscous solution was transferred to ceramic evaporating dish and was left at room temperature for 24 h until the solvent was completely evaporated. Eventually, a transparent, flexible and elastic thin film was obtained that could be cut with any shape and stick on a substrate. Note that the thickness of the film is c.a. 10 µm, hence it is able to work in transmittance mode using a reflectance setup.

4.4 Instrumentation

Electrochemical Impedance Spectroscopy (EIS) experiments were performed at room temperature using Solartron 1287 potentiostat/galvanostat interfaced to a frequency response analyser (Solartron 1260). EIS was measured over the frequency range from 1 MHz to 0.1 Hz at a potentiostatic signal amplitude of 15 mV. Interdigitated electrodes of Au with 54×2 bands 10 µm of width and 1500 µm of length were used for impedance measurements.

Electrochemical characterization of EC-Magenta and EC-Magenta paste, potentiostat VSP100 model and EC-

Lab V9.51 software was used. Absorbance spectroelectrochemical measurements, potentiostat was coupled to Hamamatsu spectrophotometer L10290 model. DRP-SPELEC1050 model was used in further spectroelectrochemical studies enabling recording reflectance and transmittance spectra of opaque screen-printed electrodes.

Morphology and chemical analysis of EC-Magenta paste was studied with Auriga-40 (Carl Zeiss) Scanning Electron Microscopy (SEM) carried out by CNM Inspection Laboratory.

Acknowledgements

GG and SS acknowledge the Spanish Ministry for Education, Culture and Sports for financial support through CTQ2015 65439-R from MINECO/FEDER. SS and MA are supported by FEDER funds managed by the Catalan Secretary of Universities and Research through project PROD-0000114 (Enterprise and Knowledge, Industry Department, Generalitat de Catalunya). JdC gratefully acknowledges financial support through a 2016 BBVA Foundation Grant for Researchers and Cultural Creators. The authors are grateful to Milliken for providing the electroconductive powders featured in this work. Finally, the authors are pleased to acknowledge the Reynolds Group (Drs. Anna M. Österholm, Eric Shen, and John R. Reynolds) of Georgia Institute of Technology, Atlanta (USA) for generously providing the ECP-Magenta polymer, and for their continued support, availability, helpful discussions and technical advice.

References

[1] R. J. Mortimer, *Annu. Rev. Mater.* **2011**, *41*, 241–268.
[2] C. M. Lampert, *Sol. Energy Mater. Sol. Cells* **2003**, *76*, 489–499.
[3] C. G. Granqvist, *Thin Solid Films* **2014**, *564*, 1–38.
[4] A. Azens, C. G. Granqvist, *J. Solid State Electrochem.* **2003**, *7*, 64–68.
[5] P. Chandrasekhar, B. J. Zay, C. Cai, Y. Chai, D. Lawrence, *J. Appl. Polym. Sci.* **2014**, *131*, 1–21.
[6] R. J. Mortimer, D. R. Rosseinsky, P. M. S. Monk, *Electrochromic Mater. Devices* **2015**, *77*, 1–638.
[7] V. Beni, D. Nilsson, P. Arven, P. Norberg, G. Gustafsson, A. P. F. Turner, *ECS J. Solid State Sci. Technol.* **2015**, *4*, S3001–S3005.
[8] P. A. Eraman, J. Kawahara, M. Berggren, *Org. Electron. Phys., Mater. Appl.* **2013**, *14*, 3371–3378.
[9] A. Mahi, R. Brooke, X. Liu, D. Zhao, P. Andersson Ersman, M. Fahlman, M. P. Jonsson, M. Berggren, X. Crispin, *J. Mater. Chem. C* **2016**, *4*, 9680–9686.
[10] A. L. Dyer, A. M. Österholm, D. E. Shen, K. E. Johnson, J. R. Reynolds, *Electrochromic Mater. Devices* **2015**, 113–184.
[11] A. Elschner, *PEDOT* **2011**.
[12] J. Rammelt, D. E. Shen, T. Mustonen, N. Fruehauf, *ACS Appl. Mater. Interfaces* **2015**, *7*, 12001–12008.
[13] A. L. Dyer, E. J. Thompson, J. R. Reynolds, *ACS Appl. Mater. Interfaces* **2011**, *3*, 1787–1795.
[14] B. D. Reeves, C. R. G. Grenier, A. A. Argun, A. Cirpan, T. D. McCarley, J. R. Reynolds, *Macromolecules* **2004**, *37*, 7559–7569.
[15] D. Eric Shen, A. M. Österholm, J. R. Reynolds, *J. Mater. Chem. C* **2015**, *3*, 9715–9725.
[16] R. R. Søndergaard, M. Hösel, M. Jørgensen, F. C. Krebs, *J. Polym. Sci. Part B Polym. Phys.* **2013**, *51*, 132–136.
[17] J. Padilla, A. M. Österholm, A. L. Dyer, J. R. Reynolds, *Sol. Energy Mater. Sol. Cells* **2015**, *140*, 54–60.
[18] A. M. Österholm, D. E. Shen, D. S. Gottfried, J. R. Reynolds, *Adv. Mater. Technol.* **2016**, *1*.
[19] A. L. Dyer, M. R. Craig, J. E. Babiarz, K. Kiyak, J. R. Reynolds, *Macromolecules* **2010**, *43*, 4460–4467.
[20] Y. Yin, W. Li, X. Zeng, P. Xu, I. Murtaza, Y. Guo, Y. Liu, T. Li, J. Cao, Y. He, H. Meng, *Macromolecules* **2018**, *51*, 7853–7862.
[21] P. Matyba, H. Yamaguchi, G. Eda, M. Chhowalla, L. Edman, N. D. Robinson, *ACS Nano* **2010**, *4*, 637–642.
[22] S. H. Ju, B. K. Ju, J. H. Choi, Y. M. Kim, Y. W. Park, K. K. Paek, J. W. Lee, J. W. Yang, J. W. Huh, J. W. Lee, *J. Appl. Phys.* **2008**, *103*, 44502.
[23] J. Birnstock, J. Blässing, A. Hunze, M. Scheffel, M. Stößel, K. Heuser, G. Wittmann, J. Wörle, A. Winnacker, *Appl. Phys. Lett.* **2001**, *78*, 3905–3907.
[24] F. C. Krebs, *Sol. Energy Mater. Sol. Cells* **2009**, *93*, 394–412.
[25] J. P. Coleman, A. T. Lynch, P. Madhukar, J. H. Wagenknecht, *Sol. Energy Mater. Sol. Cells* **1999**, *56*, 375–394.
[26] H. Fellow, *J. Org. Chem.* **1969**, *56*, 4248–4250.
[27] J. Liu, J. P. Coleman, *Mater. Sci. Eng. A* **2000**, *286*, 144–148.
[28] M. A. Pellitero, A. Guimerà, M. Kitsara, R. Villa, C. Rubio, B. Lakard, M. L. Doche, J. Y. Hihn, F. J. del Campo, *Chem. Sci.* **2017**, 1995–2002.
[29] M. A. Pellitero, J. Fremeau, R. Villa, G. Guirado, B. Lakard, J. Y. Hihn, F. J. del Campo, *Sensors Actuators B Chem.* **2019**.
[30] M. A. Pellitero, A. Colina, R. Villa, F. J. del Campo, *Electrochem. Commun.* **2018**, *93*, 123–127.
[31] C. Zhong, Y. Deng, W. Hu, J. Qiao, L. Zhang, J. Zhang, *Chem. Soc. Rev.* **2015**, *44*, 7484–7539.
[32] F. A. Alamer, M. T. Otley, Y. Zhu, A. Kumar, G. A. Sotzing, *Sol. Energy Mater. Sol. Cells* **2015**, *132*, 131–135.
[33] T. P. Lodge, T. Ueki, *Acc. Chem. Res.* **2016**, *49*, 2107–2114.
[34] R. D. Armstrong, *J. Electroanal. Chem.* **1974**, *52*, 413–419.
[35] V. K. Singh, R. K. Singh, *J. Mater. Chem. C* **2015**, *3*, 7305–7318.
[36] Shulu, V. K. Singh, R. K. Singh, *J. Mater. Chem. C* **2015**, *3*, 7305–7318.
[37] Z. Tang, L. Qi, G. Gao, *Polym. Adv. Technol.* **2010**, *21*, 153–157.
[38] B. Dong, L. Zheng, J. Xu, H. Liu, S. Pu, *Polymer (Guildf.)* **2007**, *48*, 5548–5555.
[39] O. Laczka, E. Baldrich, F. X. Muñoz, F. J. Del Campo, *Anal. Chem.* **2008**, *80*, 7239–7247.
[40] O. Laczka, E. Baldrich, F. X. Muñoz, F. J. del Campo, *Anal. Chem.* **2008**, *80*, 7239–7247.
[41] E. P. Randviir, D. A. C. Brownson, J. P. Metters, R. O. Kadara, D. E. Banks, *Phys. Chem. Chem. Phys.* **2014**, *16*, 4598–4611.
[42] A. J. Bard, L. R. Faulkner, *Electrochemical Methods: Fundamentals and Applications*, 2nd ed.: New York, **2001**.
[43] S. Zhang, G. Sun, Y. He, R. Fu, Y. Gu, S. Chen, *ACS Appl. Mater. Interfaces* **2017**, *9*, 16426–16434.

Received: March 5, 2019
Accepted: April 12, 2019
Published online on ■■, ■■

FULL PAPER

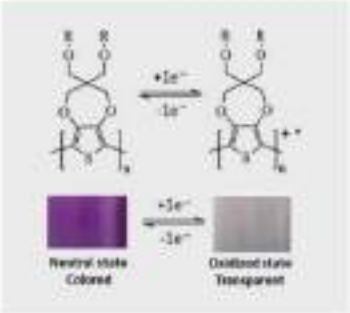

*S. Santiago, M. Aller, F. J. del Campo, G. Gutiérrez**

ARTICLE IN PRESS

Biosensors and Bioelectronics xxx (xxxx) xxx

Contents lists available at ScienceDirect

Biosensors and Bioelectronics

journal homepage: http://www.elsevier.com/locate/bios

A self-powered skin-patch electrochromic biosensor

Sara Santiago-Malagón [a], Diego Río-Colín [b], Haniyeh Azizkhani [a], Miguel Aller-Pellitero [c,d], Gonzalo Guirado [a], F. Javier del Campo [c,e,f,*]

[a] Universitat Autònoma de Barcelona, Bellaterra, Spain
[b] Universidad Del País Vasco, UPV-EHU, Campus de Leioa, Vizcaya, Spain
[c] Instituto de Microelectrónica de Barcelona, IMB-CNM (CSIC), Campus de la Universitat Autònoma de Barcelona, Esfera UAB, 08193, Bellaterra, Barcelona, Spain
[d] Johns Hopkins University School of Medicine, Baltimore, MD, USA
[e] BCMaterials, Basque Center for Materials, Applications and Nanostructures, UPV/EHU Science Park, 48940, Leioa, Spain
[f] IKERBASQUE, Basque Foundation for Science, 48009 Bilbao, Spain

ARTICLE INFO

Keywords:
Electrochromism
Biosensors
Self-powered devices
Wearables
Lactate biosensor
Sweat sensing

ABSTRACT

One of the limitations of many skin-patch wearable sensors today is their dependence on silicon-based electronics, increasing their complexity and unit cost. Self-powered sensors, in combination with electrochromic materials, allow simplifying the construction of these devices, leading to powerful analytical tools that remove the need for external detection systems. This work describes the construction, by screen-printing, of a self-powered electrochromic device that can be adapted for the determination of metabolites in sweat by the naked eye in the form of a 3 × 15 mm colour bar. The device comprises a lactate oxidase and osmium polymer –based anode connected to a coplanar 3 × 15 mm Prussian Blue, PB, cathode printed over a transparent poly(3,4-ethylenedioxythiophene) polystyrene sulfonate, PEDOT:PSS electrode. An ion-gel composed of Poly(vinylidene fluoride-co-hexafluoropropylene), PVDF-co-HFP, a gelling agent, and ionic liquid 1-Ethyl-3-methylimidazolium trifluoromethanesulfonate, EMIM-Tf, effectively separates the cathodic display from the biosensing anode, protecting it from the sample. Despite its cathodic electrochromism, the PEDOT:PSS has a transmission above 90% and does not mask the Prussian Blue colour change because the cathode does not operate below 0 V vs Ag/AgCl at any time. The sensor displays lactate concentrations in the range of 0–10 mM over the length of the electrochromic display, which has a contrast ratio of 1.43. Although full response takes up to 24 min, 80% of the colour change is displayed within 10 min.

1. Introduction

Electrochromic materials change optical properties as a function of their oxidation state (Mortimer, 2011; Mortimer et al., 2015). Although they are most commonly used in the fabrication of displays and optoelectronic devices such as anti-glare rearview mirrors, dimmable windows, and electrochromic printed displays (Andersson et al., 2000; Singh et al., 2017), electrochromic materials can also be successfully used in sensing (Aller-Pellitero et al., 2019; Vishnikin et al., 2019). The main advantages of electrochromic devices are their relatively low power consumption compared to other technologies, and the ease of fabrication through large-area processes, which also implies low unit costs. Besides, electrochromic sensors simplify device construction by adding the function of information display to the (electrochemical) sensing event. However, extracting chemical information through electrochromic materials is non-trivial and remains as one of the leading design challenges facing electrochromic (bio)sensors (Aller Pellitero and del Campo, 2019). In a recent literature survey, we found that electrochromic sensors expressed their analytical results either by changes in colour hue (Lee and Cronin, 2012; Popov et al., 2019; Vishnikin et al., 2019; Zhang et al., 2017) or by creating colour gradients (Limo et al., 2015) and coloured bands of different length (Aller Pellitero and del Campo, 2019). Systems based on colour hue readings require additional instrumentation, such as a spectrophotometer or, in a simpler approach, a smartphone camera, and their corresponding colour analysis software, which correlates colour intensity with an analyte concentration. While this facilitates automation and affords higher sensitivities, it also imposes restrictions on the users and limits the number of possible

* Corresponding author. Instituto de Microelectrónica de Barcelona, IMB-CNM (CSIC), Campus de la Universitat Autònoma de Barcelona, Esfera UAB, 08193, Bellaterra, Barcelona, Spain.
E-mail address: javier.delcampo@bcmaterials.net (F.J. del Campo).

https://doi.org/10.1016/j.bios.2020.112679
Received 5 October 2020; Received in revised form 20 November 2020; Accepted 1 December 2020
Available online 8 December 2020
0956-5663/

Please cite this article as: Sara Santiago-Malagón, *Biosensors and Bioelectronics*, https://doi.org/10.1016/j.bios.2020.112679

form-factors. In contrast, devices based on the translation of chemical information into colour lengths can be read and interpreted by the naked eye without the need for any additional instrumentation (Aller-Pellitero et al., 2017, 2020), providing semi-quantitative results.

Despite their low consumption, power remains an essential issue of electrochromic sensors and biosensors. Most miniaturized de-power sources used in portable sensors and biosensors, including wearables, are based on batteries (Bandodkar et al., 2020) and fuel cells (Jia et al., 2020; Ortega et al., 2019). These power sources can be turned into self-powered sensors by making their power output proportional to an analyte concentration (Crevillen and Mínguez, 2018; Huang et al., 2020; Yu et al., 2019). Most self-powered sensors show limited performance due to the need to produce enough energy to power all the functions around the sensor, such as the display of information or data extraction. Recent progress in low-power electronics and biofuel cell technology (Ruff, 2017; Xiao et al., 2019), have improved the feasibility of these devices. However, manufacturing remains a significant limitation of most self-powered sensors, as most cases involve the heterogeneous integration of discrete and silicon-based components along with the sensor. This makes these disposable devices uneconomical and highly damaging to the environment.

In addition to providing chemical information visually through changes in their optical properties the redox properties of electrochromic materials make them excellent candidates for the construction of self-powered sensors (Yu et al., 2018; Zhorzeveska et al., 2014), even using screen-printing alone (Aller Pellitero et al., 2020), which makes these devices amenable to mass production.

In this work, we are taking this concept to a wearable form factor on a flexible substrate. Sweat sensing technologies boomed less than a decade ago, integrating electrochemical sensing into tattoos and skin patches (Bellassihil et al., 2018; Kim et al., 2011; Rose et al., 2014; Windmiller et al., 2012). Interestingly, despite their considerable evolution (Kim et al., 2019), they face similar manufacturing and cost issues as self-powered sensors: namely connectivity and the heterogeneous integration of discrete electronic components. We believe that multifunctional components (Huang et al., 2020) can hugely simplify the construction of new wearable sensing devices, making their production affordable and appealing. Such multifunctional components, in turn, are enabled by unique combinations of multi-responsive materials (Gorrin et al., 2020; Mendes-Felipe et al., 2019; Oliveira et al., 2018) and manufacturing techniques. The ultimate aim is to develop new devices that are easy to use without the need for advanced training or complex scientific instrumentation, and that can be easily manufactured by large-area printing methods. Here we present a self-powered lactate skin-patch electrochromic biosensor that can be fully screen-printed and easily read by the naked eye. We show how device design is strongly intertwined with materials and fabrication processes. The choice of the transparent conductor is particularly important as it affects both device construction and performance. This work describes a device where a lactate biosensor anode is coupled to a Prussian Blue (PB) cathode to provide a visual concentration readout. However, changing the enzyme system at the anode will enable the detection of other analytes in sweat or any other media. Because the display is not in direct contact with the sample, the technology can be used with dark or turbid samples as well as clear ones.

2. Materials and methods

2.1. Reagents and materials

All chemicals and materials were used as received without further purification. **Ion-gel electrolyte:** potassium trifluoromethanesulfonate (KTf) and poly(vinylidene fluoride-co-hexafluoropropylene) (P(VDF-co-HFP) were acquired from Sigma-Aldrich (ES), and ionic liquid 1-Ethyl-3-methylimidazolium trifluoromethanesulfonate (EMIM-Tf) was acquired from Solvionic (FR). **Other reagents:** Potassium hexacyanoferrate (II) trihydrate, potassium chloride, ferric chloride, and potassium nitrate were purchased from Sigma-Aldrich (ES). A solution of 0.1 M potassium chloride (KCl) from Sigma-Aldrich and 0.05 M phosphate buffer (PBS) pH 7 from Fluka (ES) was selected as aqueous supporting electrolyte for the measurements using the self-powered prototypes. SoftWear 9319H nonwoven double-sided pressure sensitive adhesive (PSA) tape kindly provided by Adhesives Research (IE) was used for attaching the patch to the user's skin. Autotype CT-4 Polyethylene terephthalate, PET, sheets were sourced from MacDermid Autotype (UK).

The fabrication of conventional 3-electrode screen printed electrodes, as well as the lactate biosensor construction, is provided as part of the electronic supplementary information (ESI).

2.2. Gel polymer electrolyte

One of the most successful approaches to achieving ion-gel electrolytes with high ionic conductivities is the use of Poly(vinylidene fluoride-co-hexafluoropropylene) (P(VDF-co-HFP)) ionic liquid-based ion-gels (Dobbelin et al., 2010). This type of electrolytes, loaded with c. a. 70–80 % wt. of ionic liquid, can reach conductivities up to 1.06 mS cm^{-1}, transparencies around 83% of transmittance, and a broad electrochemical window (3.2 V), without losing flexibility or integrity (Santiago et al., 2020). The composition of the gel electrolyte used here, which has an ionic conductivity ca. 4 mS cm^{-1}, has been reported recently (Aller-Pellitero et al., 2020), but a short summary will be given for convenience. 0.14 g of the gelling agent, P(VDF-co-HFP) were dissolved in 0.5 mL acetone while stirring at 2000 rpm at 60 °C for 15–30 min until all the P(VDF-co-HFP) was dissolved. Note that the mixture yellows out above 70 °C. Next, 50 mg of KTf and 340 μL of ionic liquid were added to the mixture and stirred while heating for up to 1 h in total. Printed layers (3 coats) were measured using a stylus profilometer, yielding values ranging between 10 and 20 μm.

2.3. Design and fabrication of the electrochromic biosensor

The fully-printed self-powered electrochromic biosensor concept recently presented in (Aller-Pellitero et al., 2020) has been adapted to take a skin patch form factor, as shown in Fig. 1. In contrast to our previous work, which followed a straightforward coplanar construction, this time biosensor and display must face opposite sides, because the electrochromic material must remain visible to the user through the PET substrate while the biosensor stays in contact with the skin. Also, the biosensor was resized to match the charge on the electrochromic display and ensure readable colour changes within the biosensor dynamic range. We used a 100 μm-thick transparent PET substrate for our experimental work, but we produced a series in 30 micron-PET with the same functionality, but which felt more comfortable to wear. Fig. 1 outlines the fabrication process, where the PET substrate was the top cover of the device, which was thence built "backwards".

First, the substrates were prepared by engraving a series of registration marks in them. These registration marks served as a reference for the subsequent printing and cutting operations. Fig. 1 shows that both indium tin oxide, ITO, (or other forms of transparent mixed tin oxide) and PEDOT:PSS electrodes can be used in the construction. In contrast to PEDOT:PSS, which can be screen-printed and therefore streamline the fabrication process, ITO electrodes require wet-etch patterning (Aller-Pellitero et al., 2017). Although it is easy to make a suitable stencil out of masking vinyl, the process is more tedious and, on top of that, ITO on PET can be heterogeneous and present very variable conductivities even on the same sheet (Boehme and Clayton, 2005). Thus, in the present case, transparent conductor electrodes were printed in step two using PEDOT:PSS. These transparent electrodes provided necessary electrical contact between the biosensor (anode) and the PB display (cathode). Next, the biosensor graphite transducers were printed together with the text, which was mirror-imaged. The next step involved printing a white colour background layer to provide high contrast and facilitate reading

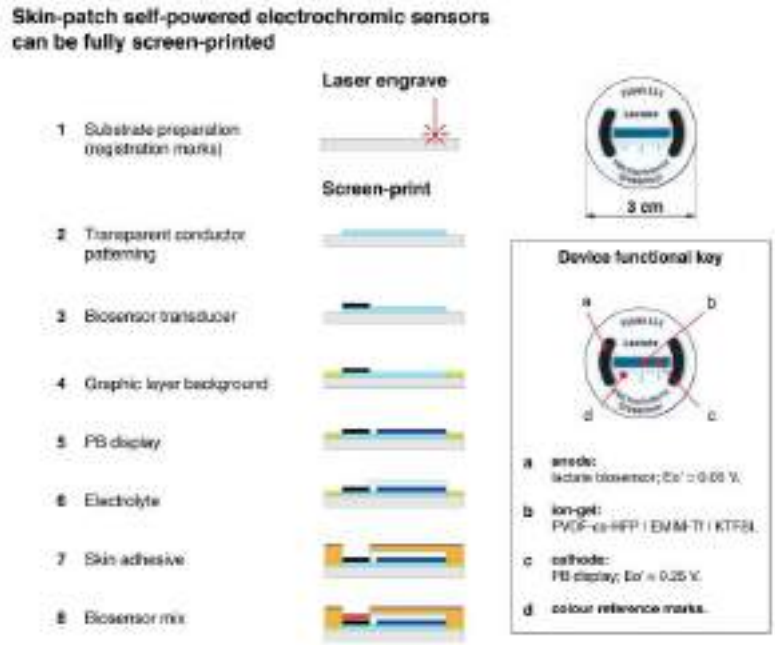

Fig. 1. Diagrammatic representation of the fabrication process and photographs from two different prototype versions. The inset highlights the function of the device various components.

both text and the display. The electrochromic PB display bars were printed next using an 80 durometer squeegee to ensure a thinner deposit. Standard screen-printing squeegees are made in lower durometer polyurethane rubber, typically sh70. The amount of PB deposited controls the device sensitivity and its response time; more material (i.e., thicker layers) may be used if higher concentrations need to be measured or if the biosensor has a very high current output. PB reference marks evenly distributed around the display (See device photographs in Fig. 1) served two purposes: first, they provided a colour reference for subsequent image data analysis and, second, they act as a spatial reference to determine more accurately the extent of the colour change along the longitudinal display axis. Fourth to be printed was a white dielectric that provided a background to the text and display, and facilitated reading out the results. The fifth, and last printed layer, was the electrolyte ion-gel, which had to be printed hot (60–70 °C) to prevent it from gelling on the screen. Three ion-gel layers were printed in the reported prototypes to reduce iR-drop losses due to the low electrolyte thickness (Aller Pellitero et al., 2019). Note that the ion-gel covers the PB cathode and the gap between this, and the biosensor. The reason is to provide the cathode with a stable electrolyte environment irrespective of sweat pH and electrolyte composition and ensure a consistent response dependent on the analyte concentration only. Last, although an adhesive could be printed too, in our case, we used a non-woven, medical-grade PSA. This adhesive layer was laser-cut to expose the biosensor while protecting the ion-gel. Last, the complete devices were laser-cut, and the graphite electrodes functionalised as described above.

2.4. Instrumentation

PET substrates, electrodes and printed devices were cut using a 30 W CO_2 laser engraver by Epilog Mini 24 (Laser Project, ES). Electrochemical and spectroelectrochemical measurements were done using a SPELEC UV-vis spectroelectrochemistry instrument (Metrohm-Dropsens, ES) controlled by DropView SPELEC software (version 3.0), installed on a PC running Windows 10.

2.5. Electrochemical measurements

Cyclic voltammetry (CV) was carried out using either a CHI600E (CH Instruments, Inc.) potentiostat and controlled by CHI660e software or a PalmSens 3 (PalmSens, NL) potentiostat controlled from a Windows 10-based laptop running PSTrace 5.8 (Palmsens, NL). Solutions were degassed by bubbling argon whenever possible to remove oxygen, which can otherwise mask the PEDOT:PSS reduction wave. The open circuit potential was determined prior to any voltammetric experiments to ensure that cyclic voltammograms started at potential of zero current.

2.6. Image analysis device response analysis

Electrode images were captured using a Nikon D3300 camera, while images from the prototypes were captured using an iPhone. Image analysis was performed using Fiji (Schindelin et al., 2012), an ImageJ 1x distribution (Schneider et al., 2012). Best sensitivities were obtained from analysis of the red component of RGB images. A large area, ideally covering the whole electrode, was selected using the oval tool, and RGB information was obtained using the "RGB_Measure.Plus" free plugin. Note that the images shown in Figs. 3 and 4 have not been treated in any way.

3. Results & discussion

3.1. Spectroelectrochemical characterisation of screen-printed PB

The formulation and electrochemical response of the PB paste used here has been reported previously (Aller Pellitero et al., 2019). Here, we

provide additional information regarding its spectroelectrochemical behavior (Ruleova et al., 1997; Mortimer and Reynolds, 2005). Fig. 2 shows cyclic voltammograms, UV–Vis spectra, and the corresponding voltabsorptograms at 680 nm of screen-printed 2.5 mm diameter disk PB and PEDOT:PSS electrodes. Fig. 2a shows the excellent electrochemical response of PB electrodes. The process around 0.2 V vs Ag/AgCl corresponds to the reversible reduction of PB to Prussian White, PW. The second process, found around 0.9 V vs Ag/AgCl, corresponds to the quasi-reversible oxidation of PB to Berlin Green, BG. However, because the device presented here works in a potential region between −0.1 and 0.3 V vs Ag/AgCl, the oxidation of PB to BG is not discussed. Fig. 2b corresponds to the absorption spectra, recorded in reflection mode, simultaneously with the cyclic voltammogram. The spectra show how light absorption decreases (reflectance increases) with potential as PB is bleached above 0.4 V vs Ag/AgCl to PW below 0.1 V vs Ag/AgCl. The voltabsorptograms depicted in Fig. 2c are the result of taking the time derivative of the absorption signal measured at 680 nm and represent the potentials where the colour changes take place, independently of background capacitive currents. This is a handy feature of voltabsorptograms, as they can pinpoint redox phenomena more clearly than cyclic voltammograms (Garcia-Ruiz et al., 2019). To facilitate the interpretation of the voltabsorptogram in the light of the CV, both curves have been coloured similarly in the figure. Orange and blue represent the forward and backward potential scan, respectively. Note that the data is expressed in terms of absorbance, so darker colours correspond to higher absorbance values and vice versa. The black trace in the figures represents the portion of the potential scan between the switching potential at the end of the backward scan, and the starting potential. The colour contrast ratio (CR) (Mortimer et al., 2015) of the PB electrode at 680 nm, determined as the ratio between the maximum and the minimum reflectance observed in the redox process between PB and PW, is 1.43. Note that some authors have claimed that for an electrochromic change to be noticed by the human eye, CR > 3–4 are recommended (Monk et al., 1995). Despite being close or even below this arbitrary limit, the PB/PW system is routinely (Ismail et al., 2020; Mortimer, 2011; Sekaranayora et al., 2014; Zhang et al., 2017, 2019) used in electrochromic devices due to its ease of preparation and use in many forms.

3.2. Spectroelectrochemical characterization of screen-printed PEDOT:PSS

As Fig. 1 shows, the present device uses a transparent electrode. ITO coated PET sheets are commercially available in different grades of optical transmittance and electrical resistivity, and in sheet thicknesses down to 30 μm. However, these materials are costly and require additional processing compared to PEDOT:PSS, which can readily be applied by screen-printing. This is the reason why we chose PEDOT:PSS as our transparent electrode despite its relatively lower conductivity (ca. 400 Ω $\square^{-1}$) compared to ITO on PET (ca. 60–75 Ω $\square^{-1}$). Although the conductivity of PEDOT:PSS electrodes can be increased by printing thicker layers, this results in lower light transmission. Besides, PEDOT:PSS is known for its cathodic electrochromism (Andersson et al., 2007; Kim et al., 2020; Kumar et al., 1998; Mortimer and Reynolds, 2005). Given that our PB display is expected to work at low potentials, we studied the effect of PEDOT:PSS electrode thickness and applied potential on the optical properties of our cathode. The goal was to find the optimum balance between electronic conduction and film transparency, so that the colour change of the PB could be observed by sight unambiguously. This is extremely important because the colour contrast ratio our PEDOT:PSS printed electrodes is $CR_{PEDOT:PSS} = 3.11$ at 685 nm which, compared to the $CR_{PB/PW} = 1.43$ of the PB/PW system means that PEDOT:PSS is much more intensely coloured and may mask the colour change of our main electrochrome system, PB. In addition to the higher contrast, the PEDOT:PSS system is coloured more efficiently at 95% switch (183 cm^2 C^{-1}) (Ibraggi et al., 2002), than the PB system (143 cm^2 C^{-1}), (Mortimer and Reynolds, 2005).

Fig. 2d shows the cyclic voltammetric response of the PEDOT:PSS electrodes used in the construction of the prototypes. The figure shows a large reduction signal starting at −0.5 V vs Ag/AgCl which, an analysis of the spectra presented in Fig. 2e, matches the voltabsorptograms in Fig. 2f. Although the apparent redox formal potential of this process is close to −750 mV vs Ag/AgCl, it is possible to observe some colour change at potentials starting at 0 V vs Ag/AgCl already. This is due to the structure of the polymer, which is likely to be composed of a mixture with different chain lengths. To check the suitability of PEDOT:PSS as transparent cathode for use in combination with the PB/PW system, we

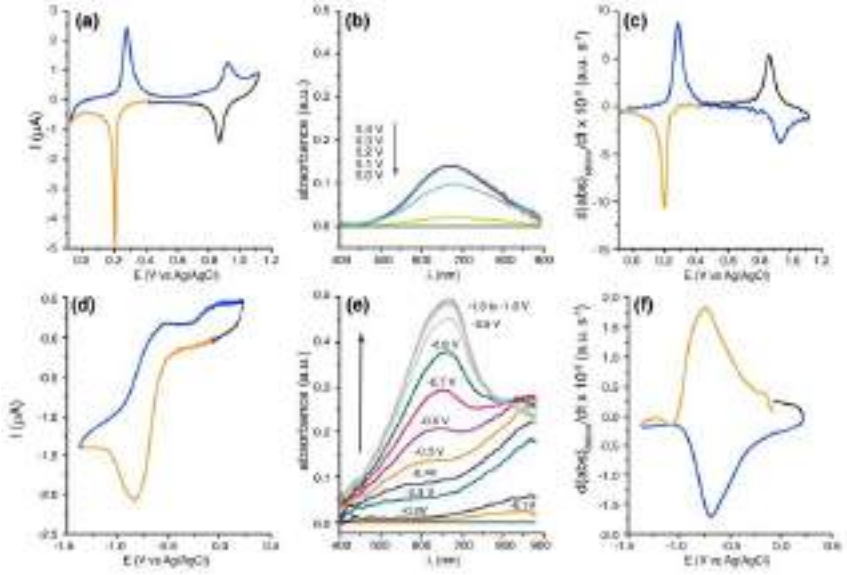

Fig. 2. (a) Cyclic voltammetry of a 3 mm PB-disk on graphite in 0.1 M KNO3. At 5 mV s-1. (b) Absorption spectra collected during cyclic voltammetry (a). (c) voltabsorptogram of the PB/PW and PB/BG system combining information from 2a and 2b at 690 nm. (d) Cyclic voltammogram recorded at 5 mV s-1 of a 2.5 mm PEDOT:PSS electrode in an Ar degassed 0.1 M KNO3 solution. (e) Absorption spectra obtained from the PEDOT:PSS electrode during voltammetry (d), and (f) voltabsorptogram of PEDOT:PSS combining data from Fig. 3d and e at 650 nm.

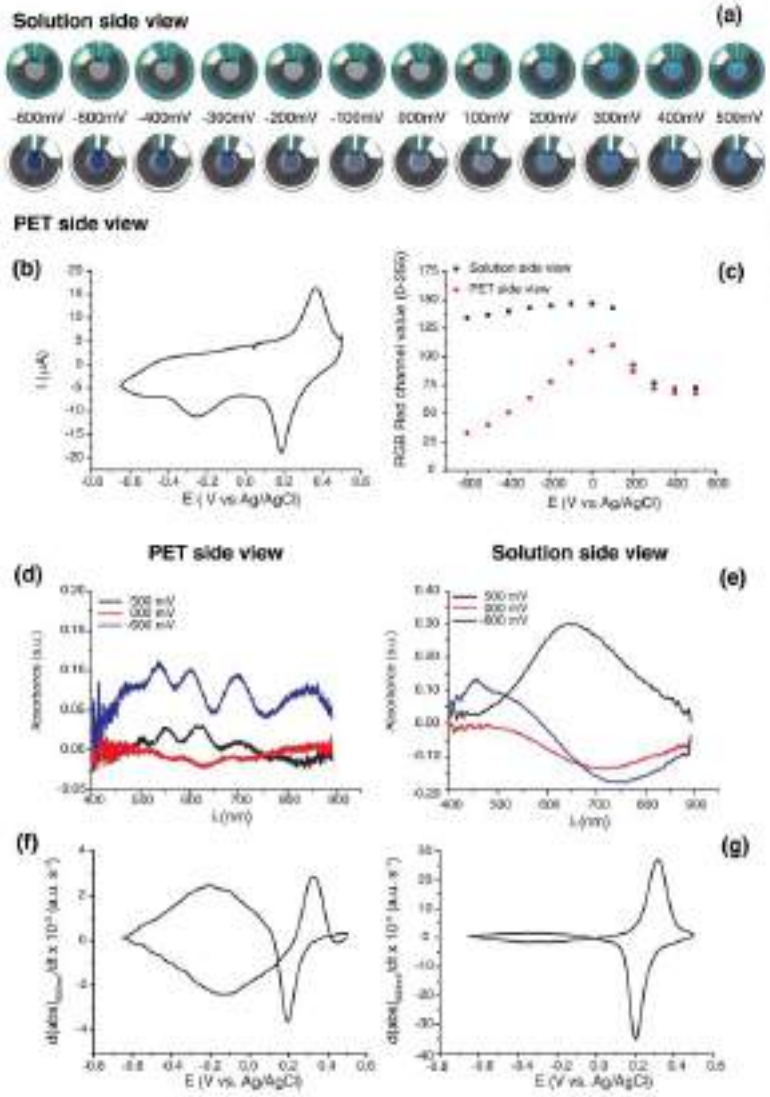

Fig. 3. (a) Solution and PET side view images of a PEDOT:PSS/PB on PET electrode during a (b) 10 mV s-1 cyclic voltammetry in 0.1 M KNO3 solution potentials are referenced versus an Ag/AgCl electrode. (c) Red channel value of the working electrode as a function of potential. Absorbtion spectra of the electrode taken from the (d) PET side and (e) solution side at three key potentials. Voltabsorptograms calculated from the (f) PET side and the (g) solution side spectra obtained in reflection mode during a 10 mV s-1 cyclic voltammetry. (For interpretation of the references to colour in this figure legend, the reader is referred to the Web version of this article.)

printed disk electrodes featuring one, two, and three layers of PEDOT:PSS.

Consequently, the PB/PW transition should be visible through a PEDOT:PSS electrode. We used disk electrodes featuring one printed layer of PB on two printed layers of PEDOT:PSS to study this configuration, which was later used in the prototypes. These disk electrodes were prepared for cyclic voltammetry experiments on 100 micron-thick transparent PET substrates too. Fig. 3a shows a series of photographs from one of these electrodes, taken during the 10 mV s^{-1} cyclic voltammetry in Ar-degassed 0.1M KCl shown in Fig. 3b. To facilitate image capture, these experiments were made in a standard 1 × 1 cm footprint spectrophotometry cuvette. The potential was scanned between 0.5 V and −0.6 V vs Ag/AgCl (0.1M $LiCH_3COO$). The top image set was taken from the solution side of the electrode, whereas the image set below corresponds to the substrate (PET) side. Thus, the layers met by light in the first case are PB/PEDOT:PSS, and in the second one PET/PEDOT:PSS/PB. This is why we find differences between both sets. First, in the solution-side view, we can clearly see the colour switching from blue to grey as potential passes the PB/PW reduction potential, around 150–200 mV. In the PET-side view, on the other hand, we observe two transitions because both PB and PEDOT:PSS are electrochromic. In spite of this, it is possible to observe the transition from PB to PW before the reduction of PEDOT:PSS marks the PW underneath it below −100 mV vs Ag/AgCl. Because image interpretation can be subjective, we have used ImageJ, an open-source image analysis software (Schindelin et al., 2012), to show how these electrodes behave and to establish the suitability of the system for the construction of the prototypes. We have selected a 1.5 mm diameter circular area within the working electrode and measured its RGB histogram. The RGB scale defines colours as the combination of red, blue and green, each ranging in a scale between

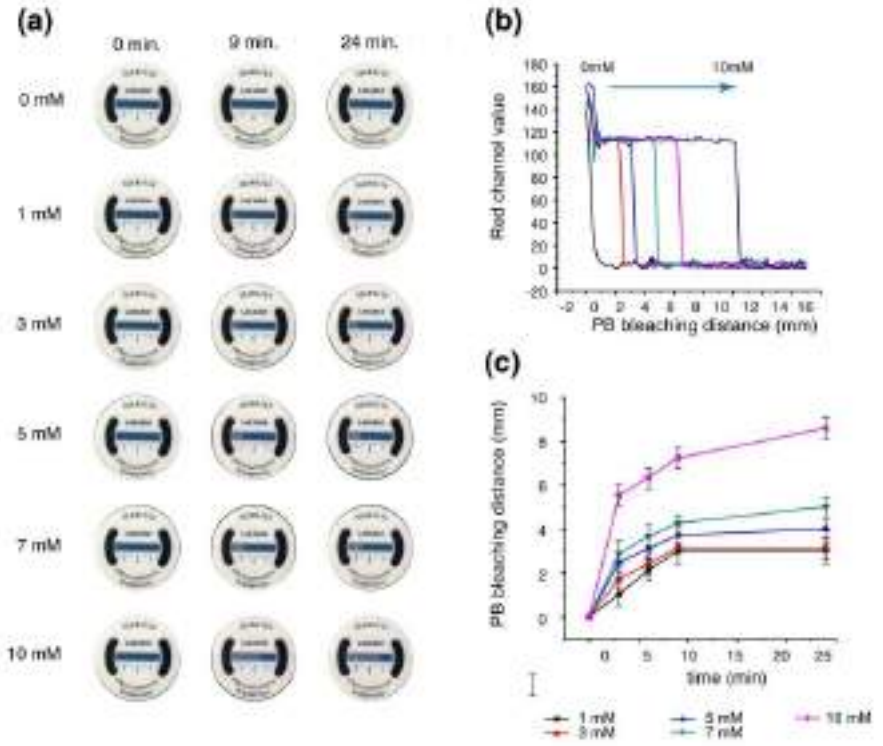

Fig. 4. a) Evolution of the display colour change as a function of lactate concentrations. (b) Red channel profile after 24 min in the presence of different lactate concentrations. (c) Transient evolution of the colour front from (b) as a function of lactate concentration. (For interpretation of the references to colour in this figure legend, the reader is referred to the Web version of this article.)

0 and 255. An RGB value of 0,0,0 denotes black, and 255,255,255 represents white. So the lower the value, the darker the tone. Fig. 3e shows the values corresponding to the red channel, which is the most sensitive in this case because it absorbs blue more strongly than the other channels. While quantification is easier from observation of the solution side, it is also possible from the substrate side. In this case, the figure shows that it may be more difficult for potentials below −100 mV because of the effect of PEDOT:PSS. However, as shown in Fig. 4a below, our lactate biosensor works above −100 mV, so in the full system we can be sure that any colour changes will only be due to the PB/PW system, even if these are slightly dulled by the PEDOT:PSS layer. Additionally, we have also studied the system spectroelectrochemical response in reflection mode, under the same conditions.

Fig. 3d and e shows typical absorption spectra at the starting potential (+300 mV), at the end potential (−600 mV), and at an intermediate potential where the self-powered system is most likely to operate (0.00 V). It is striking how different both sets of spectra are. While the solution side matches the spectra previously found for PB on graphite (Fig. 2b), the PET side spectra display distinct peaks around 550 nm, 600 nm, 700 nm and 850 nm. Of these, PB shows a broad peak between 600 and 700 nm, while PEDOT absorbs in a much broader range, so that the peaks around 500 nm and that at 850 nm may be attributed to PEDOT:PSS only. These two peaks do not appear at the solution-side spectra because the PB/PW coating, which is modifying 3 μm SiO_2-ATO microparticles, is opaque. Last, Fig. 3f and g shows the corresponding voltabsorptograms at 600 nm. Both plots show two clear signals. A sharper one at higher potentials, corresponding to the PB/PW system, and a much broader one corresponding to PEDOT:PSS. The relative magnitude of these signals in each case arises from the system construction. Thus, in the solution view voltabsorptogram (Fig. 3g), the PB signal dominates because the PEDOT:PSS layer is effectively hidden underneath. However, in the PET-side view voltabsorptogram, both the PB/PW and the PEDOT:PSS signals have comparable magnitudes. As we have seen, the deep blue colour of PEDOT:PSS dominates at potentials below −200 mV vs Ag/AgCl.

3.3. Full device response

The self-powered device presented here is a galvanic system enabled by the low oxidation potential at the lactate biosensing anode and the higher reduction potential of the PB cathode. The operation has been fully described in the past (Alba-Pellitero et al., 2018), but a summary will be given here for convenience. The presence of lactate activates the biosensor but, in contrast to conventional self-powered systems, the device internal resistance is a key design parameter that controls the extent of colour bleaching along the cathode. The electrons involved in the oxidation of lactate are relayed from the enzyme to the redox polymer, which passes them through the graphite electrode and the transparent electrode to the Prussian Blue, bleaching it. Due to the special geometry of the system, it is the PB closest to the anode that is bleached first. This changes the device internal resistance, increasing it, as the electrons need to cover a longer path before reaching new PB Fe (III) centres to reduce. In the solution side, this translates in an increasing ΔE-drop that is controlling the entire process. Thus, the cell potential, $E_{cell} = E_{cathode}-E_{anode}-iR$, which depends on analyte concentration, determines the length of the bleached area, while the biosensor

output current affects response time and colour front sharpness. In the present system, the system is known to generate open-circuit cell potentials, OCP, in the range of 0.5 V (Aller-Pellitero et al., 2020), and current densities in the range 100–300 $\mu W\ cm^{-2}$ depending on lactate concentration. Because both anode and cathode are connected by means of the transparent PEDOT:PSS electrode, it is not possible to measure the currents or the cell potentials generated in the presence of lactate. On the other hand, the device response was explored by measuring the bleaching colour of PB by image analysis in the presence of different lactate concentrations. Briefly, one of the graphite electrodes was modified using 5 μL of the biosensor solution previously described. Filter papers were soaked in PBS-buffered (pH = 7) lactate solutions ranging from 1 mM to 13 mM. Once the biosensors were ready, the devices were placed on top of these soaked papers and pictures were taken every 3 min. The colour change of the display was subsequently analysed using ImageJ. Fig. 5a summarizes the results obtained for the lactate biosensor. Fig. 5a shows photographs at the start, and then 9 and 24 min into the experiment. As expected, at higher lactate concentrations, a larger portion of the cathode was bleached (larger E_{cell}), and the response was also faster (higher current).

Fig. 4b shows the red channel profile of the PB electrodes as a function of analyte concentration, at t = 24 min. Low R (red channel) values are indicative of blue colour (red is absorbed), so as the electrode is bleached, the R value increases. Note that no colour change is observed in the absence of enzyme activity (absence of lactate), which indicates the selectivity of the device. The sharp drop in colour between the bleached and the coloured regions is striking. Previously, we had observed a blurry transition zone, due to ohmic drop effects (Aller Pellitero et al., 2018). Even screen-printed systems showed such a blurry region (Aller-Pellitero et al., 2020). However, in this case the colour change is really sharp. We attribute this to two factors. First, the resistance of the PEDOT:PSS electrode, which is higher than the ITO (Aller-Pellitero et al., 2017) and the gold (Aller-Pellitero et al., 2020) electrodes used in previous device versions and, second, to the large biosensor area which is able to convert more lactate and deliver higher currents than the conventional, 3 mm diameter disk biosensor shown in Figure ESI 3.

Previously (Aller Pellitero et al., 2017, 2020), we had used very highly conducting electrodes, so that the main iR losses appeared on the solution side (Aller Pellitero et al., 2018). Previously used ITO on glass and gold paste electrodes presented resistances of <20 $\Omega\ \square^{-1}$ and ca. 0.1 $\Omega\ \square^{-1}$, respectively. In this case, on the other hand, The measured resistance of the 2-layer PEDOT:PSS electrodes is between 65 and 75 $\Omega\ \square^{-1}$. The total resistance of this transparent electrode, from the graphite anode to the far end of the cathode ranges from 350 to 550 Ω. This resistance further increases up to ca. 1 kΩ once the PB layer has been printed on top of the PEDOT:PSS (roughly 300 $\Omega\ \square^{-1}$). Although the device response is controlled by the ion-gel resistance (it is approximately 3kΩ across the whole display), it is reasonable to think that the choice of electrode can also aid in controlling the device response, preventing the homogeneous distribution of potential across the entire electrode surface, as would happen with a conventional conductor. Fig. 4c shows the position of the colour change as a function of analyte concentration at different times. The data show how higher analyte concentrations lead to the higher biosensor currents responsible for the faster the response, in agreement with previous observations. The data also show that each concentration has an end point, which is also in agreement with our predictions for this kind of system, where colour is expected to change in a region such that the cell electromotive force (emf) is higher or equal to the system internal resistance. The system works in fact as a visual coulometer; in our experiment we are exposing the biosensor to large sample volumes, so the analyte concentration sets an emf for the system that can be assumed to remain constant throughout the experiment. This, combined with the resistance of the PEDOT:PSS electrode, explains why the colour edge appears so sharp. First, an E_{cell} is set that is only a function of lactate concentration. Next, the biosensor consumes all the PB (charge) within the region where iR drop compensates the *cell* ΔV. This also explains the wider linear range shown in Fig. 5 in the self-powered devices compared to the amperometric biosensor (see ESI Fig. 3). The display length bleached at 10 mM lactate is approximately 12 mm. Considering the biosensor area and electrolyte resistance, and assuming a current output in the range of 300–350 μA, We estimate an iR drop around 0.6–0.7 V, which is in agreement with our previous results for a similar system (Aller Pellitero et al., 2020).

Last, Fig. 5 shows data corresponding to the current density measured at the biosensor (also shown in Figure ESI 2), and the position of the colour front measured at time 24 min. The coulometric data display almost twice as wide a linear range as the amperometric sensor.

Although the biosensors used in this work were first designed to work in whole blood (Punter-Villagrasa et al., 2015), and sweat lactate can be as high as 70 or 80 mM during exercise(Baker and Wolfe, 2020), we believe that the devices presented here demonstrate working principle of the proposed technology, and that they could be adapted to monitor lactate in sweat, or other analytes in different matrices. That, however, should necessarily involve changes in biosensor construction to fit the desired sensitivity.

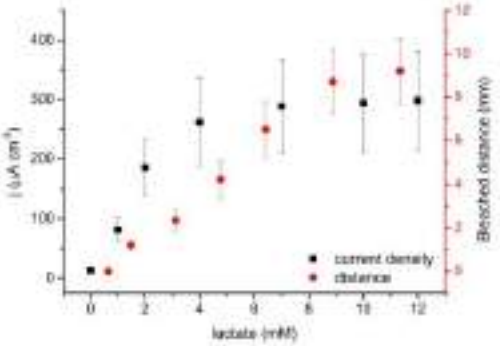

Fig. 5. Comparison between the amperometric biosensor response, expressed as current density (black squares, left axis) and the self-powered biosensor response, expressed as the position of the colour front, in mm away from the biosensor (red circles, right-hand axis). (For interpretation of the references to colour in this figure legend, the reader is referred to the Web version of this article.)

4. Conclusions

We have described the step-by-step construction and characterisation of a self-powered electrochromic sensor for the detection of sweat lactate. This device involves a transparent PEDOT:PSS electrode that connects a lactate biosensing anode, and a Prussian Blue electrochromic cathode. The biosensor is based on a classical construction involving lactate oxidase and an Osmium-based polyvinyl imidazole redox polymer, operates with an onset potential around 0 V vs Ag/AgCl and has a current output up to 350 $\mu A\ cm^{-2}$ in a lactate concentration range between 0 and 12 mM. The Prussian Blue cathode, on the other hand, presents a reduction onset potential around 0.3 V vs Ag/AgCl. The cathode contrast ratios of 1.43 enables the colour change to be observed by the naked eye through the PEDOT:PSS electrode.

We have also assessed the importance of the choice of the transparent electrode material. In this case, we have used PEDOT:PSS because it makes for a more cost-effective and environmentally friendly production process than ITO. The suitability of PEDOT:PSS as a transparent electrode for this application has been studied in depth, considering both its electrical and spectroelectrochemical properties. PEDOT:PSS is a cathodic electrochrome turning from clear to deep blue at −0.9V vs Ag/

AgCl. However, the colouration process begins slightly below 0V vs Ag/AgCl, which may eventually mask the colour loss of PB and lead to wrong readings. However, the redox mediator used in the device ensures that the device does not operate below 0V, thus making PEDOT:PSS a suitable transparent electrode to work in combination with PB in this application.

Another critical element of this device is its ion-gel electrolyte, comprised of PVDF-co-HFP, ionic liquid EMIM-TF, and potassium triflate, which protects the PB display and provides an adequate chemical environment for its operation. This is important to prevent accidental bleaching of PB by species such as ascorbic or uric acid, which are known to reduce PB (Virtuoso et al., 2019; Zhou-woo et al., 2014). Also, this ion-gel protects PB from damaging neutral to basic pHs that may be found in certain samples. The potassium salt facilitates ion exchange with the sample medium and minimizes the junction potential at the aqueous sample-organic ion-gel interface. The printed ion-gel electrolyte resistance is close to 600 $\Omega\ \square^{-1}$, and controls the device response.

The self-powered device has been studied using buffered lactate solutions. Although full response requires up to 24 min, the system reaches 85% of the final response within the first 10 min, making it suitable for use in applications such as endurance sport. The coulometric nature of the measurement extends the linear range up to 10 mM lactate, beyond the 4 mM linear range of the amperometric biosensor. It is believed that this is a combined effect of the cell potential established in the system between the display and the biosensor, and the relatively long reaction time. Considering the electrolyte resistance and the expected current output for the biosensor at 10–12 mM lactate, we can estimate a sensitivity involving the bleaching of 1 mm PB segments per mM unit of lactate.

The device presented in this work, with all its limitations, represents a step forward in the direction of more sustainable wearable biosensors. We have demonstrated that electrochromic materials can be successfully combined with biosensors to produce electrochemical devices performing three functions –energy generation, sensing, and information display– in a single electrochemical cell. Not only this, but we have also shown how to build it in a wearable form factor, with the biosensor facing one side, and the display facing the other. The presented device can be, after optimization of the transducers to fit the desired sensitivity, a promising approach for the non-invasive monitoring of target molecules excreted via perspiration.

CRediT authorship contribution statement

Sara Santiago-Malagón: Investigation, Formal analysis, Visualization. **Diego Río-Colín:** Investigation, Formal analysis, Visualization. **Hanieh Azizkhani:** Investigation, Visualization. **Miguel Aller-Pellitero:** Conceptualization, Methodology, Writing - original draft, Writing - review & editing. **Gonzalo Guirado:** Resources, Writing - review & editing. **F. Javier del Campo:** Conceptualization, Methodology, Investigation, Formal analysis, Resources, Writing - original draft, Writing - review & editing, Supervision, Funding acquisition.

Declaration of competing interest

The authors declare that they have no known competing financial interests or personal relationships that could have appeared to influence the work reported in this paper.

Acknowledgements

MA is supported by FEDER funds managed by the Catalan Secretary of Universities and Research through project SEAMLESS (PROD-0000114; Enterprise and Knowledge, Industry Department, Generalitat de Catalunya). GG and SM also thanks the Agencia Estatal de Investigación (PID 2019-106173RB-I00/AEI/10.13039/501100011033 project). The authors are grateful to Milliken for providing the electroconductive powders (ECPs) featured in this work. Special thanks to our industrial partners in this project: Fernando Benito and Juan Echavarri, from Payoset, Ignasi Riera from Inkzar, and Joaquín Albert from Arista SG, for their invaluable guidance and support on printing materials, processes, and applications. Prof. Álvaro Colina (OrcID: 0000-0003-0359-3560), from the University of Burgos is gratefully acknowledged for his advice and discussions on spectroelectrochemical procedures.

Appendix A. Supplementary data

Supplementary data to this article can be found online at https://doi.org/10.1016/j.bios.2020.112879.

References

Aller-Pellitero, M., Yeomans, J., Ulla, B., Guirado, G., Lobaid, R., Hilla, J.Y., del Campo, F.J., 2019. Screen. Acceptor. 8 (3), e00. 299–305–307.
Aller-Pellitero, M., Guimerà, A., Elmore, M., Villa, R., Rubio, C., Lobaid, R., Durbe, M.-L., Hilla, J.-Y., Javier del Campo, F., 2017. Chem. Sci. 8, 1905–2002.
Aller-Pellitero, M., Santiago-Malagón, S., Ruiz, J., Alonso, Y., Lobaid, R., Hilla, J.Y., Guirado, G., del Campo, F.J., 2020. Sensor. Actuator. B Chem. 308, 127535.
Aller-Pellitero, M., del Campo, F.J., 2019. Curr. Opin. Electrochem. 15, 68–73.
Aller-Pellitero, M., Guimerá, A., Villa, R., del Campo, F.J., 2010. J. Phys. Chem. C 112, 2566–2607.
Anderson, P., Parthiban, R., Tehrani, P., Berggren, M., 2007. Adv. Funct. Mater. 17, 2677–2682.
Baker, L.B., Wolfe, A.S., 2020. Physiological mechanisms determining eccrine sweat composition. Eur. J. Appl. Physiol. 120 (4), 719–752. Springer Berlin Heidelberg.
Bandodkar, A.J.J., Lee, K.F.F., Huang, S., Li, W., Wang, S., Jia, C.-J., Jeang, W.J.J., Huang, T., Mehta, S., Nyberg, G., Chaffiol, R., Rapier, J.A.A., Ostroff, P., Choi, J., Kao, J., Reeder, J.T., Tseng, R., Shaffiol, R., Rapier, J.A.A., 2020. Nat. Electron. 3, 554–562.
Bankar, M., Gaitan, C., 2005. Surf. Coatings Technol. 200, 962–965.
Correia, D.M., Fernandes, L.C., Martins, P.M., Garcia-Astrain, C., Costa, C.M., Reguera, J., Lanceros-Méndez, S., 2020. Adv. Funct. Mater. 30, 1907636.
Dalal, D.P., Chaffaine, S.R., Elsa, D.-H., Gómez-Romero, P., 2018. Chem. Soc. Rev. 47, 2005–2129.
Davis-Rios, J., Pacios-Bradías, J.C., Heras, A., Colina, A., 2019. Electroanalysis 31, 1259–1270.
Grupp, C.L., Walsh, D.M., Rauh, R.D., Reynolds, J.R., 2002. Chem. Mater. 14, 3464–3470.
Gualeni, M., Mansoor, S.D., 2018. ACS Sens. 3, 44–53.
Heikenfeld, J., Jajack, A., Rogers, J., Gutruf, P., Tian, L., Pan, T., Li, R., Khine, M., Kim, J., Wang, J., Kim, J., 2018. Lab Chip 18, 217–248.
Huang, L., Chen, J., Tu, Z., Tang, D., 2018. Anal. Chem. 90, 2030–2034.
Jansod, S., Chaiyasai, T., Sodu, Y., Bülbül, E., 2020. Anal. Chim. 92, 9150–9153.
Jia, S., Bandodkar, A.J., Franz, M., Arellano, R., Rogers, J.A., Alan, M.A., 2020. Biosens. Bioelectron. 165, 112393.
Kim, D.-H., Lu, N., Ma, R., Kim, Y.-S., Kim, R.-H., Wang, S., Wu, J., Won, S.M., Tao, H., Islam, A., Cobeaga, T., Rogers, J.A., 2011. Science 333, 838–843.
Kim, J., Campbell, A.S., de Ávila, B.E.-F., Wang, J., 2018. Nat. Biotechnol. 37, 389–406.
Kim, J., Imani, M., Kim, U., Jeng, H., Kim, E., 2020. Adv. Mater. Technol. 5, 1–22.
Kobets, P.J.P.J., Tampori, S., Mellà, M.A.A.M.A., Marmisolesi, E., Rosetzol, M., Marzet, E., 1997. J. Solid State Electrochem. 1, 55–63.
Kumar, A., Welsh, D.M., Morvant, M.C., Piroux, F., Abboud, K.A., Reynolds, J.R., 1998. Chem. Mater. 10, 896–902.
Lipomi, D.D., Bao, Z., Rogers, B., Gooding, J.J., Chem, S., 2015. ACS Appl. Mater. Interfaces 7, 19201–19208.
Liu, H., Crooks, R.M., 2012. Anal. Chem. 84, 2528–2532.
Morales-Felipe, C., Oliveira, J., Barbosa, C., Vilas-Vilela, J.L., Lanceros-Méndez, S., 2019. Adv. Mater. Technol. 4, 1800615.
Monk, P.M.S., Mortimer, R.J., Rosseinsky, D.R., 1995. Electrochromism Fundamentals and Applications. first ed. VCH, Weinheim.
Mortimer, R.J., 2011. Annu. Rev. Mater. Res. 41, 241–268.
Mortimer, R.J., Rosseinsky, D.R., 2013. J. Mater. Chem. 15, 2226–2233.
Mortimer, R.J., Rosseinsky, D.R., Monk, P.M.S., 2015. Electrochromic Materials and Devices. Electrochromic Materials and Devices.
Oliveira, J., Correia, V., Castro, H., Martins, P., Lanceros-Mendez, S., 2016. Addit. Manuf. 11, 269–282.
Ortega, L., Llorella, A., Esquivel, J.P., Sabaté, N., 2019. Microsystems Nanoeng. 5, 5.
Papoti, A., Bratsiotis, E., Mihalopoulos, L., Raphaïssi, G., Ramantzikos, A., Ramantzikos, A., 2018. Polymer 172, 141–145.
Ramos-Villagrán, J., Pons-Artiles, C., Colmenar-Fernández, J., Lopez-Sanchez, J., Acuña-Peña, E., Maichel-Cerda, P., Gil, J., Rivero, M., Aller-Pellitero, M., Salvate, N., Del Campo, F.J., Rodriguez-Frutos, I., 2019. A portable point-of-care device for multiparametric diabetes analytic analysis. In: IECON 2019 - 45th Annual Conference of the IEEE Industrial Electronics Society, pp. 1353–1357.
Rose, D., Ramanujam, N., Griffin, D., Ives, L., Kelley-Loughnane, N., Naik, R., Hagen, J., Papautsky, I., Heikenfeld, J., 2014. IEEE Trans. Biomed. Eng. 9284, 1.
Rull, A., 2017. Curr. Opin. Electrochem. 5, 68–75.

Bandopa, S., Munoz-Bertrel, X., Ozcan, O., 2020. J. Mod. Liq. 318, 114028.
Bilbokaitis, J., Arguedas-Cuenca, I., Pitre, E., Enyaig, C., Langois, M., Ramesh, T., Perdomo, S., Burden, C., Sadleir, G., Schnell, B., Thorsen, J.-Y., White, B.J., Shenassian, T., Elmore, E., Tamarack, P., Cardoso, A., 2012. Nat. Methods 9, 676-682.
Schneider, C.A., Rasband, W.S., Eliceiri, K.W., 2012. Nat. Methods 9, 671-675.
Schmeltzer, A.N., Bell, Y., Eriksson, M., Kravchik, A.A., Turner, A.P.F., Vagin, M.Y., 2019. Anal. Chem. 89, 9944-9947.
Singh, R., Thorne, J., Mangala, S., Ramos, A., 2017. ACS Appl. Mater. Interfaces 9, 19427-19435.
Vybiralova, P., Valkiunas, A., Kavaliauskaite, D., Ramanavicius, A., 2019. J. Electrochem. Soc. 166, B427-B432.
Wadhwalkar, J.B., Bandodkar, A.J., Valdés-Ramírez, G., Parkhomenko, S., Shriram, A. G., Wang, J., 2012. Chem. Commun. 48, 8794.
Xiao, X., Xia, H.Q., Wu, R., Bai, L., Yao, L., Magner, E., Cosnier, S., Lojou, E., Zhu, Z., Liu, A., 2019. Chem. Rev. 119, 9509-9558.
Xu, Z., Cai, G., Ren, R., Tang, D., 2018. Analyst 143, 3980-3986.
Xu, Z., Cai, G., Tong, P., Ying, D., 2018. ACS Sens. 4, 2272-2279.
Zhang, Y., Cai, Y., Shi, L., Zhou, L., Liu, H., 2017. Sensors 17, 295.
Zhang, X., Ivanoviz, B.A., Wu, Y., White, R.J., 2019. Anal. Chem. 91, 11467-11473.
Zimmovska, A., Całkowska, A., Sort, E., Tomaszewska, D., Opalko, M., Awsiuk-Nieścioruk, M., 2014. Biosens. Bioelectron. 56, 455-461.

ACS APPLIED MATERIALS & INTERFACES

www.acsami.org

Research Article

Solid Multiresponsive Materials Based on Nitrospiropyran-Doped Ionogels

Sara Santiago, Pablo Giménez-Gómez, Xavier Muñoz-Berbel, Jordi Hernando,* and Gonzalo Guirado*

Cite This: *ACS Appl. Mater. Interfaces* 2021, 13, 26461−26471

Read Online

ACCESS | Metrics & More | Article Recommendations | Supporting Information

ABSTRACT: The application of molecular switches for the fabrication of multistimuli-responsive chromic materials and devices still remains a challenge because of the restrictions imposed by the supporting solid matrices where these compounds must be incorporated: they often critically affect the chromic response as well as limit the type and nature of external stimuli that can be applied. In this work, we propose the use of ionogels to overcome these constraints, as they provide a soft, fluidic, transparent, thermally stable, and ionic-conductive environment where molecular switches preserve their solution-like properties and can be exposed to a number of different stimuli. By exploiting this strategy, we herein pioneer the preparation of nitrospiropyran-based materials using a single solid platform that exhibit optimal photo-, halo-, thermo-, and electrochromic switching behaviors.

KEYWORDS: *ionogel, molecular switches, spiropyrans, smart materials, ionic liquids, smart devices*

INTRODUCTION

Smart functional solid materials that exhibit multistimuli-responsive behavior are of crucial importance for the construction of novel dynamic systems and devices.[1−5] A major toolbox toward this goal are molecular switches.[6−11] Among them, spiropyrans are frequently preferred due to their capacity to reversibly interconvert between states with strikingly different properties (e.g., color and polarity) upon application of a broad range of stimuli.[12−16] On the one hand, spiropyran switches are well known to photoisomerize between their colorless spirocyclic (**SP**) and colored merocyanine isomers (**MC**).[15−17] On the other hand, they have also been found to respond to other external stimuli[18−20] such as pH,[21−24] metal ions,[24−27] solvent polarity,[28−30] and redox potentials.[31−33] In some cases, this allows the formation of other states apart from **SP** and **MC** (e.g., the protonated merocyanine state **MCH**$^+$, the spiropyran dimer **SP**−**SP**) that additionally modify the photochromic response of the system,[21,23,25−27,30] which further enriches the stimulus-sensitive activity of spiropyran switches.

Despite their broad functionality and versatility, the application of spiropyrans (and other switches) to the fabrication of truly smart materials and devices suffers from a major bottleneck: the influence of the surrounding matrix when these compounds are transferred from solution to a solid state (the so-called matrix effect), which often dramatically alters their switching performance.[34−37] Two main factors account for this behavior: (a) the large geometrical changes needed to interconvert between the spirocyclic and open states of spiropyrans, which are hindered in rigid environments; and (b) the strong interaction that takes place with the surrounding solid matrix, which may vary the relative energy of their different states. Although these matrix effects could be exploited to develop new stimuli-sensitive responses for spiropyrans,[26,34,38] they eventually prevent direct transfer of the optimal switching properties found in solution to the final materials. One of the main strategies proposed to overcome this drawback comprises properly selecting the nature of the matrix as to warrant minimal interaction with the switch and/or provide it with sufficient free volume as to fairly preserve its solution-like stimulus-sensitive response.[37] This is the case of nanoporous solids (e.g., metal−organic[39,40] and covalent organic[41] frameworks) and soft polymeric matrices (e.g., low-T_g polymeric domains,[36,42,43] polymer gels[44−46]).

However, even if a suitable spiropyran−matrix combination is chosen to reach optimal switching, the number and type of stimuli that can be applied to the resulting material are ultimately limited by the properties of the matrix, i.e., opaque materials will restrict spiropyran photochromism to the surface

Received: March 4, 2021
Accepted: May 19, 2021
Published: May 31, 2021

Scheme 1. Multistimuli-Responsive Spiropyran-Based Ionogel Membranes (NO_2BIPS@IG) to Be Prepared in This Study, Which Respond to Different Types of Input Signals: Light, Temperature, pH, and Electrical Current

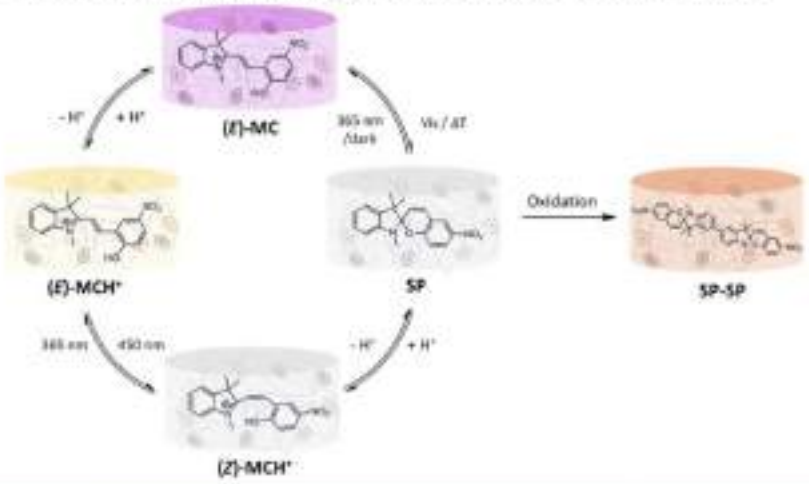

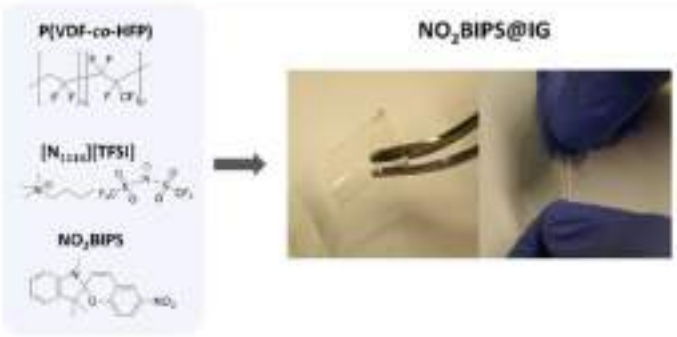

Figure 1. Key components for the fabrication of multistimuli-responsive NO_2BIPS@IG films, which were found to be transparent, flexible, and elastic.

layer, whereas electroinduced responses could only be obtained for conductive substrates. In fact, the latter most probably justifies why the electrochromic response of spiropyrans has only been explored to date in solution with a proper supporting electrolyte and organic solvents.[31−33] Therefore, to fully unleash the potential of the multistimuli-responsive behavior of spiropyrans, the development of versatile platforms that allow both solution-like switching and multiple operations under different input signals (e.g., light, electricity, pH, temperature, ions) is required. To reach this goal, we propose, herein, the use of ionogels (IGs), solid-gel polymer electrolytes that are attracting increasing attention for the fabrication of functional devices because of their unique combination of properties (i.e., elasticity, flexibility, easy preparation methodology, transparency, high ionic conductivities, and large electrochemical and chemical stability).[27−30] Although a very recent example of spiropyran-based IG has been reported, only its light-sensitive operation has been described so far.[33] Accordingly, in this work, we aim to demonstrate for the first time the multi-addressability of this class of materials, which would open the door for the fabrication of spiropyran-based smart devices with a broad variety of applications such as optical memories, electrochemical sensors, biosensors, and molecular actuators. For this, we focused our attention on 1′,3′-dihydro-1′,3′,3′-trimethyl-6-nitrospiro[2*H*]-1-benzopyran-2,2′-(2*H*)-indole (NO_2BIPS) as a benchmark system, a well-known commercial nitrospiropyran derivative capable of responding to a plethora of external stimuli (Scheme 1).[31,33,35,52−54]

RESULTS AND DISCUSSION

Fabrication of Spiropyran-Based Ionogel Membranes. Based on our previous experience on the preparation of ionogels loaded with molecular switches,[55] IG membranes were prepared by blending a fluorinated polymer (poly(vinylidene fluoride-*co*-hexafluoropropylene), P(VDF-*co*-HFP)), the trimethylbutylammonium bis(trifluoromethylsulfonyl)imide ionic liquid ($[N_{1114}][TFSI]$), and NO_2BIPS in acetone. After solvent evaporation, rubbery IG films containing free NO_2BIPS molecules were obtained (NO_2BIPS@IG, Figure 1), which were found to be transparent, flexible, and stretchable. These features arise from the convenient choice of the polymer network and the ionic liquid, where $[N_{1114}][TFSI]$ acts as a plasticizer favoring segmental

https://doi.org/10.1021/acsami.1c04159
ACS Appl. Mater. Interfaces 2021, 13, 26461−26473

ACS Applied Materials & Interfaces www.acsami.org Research Article

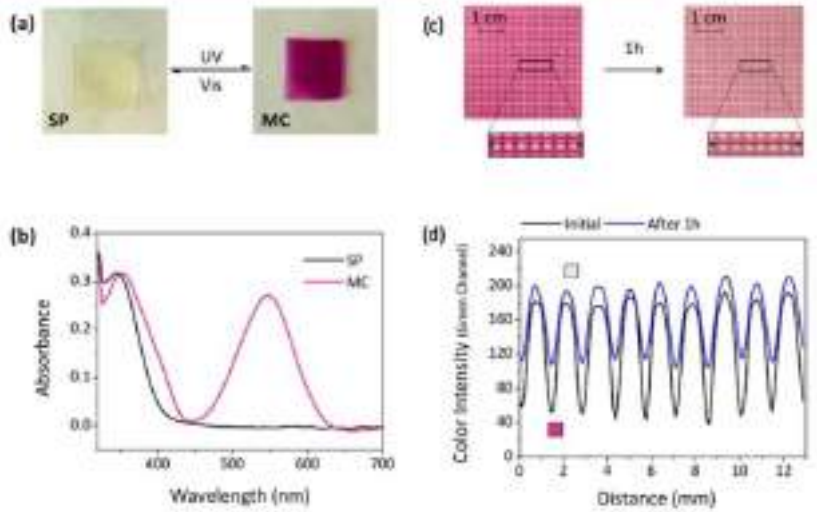

Figure 2. (a) Photochromic behavior of NO_2BIPS@IG membranes when irradiated with UV and visible light to interconvert between the SP and MC states (c_{NO_2BIPS} = 0.05 mg NO_2BIPS/g IG). (b) UV−vis absorbance spectra of the SP (initial) and MC states (λ_{exc} = 365 nm until the photostationary state (PSS) is achieved) of NO_2BIPS@IG membranes. (c) Optical images of a NO_2BIPS@IG membrane exposed to UV light (λ_{exc} = 365 nm) through a photoprotective patterned mask, after the PSS is reached (left) and after 1 h under dim UV irradiation (right) to minimize the thermal back-isomerization process. The black rectangle indicates the region of the membrane that was analyzed. (d) Color intensity cross section of the images in (c) for the membrane region within the rectangle.

mobility of the polymer chains and, hence, accounting for the final mechanical properties of the mixture. In addition, the ionic liquid provides free carriers to the material and explains the large ionic conductivities measured for the IG films (0.3 mS cm^{-1}). As for the spiropyran content in NO_2BIPS@IG, it was selected to meet two important criteria: (a) high color contrast upon application of different stimuli that could be properly quantified by means of ultraviolet−visible (UV−vis) absorption spectroscopy, and (b) good solubility in the liquid phase of the ionogel to enable optimal switching performance (c = 0.05−0.5 mg NO_2BIPS/g IG). Actually, the formation of microscopic aggregates of the spiropyran molecules in this work was not observed for any of the concentrations tested when inspecting the ionogels under the optical microscope, which contributes to their high optical transparency.

Other advantages arise from our fabrication method of spiropyran-based IGs. On the one hand, it is very simple and, in contrast to previous reports,[44,45,51] it can be directly applied to commercially available switches such as NO_2BIPS without the need of further derivatization to warrant functionalization of the liquid or solid phases of the gel. Instead, the spiropyran molecules just lie dissolved in the ionic liquid phase of our ionogels, which provides them with a soft, fluidic and conductive environment to facilitate NO_2BIPS switching upon illumination, addition of a chemical agent (e.g., acid), or application of an electrical current. In spite of this, it must be noted that no leakage of NO_2BIPS molecules from NO_2BIPS@IG films was observed in our experiments even when they were put in contact with external solutions (Figure S1). On the other hand, owing to the mechanical strength and the self-standing character of the IGs prepared, they can be easily shaped by cutting, thus offering significant advantages in the design and fabrication of smart devices using different printing methods (e.g., screen-printing or inkjet). Overall, our methodology for the preparation of spiropyran-doped IGs as versatile switching platforms drops the fabrication costs and complexity while granting access to the manufacture of flexible and stretchable smart devices.

Photochromism of NO_2BIPS@IG Membranes. The photochromic interconversion between **SP** and **MC** states still remains the most exploited switching mechanism for spiropyrans,[11] and it has been widely studied in solution for NO_2BIPS.[54,56] Therefore, it must be accurately preserved in the ionogels prepared for these materials to be of relevance. As observed in solution, the most stable isomer of NO_2BIPS found in NO_2BIPS@IG was the **SP** form, which mainly absorbs in the UV region (λ_{abs} = 346 nm) and makes the ionogel films essentially colorless and transparent at naked eye (Figure 2a,b). Actually, the UV−vis absorption spectrum measured for NO_2BIPS@IG fairly reproduced the behavior in the $[N_{1114}][TFSI]$ solution and other aprotic polar solvents (Figure S2), thus indicating that the spiropyran molecules are mainly solvated by the ionic liquid in the ionogel.

After UV irradiation (λ_{exc} = 365 nm), intense purple coloration of NO_2BIPS@IG was observed, which is indicative of extensive photoisomerization to the ring-opening isomer **MC** of the switch (Figure 2a).[54,56] In particular, a new absorption band in the visible region characteristic of **MC** formation was found (λ_{abs} = 548 nm, Figure 2b), which preserves the same spectral features registered in acetonitrile and $[N_{1114}][TFSI]$ solutions (Figure S2). This is a clear proof that polar **MC** molecules also lie well dissolved in the liquid phase of the ionogels at the concentrations studied in this work, as significant spectral changes should have occurred in the case of aggregation.[57] To assess the efficiency of the photocoloration process in the IG films, two different parameters were evaluated and compared to the behavior of NO_2BIPS in solution. First, the total conversion from **SP** to

https://doi.org/10.1021/acsami.1c04103
ACS Appl. Mater. Interfaces 2021, 13, 26460−26473

MC was found to be around 22% for the photostationary state (PSS) generated in NO_2BIPS@IG upon irradiation at 365 nm, a value rather similar to that measured for $[N_{1114}][TFSI]$ solutions (28%). Second, the quantum yield of the ring-opening photoisomerization process was calculated to be $\Phi_{SP\text{-}MC} = 0.15 \pm 0.03$ for NO_2BIPS@IG membranes, which is in good agreement with the behavior reported for NO_2BIPS in polar aprotic solvents ($\Phi_{SP\text{-}MC} = 0.24$ and 0.12 in acetone and acetonitrile, respectively).[19] Therefore, no detrimental effects on **SP**-to-**MC** photoisomerization were observed upon introduction of NO_2BIPS molecules in ionogel films.

As for the reverse back-isomerization process, it was investigated both thermally and photochemically for NO_2BIPS@IG. On the one hand, we observed that **MC**-to-**SP** back-isomerization in the dark followed a first-order kinetics with a rate constant of $k_{SP\text{-}MC} = 9.2 \times 10^{-4}$ s^{-1} at room temperature (Figure S3). This value is rather similar to those measured in the $[N_{1114}][TFSI]$ solution (1.90×10^{-3} s^{-1}, Figure S3) and in solvents of high polarity ($k_{SP\text{-}MC} = 1.0 \times 10^{-5}$ s^{-1} in ethanol at 25 °C[20]), which further confirms that NO_2BIPS molecules lie nonaggregated in solution-like domains within the ionogel films where their intrinsic photochromic properties are preserved. In addition, because of the high polarity of the ionic liquid phase of the ionogel that favors stabilization of the **MC** form, NO_2BIPS@IG shows a rather slow thermal decoloration process, which might be exploited for the preparation of long-lived printed patterns on the ionogels (Figure 2c,d). This is favored by the restricted diffusion mobility of spiropyran molecules within the membranes, which is much slower than that in liquid solution. As a result, embedding NO_2BIPS inside the ionogel matrix allows spatial confinement of the photoisomerized molecules within the irradiated areas for rather long periods (Figure 2c,d). On the other hand, if color fading is to be accelerated, irradiation with visible light can be exploited to induce fast **MC**-to-**SP** photoisomerization, which we found to occur in NO_2BIPS@IG at similar rates as in the $[N_{1114}][TFSI]$ solution. Actually, this allowed conducting repetitive SP−MC photoconversion cycles by sequential illumination with UV and visible light, which demonstrate the reversible and robust photoresponse of NO_2BIPS in the ionogels prepared (Figure S4).

Photohalochromism and Thermochromism of NO_2BIPS@IG Membranes. When dissolved in the ionic liquid $[N_{1114}][TFSI]$, NO_2BIPS preserves the photohalochromic behavior already described in other polar solvents such as acetonitrile (Figure S5), which is attributed to the basicity of the 4-nitrophenolate group of its open form.[21] Thus, upon addition of a strong acid (e.g., $HClO_4$) in the dark, the spirocyclic structure of the **SP** isomer opens to yield the (*Z*)-**MCH**$^+$ species, where the exocyclic carbon−carbon double bond maintains the cis configuration of the initial compound and its phenolate moiety is protonated (Scheme 1). This process, which can be reverted by the addition of a base, leads to a new absorption band at $\lambda_{abs} = 303$ nm characteristic of the (*Z*)-**MCH**$^+$ form. As a consequence, the solution remains essentially colorless. Similarly, acid−base titration of a solution of the **MC** isomer results in reversible formation of its protonated state (*E*)-**MCH**$^+$ with trans configuration and $\lambda_{abs} = 392$ nm, which makes the system turn from purple to yellow color (Scheme 1). In addition, the (*Z*)-**MCH**$^+$ and (*E*)-**MCH**$^+$ forms preserve the photochromic properties of the non-protonated SP−MC couple, and they can be reversibly interconverted upon carbon−carbon double bond photoisomerization with UV and violet-blue light, respectively (Scheme 1).

Interestingly, when embedded in IG membranes, NO_2BIPS molecules show a very similar photohalochromic behavior, probably due to the fact that they are principally solvated by the ionic liquid (Figure 3a,b). In particular, no change in color

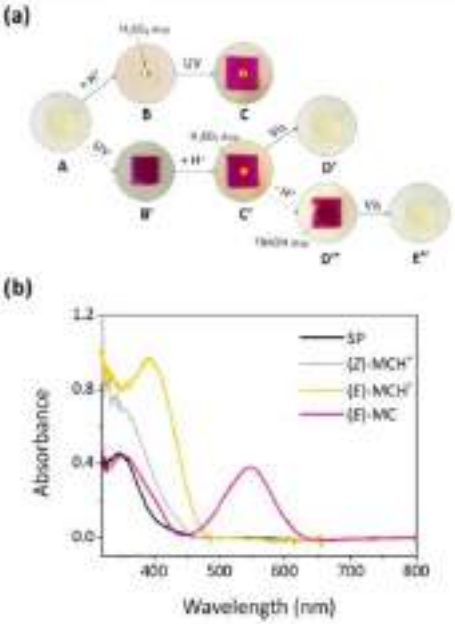

Figure 3. (a) Optical response of NO_2BIPS@IG ($\gamma_{NO_2BIPS} = 0.05$ mg NO_2BIPS/g IG) upon light and pH changes. (A) initial color (SP form), (B) drop of 10 mM H_2SO_4 solution, (C) irradiation at λ_{UV} = 365 nm. (B', C') UV irradiation of A (λ_{exc} = 365 nm) followed by addition of H_2SO_4 (D') irradiation of C' at λ_{VIS} = 445 nm, (D'', E'') addition of tetrabutylammonium hydroxide (TBAOH 10 mM) followed by visible light exposure (λ_{exc} = 445 nm). (b) UV−vis absorption spectra of the initial state of NO_2BIPS@IG (**SP**) and upon acidification ((*Z*)-**MCH**$^+$), and UV irradiation of (*Z*)-**MCH**$^+$ ((*E*)-**MCH**$^+$) and **SP** (**MC**).

was observed when a droplet of diluted H_2SO_4 was placed on top of NO_2BIPS@IG, though an increase in the absorption at $\lambda_{abs} < 400$ nm was registered, which is compatible with (*Z*)-**MCH**$^+$ formation. Unfortunately, competitive absorption by the ionogel matrix prevented proper determination of the absorption spectral maximum of this species at $\lambda_{abs} \sim 310$ nm. In spite of this, (*Z*)-**MCH**$^+$ generation could be corroborated by subsequent UV irradiation (λ_{exc} = 365 nm). While most of the membrane turned purple colored because of **SP**-to-**MC** photoisomerization, the area in contact with the acid droplet became yellow colored as expected for the (*Z*)-**MCH**$^+$-to-(*E*)-**MCH**$^+$ photoconversion process. The same effect was observed when the chemical and optical stimuli were applied in inverse order, which proves the capacity of the spiropyran molecules within the ionogel to undergo **MC**-to-(*E*)-**MCH**$^+$ transformation. Furthermore, all of these processes could be reverted by illumination with visible light and/or addition of a base, thus eventually recovering the initial colorless and transparent state of NO_2BIPS@IG. Therefore, our results

https://doi.org/10.1021/acsami.1c09154
ACS Appl. Mater. Interfaces 2021, 13, 26451−26461

demonstrate the potential of spiropyran-loaded IGs for the preparation of photohalochromic solid materials, as they allow the properties of the embedded switches to be preserved, warrant the access of wet chemicals (i.e., acid and base solutions) to the matrix, and enable confinement of the halochromic behavior to the regions of the system that are in contact with those chemicals. However, it must be mentioned that prolonged acid−base treatment of the IG membranes affected its chemical stability, which we attribute to the base-induced Hofmann elimination reaction of the quaternary ammonium cation of the $[N_{1114}][TFSI]$ IL.[58] As a consequence, a limited number of halochromic and photohalochromic cycles could be conducted before observing the degradation of the material (Figure S6).

Another stimulus to which spiropyrans can respond is temperature, as thermal heating can induce heterolytic cleavage of the $C-O_{spiro}$ bond of **SP** to yield the corresponding **MC** isomer. Although this process is not typically favored in organic media where **SP** is the most stable isomer, it could eventually occur if two main conditions are fulfilled: (a) the presence of electron-withdrawing groups stabilizing the negative charge of the phenolate moiety of **MC**, as it is the case of the nitro substituent in NO_2BIPS; and (b) dissolution in highly polar media that further contributes to the stabilization of the zwitterionic **MC** isomer (e.g., in water−methanol mixtures).[59] In view of this, the thermochromic behavior might be exhibited by NO_2BIPS@IG when the spiropyran molecules lie solvated by the highly polar ionic liquid $[N_{1114}][TFSI]$. Indeed, clear coloration both in the $[N_{1114}][TFSI]$ solution (Figure S7) and in the ionogel films was observed by just heating above 30 °C, and maximum **MC** absorption was registered at 45 °C for NO_2BIPS@IG that did not further increase at higher temperatures (λ_{abs} = 552 nm, Figure 4a,b). From the UV−vis absorption data, the maximum thermal isomerization yields in the $[N_{1114}][TFSI]$ solution and in the membranes were estimated to be 4 and 5%, respectively. This demonstrates that the thermochromic conversion from **SP** to **MC** is less efficient than that achieved upon exposure to light, probably due to the insufficient stabilization of the merocyanine form by the surrounding ionic liquid; however, the color change induced was clear and vivid enough as to be easily seen with naked eye.

It must be noted that a minor spectral shift was measured in our thermochromic experiments relative to the absorption of photochemically generated **MC** molecules (λ_{abs} = 548 nm). Although this must be ascribed to a simple thermal effect on absorption, it cannot be overlooked that the thermal ring-opening of the **SP** form of NO_2BIPS has been reported to yield different stereoisomers of **MC** bearing distinct optical properties instead of just the predominant (*E*)-**MC** structure obtained upon photoisomerization. Independent of this, fast decoloration of NO_2BIPS@IG was measured after subsequently cooling the ionogels down to room temperature, which demonstrates the reversibility of the thermochromic behavior. This was possible owing to the exceptional stability of the IGs prepared even at high temperatures, which results from the negligible vapor pressure and intrinsic thermal stability of ionic liquids (ILs). Indeed, multiple thermochromic cycles could be measured for NO_2BIPS@IG membranes without apparent degradation (Figure 4c). Therefore, these results pave the way for the fabrication of low-cost thermochromic materials based on spiropyrans for smart labeling and packaging.

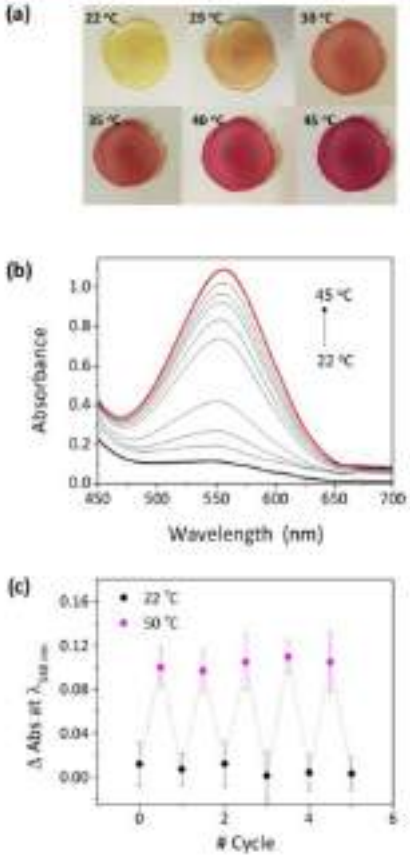

Figure 4. (a) Color change of NO_2BIPS@IG membranes (c_{NO_2BIPS} = 0.5 mg NO_2BIPS/g IG) when increasing the temperature gradually. (b) Variation of the UV−vis absorbance spectrum of NO_2BIPS@IG with temperature. (c) Variation of the absorbance at the spectral maximum of the **MC** isomer in NO_2BIPS@IG upon five consecutive thermochromic cycles. Average data is shown for three independent measurements in different membranes.

Electrochromism of NO_2BIPS@IG Membranes. In contrast to their photochromic, photohalochromic, and thermochromic behaviors, the electrochromic properties of spiropyrans have been less exploited, probably because of the difficulty to achieve redox-induced switching in solid materials. It is, therefore, in this area where the ionogels prepared in this work are expected to have a greater impact, as their large conductivities should enable the electrochemical operation of spiropyran switches. In light of this, the electrochromic and electrochemical properties of NO_2BIPS@IG were thoroughly investigated, for which we built on the previous findings about the redox-induced behavior of NO_2BIPS in solution: it dimerizes upon oxidation (Figure 5a).[49,60,61]

Based on that, we focused on analyzing the response of NO_2BIPS@IG upon electrochemical oxidation. Figure 5b shows the anodic region of the cyclic voltammogram of NO_2BIPS@IG, which presents a one-electron and irreversible oxidation wave at +0.95 V (vs Ag/AgCl) associated with the oxidation of the amino group of the indoline moiety to the

https://doi.org/10.1021/acsami.1c04159
ACS Appl. Mater. Interfaces 2021, 13, 26461−26471

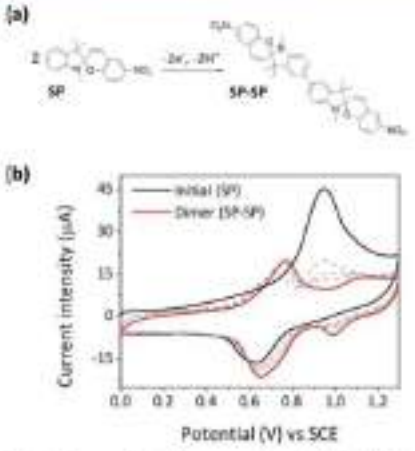

Figure 5. (a) Electrochemical conversion of NO_2BIPS into the dimeric species **SP**−**SP** upon oxidation.[32,50,61] (b) Cyclic voltammograms of NO_2BIPS@IG (c_{NO_2BIPS} = 0.5 mg NO_2BIPS/g IG) registered for a freshly prepared ionogel (solid black line) and after 30 consecutive oxidation cycles (red solid line, scan rate: 20 mV s^{-1}). Gray dashed lines correspond to intermediate voltammograms measured.

corresponding radical cation. After 30 consecutive anodic cycles at 50 mV s^{-1}, this wave disappeared, while two new oxidation signals at +0.77 and +1.10 V (vs Ag/AgCl) emerged with half the intensity. These observations are in good agreement with previous electrochemical results in solution,[32,33,60,61] and they are indicative of a dimerization process of NO_2BIPS to yield an **SP**−**SP** dimer via oxidative carbon−carbon bond formation. In fact, the oxidation waves at +0.77 and +1.10 V (vs Ag/AgCl) are attributed to the formation of the radical cation and dication of the dimer, respectively, while two new signals are also observed in the cathodic region of the voltammogram that correspond to the sequential reduction of the two nitro groups of the dimer ($E_{w,c}$ = −0.8 and −1.1 V (vs Ag/AgCl), Figure S8). Therefore, these results prove that the electrochemical behavior of NO_2BIPS@IG in solution can be directly transferred to the solid state by means of ionogel matrices. Actually, **SP** electrodimerization in these materials might be even favored by two additional factors. First, since the diffusion of NO_2BIPS molecules is largely restricted in the IL phase of the gel, the reactivity between the nearby **SP** radical cations must be further promoted. In fact, this effect has already been observed upon immobilization of NO_2BIPS onto surfaces, which assisted the electrochemical oxidative C−C aryl coupling of the switch. Second, the use of ionic liquids in IGs should also increase the stability of the reactive radical cation species through solvation, thus aiding the dimerization reaction.[62]

It is important to highlight that when applying +1.2 V (vs Ag/AgCl) using either a carbon screen-printed electrode (SPE) or an ITO-SPE electrode as a working electrode (WE), the electrochemical formation of the dimer in NO_2BIPS@IG is accompanied by a pronounced change in the color of the material, which turns intensely reddish-orange. Two main factors account for this behavior. First, **SP** dimerization is immediately followed by oxidation to the dicationic state of the dimer $[\mathbf{SP}-\mathbf{SP}]^{2+}$ at the applied potential, thus leading to the overall redox-induced **SP**-to-$[\mathbf{SP}-\mathbf{SP}]^{2+}$ transformation (Figure 6a). Second, the UV−vis absorption spectrum of the dicationic dimer $[\mathbf{SP}-\mathbf{SP}]^{2+}$ is bathochromically shifted with respect to the **SP** species (λ_{abs} = 416 and 500 nm for $[\mathbf{SP}-\mathbf{SP}]^{2+}$; Figure 6b) and, therefore, the ionogel becomes colored.

As **SP** electrodimerization is irreversible,[32,60,61] the coloration effect observed in NO_2BIPS@IG at E_{ap} = +1.2 V (vs Ag/AgCl) could not be reverted and a permanent modification of the initial colorless membrane was provoked, i.e., the material presents "electrochromism with memory" under these conditions (Figure 6a). Spectroelectrochemical measurements were conducted to characterize this electrochromic behavior, for which we fabricated a flexible device with a built-in three-electrode electrochemical cell where a 4 mm in diameter circular NO_2BIPS@IG membrane was deposited onto an ITO-SPE working electrode (Figures 6a and S10). On the one hand, a high color contrast was found in this process, as proven by the large change in transmittance measured at λ_{abs} = 500 nm when transforming **SP** into $[\mathbf{SP}-\mathbf{SP}]^{2+}$ (ΔT_1 = 90%, Figure S9). On the other hand, the switching time needed to produce 90% of such color change was observed to be rather long (t_c = 125 s, Figure 6c), probably because the electrochromic conversion implies a dimerization reaction that is limited by the spatial encounter between two **SP** molecules within the ionogel matrix where diffusion is restricted. Finally, the electrochromic efficiency (η) of the **SP**-to-$[\mathbf{SP}-\mathbf{SP}]^{2+}$ transformation was extracted from the slope of the linear region of the plot between the change in the optical density (ΔOD) and the current density needed to produce this change (Figure 6d). The obtained value, η = 245.9 cm^2 mC^{-1}, is somewhat lower than other reported results for electrochromic devices,[63] due to the large capacitive current of both the NO_2BIPS@IG membrane and the screen-printed ITO electrode used.

The electrochromic behavior of NO_2BIPS@IG can be further expanded by taking advantage of the reversible reduction of $[\mathbf{SP}-\mathbf{SP}]^{2+}$ to its radical cation $[\mathbf{SP}-\mathbf{SP}]^{+\bullet}$ and its neutral form $[\mathbf{SP}-\mathbf{SP}]$ (e.g., at E_{ap} = +0.2 V (vs Ag/AgCl)). These species show new different absorption bands in the visible (λ_{abs} = 360 and 473 nm for $[\mathbf{SP}-\mathbf{SP}]^{+\bullet}$ and λ_{abs} = 385 nm for $[\mathbf{SP}-\mathbf{SP}]$; Figure 6b) and near-IR regions (λ_{abs} = 874 and 984 nm for $[\mathbf{SP}-\mathbf{SP}]$; Figure 6b), some of which might be related to the intervalence charge transfer between the monocation and dication species.[64] As a consequence, a clear color change from reddish-orange to yellow takes place upon $[\mathbf{SP}-\mathbf{SP}]^{2+}$-to-$[\mathbf{SP}-\mathbf{SP}]$ transformation, which can be reverted after subsequent oxidation (Figure 6a). Therefore, this opens the door to use previously oxidized NO_2BIPS@IG membranes as "true electrochromic" systems, a behavior that we also characterized by means of spectroelectrochemical measurements on the flexible device shown in Figure 6a. In this case, the color contrast for the reversible electroswitching between $[\mathbf{SP}-\mathbf{SP}]^{2+}$ and $[\mathbf{SP}-\mathbf{SP}]$ was associated with a transmittance change at λ_{abs} = 500 nm of ΔT_2 = 47% (Figure S9), while the response time determined was significantly faster (t_c = 60.4 s, Figure 6c). As for the electrochromic reversibility and fatigue resistance of the $[\mathbf{SP}-\mathbf{SP}]^{2+}$-$[\mathbf{SP}-\mathbf{SP}]$ system, it was investigated upon consecutive applied voltages of E_{ap} = +1.2 and +0.2 V (vs Ag/AgCl) for 130 and 70 s, respectively (Figure 6e). After five oxidation−reduction cycles, the electrochromic response of the membranes remained rather stable as proven by the similar absorbance values measured at λ_{abs} = 500 nm for the dication and neutral forms of the spiropyran dimer. These results, together with the flexibility of

https://doi.org/10.1021/acsami.1c04158
ACS Appl. Mater. Interfaces 2021, 13, 26461−26471

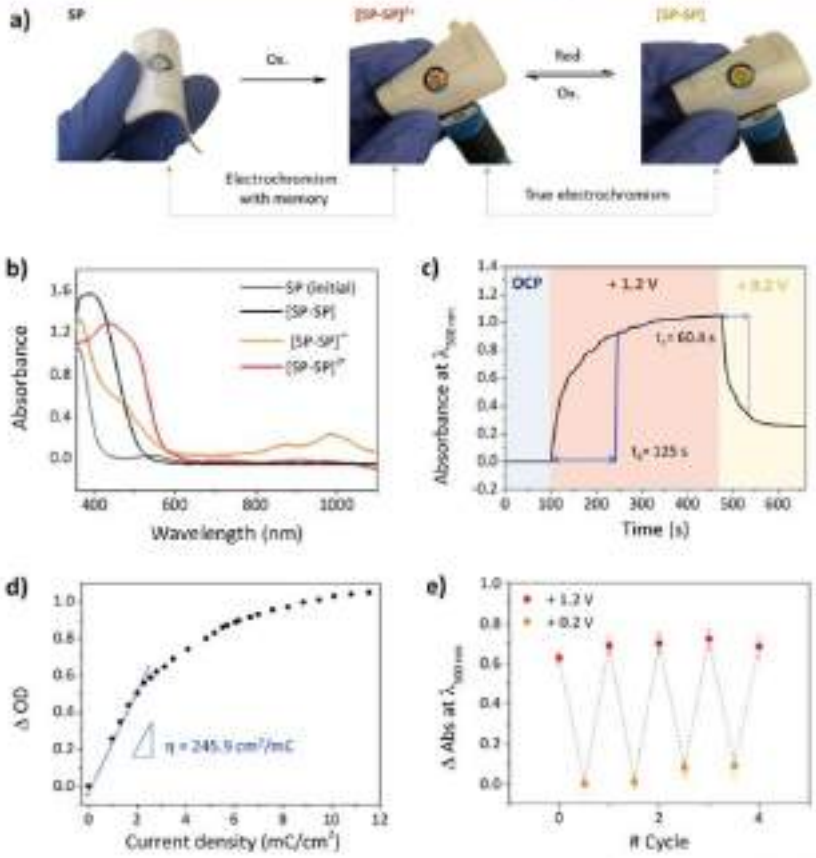

Figure 6. (a) Flexible display with a three-electrode compartment. The NO_2BIPS@IG membrane (c_{NO_2BIPS} = 0.5 mg NO_2BIPS/g IG) is in contact with an ITO-SPE working electrode (WE) and changes its color when applying electric potentials to induce irreversible SP-to-$[SP-SP]^{2+}$ and reversible $[SP-SP]^{2+}$-[SP–SP] transformations. (b) UV–vis absorption spectra of the initial state of NO_2BIPS@IG (SP) and of the different redox products formed: [SP–SP], $[SP-SP]^{+\bullet}$, and $[SP-SP]^{2+}$. (c) Change in absorbance monitored at λ_{abs} = 500 nm for the electrochromic device shown in (a) before applying any electric potential (OCP, 0–100 s), at E_{ap} = +1.2 V (vs Ag/AgCl, 100–475 s), and at E_{ap} = +0.2 V (vs Ag/AgCl, 475–655 s). (d) Plot of the optical density difference at λ_{abs} = 500 nm against the current density passed at E_{ap} = +1.2 V (vs Ag/AgCl) for the electrochromic device shown in (a). (e) Switching color reversibility measured at λ_{abs} = 500 nm for the same electrochromic device after applying consecutive cycles of E_{ap} = +1.2 V (vs Ag/AgCl) for 130 s and E_{ap} = +0.2 V (vs Ag/AgCl) for 70 s. Average data is shown for three independent measurements in different membranes.

the electrochemical device prepared, make NO_2BIPS@IG membranes very appealing electrochromic materials for the fabrication of systems of great technological interest, such as wearable sensors[63] and flexible panels.[64]

Multistimuli-Responsive Displays Based on NO_2BIPS@IG. To demonstrate the feasibility of spiropyran-loaded ionogels for practical applications, we built a simple microfluidic architecture with multistimuli-responsive performance (Figure S11). In this device, we introduced four different NO_2BIPS@IG membranes cut with distinct complex shapes using a CO_2 ablation laser, for which we took advantage of their high mechanical strength and high thermal and chemical stability. Each one of those membranes could then be exposed independently to stimuli of variable nature, as shown in Figure 7. For the U-shaped membrane, a hot liquid flow (T = 40 °C) was passed through the microfluidic cell to induce the thermochromic conversion into a pink-colored **MC** isomer. The A-shaped membrane was instead put into contact with a

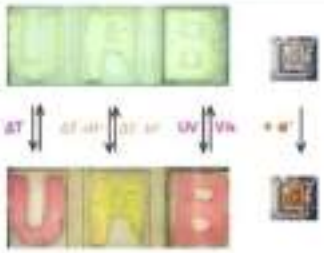

Figure 7. Multistimuli-responsive microfluidic prototype device based on NO_2BIPS@IG shaped into letters and a square (c_{NO_2BIPS} = 0.5 mg NO_2BIPS/g IG). Each form was exposed to different external stimuli: T, pH, light, and electric potential.

hot acidic solution (T = 40 °C), which led to the thermohalochromic formation of the yellow-colored (*E*)-

https://doi.org/10.1021/acsami.1c04719
ACS Appl. Mater. Interfaces 2021, 13, 26461−26471

MCH$^+$ form. In the case of the B-shaped membrane, the pink-colored **MC** state was reached upon UV irradiation (λ_{exc} = 365 nm) through a near-UV and visible transparent window. Finally, to trigger the electrochromic response of the system, the square-shaped NO_2BISP@IG membrane was placed on top of a platinum (Pt) electrode and an irreversible color change from transparent to orange was obtained because of **SP** electrodimerization to yield $[\mathbf{SP}-\mathbf{SP}]^{2+}$ at E_{ap} = +1.0 V (vs Pt). Hence, selective and reversible thermo-, halo-, photo-, and electrochromic responses could be measured for each one of them by appropriately selecting the stimulus of interest.

To further demonstrate the potential of spiropyran-loaded ionogels for the fabrication of smart devices, we decided to exploit their good mechanical properties for the preparation of multiresponsive flexible displays. With this aim, a microfluidic channel was incorporated to the flexible electrochromic device shown in Figure 6a, thus enabling the application of other stimuli different from electrical potentials to NO_2BISP@IG (Figures 8 and S10). Thus, the introduction of hot water and

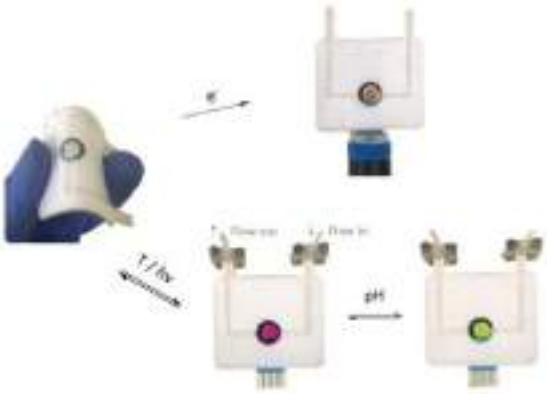

Figure 8. Flexible multistimuli-responsive microfluidic prototype based on NO_2BIPS@IG (c_{NO_2BIPS} = 0.5 mg NO_2BIPS/g IG). The material shows different color responses upon application of distinct external stimuli in a single device: *T*, pH, light, and electrical potential.

aqueous acidic solutions resulted in color changes compatible with the transformation of the colorless initial **SP** molecules in the ionogel to the pink **MC** isomer and the yellow (*E*)-**MCH**$^+$ protonated species. In addition, **SP**-to-**MC** conversion could also be induced under UV irradiation, while the system preserved its capacity to turn reddish-orange when applying a potential of +1.2 V (vs Ag/AgCl) to induce $[\mathbf{SP}-\mathbf{SP}]^{2+}$ formation. These results, together with those shown for the rigid microfluidic prototype, are unambiguous proofs that ionogels offer a wide range of advantageous properties (i.e., facile formulation, high ionic conductivities and optical transparency, chemical and thermal stability, access to chemicals from external solutions, and mechanical strength and flexibility) that make them a very promising platform for the fabrication of smart devices based on multistimuli-responsive molecular switches.

CONCLUSIONS

In this work, we have demonstrated the potential of ionogels to be used as platforms for the preparation of smart materials based on multistimuli-responsive molecular switches. With this aim, we formulated ionogels from a polyfluorinated polymer and an ionic liquid that were loaded with the photo-, halo-, thermo-, and electrosensitive NO_2BIPS spiropyran derivative. The advantages of the resulting NO_2BIPS@IG membranes were found to be multifold. First, the solution-like photochromic properties of the switch were preserved in the ionogels thanks to the light transparency of these materials and the fluid nature of their ionic liquid phase where NO_2BIPS molecules lie, which favors the large conformational changes needed for the switching process to occur. The latter also grants fast access of chemicals to NO_2BIPS@IG (e.g., acids and bases), which we exploited to trigger the characteristic halo- and photohalochromic operations of the embedded switch molecules. In addition, because of the nonvolatility of ionic liquids, the ionogel membranes obtained could be heated without degradation to stimulate the thermochromic behavior of NO_2BIPS. More importantly, NO_2BIPS@IG strongly benefits from the adequate ionic conductivity provided by the ionic liquid phase of the material, which enabled the electroinduced operation of the molecular switch. All of these features, in combination with the facile preparation, flexibility, mechanical strength, self-standing nature, and shapeability of ionogels, make these materials promising candidates for the fabrication of a range of stimuli-sensitive systems and devices for optoelectronic applications (e.g., smart displays, chemical sensors, security inks, data storage). As a proof of concept, we constructed rigid and flexible microfluidic prototype devices containing different NO_2BIPS@IG membranes that could be independently exposed to external stimuli to selectively promote their photo, halo-, thermo-, and electrochromic response.

EXPERIMENTAL SECTION

Materials. 1′,3′-Dihydro-1′,3′,3′-trimethyl-6-nitrospiro[2*H*-1-benzopyran-2,2′-(2*H*)-indole] (NO_2BIPS) was purchased from TCI Chemicals (≥98% pur.) and used without further purification. Poly(vinylidene fluoride-*co*-hexafluoropropylene) (P(VDF-*co*-HFP)) and HCl 36.5−38% were acquired from Merck and used as received. Trimethylbutylammonium bis(trifluoromethylsulfonyl)amide ($[N_{1114}][TFSI]$) was purchased from Solvionic and dried under vacuum using molecular sieves for 24 h to ensure a total water content lower than 0.001%. Acetone was purchased from Acros (≥99.5% pur.) and used as provided.

Preparation of NO_2BIPS@IG Membranes. For NO_2BIPS@IG preparation, P(VDF-*co*-HFP) and the ionic liquid $[N_{1114}][TFSI]$ were mixed in acetone in a 1:5 weight ratio. This mixture was stirred overnight at room temperature and under a N_2 atmosphere until the polymer was fully dissolved, and it was finally sonicated for 3 min. Later, the desired amount of NO_2BIPS was added to the solution and dissolved by stirring. The concentration of NO_2BIPS in the ionogel membranes (NO_2BIPS@IG) was selected taking into account the film thickness (typically, ∼60 μm) to obtain absorbance values below 1 in the UV−vis spectra. In most of the cases, this was observed for NO_2BIPS contents in the range of c_{NO_2BIPS} = 0.05−0.5 mg NO_2BIPS/g IG. The resulting viscous solution was cast into a ceramic evaporating dish and was left at room temperature for 24 h until the solvent was completely evaporated. Eventually, a transparent, flexible, and elastic thin film was obtained. Films could be stored for weeks in a glovebox without observing any detrimental effect in their stimuli-responsive properties.

Characterization of NO_2BIPS@IG Membranes. Ultraviolet−visible (UV−vis) absorption spectra were recorded in a Hanamatsu L10290 spectrophotometer and a HP 8453 spectrophotometer. Spectroelectrochemical studies were performed coupling a VSP100 potentiostat controlled by EC-Lab V9.51 software to the Hanamatsu L10290 spectrophotometer. Electrochemical and spectroelectrochem-

https://doi.org/10.1021/acsami.1c04158
ACS Appl. Mater. Interfaces 2021, 13, 26461−26471

ical measurements on NO_2BIPS@IG membranes were performed using screen-printed electrodes (SPE, DropSens), a three-electrode system composed of a carbon or optically transparent ITO as a working electrode (WE), a carbon counter electrode (CE), and a Ag/AgCl reference electrode. Since NO_2BIPS@IG membranes are photoresponsive, the spectroelectrochemical measurements were performed in discontinuous mode, recording the spectra in time for 0.5 s to avoid the long-time exposure of the sample to the light beam. An infrared probe (Laserliner ThermoSpot) was used for monitoring the temperature of the IG membrane when heated. To estimate the composition of the **SP**−**MC** mixtures prepared upon irradiation, the **MC** content in the resulting photostationary states was calculated by Lambert Beer's equation using its absorption coefficient reported in ref 54. The **SP**-to-**MC** photoisomerization quantum yield in the ionogel membrane was determined using the methodology reported in refs 67 and 68, which is described in detail in the Supporting Information.[69] **SP**-to-**MC** photoisomerization was induced with a Vilber Lourmat UV lamp equipped with two 4 W tubes emitting at 365 nm or the third harmonic of a Nd:YAG ns-pulsed laser (Brilliant, Quantel, λ_{exc} = 365 nm), while **MC**-to-**SP** back-photoisomerization was triggered with a cw laser diode at λ_{exc} = 532 nm (Z-Laser). The thermal back-photoisomerization **MC**-to-**SP** process in solution and the membranes was investigated in the dark and at room temperature using the methodology described in the Supporting Information. For the photohalochromic study, an acidic 10 mM H_2SO_4 and a basic 10 mM TBAOH aqueous solutions were prepared, and a total volume of 20 μL was cast on the top of NO_2BIPS@IG membranes. Depending on the state aimed to reach, a combination of an acidic or basic solution was used along with the irradiation at λ_{exc} = 445 nm (sciTec), λ_{exc} = 365 nm, (Brilliant, Quantel, λ_{exc} = 365 nm), or λ_{exc} = 532 nm (Z-Laser).

Fabrication of Multistimuli-Responsive Devices. The portable rigid microfluidic system was designed and fabricated using low-cost polymers poly(methyl methacrylate) (PMMA), double-sided pressure-sensitive adhesive (PSA), and poly(dimethyl siloxane) (PDMS) to demonstrate the feasibility of NO_2BIPS@IG in real scenarios (Figure S11). The polymers were fast-prototyped with a CO_2-laser writer (Epilog Mini 24, Epilog Laser). The total size of the fluidic system was 9 mm in height, 43 mm in width, and 70 mm in length. The system was formed by two structures (bottom and top) of different layers of polymers. The bottom structure (Figure S11b) was formed by 2 PMMA layers bonded with a 175 μm thick PSA layer. A bottom black-colored 3 mm thick PMMA layer was used to avoid the light beam losses during light exposure of the NO_2BIPS@IG material. The second 380 μm thick PMMA layer enabled the position of the chips used for the electrochromic tests. Two 11 × 9 mm^2 silicon chips fabricated using standard photolithographic techniques were used in this system:[9] a chip containing two in-parallel platinum (Pt) microelectrodes working as a working electrode (WE) and a chip containing three in-parallel Pt microelectrodes working as a counter (CE) and pseudo-reference electrodes (p-RE). The microelectrodes had an area of 2.5 or 5 mm^2. The bottom structure is completed by a 680 μm PDMS layer defining the outline of the four NO_2BIPS@IG material pieces used for the light, pH, temperature, and electric potential tests. This layer enabled the hosting of the NO_2BIPS@IG pieces and their perfect alignment with the microfluidic cells defined in the top structure. Four shapes are defined for the tests: a letter U, a letter A, a letter B, and a square, which are used for the temperature, pH, light, and electric potential stimulus, respectively. Regarding the electrochemical cell, other shapes are defined in the PDMS to expose the microelectrodes used as CE and p-RE. Finally, two more rectangular shapes are defined to allow the electrical connection of the chip with the potentiostat equipment. The PDMS layer also disenabled the fluidic leakage between both structures during the fluidic tests. The top structure (Figure S11c) is formed by four 500 μm thick layers bonded by 175 μm thick PSA layers. These layers defined three 75 μL and one 37.5 μL microfluidic cells used for temperature, pH, light, and electric potential stimulus, respectively. The PMMA layers also enabled the fluidic connection between them, the position of the microfluidic threads used in each inlet and outlet for all cells, and the insertion of the two spring-loaded connectors (RS Components, Switzerland) used to contact the chips with the measurement instrument. Finally, both structures were fixed using screws (2 mm diameter) to allow easy assembly and disassembly of the system (Figure S11d). Samples were flowed inside the device using acidic diluted aqueous solution of $HClO_4$ or basic diluted aqueous solution of TBAOH at different temperatures. However, in the case of the electrochemical compartment, no aqueous solution was flowed to avoid side reactions during the electrochromic performance. In this case, bare IG was used as a solid electrolyte to ensure adequate ionic conductivity.

The flexible multistimuli-responsive device (37.5 mm in width and 41 mm in length) was formed by five layers of fast-prototyped polymers mechanized with a laser writer (Figure S10). A 175 μm polycarbonate layer was used to close the microfluidic device and to define the position of the 1 mm in diameter microfluidic inlet and outlet (Layer 1). Layer 2 was made of a 175 μm thick PSA film, which defined the 1 mm in width microfluidic channels connecting the inlet and outlet in Layer 1 with a 20 μL electrochemical cell. Layer 3 was formed by a 175 μm thick PSA layer bonded to a 50 μm PMMA layer and was used to contact the electrochemical cell to the electrochemical sensor. The electrochemical sensor was fabricated with a Dropsens screen-printed ITO electrode and positioned using the hole defined in Layer 4 (175 μm thick double-sided PSA layer +50 μm PMMA layer). Finally, the flexible device was enclosed by a 50 μm thick PSA layer used as a white back-cover. A 4 mm in diameter circular NO_2BIPS@IG membrane was deposited onto the ITO-SPE working electrode of the electrochemical sensor. Samples were flowed inside the device using an acidic diluted aqueous solution of $HClO_4$ or a basic diluted aqueous solution of TBAOH at different temperatures.

■ ASSOCIATED CONTENT

Supporting Information

The Supporting Information is available free of charge at https://pubs.acs.org/doi/10.1021/acsami.1c04159.

NO_2BIPS@IG membranes water stability; photoisomerization in acetonitrile and [N1114][TFSI] solutions; determination of photoisomerization quantum yields for NO_2BIPS@IG membranes; thermal-back isomerization reaction in [N1114][TFSI] solution and the NO_2BIPS@IG membrane; photoisomerization cycles in NO_2BIPS@IG membrane; photohalochromism of NO_2BIPS in acetonitrile and [N1114][TFSI]; halochromic cycles in NO_2BIPS@IG membranes; thermochromism of NO_2BIPS in [N1114][TFSI] solution; cyclic voltammetry of NO_2BIPS@IG membranes; electrochromic characterization of NO_2BIPS@IG membranes; fabrication of rigid microfluidic devices; fabrication of flexible devices (PDF)

■ AUTHOR INFORMATION

Corresponding Authors

Jordi Hernando − *Departament de Química, Universitat Autònoma de Barcelona, Barcelona 08193, Spain;*
orcid.org/0000-0002-1126-4138;
Email: Jordi.Hernando@uab.cat

Gonzalo Guirado − *Departament de Química, Universitat Autònoma de Barcelona, Barcelona 08193, Spain;*
orcid.org/0000-0003-2128-7007;
Email: Gonzalo.Guirado@uab.cat

Authors

Sara Santiago − *Departament de Química, Universitat Autònoma de Barcelona, Barcelona 08193, Spain; Institute*

https://doi.org/10.1021/acsami.1c04159
ACS Appl. Mater. Interfaces 2021, 13, 26461−26471

de Microelectrónica de Barcelona (IMB-CNM, CSIC), Barcelona 08193, Spain

Pablo Giménez-Gómez − *Instituto de Microelectrónica de Barcelona (IMB-CNM, CSIC), Barcelona 08193, Spain;* orcid.org/0000-0003-3443-802X

Xavier Muñoz-Berbel − *Instituto de Microelectrónica de Barcelona (IMB-CNM, CSIC), Barcelona 08193, Spain;* orcid.org/0000-0002-6447-5756

Complete contact information is available at: https://pubs.acs.org/10.1021/acsami.1c04159

Author Contributions

The manuscript was written through contributions of all authors. All authors have given approval to the final version of the sending manuscript.

Notes

The authors declare no competing financial interest.

■ ACKNOWLEDGMENTS

The authors thank the Ministerio de Ciencia e Innovación and the Agencia Estatal de Investigación of Spain for financial support through the projects CTQ 2015-65439-R and PID2019-106171RB-100/AEI/10.13039/501100011033.

■ REFERENCES

(1) Qi, Z.; Schalley, C. A. Multi-Stimuli Responsive Materials. In *Chemoresponsive Materials: Stimulation by Chemical and Biological Signals*; Schneider, H.-J., Ed.; Smart Materials Series; Royal Society of Chemistry: Cambridge, 2015; Chapter 5, pp 98−135.

(2) Zhuang, J.; Gordon, M. R.; Ventura, J.; Li, L.; Thayumanavan, S. Multi-Stimuli Responsive Macromolecules and Their Assemblies. *Chem. Soc. Rev.* **2013**, *42*, 7421−7435.

(3) Ke, Y.; Wang, S.; Liu, G.; Li, M.; White, T. J.; Long, Y. Vanadium Dioxide: The Multistimuli Responsive Material and Its Applications. *Small* **2018**, *14*, No. 1802025.

(4) Fu, X.; Hosta-Rigau, L.; Chandrawati, R.; Cui, J. Multi-Stimuli-Responsive Polymer Particles, Films, and Hydrogels for Drug Delivery. *Chem* **2018**, *4*, 2084−2107.

(5) Jochum, F. D.; Theato, P. Temperature- and Light-Responsive Smart Polymer Materials. *Chem. Soc. Rev.* **2013**, *42*, 7468−7483.

(6) *Molecular Switches*; Feringa, B. L.; Browne, W. R., Eds.; Wiley-VCH Verlag GmbH & Co. KGaA: Weinheim, Germany, 2011.

(7) Zhang, J.; Wang, J.; Tian, H. Taking Orders from Light: Progress in Photochromic Bio-Materials. *Mater. Horiz.* **2014**, *1*, 169−184.

(8) Natali, M.; Giordani, S. Molecular Switches as Photocontrollable "Smart" Receptors. *Chem. Soc. Rev.* **2012**, *41*, 4010−4029.

(9) Moulin, E.; Faour, L.; Carmona-Vargas, C. C.; Giuseppone, N. From Molecular Machines to Stimuli-Responsive Materials. *Adv. Mater.* **2020**, *32*, No. 1906036.

(10) Pu, S.-Z.; Sun, Q.; Fan, C.-B.; Wang, R.-J.; Liu, G. Recent Advances in Diarylethene-Based Multi-Responsive Molecular Switches. *J. Mater. Chem. C* **2016**, *4*, 3075−3093.

(11) Bisoyi, H. K.; Li, Q. Light-Driven Liquid Crystalline Materials: From Photo-Induced Phase Transitions and Property Modulations to Applications. *Chem. Rev.* **2016**, *116*, 15089−15166.

(12) Kortekaas, L.; Browne, W. R. The Evolution of Spiropyran: Fundamentals and Progress of an Extraordinarily Versatile Photochrome. *Chem. Soc. Rev.* **2019**, *48*, 3406−3424.

(13) Berkovic, G.; Krongauz, V.; Weiss, V. Spiropyrans and Spirooxazines for Memories and Switches. *Chem. Rev.* **2000**, *100*, 1741−1754.

(14) Florea, L.; Diamond, D.; Benito-Lopez, F. Photo-Responsive Polymeric Structures Based on Spiropyran. *Macromol. Mater. Eng.* **2012**, *297*, 1148−1159.

(15) Klajn, R. Spiropyran-Based Dynamic Materials. *Chem. Soc. Rev.* **2014**, *43*, 148−184.

(16) Kortekaas, L.; Browne, W. R. The Evolution of Spiropyran: Fundamentals and Progress of an Extraordinarily Versatile Photochrome. *Chem. Soc. Rev.* **2019**, *48*, 3406−3424.

(17) Berkovic, G.; Krongauz, V.; Weiss, V. Spiropyrans and Spirooxazines for Memories and Switches. *Chem. Rev.* **2000**, *100*, 1741−1753.

(18) Mondal, B.; Ghosh, A. K.; Mukherjee, P. S. Reversible Multistimuli Switching of a Spiropyran-Functionalized Organic Cage in Solid and Solution. *J. Org. Chem.* **2017**, *82*, 7783−7790.

(19) Mialane, P.; Zhang, G.; Mbomekalle, I. M.; Yu, P.; Compain, J. D.; Dolbecq, A.; Marrot, J.; Sécheresse, F.; Keita, B.; Nadjo, L. Dual Photochromic/Electrochromic Compounds Based on Cationic Spiropyrans and Polyoxometalates. *Chem. - Eur. J.* **2010**, *16*, 5572−5576.

(20) Meng, X.; Qi, G.; Li, X.; Wang, Z.; Wang, K.; Zou, B.; Ma, Y. Spiropyran-Based Multi-Colored Switching Tuned by Pressure and Mechanical Grinding. *J. Mater. Chem. C* **2016**, *4*, 7584−7588.

(21) Kortekaas, L.; Chen, J.; Jacquemin, D.; Browne, W. R. Proton-Stabilized Photochemically Reversible E/ Z Isomerization of Spiropyrans. *J. Phys. Chem. B* **2018**, *122*, 6423−6430.

(22) Kong, L.; Wong, H.-L.; Tam, A. Y.-Y.; Lam, W. H.; Wu, L.; Yam, V. W.-W. Synthesis, Characterization, and Photophysical Properties of Bodipy-Spirooxazine and -Spiropyran Conjugates: Modulation of Fluorescence Resonance Energy Transfer Behavior via Acidochromic and Photochromic Switching. *ACS Appl. Mater. Interfaces* **2014**, *6*, 1550−1562.

(23) Chen, S.; Jiang, F.; Cao, Z.; Wang, G.; Dong, Z.-M. Photo, PH, and Thermo Triple-Responsive Spiropyran-Based Copolymer Nanoparticles for Controlled Release. *Chem. Commun.* **2015**, *51*, 12633−12636.

(24) Liu, Z.; Jiang, L.; Liang, Z.; Gao, Y. Photo-Switchable Molecular Devices Based on Metal-Ionic Recognition. *Tetrahedron Lett.* **2005**, *46*, 885−887.

(25) Fries, K. H.; Sheppard, G. R.; Bilbrey, J. A.; Locklin, J. Tuning Chelating Groups and Comonomers in Spiropyran-Containing Copolymer Thin Films for Color-Specific Metal Ion Binding. *Polym. Chem.* **2014**, *5*, 2094−2102.

(26) Natali, M.; Aakeröy, C.; Desper, J.; Giordani, S. The Role of Metal Ions and Counterions in the Switching Behavior of a Carboxylic Acid Functionalized Spiropyran. *Dalton Trans.* **2010**, *39*, 8269−8277.

(27) Paramonov, S. V.; Lokshin, V.; Fedorova, O. A. Spiropyran, Chromene or Spirooxazine Ligands: Insights into Mutual Relations between Complexing and Photochromic Properties. *J. Photochem. Photobiol., C* **2011**, *12*, 209−236.

(28) Julià-López, A.; Ruiz-Molina, D.; Hernando, J.; Roscini, C. Solid Materials with Tunable Reverse Photochromism. *ACS Appl. Mater. Interfaces* **2019**, *11*, 11884−11892.

(29) Abdollahi, A.; Alinejad, Z.; Mahdavian, A. R. Facile and Fast Photosensing of Polarity by Stimuli-Responsive Materials Based on Spiropyran for Reusable Sensors: A Physico-Chemical Study on the Interactions. *J. Mater. Chem. C* **2017**, *5*, 6588−6600.

(30) Rosario, R.; Gust, D.; Hayes, M.; Springer, J.; Garcia, A. A. Solvatochromic Study of the Microenvironment of Surface-Bound Spiropyrans. *Langmuir* **2003**, *19*, 8801−8806.

(31) Jin Fang Zhi; Baba, R.; Hashimoto, K.; Fujishima, A. Photoelectrochromic Properties of a Spirobenzopyran Derivative. *J. Photochem. Photobiol., A* **1995**, *92*, 91−97.

(32) Ivashenko, O.; Van Herpt, J. T.; Feringa, B. L.; Rudolf, P.; Browne, W. R. Electrochemical Write and Read Functionality through Oxidative Dimerization of Spiropyran Self-Assembled Monolayers on Gold. *J. Phys. Chem. C* **2013**, *117*, 18567−18577.

(33) Preigh, M. J.; Stauffer, M. T.; Lin, F. T.; Weber, S. G. Anodic Oxidation Mechanism of a Spiropyran. *J. Chem. Soc., Faraday Trans.* **1996**, *92*, 3991−3996.

(34) Kimoshi, K.; Nakamura, S.; Imamura, M.; Ishida, K.; Ueda, Y. The Mechanism for Negative Photochromism of Spiropyran in Silica. *J. Phys. Org. Chem.* **2012**, *25*, 462−466.

(35) Tork, A.; Boudreault, F.; Roberge, M.; Ritcey, A. M.; Lessard, R. A.; Galstian, T. V. Photochromic Behavior of Spiropyran in Polymer Matrices. *Appl. Opt.* **2001**, *40*, 1180−1186.
(36) Sharifian, M. H.; Mahdavian, A. R.; Salehi-Mobarakeh, H. Effects of Chain Parameters on Kinetics of Photochromism in Acrylic−Spiropyran Copolymer Nanoparticles and Their Reversible Optical Data Storage. *Langmuir* **2017**, *33*, 8023−8031.
(37) Gonzalez, A.; Kengmana, E. S.; Fonseca, M. V.; Han, G. G. D. Solid-State Photoswitching Molecules: Structural Design for Isomerization in Condensed Phase. *Mater. Today Adv.* **2020**, *6*, No. 100058.
(38) Julià-López, A.; Hernando, J.; Ruiz-Molina, D.; González-Monje, P.; Sedó, J.; Roscini, C. Temperature-Controlled Switchable Photochromism in Solid Materials. *Angew. Chem.* **2016**, *128*, 15268−15272.
(39) Schwartz, H. A.; Olthof, S.; Schaniel, D.; Meerholz, K.; Ruschewitz, U. Solution-Like Behavior of Photoswitchable Spiropyrans Embedded in Metal−Organic Frameworks. *Inorg. Chem.* **2017**, *56*, 13100−13110.
(40) Healey, K.; Liang, W.; Southon, P. D.; Church, T. L.; D'Alessandro, D. M. Photoresponsive Spiropyran-Functionalised MOF-808: Postsynthetic Incorporation and Light Dependent Gas Adsorption Properties. *J. Mater. Chem. A* **2016**, *4*, 10816−10819.
(41) Kundu, P. K.; Olsen, G. L.; Kiss, V.; Klajn, R. Nanoporous Frameworks Exhibiting Multiple Stimuli Responsiveness. *Nat. Commun.* **2014**, *5*, No. 3588.
(42) Peterson, C.; Hillmyer, M. A. Fast Photochromic Dye Response in Rigid Block Polymer Thermosets. *ACS Appl. Polym. Mater.* **2019**, *1*, 2778−2786.
(43) Nam, Y. S.; You, I.; Yarimaga, O.; Park, I. S.; Park, D. H.; Song, S.; Kim, J. M.; Lee, C. W. Photochromic Spiropyran-Embedded PDMS for Highly Sensitive and Tunable Optochemical Gas Sensing. *Chem. Commun.* **2014**, *50*, 4251−4254.
(44) Wang, W.; Hu, J.; Zheng, M.; Zheng, L.; Wang, H.; Zhang, Y. Multi-Responsive Supramolecular Hydrogels Based on Merocyanine−Peptide Conjugates. *Org. Biomol. Chem.* **2015**, *13*, 11492−11498.
(45) Li, C.; Iscen, A.; Palmer, L. C.; Schatz, G. C.; Stupp, S. I. Light-Driven Expansion of Spiropyran Hydrogels. *J. Am. Chem. Soc.* **2020**, *142*, 8447−8453.
(46) Francis, W.; Dunne, A.; Delaney, C.; Florea, L.; Diamond, D. Spiropyran Based Hydrogels Actuators—Walking in the Light. *Sens. Actuators, B* **2017**, *250*, 608−616.
(47) Sahraoui, R.; Siddiqa, A.; Razzaq, H.; Iqbal, T.; Qaisar, S. PVDF Based Ionogels: Applications towards Electrochemical Devices and Membrane Separation Processes. *Heliyon* **2018**, *4*, No. e00847.
(48) Le Bideau, J.; Viau, L.; Vioux, A. Ionogels, Ionic Liquid Based Hybrid Materials. *Chem. Soc. Rev.* **2011**, *40*, 907−925.
(49) Chen, N.; Zhang, H.; Li, L.; Chen, R.; Guo, S. Ionogel Electrolytes for High-Performance Lithium Batteries: A Review. *Adv. Energy Mater.* **2018**, *8*, No. 1702675.
(50) Kavanagh, A.; Byrne, R.; Diamond, D.; Fraser, K. J. Stimuli Responsive Ionogels for Sensing Applications—An Overview. *Membranes* **2012**, *2*, 16−39.
(51) Cao, Z.; Liu, H.; Jiang, L. Hydrogen-Bonding-Driven Tough Ionogels Containing Spiropyran-Functionalized Ionic Liquids. *ACS Appl. Polym. Mater.* **2020**, 2359−2365.
(52) Ivashenko, O.; van Herpt, J. T.; Rudolf, P.; Feringa, B. L.; Browne, W. R. Oxidative Electrochemical Aryl C−C Coupling of Spiropyrans. *Chem. Commun.* **2013**, *49*, 6737−6739.
(53) Sueishi, Y.; Ohcho, M.; Nishimura, N. Kinetic Studies of Solvent and Pressure Effects on Thermochromic Behavior of 6-Nitrospiropyran. *Bull. Chem. Soc. Jpn.* **1985**, *58*, 2608−2613.
(54) Görner, H. Photochromism of Nitrospiropyrans: Effects of Structure, Solvent and Temperature. *Phys. Chem. Chem. Phys.* **2001**, *3*, 416−423.
(55) Villabona, M.; Benet, M.; Mena, S.; Al-Kaysi, R. O.; Hernando, J.; Guirado, G. Multistimuli-Responsive Fluorescent Switches Based on Spirocyclic Meisenheimer Compounds: Smart Molecules for the Design of Optical Probes and Electrochromic Materials. *J. Org. Chem.* **2018**, *83*, 9166−9177.
(56) Lenoble, C.; Becker, R. S. Photophysics, Photochemistry, Kinetics, and Mechanism of the Photochromism of 6′-Nitroindolinospiropyran. *J. Phys. Chem. A* **1986**, *90*, 62−65.
(57) Urnanski, P. UV−Assisted Formation of Nanoaggregates from Photochromic Spiropyrans in Nonpolar Solvents. *Langmuir* **2003**, *19*, 1919−1922.
(58) Landini, D.; Maia, A.; Rampoldi, A. Stability of Quaternary Onium Salts under Phase-Transfer Conditions in the Presence of Aqueous Alkaline Solutions. *J. Org. Chem.* **1986**, *51*, 3187−3191.
(59) Shiraishi, Y.; Itoh, M.; Hirai, T. Thermal Isomerization of Spiropyran to Merocyanine in Aqueous Media and Its Application to Colorimetric Temperature Indication. *Phys. Chem. Chem. Phys.* **2010**, *12*, 13737−13745.
(60) Kortekaas, L.; Ivashenko, O.; Van Herpt, J. T.; Browne, W. R. A Remarkable Multitasking Double Spiropyran: Bidirectional Visible-Light Switching of Polymer-Coated Surfaces with Dual Redox and Proton Gating. *J. Am. Chem. Soc.* **2016**, *138*, 1301−1312.
(61) Browne, W. R.; Ivashenko, O.; Feringa, B. L.; Rudolf, P.; van Herpt, J. T. Oxidative Electrochemical Aryl C−C Coupling of Spiropyrans. *Chem. Commun.* **2013**, *49*, 6737−6739.
(62) André, F.; Hapiot, P.; Lagrost, C. Dimerization of Ion Radicals in Ionic Liquids. An Example of Favourable "Coulombic" Solvation. *Phys. Chem. Chem. Phys.* **2010**, *12*, 7506−7512.
(63) Mortimer, R. J.; Rosseinsky, D. R.; Monk, P. M. S. *Electrochromic Materials and Devices*; Wiley-VCH Verlag GmbH & Co. KGaA, 2013; Vol. 77, pp 1−638.
(64) Guichard, V.; Bourkba, A.; Poizat, O.; Buntinx, G. Vibrational Studies of Reactive Intermediates of Aromatic Amines. 2. Free-Radical Cation and Dication Resonance Raman Spectroscopy of N,N,N′,N′-Tetramethylbenzidine and N,N,N′,N′-Tetraethylbenzidine. *J. Phys. Chem. B* **1989**, *93*, 4429−4435.
(65) Yan, C.; Kang, W.; Wang, J.; Cui, M.; Wang, X.; Foo, C. Y.; Chee, K. J.; Lee, P. S. Stretchable and Wearable Electrochromic Devices. *ACS Nano* **2014**, *8*, 316−322.
(66) Kim, J.; Myoung, J. Flexible and Transparent Electrochromic Displays with Simultaneously Implementable Subpixelated Ion Gel-Based Viologens by Multiple Patterning. *Adv. Funct. Mater.* **2019**, *29*, No. 1808911.
(67) Lees, A. J. A Photochemical Procedure for Determining Reaction Quantum Efficiencies in Systems with Multicomponent Inner Filter Absorbances. *Anal. Chem.* **1996**, *68*, 226−229.
(68) Pimienta, V.; Lavabre, D.; Levy, G.; Samat, A.; Guglielmetti, R.; Micheau, J. C. Kinetic Analysis of Photochromic Systems under Continuous Irradiation. Application to Spiropyrans. *J. Phys. Chem. D* **1996**, *100*, 4485−4490.
(69) Giménez-Gómez, P.; Gutiérrez-Capitán, M.; Capdevila, F.; Puig-Pujol, A.; Jiménez-Jorquera, C.; Fernández-Sánchez, C. Compact Analytical Flow System for the Simultaneous Determination of L-Lactic and l-Malic in Red Wines. *Sci. Rep.* **2020**, *10*, No. 19404.

https://doi.org/10.1021/acsami.1c04154
ACS Appl. Mater. Interfaces 2021, 13, 26461−26471

ıemElectroChem | Research Article
doi.org/10.1002/celc.202101559
Chemist Europe
www.chemelectrochem.org

Electrocarboxylation of Spiropyran Switches through Carbon-Bromide Bond Cleavage Reaction

Sara Santiago, Clara Richart, Silvia Mena, Iluminada Gallardo, Jordi Hernando,* and Gonzalo Guirado*[a]

This manuscript deals with carbon capture and utilization to synthetize high-added chemicals using CO_2 as a C1-organic building block for C–C bond formation. The study focuses on the electrocarboxylation of 1,3,3-trimethylindolino-6'-bromobenzopyrylospiran switch (**Br-BIPS**). Prior to the electrocarboxylation process, the electrochemical reduction mechanism of **Br-BIPS** and CO_2 is disclosed in polar aprotic solvents using two different cathodes (glassy carbon and silver) under nitrogen atmosphere. Once the role of the cathode in the reduction carbon-bromide bond cleavage is understood, carboxylated spiropyran derivatives can be synthesized in moderate yields and conversion rates through an electrocarboxylation process using CO_2 silver cathode and polar aprotic solvents. The "green" efficient route described in the current work would open a new sustainable strategy for designing and building "smart" surfaces with switchable physical properties.

Introduction

Photoswitches are a class of molecules or organometallic complexes that undergo a reversible interconversion between different states triggered by light.[1] Spiropyrans are amongst the most studied of these systems, which toggle between spirocyclic (**SP**) and merocyanine (**MC**) isomers upon light-induced ring-opening and ring-closing reactions, respectively (Figure 1).[2–5] These two states show markedly distinctive geometrical and physicochemical properties, such as different effective pKa values,[6–9] dipole moments (from ~4–6 D (**SP**) to ~18 D (**MC**))[10] or emission properties.[11] However, the most remarkable change observed upon spiropyran photoisomerization is the difference in UV-vis absorbance: while **SP** is transparent in the visible range, **MC** shows a very intense absorption peak in that region. This means that light-induced **SP**-**MC** interconversion is accompanied by an intense variation in coloration, a phenomenon known as photochromism.[12,13]

Because of the large change in properties upon photoisomerization, spiropyrans have been exploited for the preparation of a wide variety of smart functional materials whose properties can be very precisely controlled using light as an external stimulus.[14–18]

For most of these applications, the photoswitchable molecules must be covalently attached to the final materials, such as polymers,[19–21] nanoparticles,[22,23] biomacromolecules[24,25] and surfaces,[26,27] which requires the introduction of suitable groups in spiropyrans to ensure chemical functionalization. Carboxylic acid groups are amongst the most preferred for this purpose, as they confer molecules with a broad reactivity that enables the covalent bonding to substrates by simple coupling reactions (e.g., amide bond formation).[28,29] However, the incorporation of carboxylic acids in spiropyrans is not straightforward, typically involves several synthetic steps (e.g., condensation of an aromatic aldehyde with enamine indole) and moderate yields.[30–32]

Figure 1. Photoisomerization of spiropyrans between the closed SP form and the open MC structure.

Actually, the chemical synthesis of carboxylic acids and their derivatives (e.g., esters or amides) imply the use of many reagents, catalysts[33] or organolithium compounds[34] at mild or strong conditions.[35,36] In this context, the electrochemical carboxylation of organic molecules to produce carboxylic acids by fixing carbon dioxide has emerged during the last years as an efficient green route compared to conventional chemical synthetic methods, especially since this process can be performed efficiently under mild conditions at atmospheric pressure and avoiding the use of additional reagents.[37–41] One of the most popular electrocarboxylation strategies of organic compounds is based on the *in situ* formation of a carbanion via reduction, which in turn undergoes a nucleophilic addition to CO_2 to yield the carboxylate functional group (Figure 2).[42] The success of this approach is strongly related to the stability (i.e., lifetime) of the anion formed in the electrolytic medium. In

[a] S. Santiago, C. Richart, Dr. S. Mena, Prof. I. Gallardo, Dr. J. Hernando, Dr. G. Guirado
Departament de Química
Universitat Autònoma de Barcelona
Bellaterra (Barcelona), 08193, Spain
E-mail: Jordi.Hernando@uab.cat
Gonzalo.Guirado@uab.cat

Supporting information for this article is available on the WWW under https://doi.org/10.1002/celc.202101559

An invited contribution to a Special Collection on Current Trends in Electrochemistry 2021 for the 1st French-Spanish Workshop on Electrochemistry

ChemElectroChem | Research Article
doi.org/10.1002/celc.202101559 | Chemist Europe

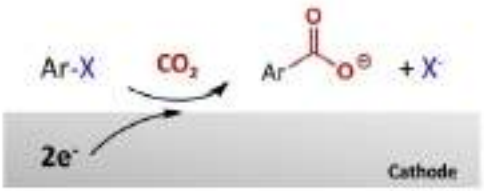

Figure 2. Representation of the electrochemical carboxylation of aryl halides using CO_2.

order to increase its lifetime, it is highly desirable to decrease the reduction potential at which the carbanion is produced. This goal can be achieved by the use of aryl halides, which can be electrochemically reduced leading to the desired anionic species after C–X bond cleavage at relatively low potentials in organic aprotic solvents.[46]

Given the advantages of electrocarboxylation processes and their reported success on simple, model aryl halides such as bromobenzene,[47] herein we attempted the carboxylation reaction of much more challenging spiropyran substrates by electrochemical reduction of a commercially available bromo-spiropyran derivative under CO_2 atmosphere. In addition, the effect of the nature of the cathode (carbon and silver) was evaluated in terms of performance and energy efficiency, since it is well known the electrocatalytic effect of using silver in the reduction of organic halides.[47–49] Our work therefore showcases a new one-pot and facile strategy for the functionalization of the spiropyran backbone using CO_2 (as a C1-building block) and electrochemical techniques. Such an attractive and environmentally friendly approach could grant access to a broad variety of carboxylated spiropyran derivatives, which could be eventually applied for the design of smart surfaces and devices.

Experimental Section

Reagents

1,3,3-trimethylindolino-6'-bromobenzopyrylospiropyran (**Br-BIPS**, pur. 98.0%) was purchased from TCI Chemicals and used without further purification. High purity CO_2 and Ar gases (C 5.0) used for the electrochemical measurements and electrosynthesis were supplied by Linde.

Anhydrous and extra pure tetrabutylammonium hexafluorophosphate, ($TBAPF_6$; pur. >99.0%), iodomethane (MeI; pur. >99.0%) and anhydrous sodium sulfate (Na_2SO_4; pur. >99.0%) were acquired from Merck. Anhydrous *N,N*-dimethylformamide (DMF; pur. >99.5%) and anhydrous dimethylsulfoxide (DMSO; pur. >99.8%) were purchased from Acros Organics. Both solvents were dried under activated molecular sieves of 4 Å prior to use to ensure water content <100 ppm for the electrochemical measurements and electrosynthesis.

Dichloromethane (DCM, pur. >98%), *n*-hexane (pur. >98%) and ethyl acetate (pur. >98%) used for the purification of the products prepared by electrosynthesis were obtained from SDS and used as received.

Instrumentation and procedure

Electrochemical studies were performed by cyclic voltammetry (CV) using the potentiostat Workstation CHInstrument and controlled by the software CHI660e V14.08. For these measurements, a three-electrode system and a thermostatic electrochemical cell was used. Glassy carbon (WE_C; 1 mm of diameter) or silver (WE_{Ag}; 3 mm of diameter) were used as working electrodes, while a platinum wire and a saturated calomel electrode (SCE) were used as counter (CE, and reference (Ref) electrodes, respectively. Both CE and Ref electrodes were separated from the solution by a salt-bridge. Solutions at different concentration of **Br-BIPS** (in the range of 3–10 mM) were prepared in DMF/0.1 M of $TBAPF_6$. Prior to each measurement, the solutions were purged with either Ar or CO_2 depending on the type of study in each case. In the case of CO_2 gas, the flow was controlled using a Mass Flow Meter.

The Bulk Electrolysis were carried out at controlled constant potential using the potentiostat EG&G Princeton Applied Research model 273 A. For these experiments, we used the same electrochemical setup as for CV measurements but replacing the small diameter sized WE_C or WE_{Ag} for a large area graphite rod (area: ~8 cm^2) or silver foil (area: ~6 cm^2), respectively. For the electrolysis of **Br-BIPS** under inert atmosphere, the solution was purged with Ar for 10 min and then the corresponding reduction potential was applied until a total charge of 2 F was passed (−2.35 V when using WE_C and −2.00 V for WE_{Ag} vs SCE). For the purification of the products after the electrolysis, firstly the solvent of the reaction mixture was removed under vacuum and then an extraction in diethyl ether: H_2O (2:1) was performed. Then, the organic phase was washed for three times with water (2:1 v/v ratio), dried with anhydrous Na_2SO_4 and the solvent evaporated in vacuo.

Analogously, for the electrolysis under CO_2 atmosphere, the solution was saturated in this gas by bubbling for 20 minutes. After that, a constant reduction potential was applied until 2 F of total charge were reached (−2.35 V when using WE_C and −2.00 V for WE_{Ag} vs SCE). Immediately after, 10 equivalents of MeI were added to the solution to derivatize the carboxylate goup introduced and facilitate the isolation of the resulting methylated product **BIPS-COOMe**. The solvent of the reaction mixture was removed under vacuum and purified performing a preparative thin layer chromatography (TLC). A mixture of *n*-hexane and ethyl acetate (80:20 v/v ratio) was used as a mobile phase.

The products **BIPS** and **BIPS-COOMe** obtained after the electrosynthesis of the reagent **Br-BIPS** under Ar and CO2 atmosphere, respectively, were characterized by attenuated total reflectance infrared spectroscopy (ATR-FTIR), H ^{1}NMR on a Brucker spectrometer DPX360 and electrospray mass spectrometry (ESI-MS).

Br-BIPS: ^{1}H NMR (360 MHz, Chloroform-*d*) δ 1.16 (s, 3H), 1.29 (s, 3H), 2.71 (d, J = 1.6 Hz, 3H), 5.72 (d, J = 10.3 Hz, 1H), 6.53 (d, J = 7.7 Hz, 1H), 6.60 (d, J = 9.3 Hz, 1H), 6.78 (d, J = 10.2 Hz, 1H), 6.85 (td, J = 7.4, 1.0 Hz, 1H), 7.07 (dd, J = 7.3, 1.3 Hz, 1H), 7.16 (ddt, J = 5.4, 3.9, 1.8 Hz, 3H). ESI-MS: m/z found for $C_{19}H_{18}BrNO$ (M + H): 358.0781 (100%); 359.0809 (24.4%); 360.0773 (97.2%); 361.0796 (19.9%).

BIPS ^{1}H NMR (360 MHz, $CDCl_3$) δ 1.18 (s, 3H), 1.32 (s, 3H), 2.74 (s, 3H), 5.68 (d, J = 10.2 Hz, 1H), 6.54 (d, J = 7.7 Hz, 1H), 6.72 (d, J = 8.1 Hz, 1H), 6.78–6.89 (m, 3H), 7.01–7.14 (m, 3H), 7.19 (td, J = 7.6, 1.3 Hz, 1H). ESI-MS: m/z found for $C_{19}H_{19}NO$ (M + H): 278.1539 (100%); 279.1572 (21.1%); 280.1604 (2.3%).

BIPS-COOMe: ^{1}H NMR (360 MHz, $CDCl_3$) δ 1.19 (s, 3H), 1.33 (s, 3H), 2.74 (s, 3H), 3.90 (s, 3H), 5.77 (d, J = 10.1 Hz, 1H), 6.55 (d, J = 7.6 Hz, 1H), 6.73 (d, J = 7.6 Hz, 1H), 6.82–6.91 (m, 2H), 7.10 (d, J = 7.2 Hz, 1H), 7.17–7.23 (m, 2H), 7.8 (s, 1H). ESI-MS: m/z found for $C_{21}H_{21}NO_3$ (M + H): 336.1581 (100%); 337.1616 (23.2%); 338.1701 (7.7%).

ıemElectroChem | Research Article
doi.org/10.1002/celc.202101559

Results and Discussion

Electrochemical reduction of Br-BIPS in DMF

Electrochemical study under inert atmosphere (Ar)

The electrochemical behavior of the compound **Br-BIPS** was studied by CV at different concentrations (1–5 mM) and scan rates (0.1–1.0 V/s) under inert conditions (Ar) using *N,N*-dimethylformamide (DMF) as a solvent and 0.1 M of $TBAPF_6$ as a supporting electrolyte. As an example, Figure 3a shows the electrochemical response of a 5 mM solution of **Br-BIPS** recorded at 0.1 V/s scan rate and using two different working cathodes: glassy carbon (WE_C) and silver (WE_{Ag}). Figure 3b shows the cyclic voltammogram in a first cathodic scan, from −1.60 V to −2.70 V vs SCE, for a 5 mM solution of **Br-BIPS** using WE_C. Two irreversible peaks were found at $E_{pc} = -2.23$ V and −2.47 V (vs SCE), which could be attributed to two- and one-electron reduction processes, respectively (Figure 3b). It is worth noting that, when W_{Ag} was used as a working electrode instead, the two-electron irreversible reduction peak of **Br-BIPS** was registered at $E_{pc} = -1.92$ V (vs SCE) (Figure 3a). This potential shift of *ca.* 280 mV to less negative values indicates the electrocatalytic effect of the use of silver as a cathode (Figure 3a).

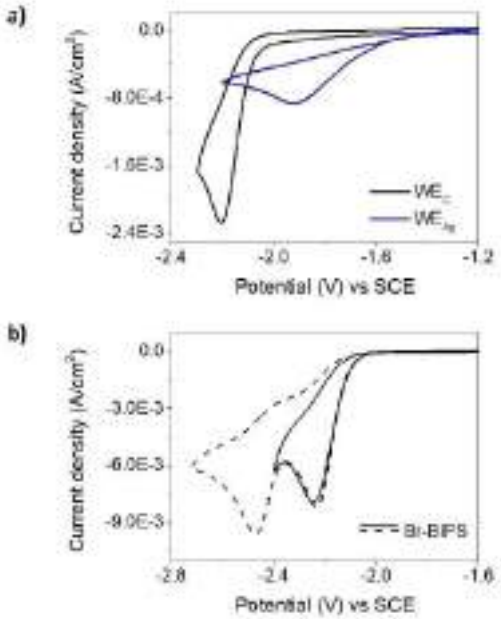

Figure 3. (a) CVs registered for a 5 mM solution of Br-BIPS in DMF/0.1 M $TBAPF_6$ under Ar atmosphere and using either glassy carbon or silver as working electrodes (scan rate = 0.1 V/s). (b) CVs registered for a 5 mM solution of Br-BIPS in DMF/0.1 M $TBAPF_6$ under Ar atmosphere and using glassy carbon as a WE (scan rate = 0.1 V/s). Two different independent measurements are shown, which differ in the minimum potential of the scan. In both cases, a two-electron irreversible wave at $E_{pc} = -2.23$ V was observed.

Irrespective of the working electrode used, the irreversibility of the two-electron reduction wave measured for **Br-BIPS** in DMF under Ar atmosphere indicates that there is an irreversible chemical reaction coupled to the electron transfer to this compound. To determine the nature of this chemical reaction, the dependence of E_{pc} with the scan rate (v) and concentration were examined by CV. From the plot of E_{pc} vs log v, a linear relationship was found with a slope value of 35 mV, whereas no variation of the cathodic peak potential was observed with the **Br-BIPS** concentration in solution (Figure S1). Hence, it is possible to conclude that the chemical reaction coupled to the first reduction process is a first order reaction.

In order to disclose the nature of the product irreversibly formed after the electrochemical reduction of **Br-BIPS**, electrolytic processes at a controlled constant potential (vs SCE) of −2.35 V (for a carbon graphite rod electrode) or −2.00 V (for a silver foil electrode) were conducted in DMF and under inert atmosphere. These electrolysis experiments were simultaneously monitored by CV with WE_C, where we observed that the reduction peak at $E_{pc} = -2.23$ V (vs SCE) associated to the reduction of **Br-BIPS** gradually decreased, and a new oxidation peak at $E_{pa} \sim +0.70$ V (vs SCE) concomitantly increased with the injection of charge (Figure S2). After the passage of 2 F, the electrolytic mixture was treated and the irreversible product formed was isolated and analyzed by ^{1}H NMR, ESI-MS, ATR-FITR and UV-vis spectroscopy. This allowed us to assign this product to the debrominated compound **BIPS**, which was obtained in a 56% yield when using the carbon graphite rod as a WE and a 91% yield for WE_{Ag}. The remaining 30% and 9% respectively correspond to unreacted starting material. Interestingly, this assignment was consistent with two significant features observed in our CV measurements. On the one hand, the anodic peak emerging during the electrolysis experiments at $E_{pa} \sim +0.70$ V (vs SCE) for WE_C could be attributed to the bromide anion produced during the debromination of **Br-BIPS** (Figure S2).[37] On the other hand, the second one-electron reduction wave registered for **Br-BIPS** at $E_{pc} = -2.47$ V (vs SCE) with WE_C matches the cathodic peak measured for a solution of pure **BIPS** in DMF under Ar atmosphere ($E_{pc} = -2.50$ V (vs SCE) using WE_C, Figure S3). Therefore, the latter further supports the formation of **BIPS** after the two-electron reduction process of **Br-BIPS**.

From all this data, we conclude that the electrochemical reduction of **Br-BIPS** proceeds through an ECE mechanism (Scheme 1). First, an electron transfer (E) takes place where the corresponding radical anion is formed ([**Br-BIPS**]$^{\bullet}$). Then, a first order chemical reaction (C) leads to the cleavage of the C–Br bond of the compound, thus producing the radical intermediate species [**BIPS**]$^{\bullet}$. Subsequently, this radical species is reduced again by a second electron transfer (E) yielding an anionic form ([**BIPS**]$^-$). This second reduction step must present a less negative potential than the first electron transfer ($E^0_2 > E^0_1$), which would explain why a single cathodic wave associated to a two-electron reduction process was observed by CV. Finally, the anionic form [**BIPS**]$^-$ is protonated by subtracting a proton from the solvent or the tetrabutylammonium ion of the supporting electrolyte, yielding the final product **BIPS**.

emElectroChem | Research Article doi.org/10.1002/celc.202101559 | Chemis Europe

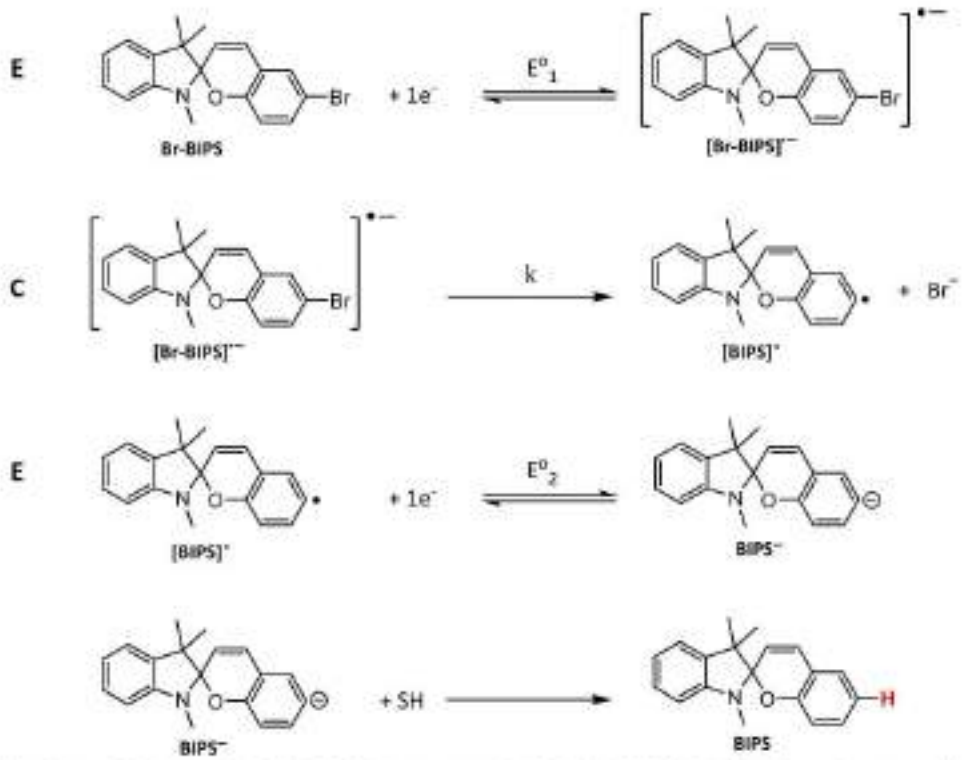

Scheme 1. Electrochemical reduction mechanism for Br-BIPS under inert atmosphere in DMF/0.1 M $TBAPF_6$ (SH is the solvent or the supporting electrolyte).

Electrochemical study under saturated atmosphere of CO_2

As the reduction of **Br-BIPS** leads to the formation of the carbanionic intermediate **BIPS**$^-$, we envisaged that this species could react with CO_2 to produce the target electrocarboxylated spiropyran derivative. To validate this hypothesis, we first investigated by CV the electrochemical properties of **Br-BIPS** in a 75 mM CO_2 DMF solution (Figure 4). Mainly, the same behavior previously observed under inert atmosphere was registered, and a two-electron irreversible reduction peak at $E_{pc} = -2.23$ V (vs SCE) or −1.92 V (vs SCE) was detected for WE_C or WE_{Ag}, respectively. Therefore, the electrocatalytic effect of the silver electrode was again demonstrated. When using WE_{Ag}, an additional irreversible cathodic wave at $E_{pc} = -2.60$ V (vs SCE) was measured, which can be attributed to the electrochemical reduction of the CO_2 present in solution.[36,44]

This was further proven by analyzing a pure DMF sample saturated with CO_2 by CV, where the same reduction peak at $E_{pc} = -2.60$ V (vs SCE) also appeared. In view of these results, it is possible to conclude that, in the presence of CO_2, the reduction of **Br-BIPS** follows the same ECE mechanism previously established under inert atmosphere, where the anionic intermediate **BIPS**$^-$ is electrogenerated.

Noticeably, when recording the full voltammogram of **Br-BIPS** under CO_2 atmosphere after the first cathodic scan (i.e., after irreversible producing **BIPS**$^-$), two different oxidation waves were observed in the anodic region (Figure 5). One of them appeared at $E_{pa} = +0.70$ V (vs SCE) for WE_C, which as previously mentioned, can be assigned to bromide anions and, therefore, is compatible with the reductive debromination of

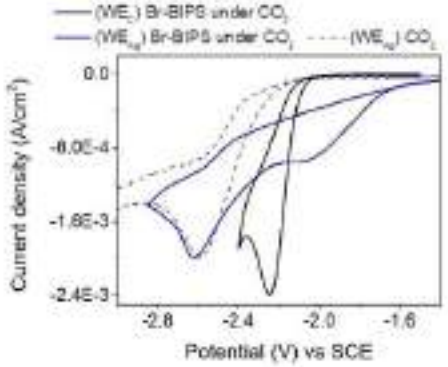

Figure 4. CVs (scan rate: 0.1 V/s) of a 5 mM solution of Br-BIPS in DMF/0.1 M $TBAPF_6$ under the presence of CO_2 using either glassy carbon (black solid line) or silver as a WE (blue solid line). For the case of WE_{Ag}, the electrochemical response of CO_2 in a neat DMF/0.1 M $TBAPF_6$ solution is also given (blue dashed line).

ChemElectroChem | Research Article doi.org/10.1002/celc.202101559 | Chemis Europe

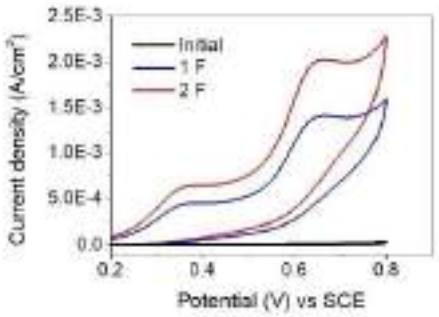

Figure 5. Cyclic voltammograms recorded to monitor the electrochemical reaction of Br-BIPS performed at a controlled constant potential in a partially saturated solution in CO_2 using glassy carbon as a WE. The CVs were recorded at 0.30 V/s in DMF/0.1 M of $TBAPF_6$ from 0.20 V to 0.80 V.

Br-BIPS. As for the second of the anodic peaks, it was registered at $E_{pa} \sim +0.40$ V (vs SCE) for WE_C and, more importantly, was not observed neither in the case of the electrochemical measurements of **Br-BIPS** nor the electrosynthesis of **BIPS** under inert atmosphere.

Consequently, this suggests that a different product is obtained when conducting the electrochemical reduction of **Br-BIPS** in the presence of CO_2, which must give rise to such an additional oxidation wave. We tentatively attributed this new peak to the oxidation of the carboxylate anion (**BIPS-COO$^-$**) obtained through the nucleophilic attack of the electrogenerated anionic form **BIPS$^-$** to the CO_2 molecules present in solution (Scheme 2). The low oxidation potential value obtained for the carboxylate **BIPS-COO$^-$** derivative is due to the aromatic electron rich system of the indole moiety. Similar anodic peak potential values were observed for other aromatic electron rich heterocycles, such as thiophenecarboxylate derivatives.[38]

To confirm the nature of the product obtained, bulk electrolysis of **Br-BIPS** in DMF and under CO_2 atmosphere were performed applying −2.35 V (vs SCE) or −2.00 V (vs SCE) for graphite rod or silver foil cathodes, respectively. The electrosynthesis was stopped after the passage of 2F (ca. 20 minutes) to avoid the obtention of non-desired overreduced compounds despite the fact that the reactant was not fully consumed, as further discussed below. To facilitate the isolation and identification of the electrocarboxylation product, 10 equivalents of CH_3I were added to the solution after the electrosynthesis to further derivatize **BIPS-COO$^-$** and obtain the methyl ester **BIPS-COOMe**. The resulting samples were treated and the products generated were purified and analyzed by ^{1}H NMR, ESI-MS, ATR-FTIR and UV-vis absorption spectroscopy. As shown in Figure 6 three main compounds were identified in this way: (i) the unreacted starting material **Br-BIPS**, which was recovered; (ii) the byproduct **BIPS** in *ca.* 30% yield for both electrodes, which should arise from the competing protonation reaction of **BIPS$^-$** with the solvent or the supporting electrolyte; (iii) the desired carboxylated product **BIPS-COOMe**, which was obtained in 16% or 35% yield when either carbon or silver cathodes were

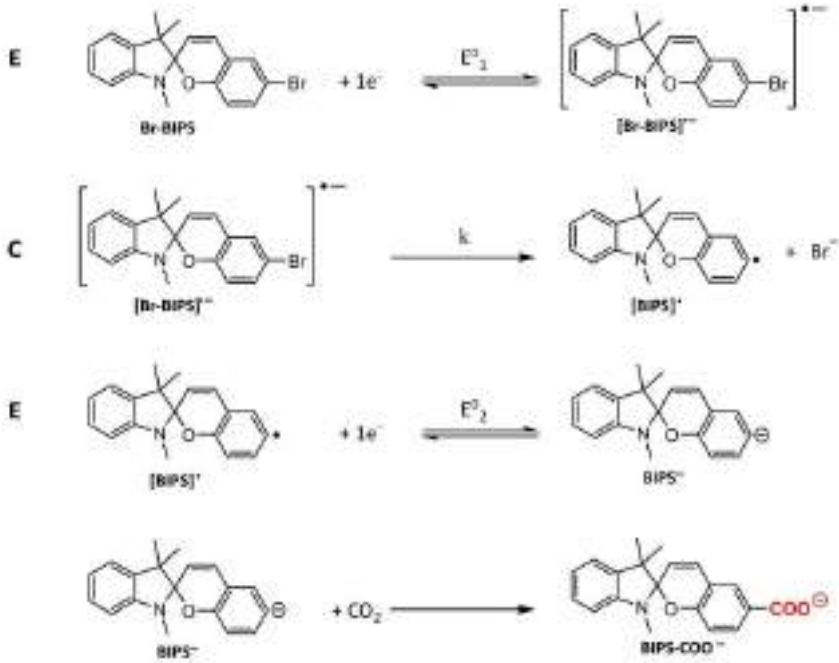

Scheme 2. Electrochemical reduction mechanism for Br-BIPS in DMF/0.1 M $TBAPF_6$ saturated with CO_2, which eventually leads to the formation of the electrocarboxylated product BIPS-COO$^-$.

ıemElectroChem | Research Article doi.org/10.1002/celc.202101559 | Chemis Europe

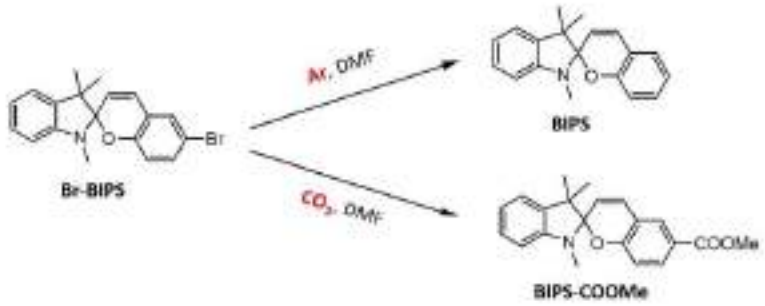

Working electrode (WE)	E_{ap} (V)	Ar sat. atmosphere	CO_2 sat. atmosphere	
		BIPS yield (%)	BIPS-COOMe yield (%)	BIPS yield (%)
Glassy C	-2.35	56	16	36
Ag	-2.00	91	35	30

Figure 6. Representation of the different products obtained depending on the conditions of the electrolysis and the yield resulted in each case.

employed (31% and 54% yield if the recovered initial reagent is taken into account). From this data, we could not only verify the electrocarboxylation of **Br-BIPS** as shown in Scheme 2, but also conclude that the use of silver cathodes to conduct this process presents several advantages resulting from their electrocatalytic properties. First, the reductive cleavage of the C–Br bond of the starting material takes place at lower potentials, which makes the reaction less energy consuming and, more importantly, increases the lifetime of the resulting reactive carbanion. Second, this leads to both larger conversion of the initial starting product (up to 65%) and formation of the target electrocarboxylated compound, which is eventually obtained at moderate yields (about 50% taking into account the reactant consumption).

The electrochemical response of the formed product **BIPS-COOMe** was compared to those of the precursor **Br-BIPS** and the byproduct of the reductive electrolysis **BIPS**. As shown in Figure 7, the potential of the cathodic peak associated with the first electron transfer toward these compounds varies depending on the nature of the substituent at the benzopyran ring. This behavior is related to the electronic character of each of these groups. In the case of **Br-BIPS**, E_{pc} is about 249 mV less negative than **BIPS**; i.e., it shows a larger tendency to be reduced than **BIPS**. This means that the inductive electron withdrawing effect of the bromide substituent in **Br-BIPS** is more important than its mesomeric electron donating effect. The nature of the irreversible two-electron transfer reduction process of **BIPS** was investigated by conducting a controlled potential electrolysis of this product at −2.6 V vs. SCE under nitrogen atmosphere. This revealed the formation of hydrogenated byproducts by reduction of **BIPS** olefinic bonds, a finding that corroborates the need of carefully controlling the conditions applied during the reductive activation of **Br-BIPS** to product the reactive species **BIPS**: because of the small difference in potential of the first cathodic waves of **Br-BIPS** and **BIPS**, the use of too long electrolysis times or large E_{ap} values could lead to the formation of undesired hydrogenated byproducts of **Br-BIPS**. Finally, in the case of **BIPS-COOMe**, a further decrement in the absolute value of E_{pc} was registered (447 mV relative to **BIPS**), which can be attributed to the presence of the strong electron withdrawing ester substituent.

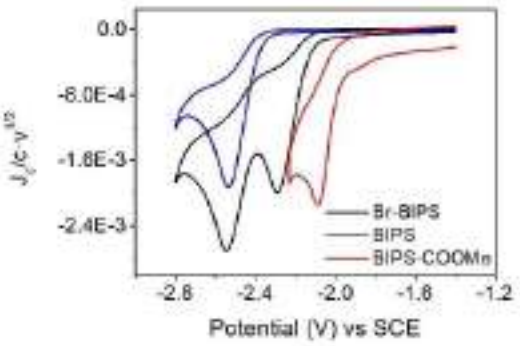

Figure 7. Normalized CV representing the electrochemical reduction response of Br-BIPS, BIPS and BIPS-COOMe in DMF/0.1 M $TBAPF_6$ with WE. Please note that the second reduction peak observed for Br-BIPS corresponds to the reduction of the BIPS molecules formed after the first electron transfer reaction.

Photochromism of electrochemically synthesized molecular switches

The photochromic response of spiropyrans **BIPS**, **BIPS-COOMe** and **Br-BIPS** (0.5 mM) was explored in dimethyl sulfoxide (DMSO) at room temperature (Figure 8). As expected, the most thermodynamically stable isomer, for all the three compounds in the dark, was found to be the spirocyclic form **SP**, with a maximum absorption peak located at ~295 nm for all three samples and a molar absorption coefficient of ε = 3310–

ıemElectroChem
Research Article
doi.org/10.1002/celc.202101559
Chemis Europe

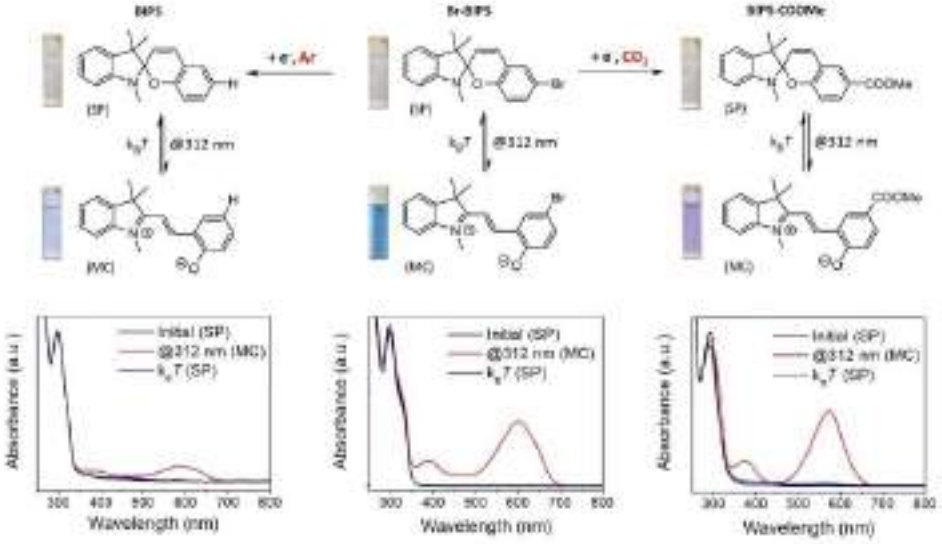

Figure 8. Absorbance UV-vis spectra of a 0.5 mM in DMSO of the reactant **Br-BIPS** showing the photochromic response of the molecular switch and the photochromic response of the switches, **BIPS** and **Br-BIPS** 0.5 mM in DMSO, electrochemically obtained. The switching between the closed (**SP**) to the colored (**MC**) forms for the different molecular switches were achieved when irradiating at @312 nm. The back conversion to the **SP** form was totally reached spontaneously over time in the dark.

4586 $M^{-1}cm^{-1}$ (Table 1). After irradiation of the samples with UV light (312 nm), the closed **SP** isomer opens via C_{spiro}–O bond breakage leading to the formation of the open **MC** form. This results in coloration of the solution as shown in Figure 8, because the merocyanine isomer formed presents a new absorption band at 573–601 nm.[39] An hypsochromic shift in absorption was noticeable when comparing the λ_{max} of the **MC** form depending on the nature of the substituting group at the 6 position in the benzopyran moiety; i.e., for **BIPS-COOMe** relative to **BIPS** and **Br-BIPS.**

It was found that, after irradiation at 312 nm for 2 minutes, all three molecular switches reached their photostationary state (PSS). The photochromic behavior of the switches was totally reversible since the initial **SP** form was recovered when the solution was let in the dark over time due to thermal back isomerization, obtaining a 100% yield back conversion. Some differences were found in the back conversion rates from **MC** to **SP**. This fact is directly related to the stability of the **MC** form, which in the case of **BIPS** was lower compared than for **Br-BIPS** and **BIPS-COOMe**. The presence of the electron-withdrawing bromo and ester substituents at the *para* position of the phenolate group of the **MC** form account for this result, as they aid stabilizing the negative charge of this group. Actually, this explains why, in the case of **Br-BIPS** and **BIPS-COOMe**, greater conversions to **MC** could be obtained compared to **BIPS** (Table 1 and Figure S5). Thus, it can be determined that it is possible to electrochemically access a variety of molecular switches with photochromic properties.

Table 1. Photochemical and electrochemical data extracted from the absorbance UV-Vis spectra and CV of **Br-BIPS**, **BIPS**, **BIPS-COOMe** upon irradiation and acidic conditions.

Name	State	λ_{max} nm (ε, $M^{-1}cm^{-1}$)	k (s^{-1}) (MC→SP)	$E_{1/2}$ (V)
Br-BIPS	SP	297, shoulder (6293)	0.01986	−2.23
	SPH$^+$	297		
	MC	601		
	MCH$^+$	428		
BIPS	SP	296 (8274)	0.0362	−2.53
	SPH$^+$	295		
	MC	585		
	MCH$^+$	418		
BIPS-COOMe	SP	292 (8719)	0.0186	−2.08
	SPH$^+$	286		
	MC	573		
	MCH$^+$	409		

emElectroChem | Research Article doi.org/10.1002/celc.202101559 | Chemist Europe

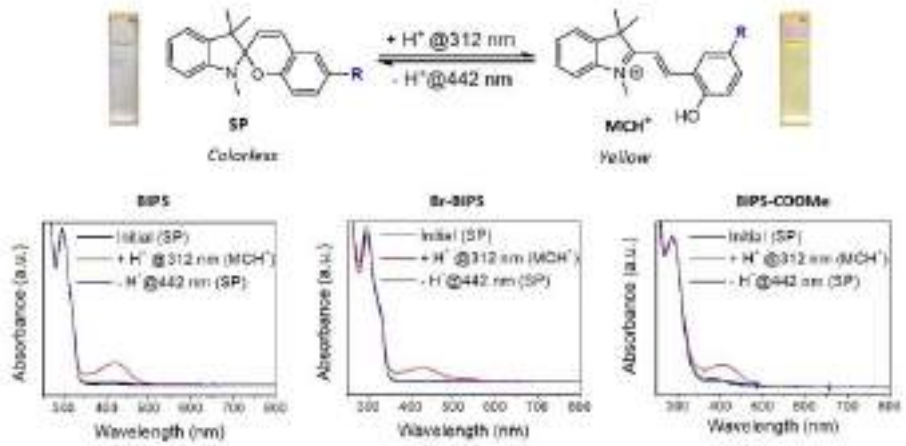

Figure 9. Switching properties of Br-BIPS, BIPS and BIPS-COOMe in slightly acidic DMSO when irradiating at 312 nm (c = 0.5 mM). Formation of the yellow-colored, protonated MCH^+ form is observed by means of absorption spectroscopy for all three compounds, which can revert back to the unprotonated SP state upon irradiation at 442 nm.

Photo-halochromism of electrochemically synthesized molecular switches

In addition, it was also determined the responsiveness of the spiropyran photoswitches developed in this work upon changes in pH, i.e., their photo-halochromism. For this, we consider the use of slightly acid media, where the **SP** form of spiropyrans is known to remain unprotonated because of its low pKa while the more basic **MC** isomer must become protonated into MCH^+.[32,33] As seen in Figure 9, this was proven by irradiating with UV light acidic DMSO solutions of **Br-BIPS**, **BIPS** and **BIPS-COOMe**: instead of observing the blue coloration arising from **MC** formation with $\lambda_{abs,\,max} > 550$ nm, we obtained yellow solutions with new absorption bands with a maximum wavelength located around 409–428 nm, which are generally ascribed to the protonated merocyanine form **MCH** (Table 1). This process was found to be totally reversible, as the MCH^+ form of **Br-BIPS**, **BIPS** and **BIPS-COOMe** could be fully converted to the initial, non-protonated spiropyran state when irradiating at 442 nm.

Conclusion

The electrochemical reduction mechanism of **Br-BIPS** has been disclosed under nitrogen and CO_2 atmospheres using cyclic voltammetry and control potential electrolysis under nitrogen and carbon dioxide atmospheres using carbon and silver cathodes. This study proves that the electrochemical reduction follows an ECE mechanism involving a C–Br reaction cleavage that takes place after the first electron transfer. Based on these data, compound **Br-BIPS** has been used for activating, valorizing and capturing CO_2, since the electrogenerated **BIPS** anion reacts with CO_2 though a nucleophilic attack. The use of silver cathodes allowed achieving moderate yields and efficiencies of electrocarboxylated products under mild conditions thanks to its electrocatalytic properties. Finally, the green efficient electrochemical route described in the current work would open a new sustainable strategy for designing and building "smart" surfaces with switchable physical properties by s using CO_2 as a C1-organic building block.

Acknowledgements

The authors thank the Ministerio de Ciencia e Innovación of Spain for financial support though the project PID2019-106171RB-I00. S.M. acknowledges the Autonomous University of Barcelona for her predoctoral PIF grant.

Conflict of Interest

The authors declare no conflict of interest.

Data Availability Statement

The data that support the findings of this study are available from the corresponding author upon reasonable request.

Keywords: Carbon-Bromide cleavage · Carbon dioxide · Electrocarboxylation · CO_2 capture · spiropyran switches

[1] B. L. Feringa, *Molecular Switches*, WILEY-VCH, Weinheim, Germany, **2001**.
[2] G. Berkovic, V. Krongauz, V. Weiss, *Chem. Rev.* **2000**, *100*, 1741–1754.
[3] R. Tong, H. D. Hemmati, R. Langer, D. S. Kohane, *J. Am. Chem. Soc.* **2012**, *134*, 8848–8855.
[4] N. Tamai, H. Miyasaka, *Chem. Rev.* **2000**, *100*, 1875–1890.
[5] L. Kortekaas, W. R. Browne, *Chem. Soc. Rev.* **2019**, *48*, 3406–3424.

[6] N. Voloshin, E. Voloshina, M. Chernov'yants, A. Chernyshev, *Russ. J. Gen. Chem.* **2002**, *72*, 1468–1472.
[7] A. A. Garcia, S. Cherian, J. Park, D. Gust, F. Jahnke, R. Rosario, *J. Phys. Chem. A* **2000**, *104*, 6103–6107.
[8] F. M. Raymo, S. Giordani, *J. Am. Chem. Soc.* **2001**, *123*, 4651–4652.
[9] C. Berton, D. M. Busiello, S. Zamuner, E. Solari, R. Scopelliti, F. Fadiel-Tirani, K. Severin, C. Pezzato, *Chem. Sci.* **2020**, *11*, 8457–8468.
[10] N. A. Murugan, S. Chakrabarti, H. Ågren, *J. Phys. Chem. B* **2011**, *115*, 4025–4032.
[11] L. Zhu, W. Wu, M.-Q. Zhu, J. J. Han, J. K. Hurst, A. D. Q. Li, *J. Am. Chem. Soc.* **2007**, *129*, 3524–3526.
[12] H. Gómez, *Phys. Chem. Chem. Phys.* **2001**, *3*, 416–423.
[13] N. W. Tyer, R. S. Becker, *J. Am. Chem. Soc.* **1970**, *92*, 1289–1294.
[14] A. Goulet-Hanssens, F. Eisenreich, S. Hecht, *Adv. Mater.* **2020**, *32*, 1905966.
[15] M.-M. Russew, S. Hecht, *Adv. Mater.* **2010**, *22*, 3348–3360.
[16] S. Santiago, P. Giménez-Gómez, X. Muñoz-Berbel, J. Hernando, G. Guirado, *ACS Appl. Mater. Interfaces* **2021**, *13*, 26461–26471.
[17] S. Wu, J. Fan, W. Wang, D. Yu, *Colloids Surf. A* **2022**, *632*, 127760.
[18] R. Feringa, H. S. Siebe, W. J. N. Klement, J. D. Steen, W. R. Browne, *Mater. Adv.* **2022**, *3*, 282.
[19] P. Hong, L. Wang, L. Bai, Z. Liu, Y. Liu, J. Yang, A. Ying, *Dyes Pigm.* **2022**, *197*, 109902.
[20] S. Tian, J. Zhang, Q. Zhou, L. Shi, W. Wang, D. Wang, *Polymers (Basel).* **2021**, *13*, 2496.
[21] M.-Q. Zhu, L. Zhu, J. J. Han, W. Wu, J. K. Hurst, A. D. Q. Li, *J. Am. Chem. Soc.* **2006**, *128*, 4303–4309.
[22] H. Zhang, Z. Chen, Y. He, S. Yang, J. Wei, *ACS Appl. Mater. Interfaces* **2021**, *4*, 4340–4345.
[23] R. Tong, H. D. Hemmatti, R. Langer, D. S. Kohane, *J. Am. Chem. Soc.* **2012**, *134*, 8848–8855.
[24] K. Tomizaki, H. Mihara, *Mol. BioSyst.* **2006**, *2*, 580.
[25] T. Sakata, Y. Yan, G. Marriott, *Proc. Nat. Acad. Sci.* **2005**, *102*, 4759–4764.
[26] N. Wagner, P. Theato, *Polymer* **2014**, *55*, 3436–3453.
[27] T. Garling, Y. Tong, T.A. Darwish, M. Wolf, R.K. Campen, *J. Phys. Condens. Matter* **2017**, *29*, 414002.
[28] J. Opel, L.-C. Rosenbaum, J. Brunner, A. Steiger, R. Zimmermann, M. Kellermeier, T. Gaich, H. Cölfen, J.-M. García-Ruiz, *J. Mater. Chem. B* **2020**, *8*, 4831–4835.
[29] A. K. Bohaty, M. R. Newton, I. Zhorov, *J. Porous Mater.* **2010**, *17*, 465–473.
[30] R. da Costa Duarte, F. da Silveira Santos, B. B. de Araújo, R. Cercena, D. Brondani, E. Zapp, P. F. B. Gonçalves, F. S. Rodembusch, A. G. Dal-Bo, *Chemosensors* **2020**, *8*, 31.
[31] M. Natali, C. Aakeröy, J. Desper, S. Giordani, *Dalton Trans.* **2010**, *39*, 8269.
[32] J. G. Pargaonkar, S. K. Patil, S. N. Vajekar, *Synth. Commun.* **2018**, *48*, 208–215.
[33] Y. Liu, J. Cornella, R. Martin, *J. Am. Chem. Soc.* **2014**, *136*, 11212–11215.
[34] T. E. Hurst, J. A. Deichert, L. Kapeniak, R. Lee, J. Harris, P. G. Jessop, V. Snieckus, *Org. Lett.* **2010**, *21*, 3882–3885.
[35] K. Kobayashi, Y. Kondo, *Org. Lett.* **2009**, *11*, 2035–2037.
[36] B. T. Sargent, E. J. Alexanian, *J. Am. Chem. Soc.* **2016**, *138*, 7520–7523.
[37] S. Mena, C. Louault, V. Mesa, I. Gallardo, G. Guirado, *ChemElectroChem* **2021**, *8*, 2649–2661.
[38] S. Mena, S. Santiago, I. Gallardo, G. Guirado, *Chemosphere* **2020**, *245*, 125557.
[39] S. Mena, G. Guirado, *C* **2020**, *6*, 34.
[40] S. Mena, J. Bernad, G. Guirado, *Catalysts* **2021**, *11*, 880.
[41] S. Mena, I. Gallardo, G. Guirado, *Catalysts* **2019**, *9*, 413.
[42] S. Mena, J. Sanchez, G. Guirado, *RSC Adv.* **2019**, *9*, 15115–15123.
[43] A. A. Isse, C. Durante, A. Gennaro, *Electrochem. Commun.* **2011**, *13*, 810–813.
[44] Z. Chemi, M. Gavel, J. Pinson, J. M. Saveant, A. Thiebault, *J. Org. Chem.* **1991**, *56*, 586–595.
[45] C. Durante, A. A. Isse, F. Todesco, A. Gennaro, *J. Electrochem. Soc.* **2013**, *160*, G3073–G3079.
[46] C. Durante, A. A. Isse, G. Sandonà, A. Gennaro, *Appl. Catal. B* **2009**, *88*, 479–489.
[47] S. Amaboldi, A. Bonetti, E. Giussani, P. R. Mussini, T. Benincori, S. Rizzo, A. A. Isse, A. Gennaro, *Electrochem. Commun.* **2014**, *38*, 100–103.
[48] S. Mena, J. Sanchez, G. Guirado, *RSC Adv.* **2019**, *9*, 15115–15123.
[49] I. Gallardo, G. Guirado, J. Marquet, *J. Electroanal. Chem.* **2000**, *488*, 64–72.
[50] J. Massaad, J. C. Micheau, C. Coudret, C. L. Serpentini, G. Guirado, *Chem. Eur. J.* **2013**, *19*, 12435–12445.
[51] S.-R. Koum, R. Se-Jung, K. Sang-Eun, L. Sung-Hoon, C. Chul-Hee, K. Sung-Hoon, K. Kwang-Nak, *Bull. Korean Chem. Soc.* **2006**, *27*, 187–188.
[52] L. Kortekaas, J. Chen, D. Jacquemin, W. R. Browne, *J. Phys. Chem. B* **2018**, *122*, 6423–6430.
[53] L. Wimberger, S. K. K. Prasad, M. D. Peeks, J. Andréasson, T. W. Schmidt, J. E. Beves, *J. Am. Chem. Soc. Rev.* **2021**, *143*, 49, 20758–20768.

Manuscript received: November 19, 2021
Revised manuscript received: December 24, 2021
Accepted manuscript online: January 10, 2022

ANNEXES

Annex I: Fundamentals of Electrochemistry

Cyclic voltammetry (CV) is a powerful and widely employed electrochemical technique frequently used to study the reduction and oxidation processes of molecular species. CV can be used as a characterization technique for the identification of chemical species, as an analytical tool and for disclosing electrochemical mechanisms and the type of chemical reactions (C) coupled to the electron transfer (ET).

In CV, the signal that the system sends is a triangular sweep of potential at a selected scan rate. This means that the initial sweep direction is reversed to the opposite scan direction once the selected start potential is established.

The output or signal obtained is a I-E curve, called cyclic voltammogram or voltammogram that shows the current intensity registered (y-axis) by the system at each applied potential imposed by the system (x-axis). Figure I.

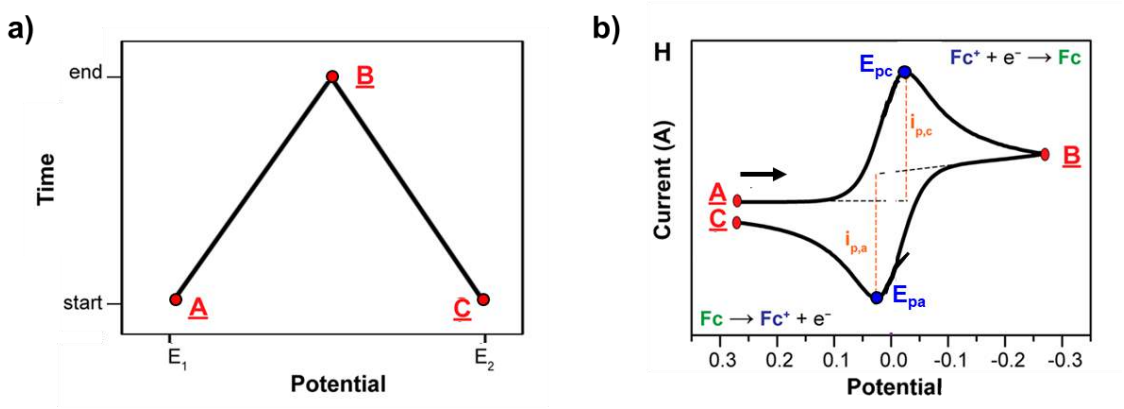

Figure I. a) Triangular signal sent in CV. Initially a potential (A) is applied to the system, which gradually changes over time until reaching a second potential (B) set by the user. The variation of the potential over time is the sweep speed and is determined by the observed slope (dE/dt). Once B is reached, the sweep reverses in the opposite direction until the final potential (C) is reached. b) Classic voltammogram obtained (output) for an ideal and reversible electrochemical system (in the example shown, for the ferrocenium/ferrocene system (Fc^+/Fc)). The direction of the sweep potential scan is indicated with an arrow on the voltammogram. E_{pc} and E_{pa} corresponds to the cathodic and anodic potential peak, respectively. Similarly, Ipc and Ipa are the faradaic current intensity related to the reduction and oxidation, respectively. Images were adapted from reference [1]

CV is a transient electrochemical method since the transport of matter to the electrode takes place only by diffusion. In this case, other mass transport phenomena such as convection and migration do not take place, so the current intensity measured by CV is a function of time.

It is also a non-destructive method since controlled potential microelectrolysis happens only on the surface of the electrode.

For this reason, assuming the following electrochemical reduction (eq. 1) on the electrode surface, the registered current intensity and the velocity of the ET is governed by the following process, where Ox is the oxidant specie, Red the reducing specie and n represents the number of electrons implied in the ET:

$$Ox + ne^- \rightleftharpoons Red \qquad \text{(eq. 1)}$$

I. I. Transport of reagents to the electrode surface by diffusion
II. ET on the electrode surface.
III. Chemical reactions before or after the electron transfer that can take plane on the electrode surface (heterogeneous) or in the bulk solution (homogeneous).
IV. Other reactions that may happen on the electrode surface such as adsorption or desorption processes.

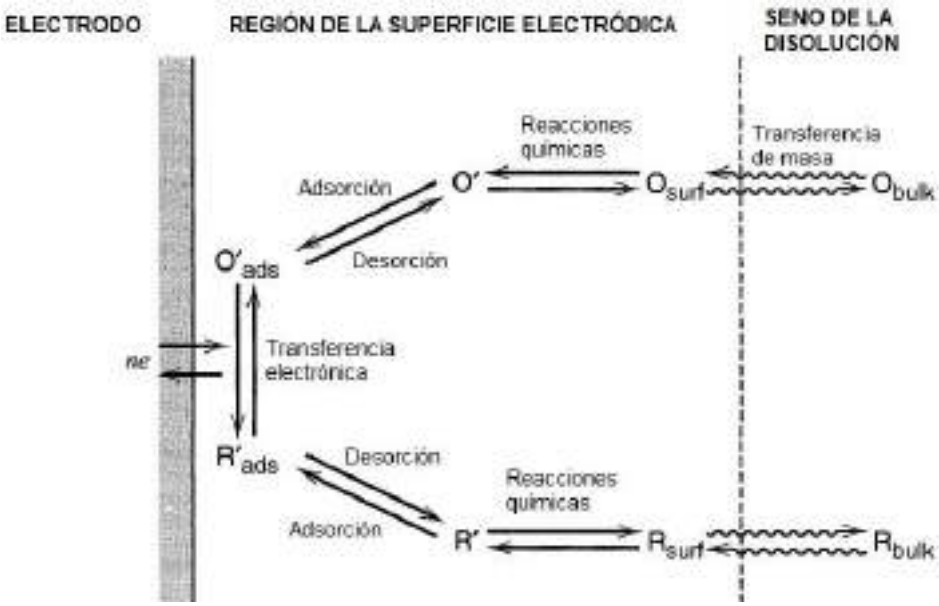

Thus, by means of the I-E responses (voltammogram) it is possible to obtain information about the kinetics of the electrochemical reactions that take place on the electrode surface.

Under conditions where no mass transport takes places, the CV is governed by the Butler-Volmer equation (1):

$$I = \pm FAk_s^{ap} exp\left[\pm\frac{\alpha F}{RT}(E - E^0)\right] \cdot \left\{(C_{Ox})_0 - (C_{Red})_0 \cdot \exp\left[\pm\frac{F}{RT}(E - E^0)\right]\right\} \quad \text{(eq. 2)}$$

$$k_s^{ap} = k_s \exp\left(\frac{-\alpha F\phi}{RT}\right) \quad \text{(eq. 3)}$$

$$k_s = k_f(E = E^0) = k_b(E = E^0) \quad \text{(eq. 4)}$$

C_{ox} and C_{red} are the concentrations of the Ox and Red species on the electrode surface. A is the electrode surface area, F is the Faraday constan (96500 $C \cdot mol^{-1}$), R is the gas constant (8.31 $J \cdot K^{-1} \cdot mol^{-1}$). The applied potential is refereed as E while, E^0 is the standard potential. α is the electronic transfer coefficient ($0 < \alpha < 1$), k_s^{ap} is the apparent ET rate constant, and Φ is the external plane of Helmontz.

However, during the ET the amount of oxidizing (Ox) and reducing (Red) species varies on the electrode surface because the concentration gradient of the species changes and produces diffusional processes. For this reason, Butler-Volmer is no longer valid.

The mass transport (J) follows the Nernst-Planck equation (eq. 5). Note that for transient methods only the diffusional contribution is considered in the equation.

$$J_i(x) = -D_i\frac{dC_i(x)}{dx} + \frac{-z_iF}{RT}D_iC_i\frac{d\phi}{dx} + C_iv(x) \quad \text{(eq. 5)}$$

C_i is the concentration of the electroactive specie (*i*) in the solution, D_i is the diffusion coefficient of *i*, and *x* is the distance to the electrode surface.

Since the I-E curves related to an ET is also time-dependent the final kinetic equation that considers the either the diffusion of species and the ET, are the following:

$$\left(\frac{\delta c_{Ox}}{\delta t}\right) = D_{Ox}\left(\frac{\delta^2 c_{Ox}}{\delta x^2}\right) \quad \text{(eq. 6)}$$

$$\left(\frac{\delta c_{Red}}{\delta t}\right) = D_{Red}\left(\frac{\delta^2 c_{Red}}{\delta x^2}\right) \quad \text{(eq. 7)}$$

In order to solve the differential equation the following boundary conditions require to be applied:

I. Diffusional transport only occurs in one direction because the surface electrode is flat.

II. Diffusional coefficients of Ox and Red species are assumed equal ($D_{Ox} = D_{Red}$)

III. At time t = 0 → x ≥ 0
When: t ≥ 0 y x = ∞ → $c_{Ox} = c_{Ox}$ y $c_{Red} = 0$ (at the bulk solution)

IV. When x = 0 and t > 0 (that is to say, the electrode surface), the Nernst/Volmer equation is fulfilled and there is no accumulation of chemical substances, then:

$$\left(\frac{\delta c_{Ox}}{\delta x}\right) + \left(\frac{\delta c_{Red}}{\delta x}\right) = 0 \qquad \text{(eq. 8)}$$

$$c_{Ox} = c_{Red} \cdot e^{\left(\frac{(E-E^0)F}{RT}\right)} \qquad \text{(eq. 9)}$$

Where E is the applied potential, $E = E_i + vt$ and the current defined as follows:

$$I = FAD \cdot \left(\frac{\delta c_{Ox}}{\delta x}\right) \qquad \text{(eq. 10)}$$

a) Fast Electron Transfer (ET)

For a reversible ET, the value of the intensity as in figure X b), the intensity of the cathodic and anodic peaks are the same ($I_{p,a} = I_{p,c}$) and the value of $E_{p,c}$ and $E_{p,a}$ are constant throughout the range of scanning speeds. This type of behavior indicates that there is no chemical reaction (C) associated with ET.

$$Ox + ne^- \overset{E}{\rightleftharpoons} Red$$

Solving the system of differential equations associated with the concentration variation of the Ox and Red species in this type of electrochemical mechanism, the I-E curve could be defined with the following parameters calculated theoretically by the following equations:

$$I_p = 0.446 \cdot F \cdot A \cdot c \cdot D^{1/2} \cdot \left(\frac{Fv}{RT}\right)^{\frac{1}{2}} \qquad \text{(eq. 11)}$$

$$E_p = E^0 - 1.11 \cdot \left(\frac{RT}{F}\right) \qquad \text{(eq. 12)}$$

$$\Delta E_p = E_p - E_{\frac{p1}{2}} = 2.20 \cdot \left(\frac{RT}{F}\right) \qquad \text{(eq. 13)}$$

Thus, the value of the intensity of the peak is a function of the concentration (c) and the square root of scan rate (v). The current intensity obtained for each sweep speed can be normalized as follows from equation X:

$$\frac{I_p}{c \cdot v^{1/2}} \qquad \text{(eq.14)}$$

This relationship will allow knowing the number of electrons involved in an ET of a problem substance. To do this, different concentrations of an electrochemical substance with ideal reversible behavior (electrochemical calibration pattern) will be prepared, of which the number of electrons involved in the ET is known from references reported in the literature, and the value will be determined by means of the eq X.

Dividing the value obtained for the standard substance by the value found for the problem sample, it will be known how many electrons are involved in the ET.

Overall, for a fast ET where there is no associated C reaction $I_p/c \cdot v^{1/2}$ E_p and ΔE_p should show no dependence on sweep speed.

b) Slow Electron Transfer (ET)

When the electronic transfer takes place slowly, the voltammogram is observed with a large peak separation between E_{pa} and E_{pc}. From a mathematical point of view, two new kinetic parameters α (electronic transfer coefficient) and k_s^{ap} (apparent electronic transfer rate constant) are involved in the previous equations that define the electrochemical parameters.

$$I_p = 0.496 \cdot F \cdot A \cdot c^0 \cdot D^{1/2} \cdot \alpha^{1/2} \cdot v^{1/2} \left(\frac{F \cdot v}{RT}\right)^{1/2} \qquad \text{(eq. 15)}$$

$$E_p = E^0 - 0.78 \cdot \left(\frac{RT}{\alpha F}\right) - \left(\frac{RT}{2F}\right) \cdot ln\left(\frac{\alpha DF}{RT}\right) + \left(\frac{RT}{\alpha F}\right) \cdot \ln k_s^{ap} - \left(\frac{RT}{2\alpha F}\right) \cdot \ln v \quad \text{(eq. 16)}$$

$$\Delta E_p = E_p - E_{\frac{p1}{2}} = 1.875 \cdot \left(\frac{RT}{F\alpha}\right) \qquad \text{(eq. 17)}$$

As can be deduced from the equations, for this type of mechanism, there is a dependence of Ep on the scan rate:

$$\left(\delta E_p / \delta \log v\right) = -\frac{29}{\alpha} \qquad \text{at } 298 \text{ K} \qquad \text{(eq. 18)}$$

For values of ks greater than 1 cm s^{-1}, the ET is considered fast, while if it reaches values of 0.1 cm s-1, it is a slow ET both at low and high v.

From a chemical point of view, in these processes, a stable radical species is formed in the time of voltammetry when it is possible to detect the reversibility of the peak. However, when the radical species is not sufficiently stable in the time of voltammetry (that is, it undergoes a chemical reaction), the voltammogram becomes irreversible.

By applying different scan rate during the CV scan, it will be possible to determine the speed of the associated chemical reaction that will allow us to detect a stable species on that time scale.

i. EC_1 Mechanism: ET coupled to a first order chemical reaction

In this mechanism, a first ET takes place followed by a stage C:

$$Ox + ne^- \overset{E}{\rightleftharpoons} Red \xrightarrow[k]{C} P \qquad \text{(eq.19)}$$

The concentrations of the electroactive species involved in ET are defined as follows:

$$\left(\frac{\delta c_{Ox}}{\delta t}\right) = D_{Ox}\left(\frac{\delta^2 c_{Ox}}{\delta x^2}\right) \qquad \text{(eq. 20)}$$

$$\left(\frac{\delta c_{Red}}{\delta t}\right) = D_{Red}\left(\frac{\delta^2 c_{Red}}{\delta x^2}\right) - k \cdot c_{Red} \qquad \text{(eq. 21)}$$

The system of differential equations is solved by imposing the same boundary conditions. However, in the case of an EC_1 mechanism, the term λ appears, which gives kinetic information related to ET and stage C. Specifically, it measures the competition between both stages.

$$\lambda = \left(\frac{RT}{F}\right)\left(\frac{k}{v}\right) \qquad \text{(eq. 22)}$$

When it happens that f λ → 0 (k → 0 or v → ∞), there is only control by diffusion. In CV, the effect of stage C is not observed, since it takes place more slowly than the diffusion of the species. The electrochemical parameters are therefore calculated in the same way as for a fast ET.

$$I_p = 0.446 \cdot F \cdot A \cdot c^0 \cdot D^{1/2} \cdot \left(\frac{Fv}{RT}\right)^{\frac{1}{2}} \quad \text{(eq. 23)}$$

$$E_p = E^0 - 1.11 \cdot \left(\frac{RT}{F}\right) \quad \text{(eq. 24)}$$

$$\Delta E_p = E_p - E_{\frac{p1}{2}} = 2.20 \cdot \left(\frac{RT}{F}\right) \quad \text{(eq. 25)}$$

$$\left(\frac{\delta E_p}{\delta log v}\right) = 0 \quad \text{(eq. 26)}$$

In a second case where If λ → ∞ (k → ∞ or v → 0), the determining stage of the reaction is stage C. In these cases the term α and Ks are introduced

$$I_p = 0.496 \cdot F \cdot S \cdot c^0 \cdot D^{1/2} \cdot \alpha^{1/2} \cdot v^{1/2} \left(\frac{F}{RT}\right)^{1/2} \quad \text{(eq. 27)}$$

$$E_p = E^0 - 0.78 \cdot \left(\frac{RT}{F}\right) - \left(\frac{RT}{2F}\right) \cdot ln\left(\frac{kc}{v} \cdot \frac{RT}{F}\right) \quad \text{(eq. 28)}$$

$$\Delta E_p = E_p - E_{\frac{p1}{2}} = 1.875 \cdot \left(\frac{RT}{F\alpha}\right) \quad \text{(eq. 29)}$$

$$\left(\frac{\delta E_p}{\delta log v}\right) = -29.6\ (mV) \quad \text{(eq. 30)}$$

Unlike a slow ET where no chemical reaction is coupled, it is the width of the ΔE_p peak. While for a slow ET where there is no C, values of ~94 mV are obtained, for an EC_1 mechanism a value of ~47 mV is obtained.

In addition, the dependence of the Ep with the scanning speed is also a factor that characterizes the EC_1-type mechanisms.

By CV, by modifying the scanning speed, it is possible to obtain a voltammogram with peaks that are reversible (at high speeds) or irreversible (at slow speeds). The speed at which the ET observed in the voltammogram becomes reversible allows knowing the kinetic constant associated with the chemical reaction.

ii. EC_2 Mechanism: ET coupled to a second order chemical reaction

In this type of mechanism, it consists of a first ET stage followed by a second-order chemical reaction. This type of process is typical of dimerizations.

$$Ox + ne^- \overset{E}{\rightleftharpoons} Red \qquad \text{(eq. 31)}$$

$$2\ Red \xrightarrow[k]{C} P \qquad \text{(eq. 32)}$$

The concentrations of the species are defined by the following differential equations:

$$\left(\frac{\delta c_{Ox}}{\delta t}\right) = D_{Ox}\left(\frac{\delta^2 c_{Ox}}{\delta x^2}\right) \qquad \text{(eq. 33)}$$

$$\left(\frac{\delta c_{Red}}{\delta t}\right) = D_{Red}\left(\frac{\delta^2 c_{Red}}{\delta x^2}\right) - 2k \cdot c_{Red} \qquad \text{(eq. 34)}$$

As in the case of an EC_1 mechanism, the term λ gives kinetic information related to the chemical reaction associated with ET.

$$\lambda = \left(\frac{RT}{F}\right)\left(\frac{k}{v}\right) \qquad \text{(eq. 35)}$$

There are two different situations. i) If λ → 0 (occurs when k → 0 or when v → ∞) the process is controlled only by diffusion, so the voltammogram shows a behavior similar to a fast ET. For this case, the equations that determine the electrochemical parameters would be the same as those in section a). ii) When λ → ∞ (in the case where k□∞ or when v → 0), the process is controlled by the chemical reaction. In this case, the following expressions are obtained:

$$I_p = 0.496 \cdot F \cdot S \cdot c^0 \cdot D^{1/2} \cdot \alpha^{1/2} \cdot v^{1/2}\left(\frac{F}{RT}\right)^{1/2} \qquad \text{(eq. 36)}$$

$$E_p = E^0 - 0.78 \cdot \left(\frac{RT}{F}\right) - \left(\frac{RT}{2F}\right) \cdot ln\left(\frac{kc}{v} \cdot \frac{RT}{F}\right) \qquad \text{(eq. 37)}$$

$$\Delta E_p = E_p - E_{\frac{p1}{2}} = 1.875 \cdot \left(\frac{RT}{F\alpha}\right) \qquad \text{(eq. 38)}$$

Thus, the different mechanisms found in this thesis were determined by studying the relationship between the parameters $\delta E_p/\delta log\ v$ and $\delta E_p/\delta log\ c$. Table I.

Table I. Types of electrochemical mechanisms according to the variation of the oxidation/reduction potential peak versus the variation of log of the scan rate and the variation of log of the concentration.

Mechanism	$\delta E_p/\delta log\ v$	$\delta E_p/\delta log\ c$
Fast E	0	0
Slow E	± 29.6 / α	0
EC_1	± 29.6	0
EC_2	± 19.6	± 19.6

Reference:

(1) J. Bard, A.; Faulkner, L. Electrochemical Methods: Fundamentals and Applications, Ed. 2.; Wiley, Ed; Texas, 2001.

Annex II: Screen-Printing Technique

Screen-printing technology is a stamping procedure that consists of the passage of an ink through a mesh with open areas previously defined. With the aid of a stencil, the ink can pass through and deposit it on a substrate (placed at the bottom of the system). Figure II. This technique allows printing a wide variety of shapes and designs, with micrometric precision thanks to the use of photolithographed meshes and controlling the wire density of the mesh.

Currently, screen-printing can be used for the fabrication of electronic devices in any laboratory without the need for a clean room. This technique is characterized by allowing the mass-production of printed systems in a very reproducible way.

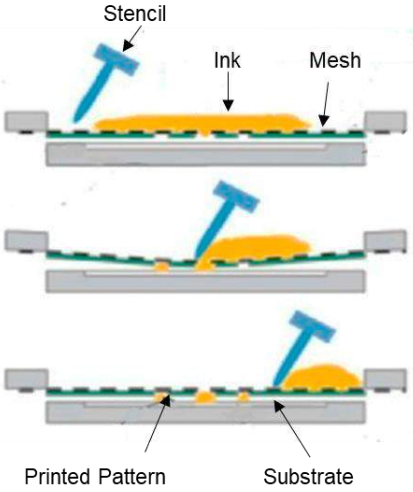

Figure II. Schematic representation of the steps in the screen-printing process.